

NAVAL POSTGRADUATE SCHOOL Monterey, California



19971124 013

DISSERTATION

**EXPERIMENTAL AND COMPUTATIONAL ANALYSIS
OF SEPARATION BUBBLE BEHAVIOR FOR
COMPRESSIBLE, STEADY AND OSCILLATORY
FLOWS OVER A NACA 0012 AIRFOIL
($M_\infty = 0.3$, $Re_c = 540,000$)**

by

Robert D. Van Dyken

March 1997

Dissertation Advisor:

Max F. Platzer

Co-Advisor:

M. S. Chandrasekhara

DTIC QUALITY INSPECTED 2

Approved for public release; distribution is unlimited.

REPORT DOCUMENTATION PAGE

Form Approved
OMB No. 0704-0188

Public reporting burden for this collection of information is estimated to average 1 hour per response, including the time for reviewing instructions, searching existing data sources, gathering and maintaining the data needed, and completing and reviewing the collection of information. Send comments regarding this burden estimate or any other aspect of this collection of information, including suggestions for reducing this burden, to Washington Headquarters Services, Directorate for Information Operations and Reports, 1215 Jefferson Davis Highway, Suite 1204, Arlington, VA 22202-4302, and to the Office of Management and Budget, Paperwork Reduction Project (0704-0188), Washington, DC 20503.

1. AGENCY USE ONLY (Leave blank)		2. REPORT DATE March 1997		3. REPORT TYPE AND DATES COVERED PhD. Dissertation	
4. TITLE AND SUBTITLE EXPERIMENTAL AND COMPUTATIONAL ANALYSIS OF SEPARATION BUBBLE BEHAVIOR FOR COMPRESSIBLE, STEADY AND OSCILLATORY FLOWS OVER A NACA 0012 AIRFOIL ($M_\infty = 0.3$, $Re_c = 540,000$)				5. FUNDING NUMBERS	
6. AUTHOR(S) Robert D. Van Dyken					
7. PERFORMING ORGANIZATION NAME(S) AND ADDRESS(ES) Naval Postgraduate School Monterey, CA 93943-5000				8. PERFORMING ORGANIZATION REPORT NUMBER	
9. SPONSORING/MONITORING AGENCY NAME(S) AND ADDRESS(ES)				10. SPONSORING/MONITORING AGENCY REPORT NUMBER	
11. SUPPLEMENTARY NOTES The views expressed in this thesis are those of the author and do not reflect the official policy or position of the Department of Defense or the U.S. Government.					
12a. DISTRIBUTION/AVAILABILITY STATEMENT Approved for public release; distribution is unlimited.				12b. DISTRIBUTION CODE	
13. ABSTRACT (Maximum 200 words) In this thesis, the separation bubble behavior and its effect on the steady and dynamic stall characteristics of a thin airfoil in a compressible flow at a transitional Reynolds number was studied. For such flows, laminar separation occurs near the airfoil leading edge, but turbulent reattachment occurs within a short distance downstream, forming a separation bubble in the underlying region. Two experimental techniques, point diffraction interferometry (PDI) and laser doppler velocimetry (LDV), were used to acquire detailed flowfield information that showed the development of the leading-edge separation bubble and its subsequent bursting at higher angles of attack. The initiation of the stall process from the leading-edge separation bubble as opposed to trailing-edge flow reversal pointed to the need for transitional flow analysis. Both in the boundary layer and Reynolds-averaged, Navier-Stokes (N-S) analysis methods, transition models were incorporated to determine the location and extent of the transition zone that best modeled the measured separation bubble behavior. Computed results for steady flow gave remarkable agreement with the measurements. The computations compared favorably with the measurements for an airfoil oscillating in pitch about the quarter-chord point during the airfoil upstroke. However, the computations did not predict the light stall and vorticity-shedding process that was measured during the airfoil downstroke.					
14. SUBJECT TERMS Airfoil Flows, Separation Bubbles, Light Dynamic Stall, Transition Modeling, Vorticity Shedding Processes				15. NUMBER OF PAGES 203	
				16. PRICE CODE	
17. SECURITY CLASSIFICATION OF REPORT UNCLASSIFIED	18. SECURITY CLASSIFICATION OF THIS PAGE UNCLASSIFIED	19. SECURITY CLASSIFICATION OF ABSTRACT UNCLASSIFIED	20. LIMITATION OF ABSTRACT SAR		

Approved for public release; distribution is unlimited.

EXPERIMENTAL AND COMPUTATIONAL ANALYSIS OF
SEPARATION BUBBLE BEHAVIOR FOR COMPRESSIBLE,
STEADY AND OSCILLATORY FLOWS OVER A NACA 0012
AIRFOIL AT $M=0.3$ AND A REYNOLDS NUMBER OF 540,000

Robert D. van Dyken

Aeronautical Engineer, Naval Air Warfare Center, Weapons Division

B.S., Montana State University, 1971

M.S., California State University at Northridge, 1988

Submitted in partial fulfillment of the requirements for the degree of

DOCTOR OF PHILOSOPHY IN AERONAUTICAL ENGINEERING

from the

NAVAL POSTGRADUATE SCHOOL

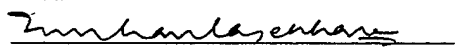
March 1997

Author:



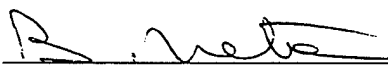
Robert D. van Dyken

Approved by:



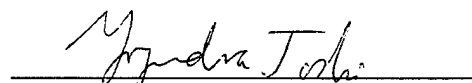
M.S. Chandrasekhara, Co-Advisor

Research Professor of Aeronautics



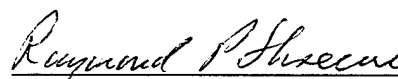
B. Neta

Professor of Mathematics



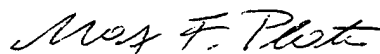
Y. Joshi, Associate Professor of

Mechanical Engineering



R.P. Shreeve

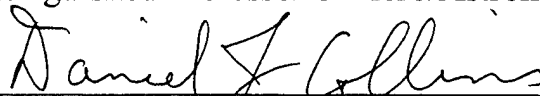
Professor of Aero/Astronautics



M.F. Platz, Dissertation Supervisor

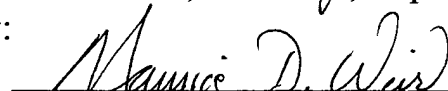
Distinguished Professor of Aero/Astronautics

Approved by:



D.J. Collins, Chairman, Department of Aero/Astronautics

Approved by:



Maurice D. Weir, Associate Provost of Instruction

ABSTRACT

In this thesis, the separation bubble behavior and its effect on the steady and dynamic stall characteristics of a thin airfoil in a compressible flow at a transitional Reynolds number was studied. For such flows, laminar separation occurs near the airfoil leading edge, but turbulent reattachment occurs within a short distance downstream, forming a separation bubble in the underlying region. Two experimental techniques, point diffraction interferometry (PDI) and laser doppler velocimetry (LDV), were used to acquire detailed flowfield information that showed the development of the leading-edge separation bubble and its subsequent bursting at higher angles of attack. The initiation of the stall process from the leading-edge separation bubble as opposed to trailing-edge flow reversal pointed to the need for transitional flow analysis. Both in the boundary layer and Reynolds-averaged, Navier-Stokes (N-S) analysis methods, transition models were incorporated to determine the location and extent of the transition zone that best modeled the measured separation bubble behavior. Computed results for steady flow gave remarkable agreement with the measurements. The computations compared favorably with the measurements for an airfoil oscillating in pitch about the quarter-chord point during the airfoil upstroke. However, the computations did not predict the light stall and vorticity-shedding process that was measured during the airfoil downstroke.

TABLE OF CONTENTS

I. INTRODUCTION	1
II. REVIEW OF LOW-SPEED AIRFOIL FLOWS WITH LEADING-EDGE SEPARATION BUBBLES	5
A. INTRODUCTION	5
B. FUNDAMENTAL FLOW PHYSICS OF LEADING-EDGE SEPARATION BUBBLES	5
C. TRANSITION ONSET PREDICTION	10
D. TRANSITION LENGTH PREDICTION	10
E. EFFECT OF AIRFOIL OSCILLATION ON LEADING-EDGE SEPARATION BUBBLES	11
F. ANALYSIS METHODS FOR AIRFOIL FLOWS WITH SEPARATION BUBBLES	12
III. EXPERIMENTAL SETUP AND MEASUREMENT TECHNIQUES	15
A. INTRODUCTION	15
B. EXPERIMENTAL TEST FACILITY	15
C. UNSTEADY LDV MEASUREMENT TECHNIQUE	17
D. STROBOSCOPIC PDI MEASUREMENT TECHNIQUE	20
1. Implementation	20
2. Fringe Counting To Determine Mach Number	22
E. MEASUREMENT UNCERTAINTIES	23
F. DATA VALIDATION (LDV SYSTEM)	24
IV. DESCRIPTION OF COMPUTATIONAL ANALYSIS METHODS	31
A. UNSTEADY POTENTIAL FLOW CODE (UPOT)	31
1. Introduction	31
2. Theory and Numerical Method	32
B. STEADY BOUNDARY LAYER FLOW CODE	35
1. Introduction	35
2. Theory and Models	36
3. Numerical Implementation	38
C. NAVIER-STOKES (N-S) CODE METHODOLOGY	44
1. Introduction	44
2. Numerical Method	45
3. Numerical Implementation	46

4. Transition Modeling	48
5. Boundary Conditions and Gridding	51
D. COMPUTATIONAL UNCERTAINTIES	52
V. EXPERIMENTAL RESULTS	55
A. FLOW OVER STEADY NACA 0012 AIRFOIL	55
1. Pressure Distributions From the PDI Interferograms	60
2. Mach Number From PDI Density Ratio	62
3. U-Component (LDV) Velocity Contours	63
B. UNSTEADY/OSCILLATING NACA 0012 AIRFOIL	66
1. Deep Dynamic Stall ($\alpha = 10^\circ - 10^\circ \sin \omega t$)	66
2. Light Dynamic Stall Flow ($\alpha = 10^\circ - 2^\circ \sin \omega t$)	74
a. PDI Images	74
b. Pressure Distribution From PDI Images	76
c. Phase Distribution of LDV Velocities at (X/C) Locations	78
d. LDV Velocity Profiles (U / U_∞)	82
e. LDV Velocity Magnitude Contours	89
f. LDV Vorticity Magnitude Contours	89
VI. COMPUTED RESULTS	97
A. FLOW OVER STEADY NACA 0012 AIRFOIL	97
1. Pressure Distributions	97
2. Skin-Friction Coefficient Distribution on Suction Surface	100
3. Displacement Thickness Distribution on Suction Surface	105
4. Boundary-Layer Velocity Profiles on Suction Surface	106
B. OSCILLATORY FLOW OVER NACA 0012 AIRFOIL	117
1. UPOT Pressure Distributions ($\alpha = 10^\circ - 10^\circ \sin \omega t$)	117
2. UPOT Pressure Distributions ($\alpha = 10^\circ - 2^\circ \sin \omega t$)	120
3. N-S Pressure Distributions ($\alpha = 10^\circ - 2^\circ \sin \omega t$)	124
4. N-S Skin-Friction Coefficients	127
5. N-S Velocity Profiles	128
6. N-S Lift, Drag, and Moment	131
VII. COMPARISONS OF MEASURED AND COMPUTED RESULTS	135
A. INTRODUCTION	136
B. STEADY FLOW RESULTS	137
1. Transition Onset and Length Effects	137
2. Density Contour Comparisons	140

3. Pressure Distribution and Skin-Friction Comparisons	144
4. Velocity Profile Comparisons	149
C. OSCILLATING AIRFOIL FLOW ($\alpha = 10^\circ - 2^\circ \sin \omega t$, $k = 0.1$)	152
1. Density Contour Comparisons	153
2. Pressure Distributions and Computed Skin-Friction Coefficients	157
3. Transition Onset, Flow Separation and Reattachment	160
4. Velocity Profile Comparisons	162
VIII. CONCLUSIONS AND RECOMMENDATIONS	167
REFERENCES	171
INITIAL DISTRIBUTION LIST	179

LIST OF FIGURES

1.1	Dynamic Stall Events on the NACA 0012 Airfoil	2
2.1	Airfoil Performance as a Function of Chord Reynolds Number	7
2.2	Structure of Flow With Laminar Separation Bubble	8
3.1	Side View of the Compressible Dynamic Stall Facility	16
3.2	Schematic of the LDV System in Use in the CDSF	18
3.3	Unsteady-Flow LDV Data-Acquisition-Method Schematic	18
3.4	Measurement Locations (6x21) Overlaid on Computational Grid (275x81). $\alpha = 8^\circ$, NACA 0012 Airfoil	19
3.5	Principle of Point Diffraction Interferometry	20
3.6	Schematic of the PDI Optical Arrangement	21
3.7	Histograms of Normalized U Component Velocity at $x/c = 0.000$; $y/c = 0.083$. $M_\infty = 0.3$, $\alpha = 8^\circ$, $k = 0.0$, $Re = 540,000$	25
3.8	Histograms of Normalized U- and V-component Velocities at $x/c =$ -0.133 , $y/c = 0.083$. $M_\infty = 0.3$, $\alpha = 10^\circ - 10^\circ \sin \omega t = 10^\circ$ (up), $k = 0.1$	26
3.9	Phase Distribution of Normalized U- and V-component Velocities at $x/c = -0.133$, $y/c = 0.083$. $M_\infty = 0.3$, $\alpha = 10^\circ - 10^\circ \sin \omega t$, $k = 0.1$	27
3.10	Histograms of Normalized U- and V-component Velocities at $x/c =$ 0.033 ; $y/c = 0.083$. $M_\infty = 0.3$, $\alpha = 10^\circ - 2^\circ \sin \omega t = 10$ degrees (up).	28
3.11	Phase Distribution of Normalized U- and V-component Velocities at $x/c = 0.033$, $y/c = 0.083$. $M_\infty = 0.3$, $\alpha = 10^\circ - 2^\circ \sin \omega t$, $k = 0.1$	29
4.1	Extension of Panel Methods Representation for Unsteady Flow	34
4.2	Net Rectangle for Difference Approximations	40
5.1	Interferogram of the Flow Near the Airfoil Leading Edge. $M_\infty = 0.3$, $\alpha = 0^\circ$, $k = 0.0$, $Re = 540,000$	56
5.2	Interferogram of the Flow Near the Airfoil Leading Edge. $M_\infty = 0.3$, $\alpha = 6^\circ$, $k = 0.0$, $Re = 540,000$	56
5.3	Interferogram of the Flow Near the Airfoil Leading Edge. $M_\infty = 0.3$, $\alpha = 8^\circ$, $k = 0.0$, $Re = 540,000$	57
5.4	Interferogram of the Flow Near the Airfoil Leading Edge. $M_\infty = 0.3$, $\alpha = 10^\circ$, $k = 0.0$, $Re = 540,000$	58
5.5	Interferogram of the Flow Near the Airfoil Leading Edge. $M_\infty = 0.3$, $\alpha = 11.95^\circ$, $k = 0.0$, $Re = 540,000$	59

5.6	Interferogram of the Flow Near the Airfoil Leading Edge. $M_\infty = 0.3$, $\alpha = 12.05^\circ$, $k = 0.0$, $Re = 540,000$	59
5.7	Pressure Distributions Derived from PDI Measurements. $M_\infty = 0.3$, $\alpha = 6^\circ$, 8° , and 10° , $k = 0.0$, $Re = 540,000$	61
5.8	Pressure Distributions Derived from PDI Measurements. $M_\infty = 0.3$, $\alpha = 7^\circ$, 9° , and 11° , $k = 0.0$, $Re = 540,000$	61
5.9	Pressure Distributions Derived from PDI Measurements. $M_\infty = 0.3$, $\alpha = 11.95^\circ$ and 12.05° , $k = 0.0$, $Re = 540,000$	62
5.10	Density Contours from Interferograms in Flow Near Airfoil Leading Edge. $M_\infty = 0.3$, $\alpha = 10^\circ$, $k = 0.0$, $Re = 540,000$	63
5.11	Normalized Velocity Contours (U-component, LDV) Near the Airfoil Leading Edge. $M_\infty = 0.3$, $\alpha = 8^\circ$, $k = 0.0$, $Re = 540,000$	64
5.12	Normalized Velocity Contours (U-component, LDV) Near the Airfoil Leading Edge. $M_\infty = 0.3$, $\alpha = 12.05^\circ$, $k = 0.0$, $Re = 540,000$	65
5.13	Interferograms of the Flow Near the Leading Edge of the Oscillating Airfoil. $M_\infty = 0.3$, $\alpha = 10^\circ - 10^\circ \sin \omega t$, $k = 0.1$	67
5.14	Interferograms of the Flow Near the Leading Edge of the Oscillating Airfoil. $M_\infty = 0.3$, $\alpha = 10^\circ - 10^\circ \sin \omega t$, $k = 0.1$	68
5.15	Phase Distribution of U-Component Velocities at $x/c = -0.100$. (Velocity offset by $0.2 U_\infty$ at each height.) $M_\infty = 0.3$, $\alpha = 10^\circ - 10^\circ \sin \omega t$, $k = 0.1$	69
5.16	Phase Distribution of V-Component Velocities at $x/c = -0.100$. (Velocity offset by $0.2 U_\infty$ at each height.) $M_\infty = 0.3$, $\alpha = 10^\circ - 10^\circ \sin \omega t$, $k = 0.1$	70
5.17	Phase Distribution of U-Component Velocities at $x/c = 0.067$. (Velocity offset by $0.2 U_\infty$ at each height.) $M_\infty = 0.3$, $\alpha = 10^\circ - 10^\circ \sin \omega t$, $k = 0.1$	71
5.18	Phase Distribution of V-Component Velocities at $x/c = 0.067$. (Velocity offset by $0.2 U_\infty$ at each height.) $M_\infty = 0.3$, $\alpha = 10^\circ - 10^\circ \sin \omega t$, $k = 0.1$	72
5.19	Velocity Magnitude $ V $ Profiles at $x/c = 0.067$. (Profiles offset by $0.2 U_\infty$ at each AOA.) $M_\infty = 0.3$, $\alpha = 10^\circ - 10^\circ \sin \omega t$, $k = 0.1$	73
5.20	Interferograms of the Flow Near the Airfoil Leading Edge. $M_\infty = 0.3$, $\alpha = 10^\circ - 2^\circ \sin \omega t$, $k = 0.1$	75

5.21	Pressure Distributions Near the Airfoil Leading Edge (upstroke). $M_\infty = 0.3, \alpha = 10^\circ - 2^\circ \sin \omega t, k = 0.1$	77
5.22	Pressure Distributions Near the Airfoil Leading Edge (downstroke). $M_\infty = 0.3, \alpha = 10^\circ - 2^\circ \sin \omega t, k = 0.1$	78
5.23	Phase Distribution of Normalized U- and V-Component Velocities at $x/c = -0.100$. (Velocity offset by $0.2 U_\infty$ at each height.) $M_\infty = 0.3, \alpha = 10^\circ - 2^\circ \sin \omega t, k = 0.1$	80
5.24	Phase Distribution of Normalized U- and V-Component Velocities at $x/c = 0.017$. (Velocity offset by $0.2 U_\infty$ at each height.) $M_\infty = 0.3, \alpha = 10^\circ - 2^\circ \sin \omega t, k = 0.1$	81
5.25	Phase Distribution of Normalized U- and V-Component Velocities at $x/c = 0.033$. (Velocity offset by $0.2 U_\infty$ at each height.) $M_\infty = 0.3, \alpha = 10^\circ - 2^\circ \sin \omega t, k = 0.1$	83
5.26	U-Component Velocity Profiles at $x/c = -0.10$ and $x/c = 0.00$. (Velocity offset by $0.2 U_\infty$ at each AOA.) $M_\infty = 0.3, \alpha = 10^\circ - 2^\circ \sin \omega t, k = 0.1$	84
5.27	U-Component Velocity Profiles at $x/c = 0.017$ and $x/c = 0.033$. (Velocity offset by $0.2 U_\infty$ at each AOA.) $M_\infty = 0.3, \alpha = 10^\circ - 2^\circ \sin \omega t, k = 0.1$	85
5.28	U-Component Velocity Profiles at $x/c = 0.067$ and $x/c = 0.083$. (Velocity offset by $0.2 U_\infty$ at each AOA.) $M_\infty = 0.3, \alpha = 10^\circ - 2^\circ \sin \omega t, k = 0.1$	87
5.29	U-Component Velocity Profiles at $x/c = 0.100$ and $x/c = 0.133$. (Velocity offset by $0.2 U_\infty$ at each AOA.) $M_\infty = 0.3, \alpha = 10^\circ - 2^\circ \sin \omega t, k = 0.1$	88
5.30	Velocity Magnitude $ V $ Contours Near Airfoil Leading Edge. $M_\infty = 0.3, \alpha = 10^\circ - 2^\circ \sin \omega t = 9^\circ$ (up / down), $k = 0.1$	90
5.31	Vorticity Contours (z-Component) Near the Airfoil Leading Edge. $M_\infty = 0.3, \alpha = 10^\circ - 2^\circ \sin \omega t = 8^\circ$ (bottom) and 12° (top), $k = 0.1$	91
5.32	Vorticity Contours (z-Component) Near the Airfoil Leading Edge. $M_\infty = 0.3, \alpha = 10^\circ - 2^\circ \sin \omega t = 11^\circ$ (up) and 11.53° (down), $k = 0.1$	93
5.33	Vorticity Contours (z-Component) Near the Airfoil Leading Edge. $M_\infty = 0.3, \alpha = 10^\circ - 2^\circ \sin \omega t = 10.68^\circ$ and 10° (down), $k = 0.1$	94
6.1	Surface Pressure Distribution Near Airfoil Leading Edge, UPOT. $\alpha = 0^\circ, 4^\circ, 8^\circ$ and 12°	98

6.2	Surface Pressure Distribution Near Airfoil Leading Edge, UPOT. $\alpha = 2^\circ, 6^\circ$ and 10°	98
6.3	Surface Pressure Distribution Near Airfoil Leading Edge, UPOT and N-S Codes. N-S Analysis, $M_\infty = 0.3$, $\alpha = 0^\circ, 6^\circ$ and 12° , $Re = 540,000$, $G_{\gamma_{tr}} = 200$	99
6.4	Surface Pressure Distribution Near Airfoil Leading Edge, N-S Code, Transition Onset Locations Specified. $M_\infty = 0.3$, $\alpha = 8^\circ, 10^\circ$ and 12° , $Re = 540,000$, $G_{\gamma_{tr}} = 200$, or 100 for (x/c) transition = 0.0177	100
6.5	Suction Surface Skin-Friction Distributions, Panel/Boundary- Layer Code (100 Panels), Transition Onset Specified	102
6.6	Suction Surface Skin-Friction Distributions, Panel/Boundary- Layer Code (214 Panels), Transition Onset Specified	102
6.7	Suction Surface Skin-Friction Distributions, (N-S Code, 275x81), Transition Onset Locations Specified, $M_\infty = 0.3$, $Re = 540,000$, $G_{\gamma_{tr}} = 200$	104
6.8	Suction Surface Displacement Thickness Distributions, Panel/ Boundary-Layer Code (214 Panels), Transition Onset Locations Specified. $Re = 540,000$	105
6.9	Suction Surface Displacement Thickness Distributions, N-S Code, 275x81, Transition Onset Locations Specified. $M_\infty = 0.3$, $Re = 540,000$, $G_{\gamma_{tr}} = 200$	106
6.10	Boundary-Layer Velocity Profiles (Panel/Boundary-Layer Code - 214 Panels). $\alpha = 0^\circ$, $(x/c)_{tr} = 0.515$, $Re = 540,000$	107
6.11	Boundary-Layer Velocity Profiles (Panel/Boundary-Layer Code - 214 Panels). $\alpha = 2^\circ$, $(x/c)_{tr} = 0.35$, $Re = 540,000$	107
6.12	Boundary-Layer Velocity Profiles (Panel/Boundary-Layer- Code - 214 Panels). $\alpha = 4^\circ$, $(x/c)_{tr} = 0.177$, $Re = 540,000$	108
6.13	Boundary-Layer Velocity Profile Predictions (Panel/Boundary- Layer Code - 214 Panels). $\alpha = 6^\circ$, $(x/c)_{tr} = 0.023$	109
6.14	Boundary-Layer Velocity Profiles (Panel/Boundary-Layer Code - 214 Panels). $\alpha = 8^\circ$, $(x/c)_{tr} = 0.022$, $Re = 540,000$	109
6.15	Boundary-Layer Velocity Profiles (Panel/Boundary-Layer Code- 100 and 214 Panels). $\alpha = 6^\circ$, $(x/c)_{tr} = 0.023$, $Re = 540,000$	110

6.16	Boundary-Layer Velocity Profiles (N-S Code, 275x81). $M_\infty = 0.3$, $\alpha = 0^\circ$, $Re = 540,000$	111
6.17	Boundary-Layer Velocity Profiles (N-S Code, 275x81). $M_\infty = 0.3$, $\alpha = 4^\circ$, $Re = 540,000$	112
6.18	Boundary-Layer Velocity Profiles (N-S Code, 275x81). $M_\infty = 0.3$, $\alpha = 8^\circ$, $Re = 540,000$	113
6.19	Boundary-Layer Velocity Profiles (N-S Code, 275x81). $M_\infty = 0.3$, $\alpha = 10^\circ$, $Re = 540,000$	114
6.20	Boundary-Layer Velocity Profiles (N-S Code, 275x81). $M_\infty = 0.3$, $\alpha = 12^\circ$, $Re = 540,000$	115
6.21	Boundary-Layer Velocity Profile Comparisons (N-S and Panel/ Boundary-Layer Codes), $\alpha = 0^\circ$, $Re = 540,000$; N - S Analysis, $M_\infty = 0.3$	116
6.22	Boundary-Layer Velocity Profile Comparisons (N-S and Panel/ Boundary-Layer Codes), $\alpha = 4^\circ$, $Re = 540,000$; N - S Analysis, $M_\infty = 0.3$	116
6.23	Unsteady Surface Pressure Distributions Near the Airfoil Leading Edge (UPOT). $\alpha = 10^\circ - 10^\circ \sin \omega t = 8^\circ, 10^\circ$ and 12° (up / down), $k = 0.1$	118
6.24	Steady and Unsteady Surface Pressure Distributions Near the Airfoil Leading Edge (UPOT). $\alpha = 10^\circ - 10^\circ \sin \omega t = 12^\circ$ (up), $k = 0.1, 0.2, 0.5$ and 1.0	119
6.25	Unsteady Surface Pressure Distributions Near the Airfoil Leading Edge (UPOT). $k = 0.1, 0.2$, and 0.5	120
6.26	Unsteady Surface Pressure Distributions Near the Airfoil Leading Edge (UPOT). $k = 0.1, 0.2, 0.5$, and 1.0	122
6.27	Transition Onset Locations for Steady and Oscillatory Airfoil Computations. $M_\infty = 0.3$, $\alpha = 10^\circ - 2^\circ \sin \omega t$, $k = 0.0$ and 0.1 , $Re = 540,000$	124
6.28	Unsteady Surface Pressure Coefficients Near the Airfoil Leading Edge, (N-S Code, 275x81). $M_\infty = 0.3$, $\alpha = 10^\circ - 2^\circ \sin \omega t$, $k = 0.1$, $G_{\gamma_{tr}} = 200$	125

6.29	Unsteady Surface Pressure Coefficient near the Airfoil Leading Edge, (UPOT and N-S Codes). $\alpha = 10^\circ - 2^\circ \sin \omega t = 8^\circ$ (bottom), 10° (up / down), 12° (top), $k = 0.1$. N-S Analysis, $M_\infty = 0.3$, $Re = 540,000$, $G_{\gamma_{tr}} = 200$	126
6.30	Skin-Friction Coefficient Distributions (N-S Code, 275x81). $M_\infty = 0.3$, $\alpha = 10^\circ - 2^\circ \sin \omega t = 8^\circ, 8.8^\circ, 10^\circ$ and 11.2° , $k = 0.1$, $G_{\gamma_{tr}} = 200$	127
6.31	Boundary-Layer Velocity Profiles (N-S Code, 275x 81). $M_\infty = 0.3$, $\alpha = 10^\circ - 2^\circ \sin \omega t = 10^\circ$ (up), $k = 0.1$, $G_{\gamma_{tr}} = 200$	128
6.32	Boundary-Layer Velocity Profiles (N-S Code, 275x 81). $M_\infty = 0.3$, $\alpha = 10^\circ - 2^\circ \sin \omega t$, $k = 0.1$, $G_{\gamma_{tr}} = 200$	130
6.33	Unsteady Computed Lift, Drag, and Pitching Moment Coefficients (Panel/Boundary Layer and N-S Codes). N-S Analysis, $M_\infty = 0.3$, $G_{\gamma_{tr}} = 200$	132
7.1	Effect of ($G_{\gamma_{tr}}$) Transition Value on Intermittency Distribution. $M_\infty = 0.3$, $\alpha = 8^\circ$, $Re = 540,000$, $(x / c)_{tr} = 0.04$	138
7.2	Effect of ($G_{\gamma_{tr}}$) Transition Value on Pressure and Skin-Friction Distributions. $M_\infty = 0.3$, $\alpha = 8^\circ$, $(x / c)_{tr} = 0.04$	139
7.3	Effect of Transition Onset Location on Pressure and Skin-Friction Distributions. $M_\infty = 0.3$, $\alpha = 8^\circ$, $Re = 540,000$, $G_{\gamma_{tr}} = 200$	140
7.4	Computed and Measured Density Contours (PDI) Near the Airfoil Leading Edge. $M_\infty = 0.3$, $\alpha = 0^\circ$, $Re = 540,000$	141
7.5	Computed and Measured Density Contours (PDI) Near the Airfoil Leading Edge. $M_\infty = 0.3$, $\alpha = 6^\circ$, $Re = 540,000$	142
7.6	Computed and Measured Density Contours (PDI) Near the Airfoil Leading Edge. $M_\infty = 0.3$, $\alpha = 10^\circ$, $Re = 540,000$	143
7.7	Computed and Measured Density Contours (PDI) Near the Airfoil Leading Edge. $M_\infty = 0.3$, $\alpha = 11.9^\circ$, $Re = 540,000$	144
7.8	Computed and PDI Derived Pressure Distributions Near the Airfoil Leading Edge. $M_\infty = 0.3$, $\alpha = 6^\circ$, $Re = 540,000$, $(x / c)_{tr} = 0.04$, $G_{\gamma_{tr}} = 200$	145
7.9	Computed and PDI Derived Pressure Distributions Near the Airfoil Leading Edge. $M_\infty = 0.3$, $\alpha = 8^\circ$, $Re = 540,000$, $(x / c)_{tr} = 0.034$, $G_{\gamma_{tr}} = 200$	146

7.10	Computed and PDI Derived Pressure Distributions Near the Airfoil Leading Edge. $M_\infty = 0.3$, $\alpha = 10^\circ$, $Re = 540,000$, $(x/c)_{tr} = 0.023$, $G_{\gamma_{tr}} = 200$	147
7.11	Computed and PDI Derived Pressure Distributions Near the Airfoil Leading Edge. $M_\infty = 0.3$, $\alpha = 12^\circ$, $Re = 540,000$, $(x/c)_{tr} = 0.012$, $G_{\gamma_{tr}} = 200$	148
7.12	Angle-of-Attack Effect on Intermittency, Transition Onset Specified. $M_\infty = 0.3$, $\alpha = 8^\circ$, $Re = 540,000$, $G_{\gamma_{tr}} = 200$	149
7.13	Computed and Measured Velocity Profiles Near the Airfoil Leading Edge. $M_\infty = 0.3$, $\alpha = 8^\circ$, $Re = 540,000$	150
7.14	Computed and Measured Velocity Profiles Near the Airfoil Leading Edge. $M_\infty = 0.3$, $\alpha = 10^\circ$, $Re = 540,000$	151
7.15	Computed and Measured Velocity Profiles Near the Airfoil Leading Edge. $M_\infty = 0.3$, $\alpha = 11.95^\circ$, $Re = 540,000$	152
7.16	Computed and Measured Density Contours (PDI) Near the Airfoil Leading Edge. $M_\infty = 0.3$, $\alpha = 10^\circ - 2^\circ \sin \omega t = 8^\circ$, $k = 0.1$, $(x/c)_{tr} = 0.025$, $G_{\gamma_{tr}} = 200$	154
7.17	Computed and Measured Density Contours (PDI) Near the Airfoil Leading Edge $M_\infty = 0.3$, $\alpha = 10^\circ - 2^\circ \sin \omega t = 8.8^\circ(\text{up})$, $k = 0.1$, $(x/c)_{tr} = 0.025$, $G_{\gamma_{tr}} = 200$	155
7.18	Computed and Measured Density Contours (PDI) Near the Airfoil Leading Edge. $M_\infty = 0.3$, $\alpha = 10^\circ - 2^\circ \sin \omega t = 10^\circ(\text{up})$, $k = 0.1$, $(x/c)_{tr} = 0.025$, $G_{\gamma_{tr}} = 200$	156
7.19	Computed and Measured Density Contours (PDI) Near the Airfoil Leading Edge. $M_\infty = 0.3$, $\alpha = 10^\circ - 2^\circ \sin \omega t = 11.2^\circ(\text{up})$, $k = 0.1$, $(x/c)_{tr} = 0.025$, $G_{\gamma_{tr}} = 200$	157
7.20	Computed and PDI Derived Pressure Distributions Near the Airfoil Leading Edge. $M_\infty = 0.3$, $\alpha = 10^\circ - 2^\circ \sin \omega t = 8$ and 12° , $k = 0.1$, $(x/c)_{tr} = 0.025$ and 0.012 , $G_{\gamma_{tr}} = 200$	159
7.21	Computed and PDI Derived Pressure Distributions Near the Airfoil Leading Edge. $M_\infty = 0.3$, $\alpha = 10^\circ - 2^\circ \sin \omega t = 10^\circ(\text{up / down})$, $k = 0.1$, $(x/c)_{tr} = 0.025$ and 0.020 , $G_{\gamma_{tr}} = 200$	159
7.22	Flow Separation and Reattachment Estimates by Steady and Oscillatory Computations. $M_\infty = 0.3$, $\alpha = 10^\circ - 2^\circ \sin \omega t$, $k = 0.1$	161

7.23	Computed and Measured Velocity Profiles Near the Airfoil Leading Edge. $M_\infty = 0.3$, $\alpha = 10^\circ - 2^\circ \sin \omega t = 8^\circ$, $k = 0.1$	164
7.24	Computed and Measured Velocity Profiles Near the Airfoil Leading Edge. $M_\infty = 0.3$, $\alpha = 10^\circ - 2^\circ \sin \omega t = 8.8^\circ(\text{up})$, $k = 0.1$	164
7.25	Computed and Measured Velocity Profiles Near the Airfoil Leading Edge, $M_\infty = 0.3$, $\alpha = 10^\circ - 2^\circ \sin \omega t = 10 \text{ degrees}(\text{up})$, $k = 0.1$	165
7.26	Computed and Measured Velocity Profiles Near the Airfoil Leading Edge. $M_\infty = 0.3$, $\alpha = 10^\circ - 2^\circ \sin \omega t = 11.2^\circ(\text{up})$, $k = 0.1$	166
8.1	Transition Onset and Transition Length Values for NACA 0012 Airfoil Flow, $M_\infty = 0.3$, $0^\circ < \alpha < 12^\circ$, $10^4 < \text{Re} < 10^6$	169

LIST OF SYMBOLS, ACRONYMS, AND/OR ABBREVIATIONS

AC	alternating current
BL2D	boundary layer equation based code
CDSF	Compressible Dynamic Stall Facility (NASA Ames Research Center)
C_f	local skin-friction coefficient
FML	Fluid Mechanics Laboratory (NASA Ames Research Center)
Hz	hertz, cycles per second
L/D	lift to drag ratio
LDV	laser doppler velocimetry
M_∞	free-stream Mach number
N-S	Navier-Stokes
QPLOT	engineering data plotting package (VAX system)
PDI	point diffraction interferometry
PSE	Parabolized Stability Equation
PSL	polystyrene latex particles
Re	Reynolds Number, based on airfoil chord
RMS	root mean square or standard deviation of recorded laser particles
U_∞	free-stream velocity
UPOT	Unsteady Potential Flow Panel Code
α	angle of attack (also AOA)
γ	vorticity
$\gamma_{tr}(x)$	intermittency (% of flow having turbulent characteristics)
μm	micrometer (10^{-6})
μs	microsecond (10^{-6})
σ	range of acceptable data from the mean value
2-D	two-dimensional

ACKNOWLEDGMENTS

To the Naval Air Warfare Center Weapons Division (NAWCWPNS), China Lake, Calif., thanks for providing the opportunity and financing to continue my education.

To Dr. T. L. Doligalski and the Army Research Office for support with funding for the tests at the Fluid Mechanics Laboratory at NASA Ames Research Center and monitoring of experimental progress, to Maj. D. B. Fant and the Air Force Office of Scientific Research, to Mr. T. S. Momiyama and NAVAIR, to Dr. S. S. Davis of the Fluid Dynamics Research Branch, to Mr. P. J. Trosin of Sterling Federal Systems, to the educators at the Naval Postgraduate School, especially my committee members, and also to the computational personnel at NASA Ames Research Center, I give many thanks for your time, support, grants, analysis programs, and facilities for the experimental and computational investigations.

I am thankful and humbly grateful to my advisors, Dr. M. F. Platzer, who taught me much more than just aerodynamics, impressing me continually with the "big picture" and directing a steady course, and to Dr. M. S. Chandrasekhara, who patiently guided me through new frontiers in measurements.

Thanks and appreciation to Dr. John Ekaterinaris for granting critical computer and numerical analysis expertise, to Dr. Ismail Tuncer, Dr. Mike Wilder and Dr. Sajeer Ahmed for their able assistance with data reduction, analysis, and testing, to Dr. Rich Margason for sharing similar classroom experiences and encouraging me to keep at it, to Mr. Ed Jeter for providing meaningful work, particularly related to my skills, and to my entire family for standing by me during a seemingly endless journey.

Most importantly, I am deeply indebted to my wife Kymn and best friend, who continues to build me up and first encouraged me to pursue this dream.

I. INTRODUCTION

It is the objective of this thesis investigation to contribute to the understanding and prediction of the dynamic stall phenomenon, which is observed to occur when an airfoil is pitched rapidly past the dynamic stall angle. Dynamic stall may be encountered on helicopter and propeller blades, on fighter aircraft wings and on turbomachinery blades. Usually, dynamic stall is an event one seeks to avoid because it may generate unacceptably high stresses, which may cause blade failures. However, more recently it has also been recognized that the brief period of increased lift that occurs during the dynamic stall process might be usable on fighter aircraft to improve maneuverability. Hence, there is a continuing need and interest in a number of important technical fields to improve our knowledge of the dynamic stall phenomenon.

In general, one distinguishes between two types of dynamic stall. Deep dynamic stall occurs when the airfoil is pitched to angles significantly above the static stall angle, and light dynamic stall occurs when the static stall angle is exceeded only slightly. In both cases, a so-called dynamic stall vortex is observed to form near the leading edge of the airfoil, which grows in size while moving toward the trailing edge. During this phase of the dynamic stall process, the lift continues to increase quite substantially above the maximum static lift value achievable for a given airfoil. However, as soon as the dynamic stall vortex reaches the trailing edge, the lift starts to break down quite abruptly. This is accompanied by a sharp spike in the pitching moment. This general sequence of events is illustrated in Figure 1.1. Naturally, the precise physics of the dynamic stall phenomenon is much more complicated and depends on many important parameters, such as airfoil shape, Reynolds number, Mach number, etc. To review the dynamic stall physics in more detail, refer to the recent surveys of Carr [Ref. 1] and Carr and Chandrasekhara [Ref. 2].

In the past, most experimental investigations of dynamic stall were restricted to incompressible flow studies using either water tunnels because of their superior flow visualization capability or relatively inexpensive low-speed wind tunnels. However, it became increasingly apparent that the compressibility

of the air may have an important effect on the dynamic stall process even though the free-stream Mach number may be less than 0.3 (normally cited as the threshold beyond which compressibility has to be considered in steady-state flow analysis). Therefore, a special dynamic stall wind tunnel was built in the Fluid Mechanics Laboratory of the National Aeronautics and Space Administration (NASA) Ames Research Center, Moffett Field, Calif. which made it possible to raise the free-stream Mach number to 0.45. Furthermore, the airfoil was mounted such that it permitted an unobstructed view of the dynamic stall flowfield. This made it possible to visualize and measure the precise flow details and events that lead to the formation of the dynamic stall vortex.

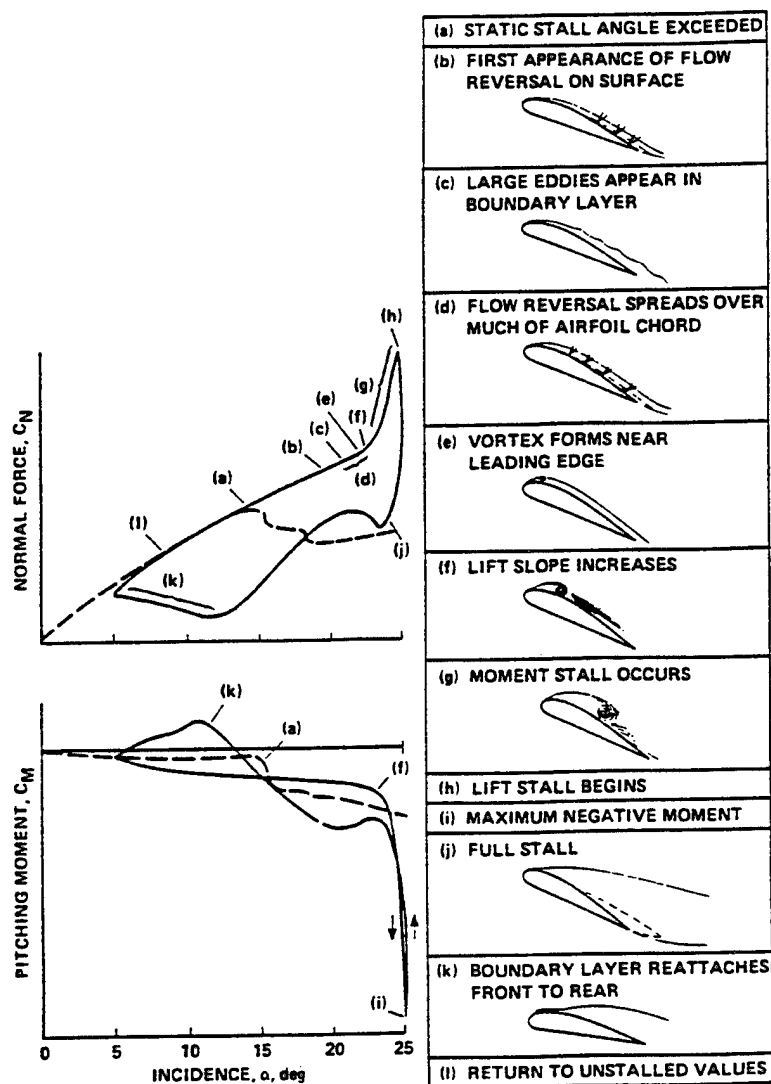


Figure 1.1 Dynamic Stall Events on the NACA 0012 Airfoil [Ref. 1].

In this thesis, a National Advisory Committee for Aeronautics (NACA) 0012 airfoil is studied in a flow of Mach number 0.3 and Reynolds number 540,000. This choice of Mach and Reynolds number allows the study of compressibility effects in a Reynolds number range where it is known that a separation bubble forms near the leading edge of the airfoil. The central question addressed in this thesis investigation is the study of separation bubble behavior near static and dynamic stall for the purpose of understanding the flow physics, which leads to the initiation of static and dynamic stall. To this end, a new flow visualization technique, point diffraction interferometry (PDI) was used to measure the density gradients in the flow, and laser-doppler velocimetry (LDV) was applied to measure the velocity field near the leading edge. The second question addressed is the assessment of currently available computational methods concerning their adequacy or inadequacy to predict the type of flow described.

Therefore, the results of the investigation are documented as follows: Chapter II provides a review of airfoil flows with separation bubbles, Chapter III contains a description of the experimental setup and measurement techniques used in this investigation, Chapter IV provides a characterization of the computational methods, Chapter V summarizes the experimental results, and Chapter VI documents the computational results, and finally, Chapter VII gives data comparisons between the measurements and the predictions. Chapter VIII presents the conclusions and recommendations.

II. REVIEW OF LOW-SPEED AIRFOIL FLOWS WITH LEADING-EDGE SEPARATION BUBBLES

A. INTRODUCTION

Information about the stalling characteristics of airfoils is extremely important for the design of aircraft wings, helicopter blades, propellers, turbo-machinery blades, windmills, etc. In the early 1930s, Jones [Ref. 3] suggested to distinguish between trailing-edge stall and two types of stall caused by flow separation near the airfoil leading edge. In the late 1940s, McCullough and Gault [Ref. 4] performed detailed measurements and confirmed the existence of three types of stall, namely trailing-edge stall characterized by the movement of the separation point of the turbulent boundary layer forward from the trailing edge with increasing incidence; leading-edge stall caused by an abrupt separation of the laminar boundary layer near the leading edge without subsequent reattachment; and thin-airfoil stall where laminar-flow separation occurs near the leading edge, followed by turbulent flow reattachment that moves progressively downstream to the trailing edge with increasing incidence. As a result, a recirculatory flow region forms between the separation and reattachment points that is generally referred to as a separation bubble.

It is the objective of the present investigation to make a contribution to the understanding of the physics of the separation bubble. Therefore, the review of previous work is limited to studies of airfoil flow at Mach numbers equal to or less than 0.3 where leading-edge separation bubbles were found to occur.

B. FUNDAMENTAL FLOW PHYSICS OF LEADING-EDGE SEPARATION BUBBLES

The type of bubble that forms depends on the airfoil shape. In a comprehensive review of separation bubbles, Tani [Ref. 5] drew attention to the need to further distinguish between long and short bubbles. The measurements of McCullough and Gault revealed the presence of a separation bubble near the leading edge of the NACA 63-009 airfoil at an incidence of 4° and a Reynolds number of 5.8×10^6 . Separation of the laminar boundary layer took place before

stall near the leading edge of an airfoil at low incompressible flow speeds to form the separation bubble even at a Reynolds number greater than 1 million. An increase in incidence caused the bubble to move forward and contract in streamwise extent, which was on the order of 1% airfoil chord. A small region of constant pressure existed within the bubble. At higher angles of incidence, the flow no longer reattached to the surface downstream of the laminar separation, or in effect, experienced short bubble burst. This occurred at an incidence of 9° and caused a complete redistribution of the pressure and an abrupt loss of lift. In contrast, a separation bubble first occurred at low incompressible speeds and the same Reynolds number of 5.8×10^6 on the NACA 64A006 airfoil at 3° incidence. As the incidence was increased to 5° , the bubble broke down, causing a slight drop in lift. However, this bubble-burst did not lead to complete flow separation. Instead, the flow separation persisted over some distance and reattached farther downstream. As the incidence was increased, the reattachment point moved progressively downstream until it reached the trailing edge at about 9° incidence angle. This is referred to as the long bubble.

Tani suggested to distinguish short from long bubbles by their effect on the airfoil pressure distribution rather than by their different lengths. The presence of separation bubbles makes the pressure distribution markedly different from that in inviscid flow. In particular, for a long bubble a sharp suction peak near the leading edge is not realized. Instead, a pressure plateau of reduced level extends over the length of the separation bubble. On the other hand, the suction peak continues to increase followed by a small pressure plateau up to the stall angle of attack for a short bubble in a high Reynolds number flow. For the flow of consideration in this thesis at a Reynolds number 540,000 and $M_\infty = 0.3$, the leading-edge short bubble is shown to have a more extensive effect on the pressure distribution.

The formation of a separation bubble clearly depends on the existence of an adverse pressure gradient that is steep enough to cause laminar separation. However, no bubble will form if the Reynolds number is sufficiently high and the flow transitions from laminar to turbulent ahead of the point where flow separation would have occurred if the boundary layer had remained laminar. On the other hand, at a sufficiently low Reynolds number the separated flow will be

unable to reattach and, again, no bubble will be formed. Therefore, a Reynolds number range exists within which separation bubbles form. Below the critical Reynolds number for bubble formation the lift is low and the drag is high. As shown by McMasters and Henderson [Ref. 6], the maximum L/D of an airfoil improves dramatically in the range of Reynolds numbers from 10^4 to 10^6 , which is shown in Figure 2.1 [Ref. 7]. For $Re > 10^6$, typical of large aircraft, boundary layer transition occurs upstream of the theoretical laminar separation point. As a consequence, the turbulent boundary layer is much more resistant to separation, and the flow remains attached to relatively high incidence angles. Eventually, the stall will occur as a result of the forward movement of the separation point from the trailing edge.

In the range of Reynolds numbers from 10^4 to 10^6 , many complicated phenomena take place within the boundary layer. Separation, transition, and reattachment can all occur within a short distance. As shown in Figure 2.1, surface roughness has an important effect. Similarly, the turbulence level of the free stream is known to affect the aerodynamic characteristics.

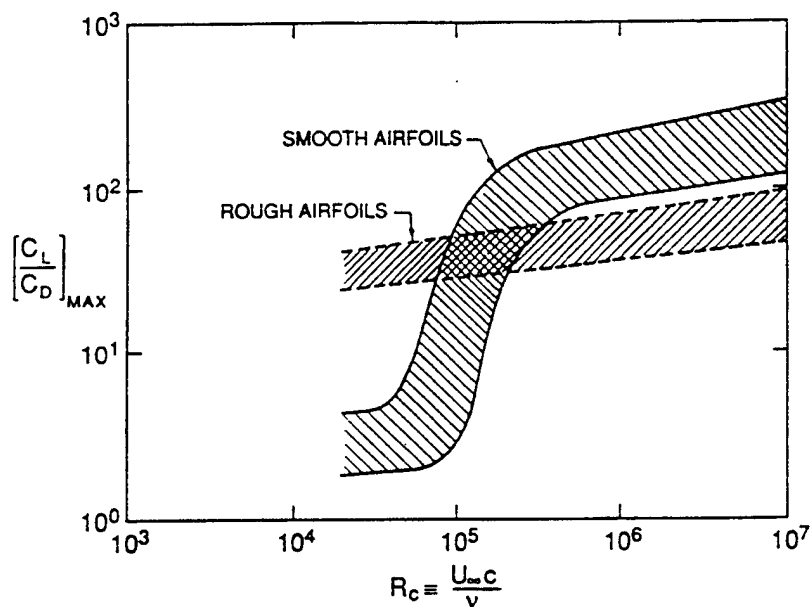


Figure 2.1. Airfoil Performance as a Function of Chord Reynolds Number [Ref. 7].

The basic flow physics of bubble formation appears to have been first explained by von Doenhoff in NACA TN 639 of March 1938 [Ref. 8]. He suggested that the onset of turbulence in the separated flow is responsible for the reattachment because the turbulent entrainment caused the flow to return to the airfoil surface. The typical structure of a laminar separation bubble was described by Horton in 1968 [Ref. 9]. Figure 2.2 shows the flowfield in the vicinity of a laminar separation bubble. At the separation point, the dividing streamline is observed to rise slowly away from the wall. After the boundary layer undergoes transition to turbulent flow, the streamline quickly reattached to the wall. The center of the reversed flow vortex lies near the reattachment point and causes the fluid to move faster in this region. Within the separated region, the wall pressure remains constant near the separation point, while a steep pressure gradient accompanies the high-velocity region near the reattachment point. Tani noted that the size of the separation bubble was reduced as the adverse pressure gradient increased [Ref. 5]. This was explained by the more rapid boundary layer transition.

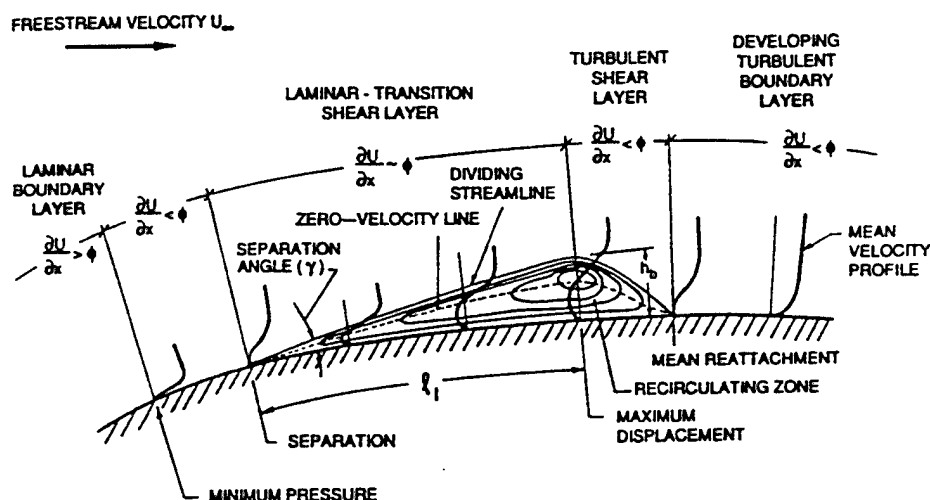


Figure 2.2. Structure of Flow With Laminar Separation Bubble [Ref. 7].

Tani postulated that the Reynolds number based on the boundary layer thickness at the separation point provides a better measure than the chord-based Reynolds number. He suggested, based on available experiments, that the

Reynolds number based on the displacement thickness at separation must exceed 780 if reattachment is to occur. Later, Owen and Klanfer [Ref. 10] put forward a similar criterion. This Tani, Owen, Klanfer criterion can be interpreted as an assurance that transition will occur in the separated flow.

Crabtree [Ref. 11] sought to develop a criterion for bubble breakdown. He made the assumption that the breakdown occurs because a maximum possible pressure value exists that can be recovered in the turbulent entrainment process, which causes the flow reattachment. He found from the analysis of the available experimental results that the value of the pressure recovery coefficient increases with either an increase in incidence at constant Reynolds number or with a decrease in Reynolds number at constant incidence. The latest measurements by Malkiel and Mayle [Ref. 12] showed that the intermittency development in separation bubbles is well modeled with the turbulent spot theory used in attached boundary layers.

The foregoing discussion of the main features of separation bubbles makes it clear that the transition to turbulent flow has a controlling effect on the extent of laminar separation bubbles. At chord Reynolds numbers less than 10^6 , the local Reynolds number based on the boundary layer development is often too low for the Tollmien-Schlichting instabilities to promote natural transition before the laminar boundary layer reaches separation. Once laminar separation has occurred, the resulting inflectional velocity profiles promote a more rapid amplification of boundary layer fluctuations, which eventually reach transition levels. Laminar separation is also accompanied by a significant increase in the boundary layer thickness. After transition, increased mixing promotes growth of the turbulent separated shear layer, which eventually reattaches to the airfoil surface. A decrease in Reynolds number tends to delay transition within the separation bubble. On the other hand, the addition of external disturbances, such as free stream turbulence, acoustic disturbances, or surface roughness promote transition within the separation bubble. Accordingly, the transition onset location must be considered a critical parameter and its prediction becomes a crucial element in the development of prediction methods for airfoil flows with leading-edge separation bubbles.

C. TRANSITION ONSET PREDICTION

A widely used empirical criterion for the onset of boundary layer transition in high Reynolds number airfoil flows, $Re > 10^6$, has been given by Michel [Ref. 13]. Early attempts at transition prediction in the Reynolds number range from 10^4 to 10^6 focused on correlation of local flow parameters and local Reynolds numbers, proposed by Gault [Ref. 14], Gaster [Ref. 15], Horton [Ref. 9], O'Meara and Mueller [Ref. 16]. More recently, linear stability calculations have been introduced. Such calculations assume an e^n transition criterion based on the stability of Falkner-Skan reverse-flow profile solutions. This approach assumes that the onset of transition can be correlated with the location where the amplification of the Tollmien-Schlichting instabilities has reached a certain level, expressed by the value of (n) in e^n . This value is usually assumed to be in the range from 8 to 9. Additional details about this method can be found, for example, in Cebeci and Bradshaw [Ref. 17]. Another promising procedure for the prediction of transition has been recently developed by Herbert and Bertolotti [Ref. 18] and is known as the parabolized stability equation (PSE) method.

D. TRANSITION LENGTH PREDICTION

The key variable in describing a boundary layer during transition from laminar to turbulent flow is the intermittency, $\gamma_{tr}(x)$, defined as the fraction of time that the flow is turbulent. Therefore, the transition zone may be defined as beginning where $\gamma_{tr}(x)$ has just departed from zero and extending to where it is unity. In constant pressure boundary layers, a large amount of experimental data has been gathered and a satisfactory model based on Emmons' theory of spots and Narasimha and Dhawan's [Ref. 19] hypothesis of concentrated breakdown have been developed. Chen and Thyson [Ref. 20] extended this model to account for the effect of pressure gradient by making the hypothesis that the turbulent spot propagation velocity at any point x is proportional to the local free-stream velocity, but the transition growth of the spot across streamlines is assumed to be unaffected. This Chen-Thyson transition model is widely used for attached high Reynolds number airfoil flows, as documented by Cebeci and Bradshaw [Ref. 17]. The effect of pressure gradient is to lengthen the transition zone in favorable gradient pressure flows and to shorten it in adverse pressure

gradient flows. This effect is incorporated in the Chen-Thyson model by the choice of the transition length value. A lower transition length value forces transition to take place over a shorter distance. Recently, Cebeci [Ref. 21] has proposed a correlation formula to include the effect of Reynolds number so that the Chen-Thyson model can be applied in the Reynolds number range from 10^4 to 10^6 . Another transition length model that attempts to account for the effects of free-stream turbulence and pressure gradients has been suggested by Abu-Ghannam and Shaw [Ref. 22]. It assumes the existence of similarity in the spot-generation rate. Very recently, Gostelow et al. [Ref. 23] developed a new model to calculate the transition length as a function of pressure gradient and free-stream turbulence level, which is based on extensive new measurements of the spot-generation rate in attached boundary layers.

It is important to recall that no transition measurements exist as yet in free shear layers. Hence, the use of the Chen-Thyson, Abu-Ghannam and Shaw, or Gostelow and Walker transition length models for the modeling of the transition process in separation bubbles is tentative at best. For this reason, in the present study the sensitivity of leading-edge separation bubble calculations to the choice of both the transition onset location and the transition length is examined.

E. EFFECT OF AIRFOIL OSCILLATION ON LEADING-EDGE SEPARATION BUBBLES

It is well known that the dynamic stall phenomena caused by oscillating an airfoil about a mean angle of attack that is close to the static stall angle are quite different from the static stall phenomena. For a review of the extensive literature on dynamic airfoil stall, the author refers the reader to the review papers by McCroskey [Ref. 24], Carr [Ref. 1], Carr and McCroskey [Ref. 25], and Carr and Chandrasekhara [Ref. 26] that discuss the available experimental and computational results. It is apparent from this literature survey that little work has been devoted to the study of the so-called "light dynamic stall" problem in the Reynolds number regime from 10^4 to 10^6 in order to understand the effect of small amplitude oscillations on the separation bubble behavior. Therefore, it was a major objective of the present work to investigate this effect. To this end, a NACA 0012 airfoil was oscillated in pitch about the quarter-chord in a free-stream

flow at a Mach number of 0.3 and a Reynolds number of 540,000. Two experimental techniques were used to acquire detailed flowfield information, namely point diffraction interferometry (PDI) and laser doppler velocimetry (LDV). These experimental methods and results are documented in Chapters III and V, respectively. The computational analysis methods and results are described in Chapters IV and VI. The comparisons between the computations and experiments are given in Chapter VII.

F. ANALYSIS METHODS FOR AIRFOIL FLOWS WITH SEPARATION BUBBLES

Over the past 30 years, so-called viscous-inviscid interaction methods have been developed to overcome the limitation of classical boundary-layer methods in the analysis of attached airfoil flows due to the breakdown of the equations at the point of flow separation. Instead of computing the pressure distributions from an inviscid flow computation and using it as input into the boundary layer computations, the coupling between the viscous and inviscid parts of the flowfield is achieved by an inverse boundary layer calculation. Various such coupling methods have been developed for the calculation of steady airfoil flows. The two most widely used viscous-inviscid interaction codes were developed by Cebeci [Ref. 27] and the airfoil design-analysis code developed by Drela and Giles [Ref. 28] at Massachusetts Institute of Technology (MIT) at Cambridge, Mass. Example calculations of steady separation bubbles at Reynolds numbers 10^5 - 10^6 have been given by Evangelista et al [Ref. 29], using the Drela and Giles code and by Walker et al. [Ref. 30], using the Cebeci code. The latter authors found that the separation bubble occurring on a NACA 65-213 airfoil at a Reynolds number of 240,000 could be predicted quite well, provided the transition length constant was reduced from 1200 to between 20 and 40, thereby reducing the transition length in the Chen-Thyson model.

Relatively little work has been done to extend the viscous-inviscid interaction methods to the analysis of the flow over oscillating airfoils at low Reynolds numbers. The numerical solution of the Reynolds-averaged Navier-Stokes (N-S) equations is becoming an increasingly attractive alternative to the viscous-inviscid interaction approaches because of the increasing availability and

speed of modern workstations. This approach offers the advantage of solving compressible, steady and unsteady attached, mildly separated and fully separated flows with one and the same computational method. Viscous-inviscid interaction approaches, on the other hand, are limited to flows with relatively small regions of separation. Therefore, in this thesis, the N-S approach was chosen as the main method for the analysis of the flow over the steady or oscillating NACA 0012 airfoil. This approach is supplemented by an unsteady inviscid, incompressible panel code and a direct boundary layer code. These three codes are described in Chapter IV.

III. EXPERIMENTAL SETUP AND MEASUREMENT TECHNIQUES

A. INTRODUCTION

A novel facility known as the Compressible Dynamic Stall Facility (CDSF) has been designed at the NASA Ames Research Center Fluid Mechanics Laboratory (FML) to quantitatively document the compressibility effects on dynamic stall of rapidly pitching airfoils. The wind-tunnel facility is in use for experimental research of oscillating airfoil dynamic stall that applies to helicopter rotors [Ref. 31]. The research also has application for maneuvering missile fins and aircraft surfaces in addition to those discussed in the Introduction. For control or eventual beneficial use of dynamic stall, a clearer understanding of the flow phenomena that affect the inception and development of the dynamic-stall process is required. The CDSF test section uses optical glass windows to support an airfoil with pins that are smaller than the airfoil thickness to give an unobstructed view through the tunnel of the flow over a NACA 0012 test airfoil surface. The flow can be studied near the airfoil leading edge where the separation bubble forms and the dynamic stall process occurs, which is the area of focus for this work, as well as away from the airfoil surface. Point diffraction interferometry (PDI) and laser doppler velocimetry (LDV) measurements are used to characterize (1) flows over steady airfoils, (2) high-amplitude, deep-dynamic stall airfoil flows, and (3) low-amplitude, lightly stalled compressible flows. For the light dynamic stall, the measurements showed that the viscous effects normal to the airfoil upper surface were on the order of the airfoil thickness, giving ample data to evaluate the capability of various numerical methods to predict the flow characteristics over the leading edge of the airfoil. A major part of this work investigated the effect of small amplitude oscillations on the separation bubble behavior.

B. EXPERIMENTAL TEST FACILITY

The CDSF is operated as one of four in-draft tunnels at the FML complex, driven by a 6-MW, 108-m³/s, continuous-running evacuation compressor, described in detail by Carr and Chandrasekhara [Ref. 32]. The flow in the tunnel is controlled by a choked, variable-area downstream throat capable of producing Mach numbers from 0 to 0.5, allowing the study of a wide range of free-stream

conditions from incompressible to moderately compressible. The evacuation compressor drives the system and automatically maintains sufficient vacuum downstream of each test facility in the tunnel complex to cause sonic velocity in the smallest cross section of each test chamber. This choked-throat is used to isolate each test bay and maintain clean, constant flow conditions for a wide range of operating conditions during simultaneous operation of multiple tunnels.

The CDSF test section is 35-cm high, 25-cm wide, and 100-cm long. The 15.2-cm-diameter, 2.54-cm-thick, D-shaped interferogram-quality glass (BK-7) windows are supported in magnesium frames that are mounted on bearing races, which permit rotation of the window. A seal prevents leakage of air into the test section. Detailed mechanical design information on the drive mechanism can be found in Sticht [Ref. 33]. The window/airfoil combination is driven in sinusoidal oscillation by a four-bar, push-rod-flywheel system, about the 25% chord position. A variable-speed AC-drive motor with a controller is used to maintain the airfoil oscillation frequency to within 1% of the desired value. The drive mechanism is capable of oscillating the airfoil about mean incidence angles of 0 to 15°, oscillation amplitudes of 2 to 10°, and frequencies up to 100 Hz. The phase angle in the cycle is determined by an optical encoder keyed to the flywheel. Figure 3.1 shows a schematic of the drive system and includes specific details about the drive system.

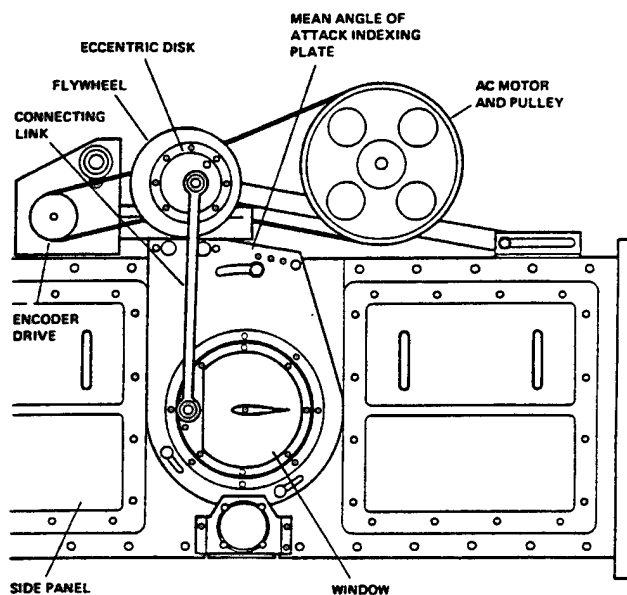


Figure 3.1. Side View of the Compressible Dynamic Stall Facility [Ref. 32].

The primary instrumentation for this study was non-intrusive, including a two-component LDV and a stroboscopic PDI system. Three high-resolution encoders provided accurate position and frequency information. The mean angle of attack was indicated by an absolute position encoder with 3600 counts per revolution (0.1 deg/count). The instantaneous angle of attack was provided by an incremental encoder mounted on the window. The frequency and phase angle were provided by another incremental encoder with 800 counts/cycle of oscillation and was keyed to the flywheel drive shaft. All encoder outputs are digital and were read into a Micro VAX II computer, which was used to control the experiment. [Ref. 34]

C. UNSTEADY LDV MEASUREMENT TECHNIQUE

A TSI, Inc., two-color, two-component, four-beam, frequency-shifted, argon-ion laser-based, off-axis, forward-scatter system was used for velocity measurements. Traversing was accomplished by directing the four beams onto a 352-mm focal-length lens mounted on a computer-controlled traverse. Figure 3.2 presents a schematic of the CDSF instrumentation. The scattered light was collected at 15 degrees off-axis in the forward scatter mode by the 500-mm focal-length receiving optics. This arrangement gave a reduced probe volume length and improved the measurement resolution. The receiving optics were mounted on a separate traverse mechanism, but were slaved to the traverse on the transmitting side. The individual photo-multiplier signals were processed by TSI 1990 counters.

Special phase-locking circuitry enabled handling of the random LDV data and the unsteady-position data. There was a need to read the phase angles the instant each LDV data sample was validated, which were simultaneous Doppler signals in both the U- and V-components of velocity. The LDV data were acquired in the coincidence mode with the acceptance window width arbitrarily set to 50 μ s. The coincidence pulse was used to trigger data acquisition and freeze the rapidly changing encoder values until data transfer to the computer could be completed as shown in Figure 3.3. The data from the system were acquired by the computer in the DMA mode using an eight-channel multiplexer to check for coincidence of the data on two channels. The encoder data were also input to the

multiplexer through a system that records the encoder value only when coincident LDV data were obtained. The LDV data-acquisition scheme was described in detail by Chandrasekhara and Ahmed [Ref. 34].

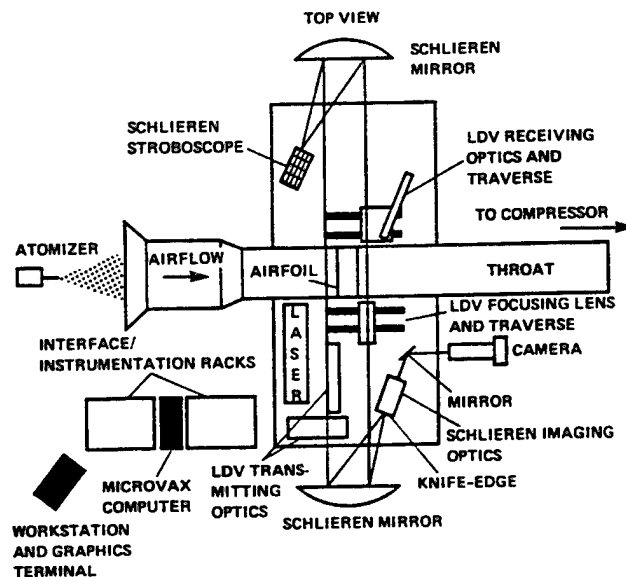


Figure 3.2. Schematic of the LDV System in Use in the CDSF [Ref. 32].

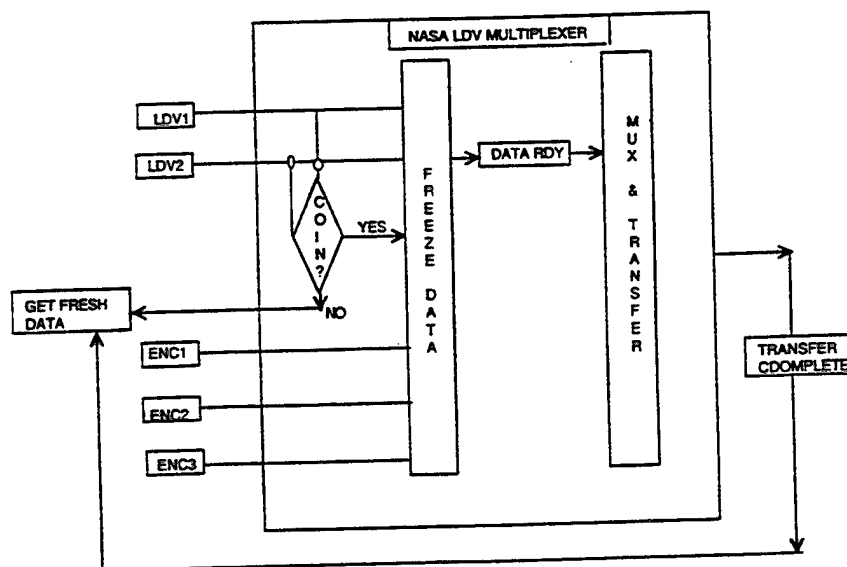


Figure 3.3. Unsteady-Flow LDV Data-Acquisition-Method Schematic [Ref. 34].

The LDV data rate was dependent on the seeding particles, which were 1- μ m-diameter polystyrene latex particles (PSL) suspended in alcohol and injected into the tunnel inlet by a TSI 9306 six-jet atomizer. The particles traveled 3 meters before passing through the probe volume in the test section, and by that time the alcohol had evaporated, leaving only the PSL.

The flow Mach number for the tests was 0.3 and the Reynolds number was 540,000. The airfoil oscillation frequency was 21.6 Hz or a reduced frequency of 0.1 based on the full chord. The flow over the NACA 0012 airfoil was investigated at steady angles of attack and for oscillations about the quarter chord point, $\alpha = 10^\circ - 10^\circ \sin \omega t$ and $\alpha = 10^\circ - 2^\circ \sin \omega t$.

Data were acquired in a rectangular x-y grid. The origin was determined at the leading edge of the airfoil when the angle of attack was 0 degree. The LDV probe volume was traversed in the range $-0.167 < x/c < 0.167$, and $0.083 < y/c < 0.167$. The rectangular measurement grid embedded in the computational grid is shown in Figure 3.4. The resolution in both the x and y direction was 1.27 mm. The measurement grid remained stationary as the airfoil rotated about the quarter-chord point.

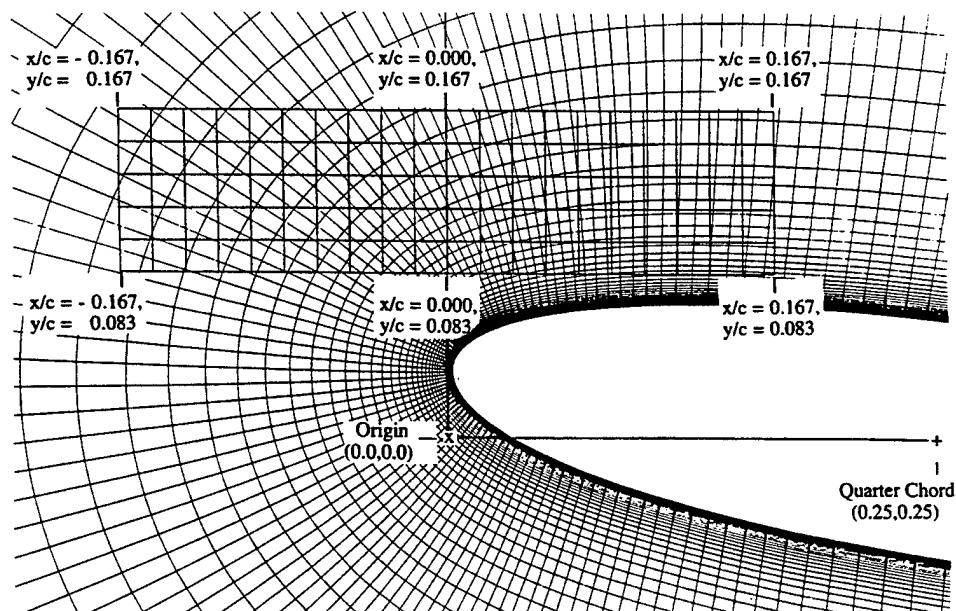


Figure 3.4 Measurement Locations (6x21) Overlaid on Computational Grid (275x81). $\alpha = 8^\circ$, NACA 0012 Airfoil.

D. STROBOSCOPIC PDI MEASUREMENT TECHNIQUE

The PDI technique permits the real time recording of flow interferograms. The PDI technique as used in the present test is based on a variation of the work by Smartt [Ref. 35 and 36]. The PDI technique, described by Carr et al. [Ref. 37], used a "pin hole" point discontinuity in an exposed photographic plate to diffract a portion of the incoming light. The plate was placed at the focal plane of the point source, producing a reference spherical wave front from the "pin hole" by diffracting a portion of the incident light. The light passing through the photographic plate surrounding the pinhole interacted with the reference wave front, giving the interference fringes as seen in Figure 3.5. The optical path difference caused by density variations in the flowfield produced the interference fringes.

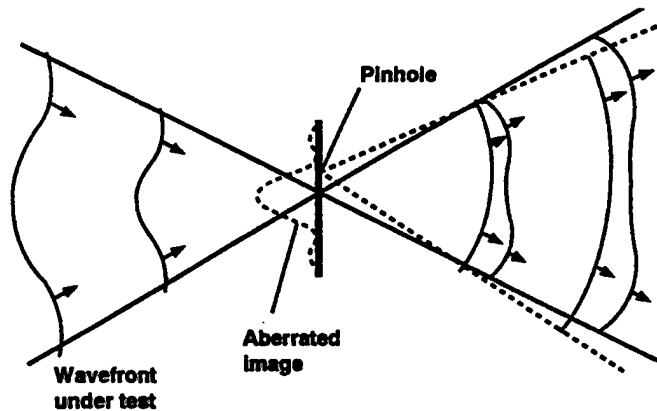


Figure 3.5. Principle of Point Diffraction Interferometry [Ref. 38].

1. Implementation

The interferogram images were obtained by triggering a laser light source at defined phase angles of the airfoil through the oscillation cycle to give the density gradients in the flow field. The light source was a pulsed Nd:YAG laser with a frequency doubler, operating at a wavelength of 532 nm. Figure 3.6 shows a schematic of the arrangement, having a long focal length that permits use of the standard Z-type schlieren arrangement with minimum astigmatism. The laser light was expanded through a negative lens to partially fill one schlieren mirror and directed through the test section, and then refocused by the other schlieren mirror

before passing through the exposed photographic plate. The laser replaced the conventional spark as the light source and was also pulsed with enough energy to burn off the emulsion located at the focal plane of the second mirror. The spot or "pin hole" was created by passing light through the test section at a no-flow condition. [Ref. 37]

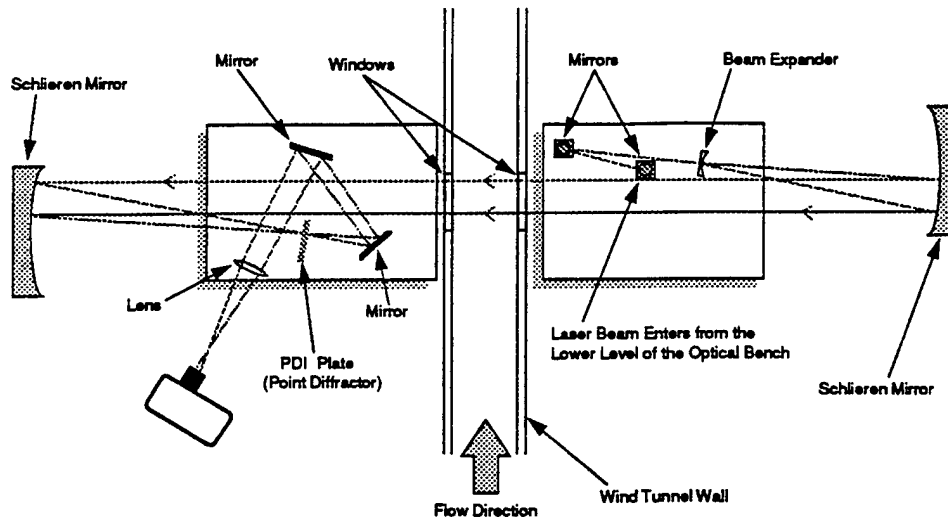


Figure 3.6. Schematic of the PDI Optical Arrangement [Ref. 39].

The tunnel was turned on and the real-time interference fringes were recorded on Polaroid film (ASA 3000) for immediate viewing. This capability was of great value for analysis of the dynamic flow field under investigation, since it permitted rapid review of the progress of the dynamic stall process and on-line retaking of any photographs that were not of the required quality. This also permitted an on-line study of the flow field as it developed, since any phase angle in the cycle could be accessed directly. This ability to actively search for the onset of dynamic stall using the PDI technique is in strong contrast to the more conventional holographic interferometers, which require a major post-processing effort before the interferogram can even be verified, much less analyzed.

The phase angle for each interferogram was chosen by setting switches on a specially designed comparator circuit box. Since the laser took a finite time to actually emit the light, additional electronics were incorporated in the circuitry to display the phase angle when the laser actually fired. This was accomplished by

sensing the light using a photo diode; when the laser fired, the output of the photodiode was used to freeze the angle-of-attack display so that the precise angle at which the image was taken could be recorded.

2. Fringe Counting To Determine Mach Number

The PDI interferometer produces images that are equivalent to those produced by Mach-Zehnder interferograms. It is a common path interferogram that is less sensitive to vibration and uses the mirrors of an existing schlieren setup to direct the laser beam. The path length difference attributable to density (or phase) changes can be related to the fringe number ε for a two-dimensional flow. The equation is

$$\varepsilon = (n - n_r) \frac{L}{\lambda_o} \quad (3.1)$$

For bright fringes, ε is zero or an integer. The dark fringes represent half integers. The refractive indexes, n and n_r , are for the signal beam and the reference beam, respectively. Using the perfect gas and the Gladstone-Dale equation [Ref. 40], the above expression can be reduced to

$$\rho - \rho_r = \frac{\lambda_o}{(n_o - 1)} \left(\frac{\varepsilon \rho_o}{L} \right) = A \varepsilon$$

The constant A can easily be determined for the present experiment because the laser wavelength, $\lambda_o = 532$ nm, the wind tunnel width, $L = 25$ cm, the refractive index of air, $(n_o - 1) = 2.733 \times 10^{-4}$ [Ref. 40], and the standard atmospheric density, $\rho_o = 1.21$ kg/m³. Thus, by dividing the above equation by ρ_o and rearranging

$$\frac{\rho}{\rho_o} = \frac{\rho_r}{\rho_o} + \frac{0.009421 \varepsilon}{\rho_o} \quad (3.2)$$

For isentropic flow, the free stream Mach number gives the density ratio ρ_r/ρ_o where $\rho_r = \rho_\infty$ corrected for wind-tunnel screen losses. Thus, by knowing the fringe number, ρ/ρ_o can be determined. A negative fringe number represents

an accelerated flow and vice versa. Since the Mach number distribution is known from the fringes, the pressure distribution can be calculated in the flow field and on the airfoil surface.

$$C_p = \frac{2}{\gamma M_\infty^2} \left(\frac{p}{p_\infty} - 1 \right)$$

To quantify the data in the interferograms, the PDI images were scanned, creating enhanced gray scale images (300 dots per inch) that were processed further on a workstation. The three registration markers, one each above and below the airfoil quarter chord point and one below the leading edge, were placed on one of the rotating windows to give proper airfoil orientation and scaling of the fringe patterns, as shown in Chapter V. The fringe program allowed the user to pick points on the image which were the centers of the dark fringes and the points where the fringes intersected with the airfoil surface. Starting at the stagnation contour, the user is prompted for the first fringe value and then all fringes are mapped over the lower and upper surfaces of the airfoil. A cursor arrow was used to select the fringe ends that intersected the airfoil surface, and by using the middle mouse button the point was mapped to the nearest pixel on the airfoil surface. Fringe incrementing could be cycled as desired from selected values of 1, 0 or -1. Zoom, back up, manual incrementing, and curve fitting options were available during data processing of each density contour or fringe. Each fringe was only 2 to 3 pixels wide near the leading edge, and it was readily apparent after curve fitting (in green on screen) each contour if the center of the fringe was properly mapped. The mapping process was immediately repeated if required by using the back-up mode. When the upper surface mapping was completed, the right mouse was used to save the entire image data in a QPLOT data format. Several PDI images and resultant QPLOT plots are part of the presentation and discussion in Chapters V and VII.

E. MEASUREMENT UNCERTAINTIES

LDV measurements were made at the mid-span plane in the center of the tunnel over a NACA 0012 airfoil that was machined to 0.001-inch accuracy. Relative uncertainties in the data were (1) ± 0.005 for Mach number, (2) ± 0.05 for angle of attack, and (3) ± 0.005 for reduced frequency. The LDV velocity data

uncertainties are estimated to be $\leq 5\%$ in attached flows. The z-component of vorticity was obtained by interpolating the velocity component data with a spline curve fit and then calculating the velocity gradients from the fitted curve. Therefore, the uncertainty of the vorticity data was estimated to be rather high at 20%, but is common to all the distributions and a discussion of comparisons was still considered valid. The fringe uncertainty in the PDI images was estimated to be one in general, but increasing to three near the airfoil leading edge where fringes converged in the region of the suction peak. Each fringe represented a density variation of $\Delta\rho/\rho_\infty = 0.0085$, and the deduced uncertainty in C_p from the fringes was then estimated at ± 0.2 .

Previous experimental studies in the facility have clearly established the two-dimensional nature of flow up to the onset of dynamic stall and even in the attached region of partially separated flows [Ref. 41 and 42]. In addition, previous tests in the tunnel attest to the flow quality as the entrance section was previously used for aeroacoustic studies [Ref. 43]. Also, excellent flow uniformity of 0.25% at 58 m/s was reported in the tunnel, in addition to low turbulence intensity (0.083%) with a bandwidth of 50 to 50,000 Hz [Ref. 43 and 44].

F. DATA VALIDATION (LDV SYSTEM)

The data-acquisition and processing software incorporated (1) checks for detecting oscillating drive frequency variations beyond a pre-set tolerance and (2) phase averaging by binning the data appropriately and plotting histograms and phase distributions of the velocity components. A minimum of 10,000 samples was collected per channel at each measurement point for the oscillatory cases along with encoder information for each sample. For the limited number of steady angle-of-attack test cases, 5,000 samples were collected at each point. Anytime the data were widely scattered, the entire data set was rejected and a new set of data was acquired. The electronic components were carefully set and maintained for the large dynamic flow range, and at some locations 30 minutes were required to complete data acquisition.

For the low-amplitude test case, the data were sorted into 36 bins, corresponding to different phase angles in a range of $\pm 5^\circ$. Also, during the data-

analysis stage, the raw data files for the high-amplitude test case were processed further by sorting the data into 120 bins at a resolution of $\pm 1.5^\circ$. Whenever the stipulated number of coincident samples (50 in this case) was not present in any bin, that bin was said to contain a "hole." A spline curve fit was used to fill the "hole" data between validated data bins, which worked successfully over most phase angles [Ref. 34].

Histograms of raw LDV indicate the quality of the recorded data, the distribution of recorded velocities, the mean velocity value normalized by U_∞ , and the root mean square (RMS) intensity or standard deviation of the recorded samples. The initial histogram is for 5,000 samples at $\alpha = 8^\circ$ and $x/c = 0.000$ and $y/c = 0.083$ in steady flow for the U-component velocity. The measured height above the airfoil surface is 4.82% chord. Over 50% of the data samples were recorded at $1.1 U_\infty$ with a mean velocity of $1.07 U_\infty$ for the entire distribution, as shown in Figure 3.7. The standard deviation of 11% is high for the attached flow condition and measurements outside the boundary layer, but is attributed to low-level noise in the system as noted by the recorded samples around $0.0 U_\infty$ and $0.5 U_\infty$, which are well outside of the 2σ range. In such cases, the data were reprocessed, excluding these samples and decreasing the intensity considerably. In this way, only mean values were considered.

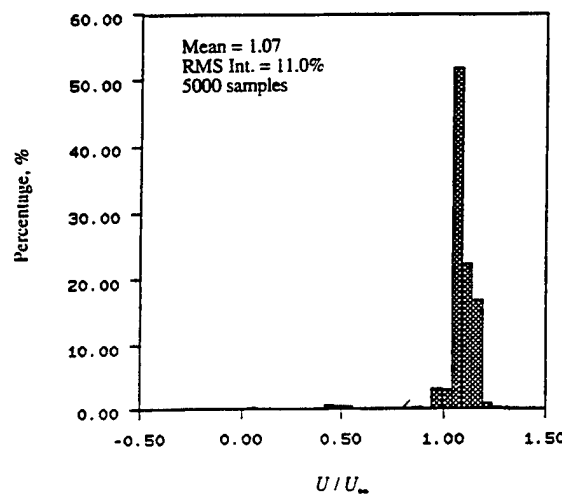


Figure 3.7. Histogram of Normalized U-component Velocity at $x/c = 0.000$; $y/c = 0.083$. $M_\infty = 0.3$, $\alpha = 8^\circ$, $k = 0.0$, $Re = 540,000$.

For the second example, histograms of both raw LDV velocity components are given for the high-amplitude oscillation case ($\alpha = 10^\circ - 10^\circ \sin \omega t$) forward of the airfoil at $x/c = -0.133$ and $y/c = 0.083$ in Figure 3.8. At the phase angle of 180 degrees ($\alpha = 10^\circ$ degrees up), the number of coincident data samples recorded was 125, or higher than the 83 samples, if evenly distributed. Near 50% of all U-component velocities were recorded at the mean velocity of $1.31 U_\infty$. Both velocity component data distributions give appearance of the desired bell curve. For the U-component, data points at $0.9 U_\infty$ and $1.05 U_\infty$ are outside 2σ and are considered as system noise that contributes to the 8.0% RMS value. The V-component samples were recorded with a wider data distribution around the mean velocity of $0.38 U_\infty$. Velocities at $0.15 U_\infty$ and $0.23 U_\infty$ can also be considered part of system noise.

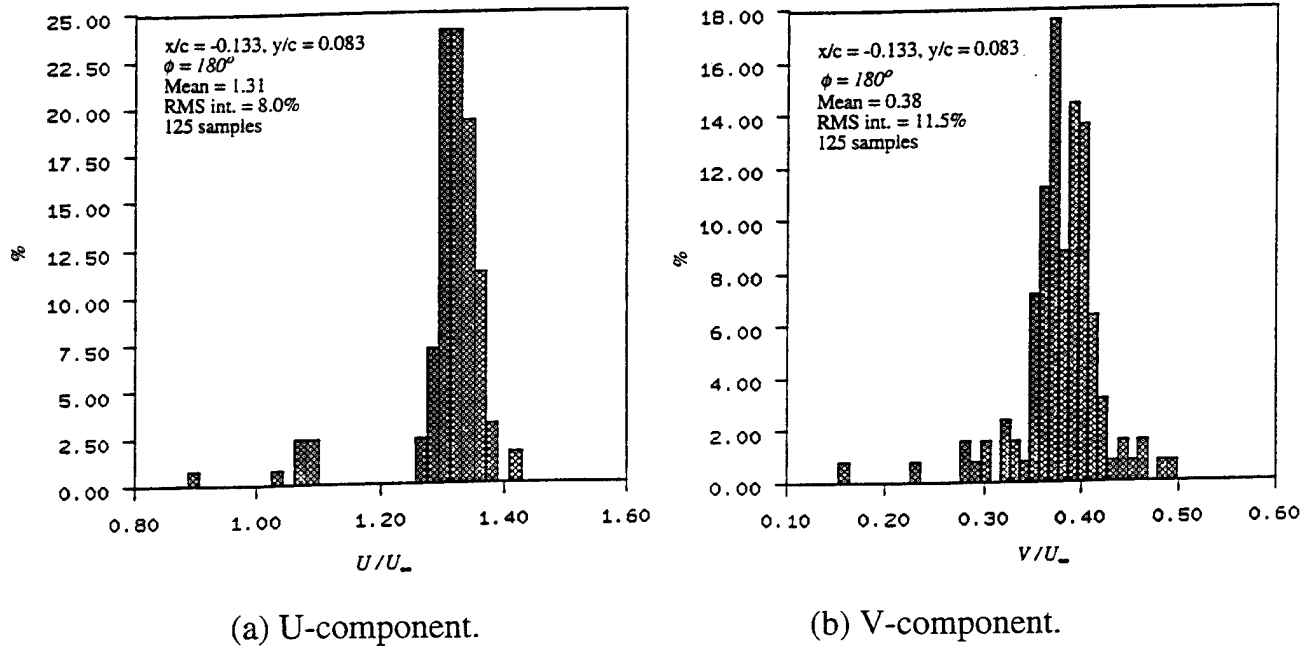


Figure 3.8. Histograms of Normalized U- and V-component Velocities at $x/c = -0.133$, $y/c = 0.083$. $M_\infty = 0.3$, $\alpha = 10^\circ - 10^\circ \sin \omega t = 10^\circ$ (up), $k = 0.1$.

Normalized velocities of both the U- and V-components were recorded throughout the oscillation cycle at the same location forward of the airfoil, as shown in Figure 3.9. The figure legend indicates that if the number of coincident particles validated in both components was less than 20, the data points were denoted by a "hole." U-component velocities follow the motion of the airfoil up to

the dynamic stall angle of attack at $\alpha = 15.9^\circ$. The U velocity increased rapidly from $1.13 U_\infty$ to $1.32 U_\infty$ while the angle of attack decreased from $\alpha = 16^\circ$ to $\alpha = 5^\circ$ down, during flow reattachment. The V-component velocities increased very rapidly during airfoil upward motion before reaching the dynamic stall angle of attack. Holes in the data were shown from 16° angle of attack on the upstroke to the same angle of attack on the downstroke because the airfoil blocked the recording of data by the off-axis forward scatter arrangement. Data "holes" were interpolated from surrounding validated samples, or were not used in the subsequent analysis. When holes were present over a wide phase angle range, the data were not used at all for the results given in Chapter V. Even though data "holes" are shown in this Figure for <20 validated samples, the data were not used if <50 samples were recorded in each bin.

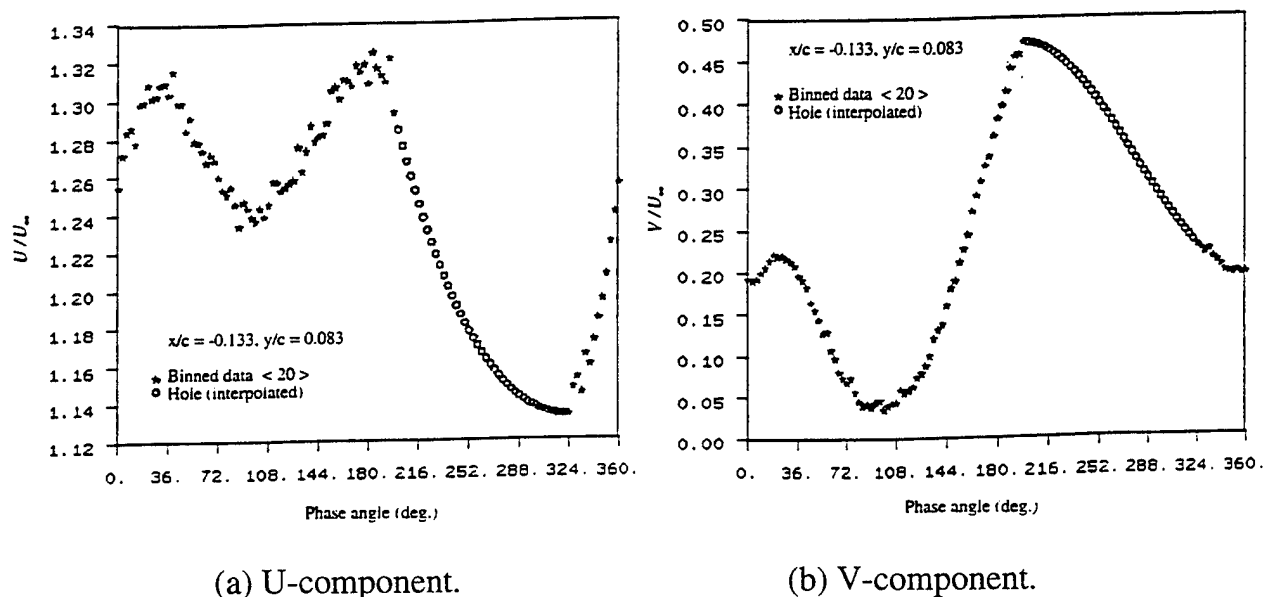


Figure 3.9. Phase Distribution of Normalized U- and V-component Velocities at $x/c = -0.133$, $y/c = 0.083$. $M_\infty = 0.3$, $\alpha = 10^\circ - 10^\circ \sin \omega t$, $k = 0.1$.

For the low-amplitude forced-oscillations ($\alpha = 10^\circ - 2^\circ \sin \omega t$), example LDV raw data histograms in Figure 3.10 show a wide range of instantaneously recorded velocities at the closest measurement location of 1.93% chord above the airfoil surface at $x/c = 0.033$. The number of coincident data samples (368) was large. The mean U-component velocity was $0.95 U_\infty$ at 10° angle of attack (up),

and instantaneous velocities ranged from $0.56 < U/U_\infty < 1.44$ with a maximum of 7% of the samples recorded at $0.85 U_\infty$. Instantaneous V-component velocities ranged from slightly less than $-0.02 U_\infty$ to $0.6 U_\infty$ with a mean average velocity of $0.20 U_\infty$, but favoring a distribution towards $0.3 U_\infty$. The range of measured velocities may be explained by the unsteady nature of the flow within the separation bubble as indicated in the bell curve distributions.

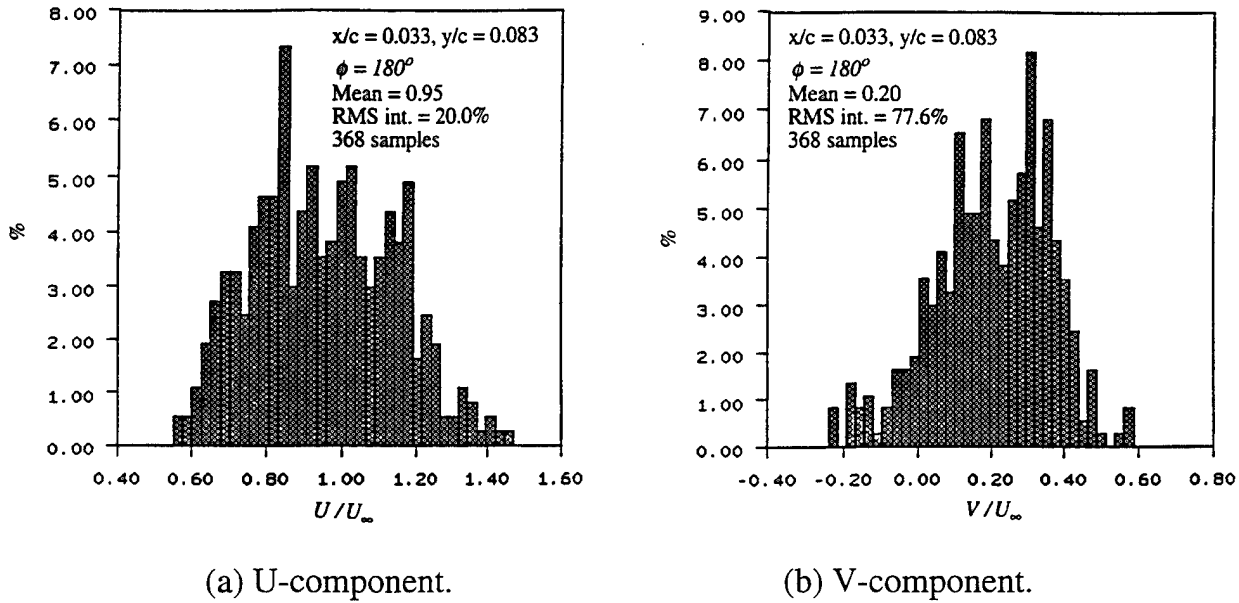
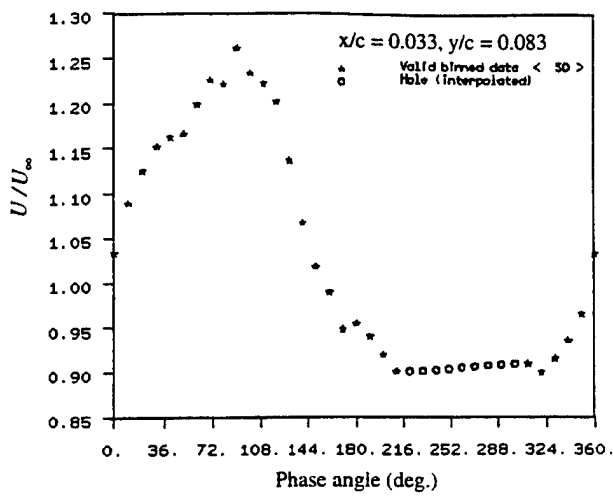


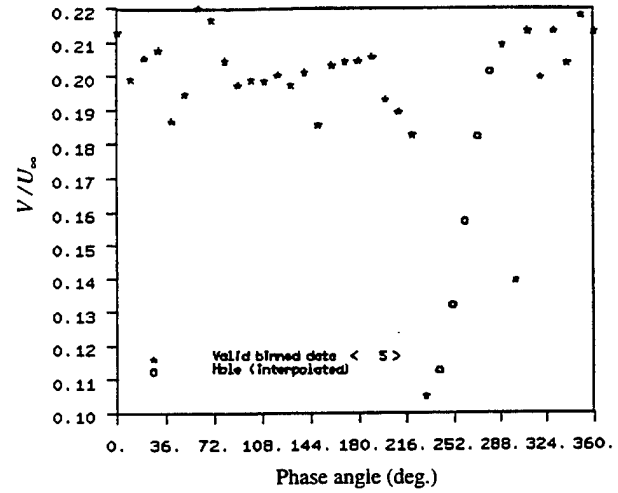
Figure 3.10. Histograms of Normalized U- and V-component Velocities at $x/c = 0.033$; $y/c = 0.083$. $M_\infty = 0.3$, $\alpha = 10^\circ - 2^\circ \sin \omega t = 10^\circ$ (up).

The maximum and minimum U-component velocities in Figure 3.11 occurred at totally different angles of attack when compared with the distribution given at the airfoil leading edge (not shown). U-component velocities increased rapidly after the light dynamic stall at 11° angle of attack (down) to a maximum value of $1.27 U_\infty$ at the bottom of the oscillation cycle. The U velocities decreased from 8 to 11° angle of attack (up), which was the opposite of what was expected because of airfoil rotation, and is due to the presence of the separation bubble at the measurement point. Validated U and V-component velocities were sparse between 11.5° angle of attack (up) and 11.6° angle of attack (down) because of the measurement location in the well developed separation bubble region. V-component velocities were low at $0.2 U_\infty$ and appeared to be fairly constant

throughout the oscillation cycle, except near the top of the oscillation cycle. The velocities were 50% less than those at the airfoil leading edge. The V-component data distribution with a reduced validated sample criteria (5) shows that "holes" were still present for angles of attack approaching the top of the oscillation cycle and shortly thereafter during the rapid occurrence of light dynamic stall. In this case, the data from 11.5° (up) to 11.6° angle of attack on the downstroke (region of partial airfoil blockage) were curve fitted from validated bins (>50) of adjoining phase angles.



(a) U-component.



(b) V-component.

Figure 3.11. Phase Distribution of Normalized U- and V-component Velocities at $x/c = 0.033$, $y/c = 0.083$. $M_\infty = 0.3$, $\alpha = 10^\circ - 2^\circ \sin \omega t$, $k = 0.1$.

IV. DESCRIPTION OF COMPUTATIONAL ANALYSIS METHODS

Potential flow, boundary layer, and N-S analysis methods were used to assess the prediction capabilities of these methods by comparing the computational results with the measured data. Potential flow analysis is generally regarded as sufficient to predict an airfoil's low incidence lift and moment characteristics at reasonably large Reynolds numbers because the flow is attached and the boundary layers on the airfoil upper and lower surfaces are thin. The skin friction and drag characteristics can be obtained by coupling the potential flow analysis with a solution of the boundary layer equations. In the classical approach, the computed potential flow pressure distribution is used as input into the boundary layer equations. This approach limits the analysis to attached flow problems only because the boundary layer equations become singular at the point of flow separation. In recent years, this limitation could be overcome by starting with a reasonable estimate for the boundary layer displacement thickness distribution, computing the pressure distribution from the potential flow analysis, and continuing this viscous-inviscid interaction process to convergence. These viscous-inviscid interaction methods permit the computation of separation bubbles and of airfoil flows with significant regions of trailing-edge stall. However, a more general and powerful approach has become available with the introduction of large-memory high-speed computers, which permit the direct numerical solution of the Reynolds-averaged N-S equations and enable the computation of steady and unsteady attached and separated airfoil flows with one and the same method. Naturally, this greater capability comes at the price of significantly larger computation times. In this thesis, the author therefore uses only the potential flow, the classical boundary layer, and the N-S methods for the analysis of the NACA 0012 airfoil experiments described in Chapter V.

A. UNSTEADY POTENTIAL FLOW CODE (UPOT)

1. Introduction

Potential flow solutions for steady or unsteady inviscid and incompressible airfoil flow are provided by the UPOT code. The conservation equations in this case reduce to the Laplace equation, which can be solved by distributing sources

and vortices on the airfoil surface. Whenever the airfoil experiences an angle of attack change, a vortex is shed from the trailing edge. The wake vortices, in turn, influence the flow over the airfoil. At each time step, airfoil pressure distribution, force and moment coefficients are calculated.

2. Theory and Numerical Method

The UPOT code is capable of computing the unsteady flow over a two-dimensional (2-D) airfoil based upon the panel method developed by Hess and Smith [Ref. 45]. In this approach, the flow is modeled by using uniform source distributions (q_j), which are allowed to vary from panel to panel, and uniform vorticity distributions (γ), which are held constant on all the panels. These distributions automatically satisfy the Laplace equation. Use of the superposition principle allows the buildup of complicated flow fields by using simple source and vortex flows, if an appropriate boundary condition can be satisfied at the airfoil surface boundary. Thus, the total velocity potential is constructed by superimposing the velocity potential for the free-stream flow, the source flows, and the vortex flows. Detailed descriptions of all equations are given in Reference 46, and only primary equations are listed here. The total velocity potential is given by

$$\Phi = V_{\infty}(x \cos \alpha + y \sin \alpha) + \sum_{j=1}^n \int_{\text{panel } j} \left(\frac{q_j}{2\pi} \ln r - \frac{\gamma}{2\pi} \theta \right) ds \quad (4.1)$$

Once the velocity potential is calculated for the steady flow problem, the velocity is evaluated by taking the grad(Φ), and the pressure is determined from the steady Bernoulli equation. The unsteady problem is discussed later.

The boundary conditions consist of the airfoil surface-flow tangency condition and the Kutta condition, which requires that the pressures be equal at the upper and lower trailing edge panels of the airfoil. This leads to a system of linear simultaneous equations for the unknown source and vortex strengths on the panels and to the influence coefficient concept. An influence coefficient is defined as the velocity induced at any point in the flow field (field point) by a unit strength singularity (source or vortex) placed anywhere in the flow field. A detailed derivation of influence coefficients is found in Reference 46. Finally, the

equations are written in matrix form and solved by the Gaussian elimination method.

$$\begin{bmatrix} a_{1,1} & . & . & . & a_{1,n+1} \\ . & . & . & . & . \\ . & . & . & . & . \\ . & . & . & . & . \\ a_{n+1,1} & . & . & . & a_{n+1,n+1} \end{bmatrix} \begin{bmatrix} q_1 \\ q_2 \\ . \\ q_n \\ \gamma \end{bmatrix} = \begin{bmatrix} b_1 \\ b_2 \\ . \\ b_n \\ b_{n+1} \end{bmatrix} \quad (4.2)$$

The unsteady problem is formulated by describing the vortex-shedding process, shown in Figure 4.1. The vortex-shedding process creates non-linearities, because the wake vortices influence the flow over the airfoil, which in turn alters the vortex-shedding process as the airfoil maneuvers in time. The disturbance potential is approximated by using backward finite differences to integrate the velocity field in two stages from upstream free-stream conditions to the leading edge of the airfoil and along the airfoil surface to each panel control point. The rate of change of the disturbance potential must be evaluated at each time step for all panel control points and now includes the contributions from the shed vorticity panel and the wake core vortices.

The total circulation in a potential flow must be preserved according to the Helmholtz vorticity conservation theorem. The vortex-shedding process requires that any change in circulation around the airfoil must be countered by a change in vorticity in the wake of opposite sign, but equal in magnitude. Thus, the vorticity in the wake element (shed vorticity panel) of length Δ_k is equal to the negative change in circulation around the airfoil for the previous time step. The overall circulation Γ_k at time-step t_k is simply γ_k multiplied by the airfoil perimeter, ℓ . The shed vorticity panel provides the desired communication to carry the solution from one time step to the next, where the vorticity conservation condition has to be satisfied at every time step.

$$\Delta_k (\gamma_w)_k = \Gamma_{k-1} - \Gamma_k = \ell (\gamma_{k-1} - \gamma_k) \quad (4.3)$$

The airfoil trailing-edge wake panel with unknown shed vorticity strength, unknown length, and unknown trailing-edge angle introduces three additional

unknowns to the system. In addition, N unknown source strengths and one unknown vorticity strength on the airfoil are all time dependent and must be solved by iteration techniques to a final solution.

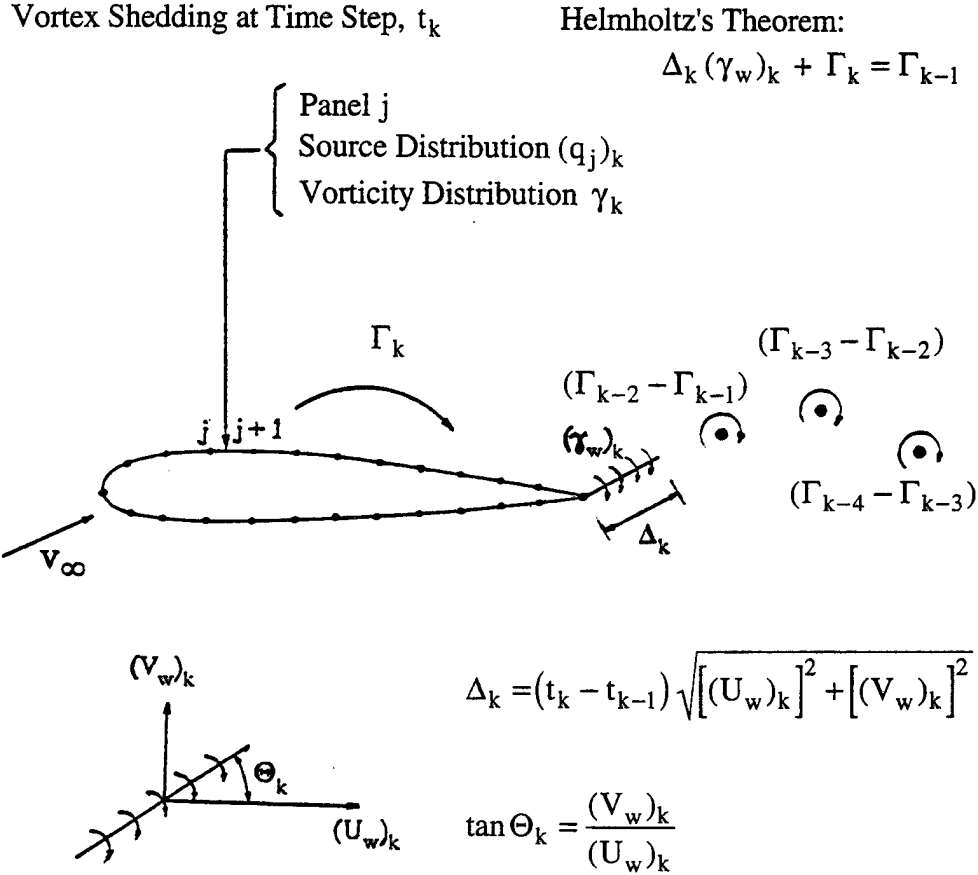


Figure 4.1. Extension of Panel Methods Representation for Unsteady Flow [Ref. 45].

The Kutta condition must include the rate of change of the potential at the trailing-edge panel, which is directly related to the rate of change of the total circulation.

$$[(V^t)_l]_k^2 + [(V^t)_n]_k^2 = 2 \left[\frac{\partial(\phi_n - \phi_l)}{\partial t} \right]_k = 2 \left[\frac{\partial \Gamma}{\partial t} \right]_k = 2(\ell) \frac{\gamma_k - \gamma_{k-1}}{t_k - t_{k-1}} \quad (4.4)$$

Two additional equations are required to solve for the $(N + 4)$ unknowns in the unsteady problem, and assumptions are required for the geometry of the wake

panel as suggested by Basu and Hancock [Ref. 47]. First, the wake panel is aligned with the direction of the local resultant velocity at its midpoint in the moving airfoil reference frame. In addition, the wake panel length is assumed to be proportional to the magnitude of the local resultant velocity at the panel midpoint and the size of the time step. These boundary conditions are written as follows:

$$\tan \Theta_k = \frac{(V_w)_k}{(U_w)_k} \quad (4.5)$$

$$\Delta_k = (t_k - t_{k-1}) \sqrt{[(U_w)_k]^2 + [(V_w)_k]^2} \quad (4.6)$$

The unsteady flow Bernoulli equation for the pressure coefficients must be written with respect to the airfoil-fixed system. Giesing [Ref. 48] showed the equation to be written as

$$C_p = \frac{P - P_\infty}{(1/2)\rho V_\infty^2} = \left(\frac{V_{\text{stream}}}{V_\infty} \right)^2 - \left(\frac{V_{\text{total}}}{V_\infty} \right)^2 - \frac{2}{V_\infty^2} \frac{\partial \phi}{\partial t} \quad (4.7)$$

For this work, 2-D aerodynamic coefficients of lift, drag, and pitching moment are computed for a NACA 0012 airfoil at steady angles of attack and during sinusoidal oscillations about the quarter-chord point by integrating pressure distributions, assuming a constant C_p on each panel.

B. STEADY BOUNDARY LAYER FLOW CODE

1. Introduction

The boundary-layer equations are incorporated into a program (BL2D) developed by Cebeci et al. [Ref. 18]. The equations and analysis are restricted to 2-D steady, incompressible, and viscous flow. Inputs to the program include the Reynolds number and estimated or prescribed transition locations, as well as panel coordinate and velocity information computed by a panel method. Even though the flow accelerates over the airfoil upper surface to Mach numbers much greater

than the free-stream value of 0.3 and is considered compressible, the incompressible BL2D code with a transition model incorporated is used to evaluate the extent of its capability to predict the flow physics evident in the measurements. Output is generated for several boundary-layer parameters, including velocity profiles, skin friction coefficients, and displacement thickness.

2. Theory and Models

The 2-D, incompressible, steady boundary-layer equations for both laminar and turbulent flows are

$$\frac{\partial u}{\partial x} + \frac{\partial v}{\partial y} = 0 \quad (4.8)$$

$$u \frac{\partial u}{\partial x} + v \frac{\partial u}{\partial y} = -\frac{1}{\rho} \frac{\partial p}{\partial x} + \nu \left(\frac{\partial^2 u}{\partial y^2} \right) - \frac{\partial(\overline{u'v'})}{\partial y} \quad (4.9)$$

$$\frac{\partial p}{\partial y} = 0 \quad (4.10)$$

where $\nu = \mu/\rho$ is the kinematic viscosity, μ is the coefficient of viscosity, and u' , v' represent the turbulent velocity fluctuations. These equations must be solved subject to the boundary condition on the airfoil surface ($u = 0$ and $v = 0$), and at the outer edge of the boundary layer, $u = u_e(x)$.

To use Equation 4.9, an expression must be found for the Reynolds shear stress term. Since it is not feasible to attempt calculating the actual value, empirical models must be used. One such model is the eddy-viscosity concept:

$$\rho \overline{u'v'} = \rho \epsilon_m \frac{\partial u}{\partial y} \quad (4.11)$$

where ϵ_m is an empirical term called the turbulent eddy viscosity. A refinement of the eddy-viscosity concept called the Cebeci-Smith (CS) [Ref. 13] eddy-viscosity model is used in the boundary layer code for this work. The CS model divides the viscous region into an inner layer and an outer layer, as described in Reference 17.

The Chen-Thyson [Ref. 20] transition length model is incorporated into the boundary layer code for this study, giving the intermittency $[\gamma_{tr}(x)]$ as

$$\gamma_{tr}(x) = 1 - \exp\left(-\frac{u_e^3}{G_{\gamma_{tr}} v^2}\right) \text{Re}_{x_{tr}}^{-1.34} (x - x_{tr}) \int_{x_{tr}}^x \frac{dx}{u_e}\right) \quad (4.12)$$

and Falkner-Skan transformation variables, ξ and η are used for the solutions. The intermittency factor, $\gamma_{tr}(x)$, models the length of the transition region, as explained further in the N-S code methodology description. Using Equation 4.11, the momentum equation for a turbulent flow (Equation 4.9) can be rewritten in the same form as for a laminar flow:

$$u \frac{\partial u}{\partial x} + v \frac{\partial u}{\partial y} = -\frac{1}{\rho} \frac{\partial p}{\partial x} + \frac{\partial}{\partial y} \left(b \frac{\partial u}{\partial y} \right) \quad (4.13)$$

where $b = \nu + \varepsilon_m$. Thus, the only computational difference between laminar and turbulent boundary layers is the addition of the turbulent eddy viscosity.

The determination of the transition location from laminar to turbulent flow is sometimes one of the most critical factors in the success of computational efforts to predict or reproduce physical phenomena. Assuming the entire flow to be turbulent may be a reasonable approximation for some applications, especially when the Reynolds number is high. In contrast, there are important flows that require more accurate predictions, especially flows in the transitional Reynolds number regime.

Until the transition mechanism and the many factors that can affect it are understood more fully, we must rely on the traditional engineering approach of modeling the start and range of the transitional flow region. In addition, experimental values have an expected range of accuracy, and empirically calculated values may deviate from the actual onset of transition. Therefore, to provide an initial estimate for the transition location when no other method of determination was available, Michel's criterion [Ref. 13] was incorporated into the code:

$$R_{\theta_{tr}} = 1.174 \left(1 + \frac{22,400}{Re_{x_{tr}}} \right) Re_{x_{tr}}^{0.46}$$

where $R_{\theta_{tr}} = u_e \theta / \nu$ is the Reynolds number based on momentum thickness at transition and $Re_{x_{tr}}$ is the Reynolds number based on the transition onset location. Otherwise, experimental data or input values are used to specify the *onset* of transition.

Then, the transitional flow region is calculated by using the Chen-Thyson model [Ref. 20], shown as $\gamma_{tr}(x)$ in Equation 4.12. The flow transition range is neither fully laminar nor fully turbulent. It is a region of *intermittency*, in which turbulent spots gradually appear with progression in the streamwise direction. Use of the transition model in this work will be shown to be essential for obtaining results in agreement with the measurements for low Reynolds number flows and will be discussed more fully in the section describing the N-S code methodology.

3. Numerical Implementation

The x/c and y/c coordinates of the airfoil are supplied as part of the input to the program called `xc` and `yc`. The program redefines these coordinates into a single parameter corresponding to an airfoil surface distance from the stagnation point:

$$x_i = x_{i-1} + \sqrt{(xc_i - xc_{i-1})^2 + (yc_i - yc_{i-1})^2}$$

The variable x_i used internally by the program in the boundary layer equations is the surface coordinate.

The grid variables are transformed with x simply scaled by a reference length, the chord of the airfoil, so that $\xi = x/c$. Since the surface distance x is used, these will not be the same as the x/c coordinates that are input. The dimensionless stream function $f(x, \eta)$ is defined by

$$f(x, \eta) = \frac{\psi}{\sqrt{u_e \nu x}}$$

For the y variable, the well known Falkner-Skan transformation is used:

$$\eta = \sqrt{\frac{u_e}{\nu x}} y$$

where y is the normal coordinate along which the thickness of the boundary layer is measured. The dimensionless similarity variable η eliminates the growth of the boundary layer in laminar flow and reduces it in turbulent flow. This enables larger steps in the streamwise direction and improves computational efficiency.

Using the new variables, Equation 4.13 and the boundary conditions may be rewritten as

$$(bf'')' + \frac{m+1}{2} ff'' + m[1 - (f')^2] = \xi \left(f' \frac{\partial f'}{\partial \xi} - f'' \frac{\partial f}{\partial \xi} \right) \quad (4.14)$$

$$\eta = 0 \quad f' = 0 \quad f(\xi, 0) = f_w(\xi) = -\frac{\sqrt{R_L}}{\sqrt{(u_e/u_\infty)\xi}} \int_0^\xi \frac{v_w}{u_\infty} d\xi$$

$$\eta = \eta_e \quad f' = 1$$

where η_e is the transformed boundary layer thickness corresponding to δ , and R_L is the Reynolds number based on the reference velocity (u_∞) and the reference length, c , the chord of the airfoil. The prime denotes differentiation with respect to η . The dimensionless pressure gradient parameter m is defined by

$$m = \frac{\xi}{u_e/u_\infty} \frac{d(u_e/u_\infty)}{d\xi}$$

The velocity components u and v are related to the dimensionless stream function

$$\text{by} \quad u = u_e f' \quad v = -\sqrt{u_e \nu x} \left[\frac{f}{\sqrt{u_e x}} \frac{d}{dx} \sqrt{u_e x} + \frac{\partial f}{\partial x} + f' \frac{\partial \eta}{\partial x} \right]$$

Equation 4.14, a second-order partial differential equation can be solved by various numerical methods, such as the Crank-Nicholson or Keller Box methods. The Keller Box method [Ref. 18] is used in this work and proves to be efficient for the boundary layer calculations, but first requires reformulating the higher-order

equations into a set of first-order equations. At each rectangular grid section, these equations are approximated by using centered-difference derivatives, averaging values at the center of the "box," as shown in Figure 4.2.

The higher-order equations are formulated into a set of first-order equations with a second-order truncation error by using the following definitions.

$$f' = u \quad u' = v \quad (4.15)$$

Equation 4.14 may now be expressed as a first-order system:

$$(bv)' + \frac{m+1}{2}fv + m[1-u^2] = \xi \left(u \frac{\partial u}{\partial \xi} - v \frac{\partial f}{\partial \xi} \right) \quad (4.16)$$

$$\eta = 0 \quad u = 0 \quad f = f_w(x), \quad \eta = \eta_e \quad u = 1$$

Note that the u and v in Equations 4.15 and 4.16 are not the velocity components. They are two new, arbitrarily selected variable names for the expression of the first-order system. The program was coded using these particular variable names, and the present numerical discussion uses them for consistency.

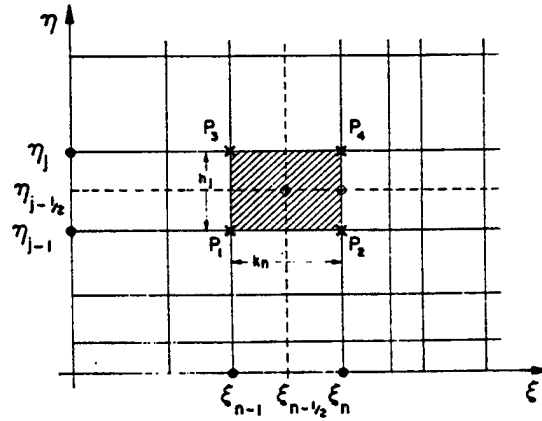


Figure 4.2. Net Rectangle for Difference Approximations [Ref. 18].

Referring to Figure 4.2, the grid points may be described as

$$\xi^n = \xi^{n-1} + k^n, \quad n = 1, 2, \dots, N \quad \xi^0 = 0$$

$$\eta_j = \eta_{j-1} + h_j, \quad j = 1, 2, \dots, J \quad \eta_0 = 0 \quad \eta_J = \eta_e$$

where the capital letters N and J are the maximum number of grid points used in the streamwise and normal directions, respectively. The superscript n is not an exponent, but a counter just like the subscript j . This upper and lower notation allows using both counters on the same variable when needed.

Considering one box of the grid, the finite difference approximations may be written for the midpoint of the right side segment, P_2P_4 , using centered difference derivatives:

$$\frac{f_j^n - f_{j-1}^n}{h_j} = \frac{u_j^n + u_{j-1}^n}{2} \equiv u_{j-1/2}^n \quad (4.17)$$

$$\frac{u_j^n - u_{j-1}^n}{h_j} = \frac{v_j^n + v_{j-1}^n}{2} \equiv v_{j-1/2}^n$$

Equation 4.16 may be approximated in the same manner for the midpoint of the box by centering first in one direction then the other. The resulting finite difference equation is

$$\frac{1}{h_j} (b_j^n v_j^n - b_{j-1}^n v_{j-1}^n) + \alpha_1 (fv)_{j-1/2}^n - \alpha_2 (u^2)_{j-1/2}^n + \alpha^n (v_{j-1/2}^{n-1} f_{j-1/2}^n - f_{j-1/2}^{n-1} v_{j-1/2}^n) = R_{j-1/2}^{n-1} \quad (4.18)$$

where

$$R_{j-1/2}^{n-1} = -L_{j-1/2}^{n-1} + \alpha^n [(fv)_{j-1/2}^{n-1} - (u^2)_{j-1/2}^{n-1}] - m^n$$

$$L_{j-1/2}^{n-1} = \left[\frac{1}{h_j} (b_j^n v_j^n - b_{j-1}^n v_{j-1}^n) + \frac{m+1}{2} (fv)_{j-1/2}^n + m(1 - (u^2)_{j-1/2}^n) \right]^{n-1}$$

$$\alpha^n = \frac{\xi^{n-1/2}}{k^n} \quad \alpha_1 = \frac{m^n + 1}{2} + \alpha^n \quad \alpha_2 = m^n + \alpha^n$$

The boundary conditions are rewritten at $\xi = \xi^n$ as

$$f_0^n = f_w \quad u_0^n = 0 \quad u_j^n = 1$$

The resulting implicit, nonlinear difference equations are linearized by Newton's method and solved by a block elimination method. Equations 4.18 comprise a set of $3J + 3$ equations and $3J + 3$ unknowns (f_j^n , u_j^n , v_j^n , where $j = 0, 1, 2, \dots, J$), with f_j^{n-1} , u_j^{n-1} , and v_j^{n-1} known. The method assumes that an approximate solution is known, either from the preceding iteration cycle or from the previous streamwise station. Then small unknown quantities are added to the approximate solution. Using the arbitrary iteration variable i (superscript n omitted for clarity), the approximate equations become

$$f_j^{i+1} = f_j^i + \delta f_j^i \quad u_j^{i+1} = u_j^i + \delta u_j^i \quad v_j^{i+1} = v_j^i + \delta v_j^i$$

with $i = 0$ corresponding to known values at the previous streamwise station, (ξ^{n-1}), these expressions may be substituted into Equations 4.17 and 4.18 for the unknowns. After dropping higher-order terms of δ , a linear system of equations results:

$$\delta f_j^i - \delta f_{j-1}^i - \frac{h_j}{2}(\delta u_j^i + \delta u_{j-1}^i) = (r_1)_j$$

$$(s_1)_j \delta v_j^i + (s_2)_j \delta v_{j-1}^i + (s_3)_j \delta f_j^i + (s_4)_j \delta f_{j-1}^i + (s_5)_j \delta u_j^i + (s_6)_j \delta u_{j-1}^i = (r_2)_j$$

$$\delta u_j^i - \delta u_{j-1}^i - \frac{h_j}{2}(\delta v_j^i + \delta v_{j-1}^i) = (r_3)_j$$

where the right-hand sides are

$$(r_1)_j = f_{j-1}^i - f_j^i + h_j u_{j-1/2}^i$$

$$(r_2)_j = R_{j-1/2}^{n-1} -$$

$$\left[\frac{1}{h_j} (b_j^i v_j^i - b_{j-1}^i v_{j-1}^i) + \alpha_1 (fv)_{j-1/2}^i - \alpha_2 (u^2)_{j-1/2}^i + \alpha^n (v_{j-1/2}^{n-1} f_{j-1/2}^i - f_{j-1/2}^{n-1} v_{j-1/2}^i) \right]$$

$$(r_3)_j = u_{j-1}^i - u_j^i + h_j v_{j-1/2}^i$$

and the coefficients are

$$(s_1)_j = \frac{1}{h_j} b_j^i + \frac{\alpha_1}{2} f_j^i - \frac{\alpha^n}{2} f_{j-1/2}^{n-1}$$

$$(s_2)_j = \frac{1}{h_j} b_{j-1}^i + \frac{\alpha_1}{2} f_{j-1}^i - \frac{\alpha^n}{2} f_{j-1/2}^{n-1}$$

$$(s_3)_j = \frac{\alpha_1}{2} v_j^i + \frac{\alpha^n}{2} v_{j-1/2}^{n-1}$$

$$(s_4)_j = \frac{\alpha_1}{2} f_{j-1}^i - \frac{\alpha^n}{2} v_{j-1/2}^{n-1}$$

$$(s_5)_j = -\alpha_2 u_j^i$$

$$(s_6)_j = -\alpha_2 u_{j-1}^i$$

The boundary conditions become

$$\delta f_0^i = 0 \quad \delta u_0^i = 0 \quad \delta u_j^i = 0$$

The equations may be arranged into a block tri-diagonal structure in matrix-vector form. The efficient block elimination method is used to solve for the small δ quantities. Iterations of Newton's method continue until quantities are small enough to be neglected.

Velocity profiles are output by the boundary layer program. At each station along the airfoil surface, the program calculates the u velocities for each value of η in the normal direction of the grid. To retrieve the physical distance normal to the airfoil surface, an inverse transformation is required:

$$y = \frac{\eta}{\sqrt{u_e/\nu x}} \quad (4.19)$$

The kinematic viscosity appears only indirectly in the non-dimensional form of the Reynolds number. Therefore, the following equation is used to give the actual y value:

$$y = \eta \sqrt{x / R_L u_e}$$

where $R_L = \rho u_\infty c / \mu$, or equivalently, $u_\infty c / \nu$, and x and u_e are used as the non-dimensional forms of x/c and u_e/u_∞ . The value of x is the airfoil surface distance.

Plotting the shape of the actual velocity profile at a given station requires the station number, the corresponding x value, the u velocities, and the corresponding y values. All values are provided by the original program or Equation 4.19. To visualize the growth of the boundary layer, the height of the boundary layer is determined by finding where the u velocity has reached the local external velocity. The edge of the boundary layer is noted when u reaches 0.995 of the local external velocity (u_e).

This steady boundary layer solution can also be used for the computation of the boundary layer characteristics on the harmonically pitching NACA 0012 airfoil because the pitch rates used in the experiment were small and the boundary layer lag effects are known to be small for small pitch rates.

C. NAVIER-STOKES (N-S) CODE METHODOLOGY

1. Introduction

A numerical solution based on the compressible thin-layer N-S approximation, incorporating an empirical transition model, is used to study compressible steady and unsteady flows over an airfoil at transitional Reynolds numbers. N-S methods require computational meshes with sufficient grid clustering near the wall for accurate predictions of the large-flow gradients in the viscous layers. The grid outer boundaries must be placed far enough (15 to 20 chord lengths) from the body of interest to apply the inflow and outflow boundary conditions. Unsteady airfoil flow solutions were computed in the past by Rumsey and Anderson [Ref. 49], Visbal [Ref. 50], and Ekaterinaris [Ref. 51] with single-grid approaches, but none accounted for transitional flow effects. The development of leading-edge separated flows are investigated by discretizing the equations with an upwind-biased, factorized, iterative scheme. Solutions obtained for two- and three-dimensional complex flow fields by Rai [Ref. 52] have proven the accuracy of upwind methods.

2. Numerical Method

For this study, the strong conservation-law form of the governing thin-layer, compressible, Reynolds-averaged, N-S equations for a body-fitted coordinate system (ξ, η) along the axial and normal direction, respectively, is as follows:

$$\partial_t \hat{\mathbf{q}} + \partial_\xi \hat{\mathbf{F}} + \partial_\eta \hat{\mathbf{G}} = \text{Re}^{-1} \partial_\eta \hat{\mathbf{S}} \quad (4.20)$$

The Euler equations are obtained when the right-hand side is set equal to zero. In Equation 4.20, $\hat{\mathbf{q}}$ is the conservative variable vector, $\hat{\mathbf{F}}$ and $\hat{\mathbf{G}}$ are the inviscid flux vectors, and $\hat{\mathbf{S}}$ represents the viscous terms in the normal direction. The conservative variable vector $\hat{\mathbf{q}}$ is

$$\hat{\mathbf{q}} = \frac{1}{J} \begin{Bmatrix} \rho \\ \rho u \\ \rho w \\ e \end{Bmatrix},$$

where $J = 1 / (x_\xi z_\eta - x_\eta z_\xi) = \xi_x \eta_z - \xi_z \eta_x$ is the Jacobian of the transformation. $\hat{\mathbf{F}}$ and $\hat{\mathbf{G}}$ are the inviscid fluxes given by

$$\hat{\mathbf{F}} = \frac{1}{J} \begin{Bmatrix} \rho U \\ \rho u U + \xi_x p \\ \rho w U + \xi_z p \\ (e + p)U - \xi_t p \end{Bmatrix} \quad \text{and} \quad \hat{\mathbf{G}} = \frac{1}{J} \begin{Bmatrix} \rho W \\ \rho u W + \eta_x p \\ \rho w W + \eta_z p \\ (e + p)W - \eta_t p \end{Bmatrix}$$

The viscous term, when the thin-layer approximation is applied and also assuming that $\lambda = -\frac{2\mu}{3}$, is given by

$$\hat{\mathbf{S}} = \frac{1}{J} \begin{Bmatrix} 0 \\ \mu m_1 u_\eta + (\mu/3)m_2 \eta_x \\ \mu m_1 w_\eta + (\mu/3)m_2 \eta_z \\ \mu m_1 m_3 + (\mu/3)m_2 m_4 \end{Bmatrix},$$

where

$$m_1 = \eta_x^2 + \eta_z^2, \quad m_2 = \eta_x u_\eta + \eta_z w_\eta,$$

$$m_3 = \frac{\partial}{\partial \eta} (u^2 + w^2)/2 + \kappa \text{Pr}^{-1} \left(\frac{\partial a^2}{\partial \eta} \right), \quad m_4 = (\eta_x u + \eta_z w),$$

a is the local speed of sound, κ is the thermal conductivity, Pr is the Prandtl number, and U, W are the contra-variant velocity components given by

$$U = u\xi_x + w\xi_z + \xi_t, \quad W = u\eta_x + w\eta_z + \eta_t$$

In Equation 4.20, all geometrical dimensions are normalized with the airfoil root-chord length, c ; the density is normalized with the free-stream density, ρ_∞ ; the velocity components u and w are normalized with the free-stream speed of sound, a_∞ ; the total energy per unit volume is normalized with $\rho_\infty a_\infty^2$; and the pressure is related to density and total energy through the equation of state for an ideal gas, $p = (\gamma - 1)[e - \frac{1}{2}\rho(u^2 + w^2)]$.

3. Numerical Implementation

The numerical integration used to compute the mean flow is performed by using a third-order, upwind-biased, factorized, iterative, implicit numerical scheme given by

$$\left[I + h_\xi (\nabla_\xi^b \tilde{A}_{i,k}^+ + \Delta_\xi^f \tilde{A}_{i,k}^-) \right]^p \times \left[I + h_\eta (\nabla_\eta^b \tilde{B}_{i,k}^+ + \nabla_\eta^f \tilde{B}_{i,k}^- - \text{Re}^{-1} \delta_\eta \tilde{M}_{i,k}) \right]^p \times$$

$$(\tilde{Q}_{i,k}^{p+1} - \tilde{Q}_{i,k}^p) = -[(\tilde{Q}_{i,k}^p - Q_{i,k}^n) + h_\xi (\hat{F}_{i+1/2,k}^p - \hat{F}_{i-1/2,k}^p) +$$

$$h_\eta (\hat{G}_{i,k+1/2}^p - \hat{G}_{i,k-1/2}^p) - \text{Re}^{-1} h_\eta (\hat{S}_{i,k+1/2}^p - \hat{S}_{i,k-1/2}^p)]$$

where $h_\xi = \Delta\tau/\Delta\xi$, etc., $\tilde{A}^\pm = (\partial\tilde{F}/\partial\tilde{Q})$, etc., are the flux Jacobian matrices, Δ , ∇ , and δ are forward, backward, and central difference operators, respectively. The quantities $\tilde{F}_{i+1/2,k}$, $\tilde{G}_{i,k+1/2}$, and $\tilde{S}_{i,k+1/2}$ are numerical fluxes.

Time accuracy of the implicit numerical solution is obtained by performing Newton iterations to convergence within each time step. The approximation to \tilde{Q}^{n+1} at each subiteration is the quantity \tilde{Q}^p . When $p \geq 2$, during a given subiteration, $\tilde{Q}^p = \tilde{Q}^{n+1}$, but when $p = 1$ and no subiterations are performed, then $\tilde{Q}^p = \tilde{Q}^n$ and $\tilde{Q}^{p+1} = \tilde{Q}^{n+1}$. By subiterating to convergence, linearization and factorization errors are minimized, because the left-hand side of Equation 4.21 can be driven to zero at each time step. The inviscid fluxes \hat{F} and \hat{G} are evaluated using Osher's [Ref. 53] upwinding scheme.

The numerical fluxes for a third-order accurate upwind-biased scheme are given by

$$\begin{aligned} \hat{F}_{i+1/2,k} = & \tilde{F}_{i+1/2,k} + 1/6 \left[\Delta F_{i-1/2,k}^+ + 2\Delta F_{i+1/2,k}^+ \right] - 1/6 \left[\Delta F_{i-3/2,k}^- + 2\Delta F_{i+1/2,k}^- \right] = \\ & \tilde{F}(Q_{i,k}, Q_{i+1,k}) + 1/6 \left[\Delta F^+(Q_{i+1,k}, Q_{i,k}) + 2\Delta F^+(Q_{i,k}, Q_{i+1,k}) \right] - \\ & 1/6 \left[\Delta F^-(Q_{i,k}, Q_{i+1,k}) + 2\Delta F^-(Q_{i+1,k}, Q_{i,k}) \right]; \end{aligned}$$

here \tilde{F} is the first-order accurate numerical flux for the Osher's scheme given by

$$\tilde{F}_{i+1/2,k} = 1/2 \left[F_{i,k} + F_{i+1,k} - \int_{Q_i}^{Q_{i+1}} \{F_q^+ - F_q^-\} dQ \right],$$

where $F_q = F_q^+ + F_q^-$, $F_q^\pm = (\partial F / \partial Q)^\pm$, and ΔF^\pm are the corrections to obtain high-order accuracy. The Osher scheme evaluates the flux, assuming a shock tube solution where F_q is piece-wise continuous, and yields good predictions of the flux. For the linearization of the left-hand side of Equation 4.21, the flux Jacobian matrices A , B are evaluated by the Steger-Warming [Ref. 54] flux-vector splitting method. The linearization errors are reduced by subiteration to convergence. Typically, two to three subiterations are sufficient to drop the residuals two orders of magnitude during the Newton iteration process. Accurate steady-state solutions can be obtained even without subiteration. Two subiterations are used for the unsteady solutions presented in this thesis.

The viscous fluxes $S_{i,k+1/2}$ are computed with central differences as follows:

$$S_{i,k+1/2} = S \left[Q_{i,k+1/2}, (Q_\eta)_{i,k+1/2}, \eta_{i,k+1/2} \right],$$

$$Q_{i,k+1/2} = 1/2(Q_{i,k} + Q_{i+1,k}), \quad (Q_\eta)_{i,k+1/2} = Q_{i,k+1} - Q_{i,k}.$$

The experimental Reynolds number based on the chord length for the test case examined is 540,000, where it has been shown that transitional flow effects should be considered in the region near the airfoil leading edge.

4. Transition Modeling

For flow over airfoils at Reynolds numbers based on the airfoil chord length of $Re_c = 500,000$, it is known that a transitional flow region exists at the leading edge. As shown by Jang et al. [Ref. 55], the incorporation of transition modeling is essential for the successful prediction of the boundary layers on airfoils.

Empirical formulations are used in engineering methods for the prediction of flow transition in boundary layers. Such methods assess flow transition criteria by (1) using momentum thickness as a parameter, (2) using turbulence models tuned to change from laminar to turbulent flow calculations with averaged transport equations, or (3) accounting for the linear stability characteristics of the boundary layer by calculating amplitude ratios for exponentially growing eigenmodes. These formulations have been used with success for incompressible and subsonic flows, but prediction of transition location with these methods is uncertain for pressure-gradient-driven compressible flows.

One such method is based on the small amplitude, locally parallel flow assumptions, which enable normal mode decomposition. Computation of normal modes and their growth rates give a criterion to predict transition onset locations by the e^n method. Various shortcomings exist with this method. Optional strategies for calculating (n) factors are not consistent with the physical constraints on the eigenmodes under the assumptions of linear stability theory, as shown by Mack [Ref. 56] and Stuckert et al. [Ref. 57]. The method is typically applied for attached flows at high Reynolds numbers.

The method used in this work was previously used by Walker et al. [Ref. 30], showing that the separation bubble occurring on a NACA 65-213 airfoil for incompressible flow and $Re_c = 240,000$ could be computed successfully by using the Chen-Thyson [Ref. 20] transition length model in combination with a viscous-inviscid interaction method. The method coupled a finite difference boundary-layer code with a potential flow code for the outer flow field. In Reference 30, to obtain computed results that were in agreement with the measurements, the transition value, $G_{\gamma_{tr}}$ had to be chosen in a range between 20 and 40 rather than the recommended value of 1200. Recent experiments by Gostelow et al. [Ref. 23] on the effects of free-stream turbulence and adverse pressure gradient on boundary-layer transition show that a change in pressure gradient from zero to even a modest adverse level is accompanied by a severe reduction in transition length. Larger values of $G_{\gamma_{tr}}$ are appropriate for attached flows at high Reynolds numbers. Physically, lower transition values force transition to take place over a shorter distance. Recently, Ekaterinaris et al. [Ref. 58] used Michel's empirical transition onset criterion [Ref. 13] and Chen-Thyson's transition length model with some success to compute the separation bubble on the NACA 0012 airfoil. The objective of the work in this thesis is to study the effect of systematic variations of the transition onset location and transition length parameters in order to determine the location and extent of the transition zone that best models the measured separation bubble behavior. Onset of transition is varied from the initial prediction given by Michel's criterion, which is based on high Reynolds number data, $Re_c \geq 10^6$. Michels' criterion predicts that boundary layer transition has occurred if the Reynolds number based on the boundary layer momentum thickness (Re_θ) is greater than the quantity $\{ 1.174 (1.0 + 22,400/Re_x) Re_x^{0.46} \}$, where Re_x is based on the airfoil surface (x) location from the stagnation point.

The Chen-Thyson intermittency equation (4.12) was incorporated into the N-S code as was done for the boundary layer analysis. The equation is repeated here for completeness.

$$\gamma_{tr}(x) = 1 - \exp \left(- \frac{u_e^3}{G_{\gamma_{tr}} v^2} Re_{x_{tr}}^{-1.34} (x - x_{tr}) \int_{x_{tr}}^x \frac{dx}{u_e} \right)$$

For $x < x_{tr}$, $\gamma_{tr}(x)$ is zero and downstream from transition onset increases exponentially to a value of one, which corresponds to a fully turbulent flow region. The $G_{\gamma_{tr}}$ value alters the slope of the transition curve and determines the length of the transition region. The transition value, $G_{\gamma_{tr}}$, can be input manually and was normally varied from the beginning estimate given by the Cebeci [Ref. 21] correlation formula

$$G_{\gamma_{tr}} = 213 \left[\log(\text{Re}_{x_{tr}}) - 4.7323 \right] / 3 \quad (4.22)$$

For the flow transition region, an effective eddy viscosity is obtained by scaling the turbulent eddy viscosity that is computed from the mean flow by $\gamma_{tr}(x)$. Therefore, $\nu_{trans} = \gamma_{tr}(x) \nu_{turb}$ in the transitional flow region.

The computation starts with a laminar solution from the stagnation point until the onset of transition is calculated by Michels' criterion or transition onset is specified. Chen-Thyson's intermittency equation (4.12) is used in the transition zone. Aft of the transitional flow region, a turbulence model is used for flow analysis. For the present calculations, the two-layer Baldwin-Lomax [Ref. 59] turbulence model or the one equation Baldwin-Barth [Ref. 60] turbulence model can be used in the analysis. The Baldwin-Barth model is used for all the results given in this thesis. The effectiveness of various turbulence models was investigated by Clarkson et al. [Ref. 61] and Ekaterinaris and Menter [Ref. 62]. The conclusions from the investigations were that for mildly separated flows, such as of concern for this work, the effect of the turbulence model on the prediction of aerodynamic loads was not very significant.

From an implementation point of view, the transition model is easily incorporated into numerical analysis codes, is simple to use, and can be combined with any turbulence model. The model accounts for local flow characteristics, and other effects, such as curvature, upstream influence, and pressure gradients are included only through the computed mean flow. The model is also independent of free-stream turbulence level and other flow disturbances. The model requires an evaluation of boundary-layer quantities and is not recommended for massively separated flow cases. The intermittency function has streamwise dependency,

while the effects normal to the wall enter through the turbulent eddy viscosity obtained by the turbulence model.

5. Boundary Conditions and Gridding

The non-slip condition is applied for velocities on the airfoil surface. For the unsteady solutions, the surface velocity is set equal to that obtained by the prescribed airfoil motion as follows:

$$u = \frac{1}{J}(\eta_t \xi_z - \xi_t \eta_z), \quad w = \frac{1}{J}(\xi_t \eta_x - \eta_t \xi_x).$$

Unsteady solutions for the oscillating airfoil are obtained by rotating the grid with the airfoil. For subsonic flow conditions at the inflow and outflow boundaries, the variables are evaluated using one-dimensional Riemann invariant extrapolation. At the inflow boundary, there are three incoming characteristics and one outgoing characteristic. The density (ρ), normal velocity (w), and the pressure (p) are the three variables specified at the inflow boundary. The fourth variable, the axial velocity (u), is extrapolated from the interior flow region. Inflow boundary conditions are given by

$$\rho_1 = \left(\frac{a_1^2}{\gamma s_1} \right)^{(1/\gamma-1)}, \quad s_1 = \left(\frac{p_\infty}{p_1^\gamma} \right), \quad a_1 = \frac{(\gamma-1)}{4}(R_1^+ - R_2^-),$$

$$u_1 = 1/2(R_1^+ + R_2^-), \quad w_1 = w_\infty, \quad p_1 = \left(\frac{\rho_1 a_1^2}{\gamma} \right),$$

where R_1^+ and R_2^- are the incoming and outgoing Riemann invariants given by

$$R_1^+ = u_\infty + 2a_\infty/(\gamma-1), \quad R_2^- = u_2 - 2a_2/(\gamma-1).$$

At the outflow boundary, there is one incoming characteristic and three outgoing characteristics. Only the pressure is specified at the outflow boundary, while the other variables are extrapolated from the interior flow region. For the density and normal velocity, simple first-order extrapolation is used, and the axial

outflow velocity is obtained from the zero-order outgoing Riemann invariant. Outflow boundary conditions are given by

$$\begin{aligned} \rho_1 &= \rho_2 & u_1 &= R_1^+ - 2a_2/(\gamma - 1), & a_1 &= \sqrt{\gamma p_1/\rho_1}, \\ a_1 &= \sqrt{\gamma p_1/\rho_1}, & w_1 &= w_2, & p_1 &= p_\infty. \end{aligned}$$

For the unsteady analysis, the oscillating airfoil along with the computational grid rotates about the one-quarter chord point ($x/c = 0.25$, $y/c = 0.0$). On the other hand, the rectangular LDV measurement grid remains stationary throughout all the tests. Therefore, an interpolation scheme was used to make direct comparisons of computed and measured velocity profiles at the stationary nodes of the measurement grid as shown in Chapter VII. The computation (275×81) and LDV measurement (6×21) grids near the leading edge of the airfoil were shown in Figure 3.4.

D. COMPUTATIONAL UNCERTAINTIES

The computations were done with grid densities ranging from 275×81 (baseline grid) to 601×161 with refined points in the transition region to establish grid independence. The baseline grid had 16 surface points in the vicinity of the separation bubble, while the dense grid had 86 points in the same region. The boundary layer had 17 and 38 points in the respective grids. The oscillatory airfoil solutions were started with a converged steady solution at 8 degrees angle of attack. The density residual for the steady angle-of-attack solutions was on the order of 10^{-6} after 4000 time steps, with each time step being 0.005. The unsteady analysis used the same time-step size with density residuals on the order of 10^{-4} , which was not surprising because of the continual flow changes that were imposed by the oscillating airfoil. Only minor differences were noted in the computed solutions. For example, at 8 degrees angle of attack, the maximum differences in pressure and skin-friction coefficient were less than 1.5%, occurring around the suction-pressure peak (-3.4 versus -3.45) near the airfoil leading edge. For the oscillatory motion cases, the computed solution continued for three cycles. The second and third cycle values for lift, drag, and moment coefficients were identical, and the results are shown for the

third cycle. Therefore, the 275×81 point grid was used for both the steady and unsteady solutions that are presented in this thesis.

V. EXPERIMENTAL RESULTS

This chapter presents the results from the LDV and PDI experimental methods described in Chapter III. Measurements were made to characterize steady, high- and low-amplitude oscillatory, deep and lightly stalled compressible flows with separation bubbles near the airfoil leading edge that affect the inception and development of the dynamic-stall process. Both the LDV and PDI measurements gave valuable data for evaluation of computational capabilities to predict the leading-edge airfoil flow field.

Initially, the leading-edge flow field over the NACA 0012 airfoil is best described by the interferograms from the PDI measurements. Each interference fringe gives a line of constant density with an associated Mach number. The fringe map can also be used to quantify the local pressure distributions on the airfoil, as shown in the next section. The registration markers for identifying proper airfoil orientation were described in Chapter III and are seen in all the PDI Figures. The interferograms focus on a region from slightly forward of the airfoil leading edge to 30-45% chord downstream.

A. FLOW OVER STEADY NACA 0012 AIRFOIL

Interferograms are shown for $\alpha = 0^\circ$ in Figure 5.1. The stagnation point is at the leading edge, which is at the center of the smallest closed density contour. The velocity increases from the stagnation point in both directions over the upper and lower surfaces. The stagnation point in the flow, which moves under the airfoil leading edge with increasing angle of attack, quantifies the density field and related Mach contours for the complete interferogram. Good flow symmetry is seen for the upper and lower surfaces of the airfoil, as expected at $\alpha = 0^\circ$.

At $\alpha = 6^\circ$, the stagnation point has moved under the leading edge of the airfoil, and the number of fringes has increased from eight to 16. The additional fringes are concentrated over the upper airfoil leading-edge surface. All density contours present a continual and gradual curvature with the upper surface, that is, no presence of a separation bubble is indicated in Figure 5.2.



Figure 5.1. Interferogram of the Flow Near the Airfoil Leading Edge. $M_\infty = 0.3$, $\alpha = 0^\circ$, $k = 0.0$, $Re = 540,000$.

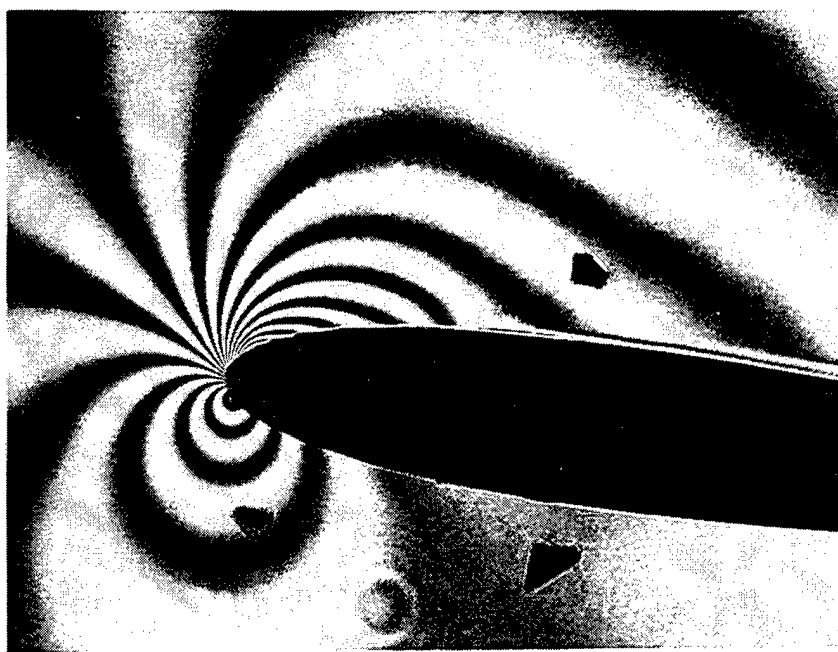


Figure 5.2. Interferogram of the Flow Near the Airfoil Leading Edge. $M_\infty = 0.3$, $\alpha = 6^\circ$, $k = 0.0$, $Re = 540,000$.

In Figure 5.3 at $\alpha = 8^\circ$, three additional fringes are seen over the airfoil leading edge, where the constant density contours show a change in shape from those previously seen at $\alpha = 6^\circ$. Just downstream of and not belonging to the suction peak itself, the contours close to the airfoil surface turn almost parallel with the airfoil surface for some distance. The region encompassing five fringes shows very little gradient in the streamwise direction, but at the downstream ends turn abruptly towards the airfoil surface. The fringes meet the airfoil surface almost perpendicularly in contrast to the gradual low angles that are shown at $\alpha = 6^\circ$. The shape of the fringe contours suggests the presence of a laminar separation bubble because, subsequently, the flat contours are shown to correspond to a plateau in the pressure distribution. The test conditions for the NACA 0012 airfoil at $Re = 540,000$ are appropriate for laminar separation bubbles. The formation of laminar separation bubbles was already confirmed by LDV measurements over the leading edge of the airfoil for low-frequency forced oscillations [Ref. 41 and 34]. The contour lines outside the separation bubble turn gradually downstream and are seen to define the boundary layer over the airfoil surface downstream of the separation bubble.

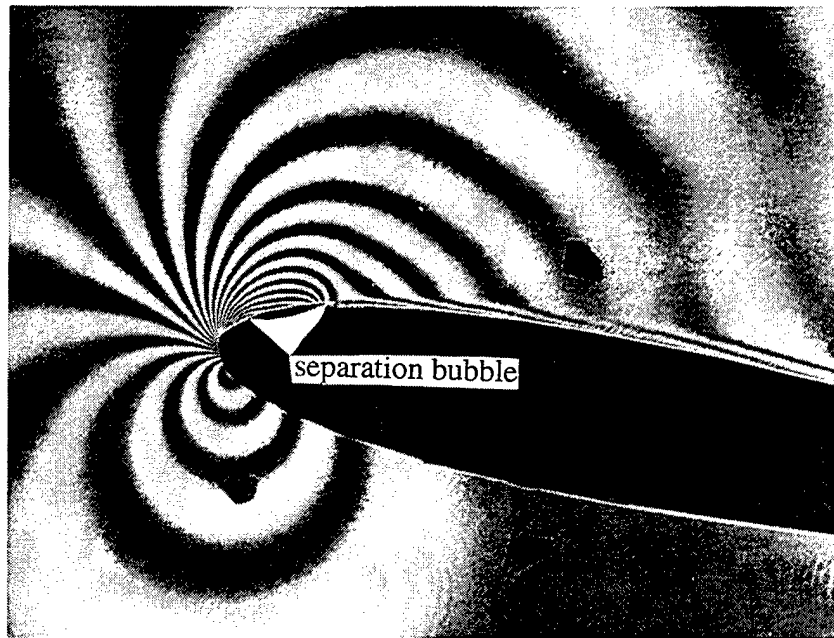


Figure 5.3. Interferogram of the Flow Near the Airfoil Leading Edge. $M_\infty = 0.3$, $\alpha = 8^\circ$, $k = 0.0$, $Re = 540,000$.

As the flow accelerates over the leading edge of the airfoil at $\alpha = 10^\circ$, five additional fringes and higher density gradients develop as shown in Figure 5.4. A dark region appears at the leading edge of the airfoil because much of the light has been severely deflected by the steep gradients converging in the area, but it has been shown not to affect the fine details of the pressure distribution. Just downstream of the suction peak, where the airfoil surface curvature is also reduced, the contours again are seen to "plateau" for some distance along the airfoil surface just as seen in Figure 5.3. Also, the fringes turn nearly perpendicular to the airfoil at the aft end of the separation bubble and a thickening boundary layer is seen downstream of the separation bubble.

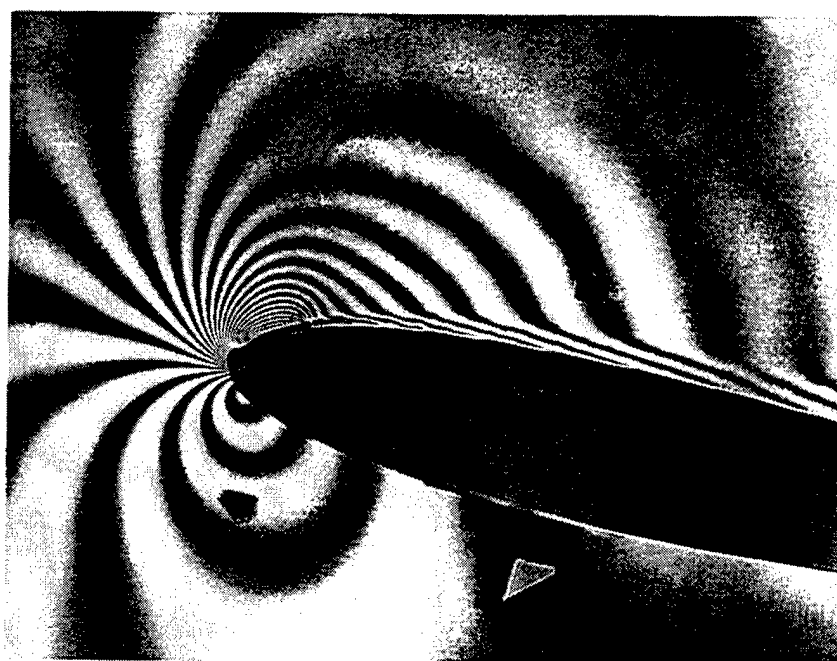


Figure 5.4. Interferogram of the Flow Near the Airfoil Leading Edge. $M_\infty = 0.3$, $\alpha = 10^\circ$, $k = 0.0$, $Re = 540,000$.

Figures 5.5 and 5.6 show the unsteady nature of the flow field in the vicinity of the airfoil stalling angle of attack at $\alpha = 12^\circ$. A separated flow condition is shown in the first case at (a) $\alpha = 11.95^\circ$, and in the second case, a well defined separation bubble resides near the leading edge at (b) $\alpha = 12.05^\circ$.

However, the fringes turning vertical towards the airfoil surface in the boundary layer at the downstream end of the separation bubble are the first evidence of stall [Ref. 63].

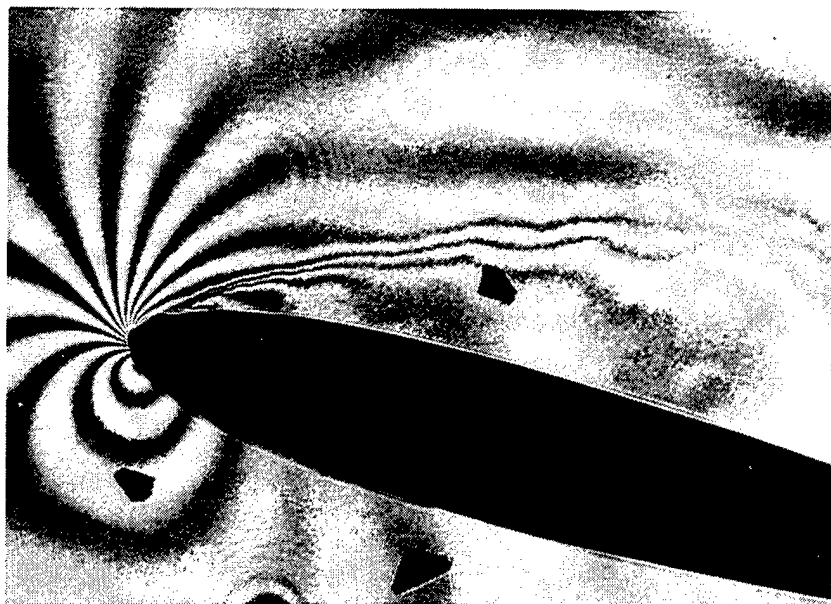


Figure 5.5. Interferogram of the Flow Near the Airfoil Leading Edge. $M_\infty = 0.3$, $\alpha = 11.95^\circ$, $k = 0.0$, $Re = 540,000$.



Figure 5.6. Interferogram of the Flow Near the Airfoil Leading Edge. $M_\infty = 0.3$, $\alpha = 12.05^\circ$, $k = 0.0$, $Re = 540,000$.

1. Pressure Distributions From the PDI Interferograms

The pressure plots were obtained by mapping the x -location of the intersection of each fringe with the airfoil surface. The fringe numbers were then converted to C_p s for the pressure distributions. The resultant pressure distributions for $0 \leq x/c \leq 0.2$ derived from the interferograms are given in the next series of plots.

In Figure 5.7, the suction peak (C_p) is shown to increase by at least (-1) for every 2° increase in angle of attack from $\alpha = 6^\circ$ to 10° . No pressure plateau is seen downstream of the suction peak for $\alpha = 6^\circ$. The innermost fringe that could be defined at $\alpha = 6^\circ$ extended for a short distance along the airfoil upper surface, resulting in a flat suction pressure peak. The flat pressure plateau aft of the suction peak for $\alpha = 8^\circ$ and $\alpha = 10^\circ$ is indicative of a separation bubble, corresponding to the density contours that turned parallel to the airfoil surface before turning abruptly towards the airfoil surface at the downstream edges. Aft of the pressure plateau, a second region of adverse pressure gradient is shown for $0.05 < x/c < 0.075$. For example, here the pressure gradient, $dC_p/d(x/c)$, is 125 while the C_p increases from -3.6 to -2.15 for $\alpha = 10^\circ$. The adverse pressure gradient aft of the suction pressure peak is generally less (≈ 60 -70). The pressures then gradually increase over the rest of the airfoil. The chordwise extent of the pressure plateau region may be used to estimate the size of the separation bubble. At $\alpha = 8^\circ$ the bubble begins at 3.0% chord and at $\alpha = 10^\circ$, the separation bubble location begins at 2.0% chord, indicating onset of the bubble closer to the leading edge at higher angles of attack as a result of an increased adverse pressure gradient. The downstream edge of the separation bubble ranges from 5.0% chord at $\alpha = 10^\circ$ to 6.0% chord at $\alpha = 8^\circ$. Presumably, the separation bubble extends to downstream locations that are part way down the adverse pressure gradient or where the turbulent flow pressure profile intersects the pressure profile with separation bubbles for this flow, much the same as that shown by Tani [Ref. 5] for a higher Reynolds number flow.

A pressure plateau is present downstream of the suction peak for the flow at each angle of attack, $\alpha = 7^\circ$, 9° , and 11° , presented in Figure 5.8. The suction pressure peaks are shown to move forward slightly on the airfoil surface with

increasing angle of attack. The length of the pressure plateau decreases noticeably with increasing angle of attack. The adverse pressure gradient downstream of the plateau and separation bubble is 125 for $\alpha = 9^\circ$ and decreases to 75 for $\alpha = 11^\circ$ in the range $0.04 < x/c < 0.065$. The suction pressure peak at $\alpha = 11^\circ$ is -4.45 compared to -4.25 at $\alpha = 10^\circ$, indicating a flow that is approaching its full lifting capacity.

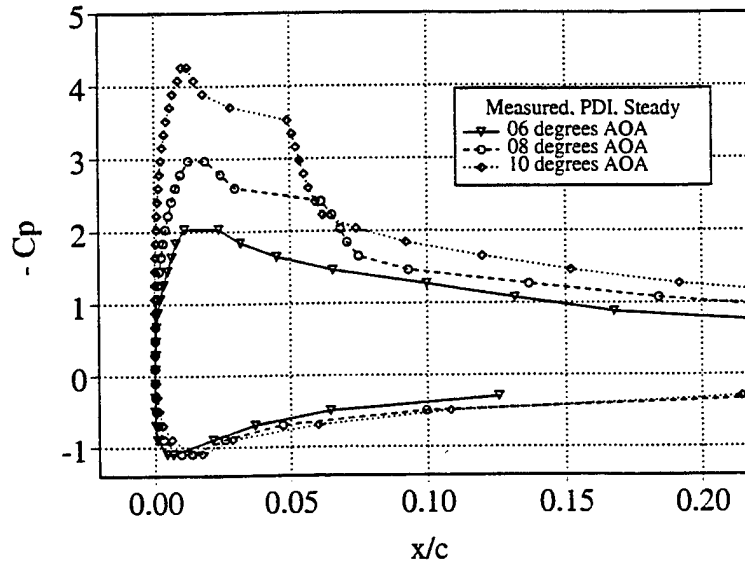


Figure 5.7. Pressure Distributions Derived From PDI Measurements. $M_\infty = 0.3$, $\alpha = 6^\circ, 8^\circ$, and 10° , $k = 0.0$, $Re = 540,000$.

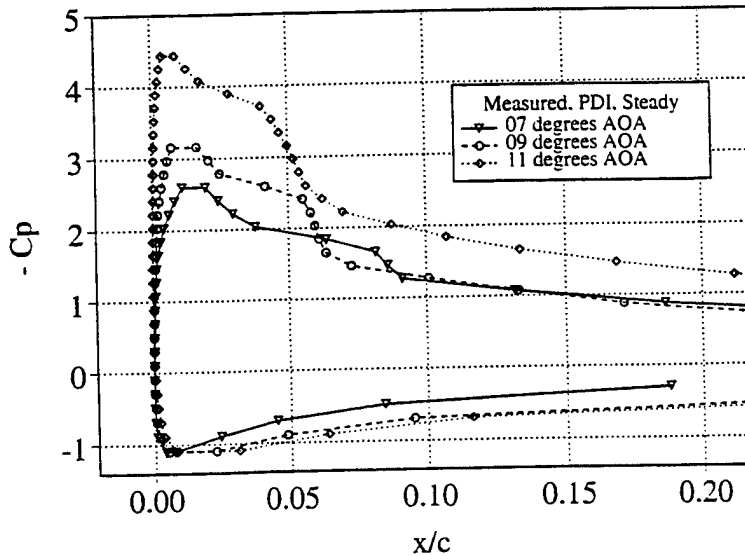


Figure 5.8. Pressure Distributions Derived From PDI Measurements. $M_\infty = 0.3$, $\alpha = 7^\circ, 9^\circ$, and 11° , $k = 0.0$, $Re = 540,000$.

Pressure distributions for a stalled flow condition at 11.95° angle of attack and a flow on the verge of stall at 12.05° angle of attack are shown in Figure 5.9. The pressures correspond to the interferograms in Figure 5.5 and 5.6. Indicative of a flow on the verge of stall, the pressure peak at 12.05° angle of attack has decreased slightly from that previously shown at 11° angle of attack. The plateau region shows the beginnings of breakdown as its downstream end is lifting away from the surface. The flat (stalled) pressure profile at 11.95° angle of attack gives pressure levels below those previously shown for 6° angle of attack forward of 5% chord over the airfoil upper surface.

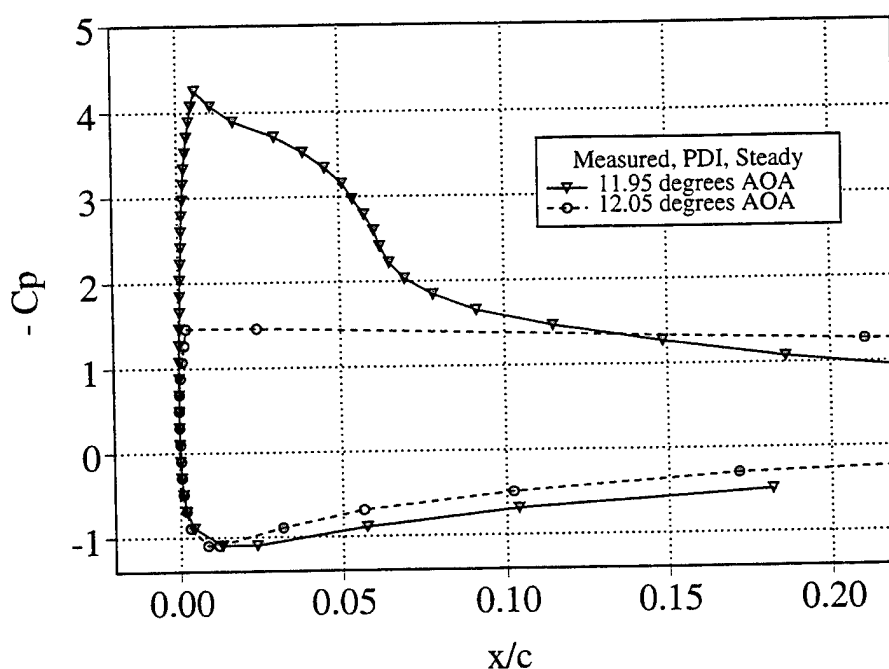


Figure 5.9. Pressure Distributions Derived From PDI Measurements. $M_\infty = 0.3$, $\alpha = 11.95^\circ$ and 12.05° , $k = 0.0$, $Re = 540,000$.

2. Mach Number From PDI Density Ratio

Figure 5.10 gives a representative case of fringes that have been converted to digital form for $\alpha = 10^\circ$ and a more detailed investigation, indicating the density ratio value on selected contours. The 0.944 density contour (one below 0.935) that was on the upper surface of airfoil at $\alpha = 0^\circ$ now meets the airfoil leading edge from nearly the horizontal. The flow is highly accelerated over the leading edge to 2.34 times the free-stream Mach number ($M = 0.701$). By including all

fringes downstream of the suction peak that run parallel with the airfoil surface and then turn perpendicular to the airfoil surface downstream of 5% chord, the separation bubble is estimated to extend from $0.025 < x/c < 0.065$ along the surface of the airfoil. Using the same fringes, the separation bubble is estimated to be 2% chord in height.

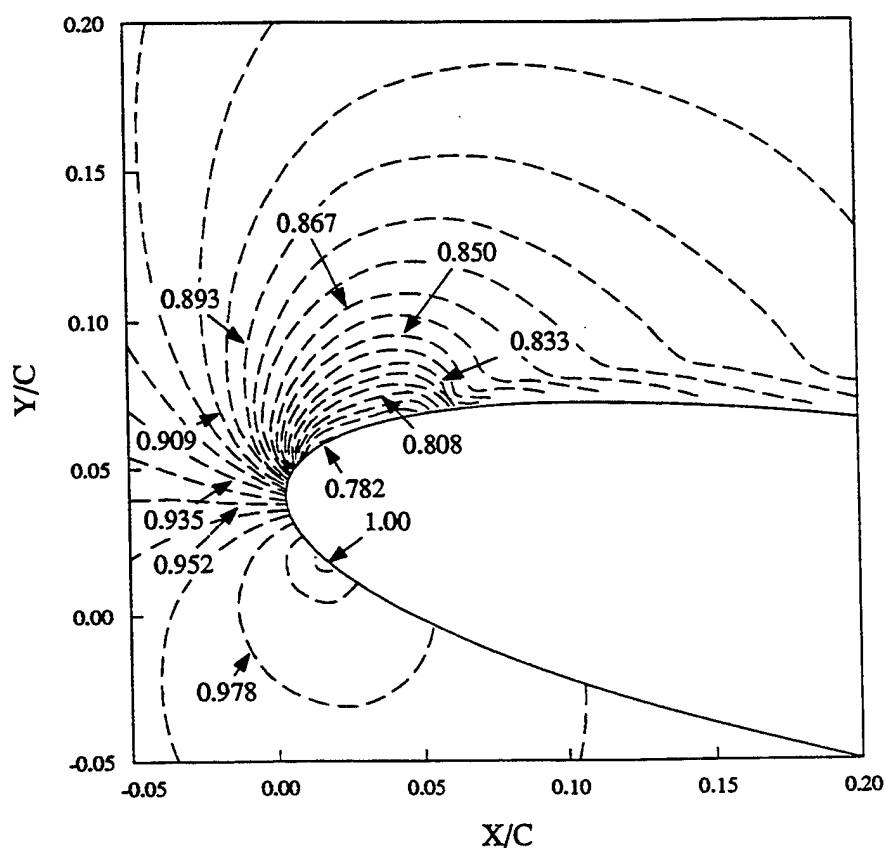


Figure 5.10. Density Contours From Interferograms in Flow Near Airfoil Leading Edge. $M_\infty = 0.3$, $\alpha = 10^\circ$, $k = 0.0$, $Re = 540,000$.

3. U-Component (LDV) Velocity Contours

The U-component velocity contours in the proximity of the airfoil surface are given for 8° angle of attack in Figure 5.11. A high-velocity region extends from 5 to 9% chord at heights of $0.021 \geq y/c \geq 0.017$ above the airfoil surface and is slightly aft of the high-velocity region indicated in the PDI measurements. The high-velocity region is forward of the surface locations $0.10 \leq x/c \leq 0.117$,

where a minimum distance of 1.6% chord exists between the measurements and the airfoil surface. A minimum measured velocity in the flowfield of $1.07 U_\infty$ occurs above the airfoil leading edge.

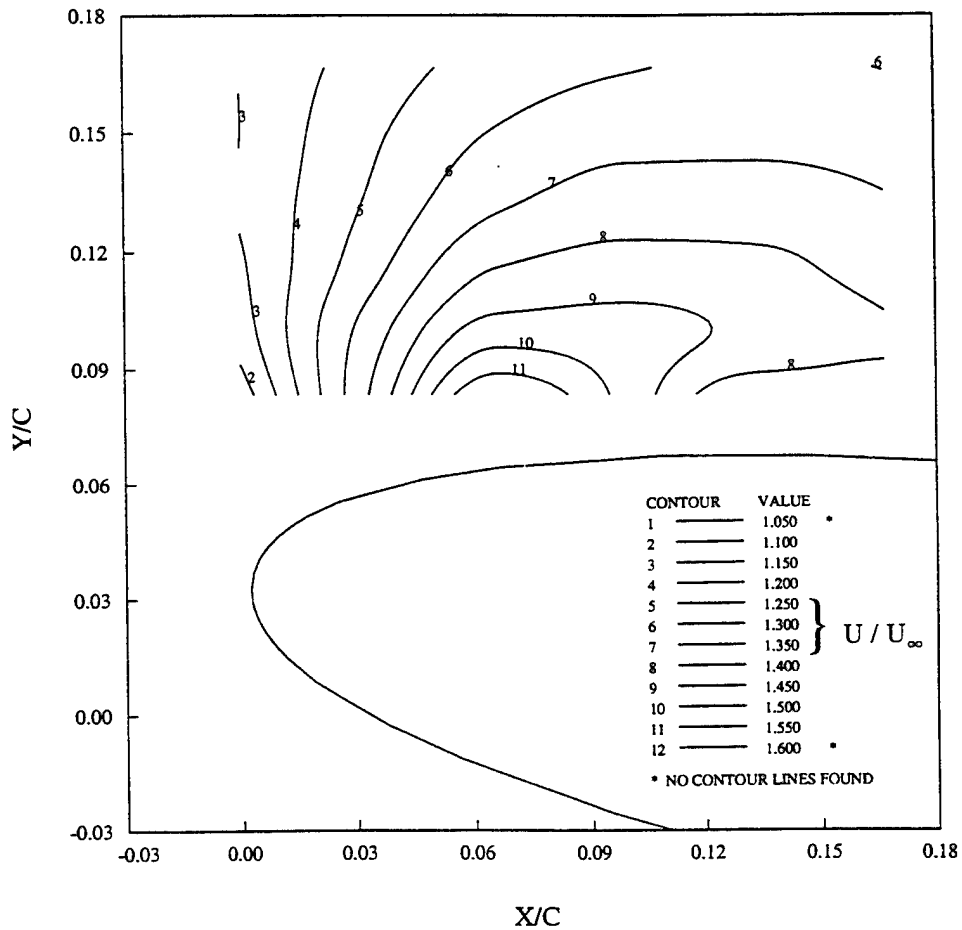


Figure 5.11. Normalized Velocity Contours (U-component, LDV) Near the Airfoil Leading Edge. $M_\infty = 0.3$, $\alpha = 8^\circ$, $k = 0.0$, $Re = 540,000$.

Velocity contours for $\alpha = 12.05^\circ$ are shown in Figure 5.12. The measurement region relative to the airfoil position is similar to that at 8° angle of attack. Slightly higher velocities ($1.68 U_\infty$) are noted because of the increased angle of attack, which occur in a slightly larger region from 4.5 to 9% chord at heights from $0.025 \geq y/c \geq 0.021$ above the airfoil surface. Measurement points closer to the airfoil surface could not be optically accessed because of laser beam blockage by the airfoil surface. The highest velocity region encompasses the separation bubble location near the airfoil surface.

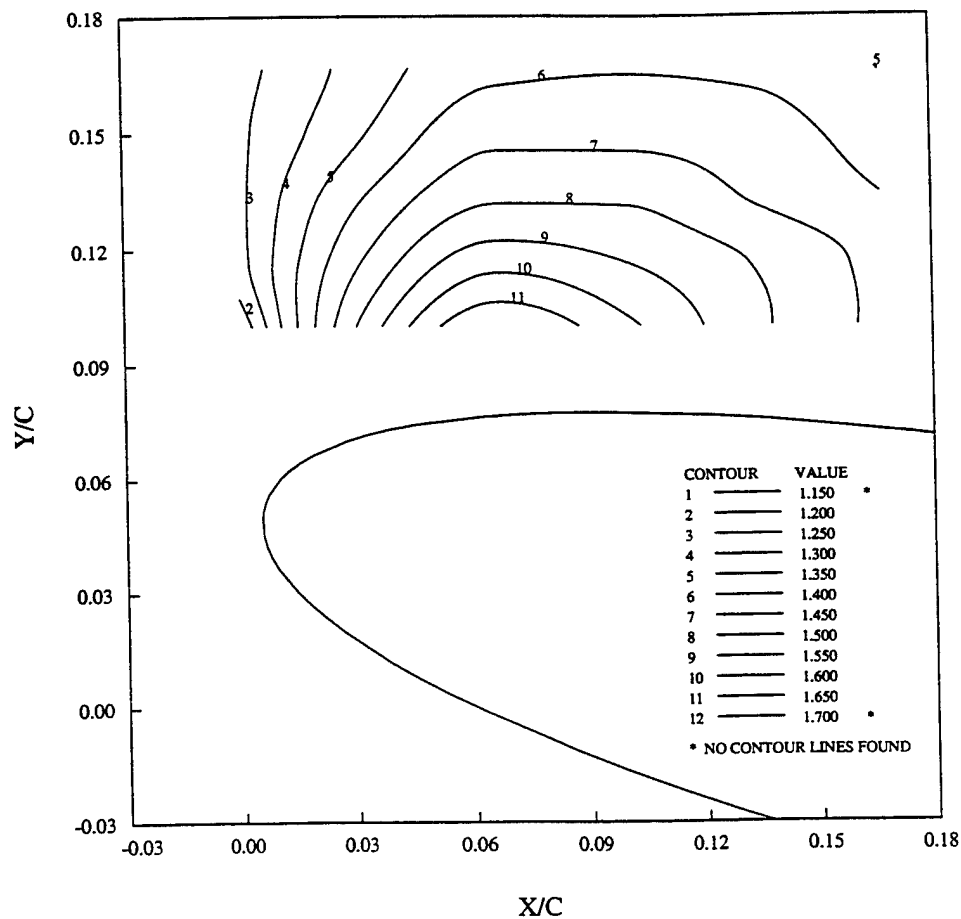


Figure 5.12. Normalized Velocity Contours (U-component, LDV) Near the Airfoil Leading Edge. $M_\infty = 0.3$, $\alpha = 12.05^\circ$, $k = 0.0$, $Re = 540,000$.

B. UNSTEADY/OSCILLATING NACA 0012 AIRFOIL

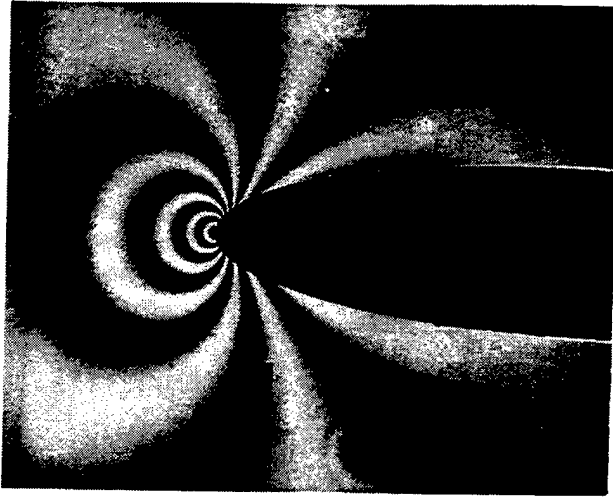
LDV results are shown in this section for two separate test cases in which the airfoil oscillation amplitude is varied about the mean angle of attack, $\alpha = 10^\circ$, such that $\alpha = 10^\circ - 10^\circ \sin \omega t$ and $\alpha = 10^\circ - 2^\circ \sin \omega t$ in a $M_\infty = 0.3$ flow. The reduced frequency ($k = 2\pi fc/U_\infty$) based on airfoil chord for each test case was 0.1. As for the steady flow results, the test Reynolds number is 540,000 and the airfoil is the NACA 0012.

Several PDI images, focusing on the first 30 to 40% airfoil chord, are used initially to describe the flow physics for the high-amplitude forced-oscillation test.

1. Deep Dynamic Stall ($\alpha = 10^\circ - 10^\circ \sin \omega t$)

This test case ($M_\infty = 0.3$, $\alpha = 10^\circ - 10^\circ \sin \omega t$) resulted in massive flow separation at the higher angles of attack. LDV measurements were more difficult in the highly accelerated and separated flow that showed extremely complex flow physics.

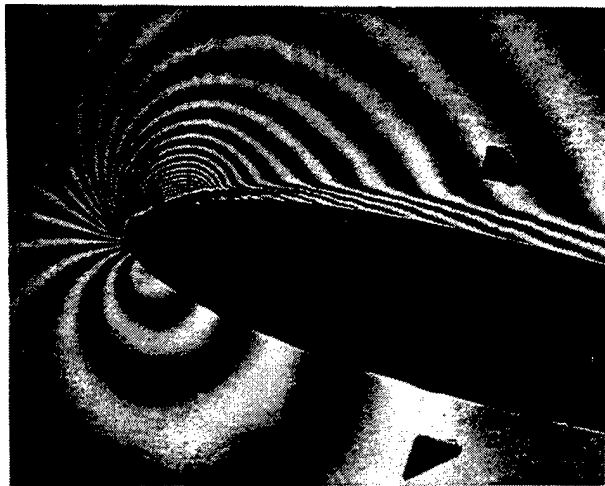
The PDI images in Figure 5.13 show the flow physics for the high-amplitude oscillation case during airfoil upward motion. At 0 degree angle of attack, the flow has fully established to the point where the picture is almost identical to that previously shown for the steady case at 0 degree angle of attack. For the unsteady case, stall does not occur at 12° angle of attack on airfoil upward motion. As is well known from Carr and Chandrasekhara [Ref. 64], the process of dynamic stall in this case starts with the formation of the dynamic stall vortex at angles of attack slightly higher than static stall. Until the vortex is shed into the wake, the airfoil continues to generate lift. The vortex release (shedding) angle as measured earlier by schlieren flow visualization experiments was shown to be $\alpha = 15.9^\circ$ [Ref. 26]. The PDI image in Figure 5.13d indicates that the flow has almost reached the fully stalled condition.



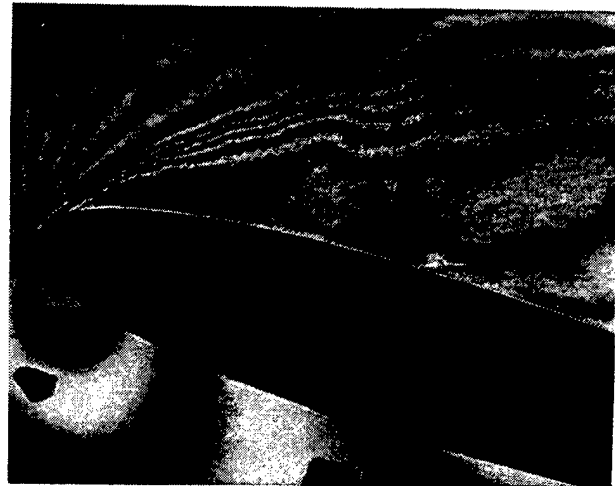
(a) $\alpha = 0^\circ$.



(b) $\alpha = 6^\circ$.



(c) $\alpha = 12^\circ$.



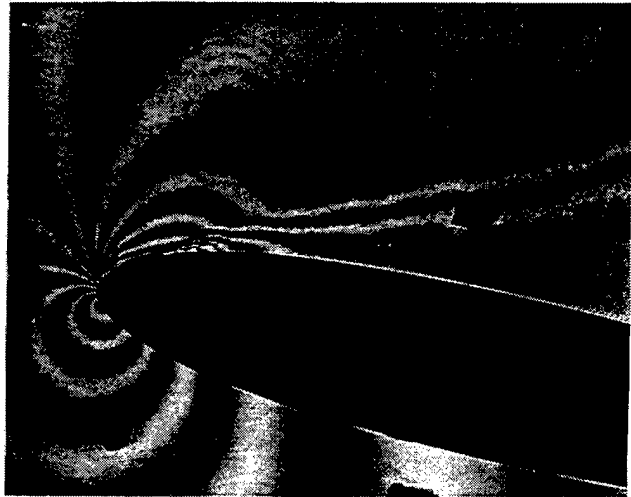
(d) $\alpha = 15.5^\circ$.

Figure 5.13. Interferograms of the Flow Near the Leading Edge of the Oscillating Airfoil. $M_\infty = 0.3$, $\alpha = 10^\circ - 10^\circ \sin \omega t$, $k = 0.1$.

A progression of flow reattachment is shown in Figure 5.14 during the airfoil downward motion. The flow remains highly separated at 12° angle of attack on airfoil downward motion, even though it is well below the dynamic stall angle of attack of 15.9° . Flow reattachment has begun at $\alpha = 11^\circ$ with several fringes now contacting the airfoil surface over the leading edge. As documented in [Ref. 42] and as shown in Figure 5.14d, complete flow reattachment does not happen until the airfoil passes 9° angle of attack. Thus, a larger hysteresis loop is present for the flow.



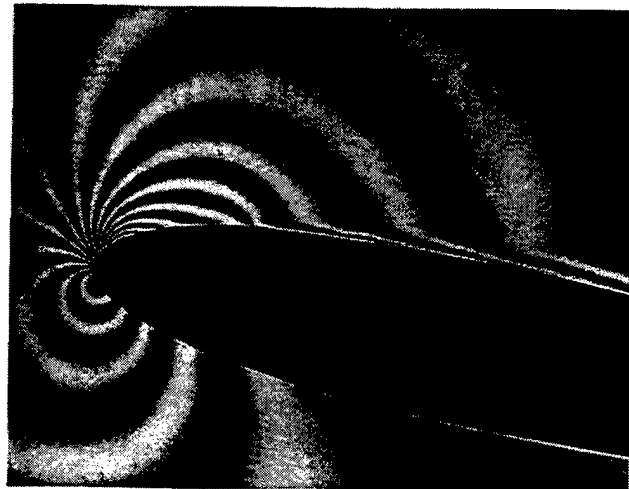
(a) $\alpha = 12^\circ$.



(b) $\alpha = 11^\circ$.



(c) $\alpha = 10.5^\circ$.



(d) $\alpha = 9^\circ$.

Figure 5.14. Interferograms of the Flow Near the Leading Edge of the Oscillating Airfoil. $M_\infty = 0.3$, $\alpha = 10^\circ - 10^\circ \sin \omega t$, $k = 0.1$.

U-component velocities throughout the oscillation cycle (vs. phase angle) are shown in Figure 5.15 at $x/c = -0.100$ offset by $0.2U_\infty$ at each increasing height for presentation purposes. Even at this upstream location, the effect of the oscillating airfoil on the flow is felt at all heights above the airfoil surface. At the lowest measurement height ($y/c = 0.083$), U velocities are slightly less than the free-stream speed and data are not continuous because the LDV beam is blocked by the airfoil. A sinusoidal relationship exists between the phase angles (angles of attack) along the x-axis, and the U velocity tends to follow the airfoil oscillatory motion up to the dynamic stall angle of attack, $\alpha = 15.9^\circ$ or $\phi = 216^\circ$. U velocities peak at 10% above the free-stream value just before reaching the dynamic stall angle of attack and then fall up to 20% because of the separated flow as the angle of attack increases to 20° . The reduced velocities continue until the flow begins to reattach at $\alpha = 11^\circ$ on the airfoil downstroke to minimum values in the cycle just after passing the dynamic stall angle of attack.

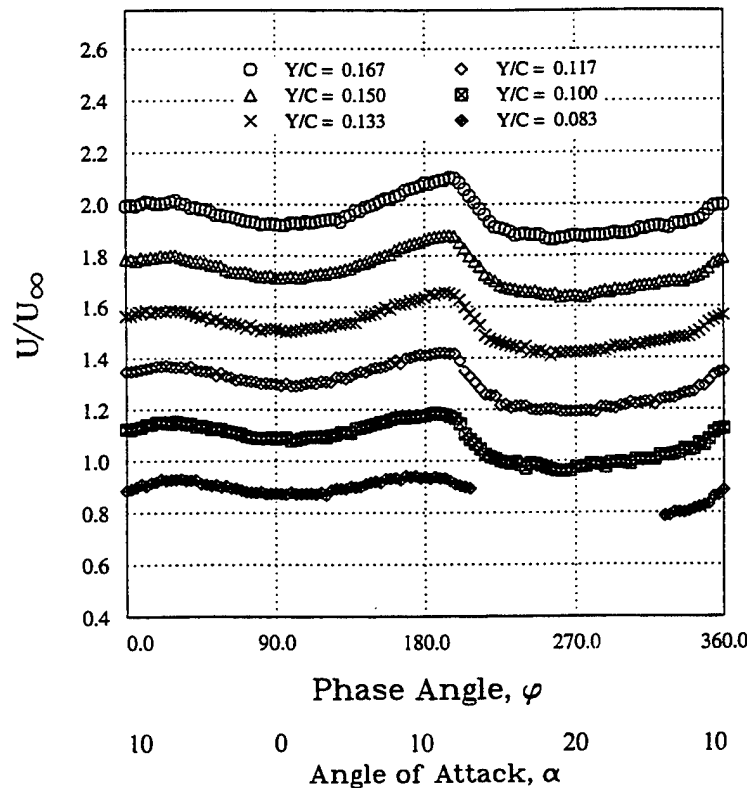


Figure 5.15. Phase Distribution of U-Component Velocities at $x/c = -0.100$. (Velocity offset by $0.2U_\infty$ at each height.) $M_\infty = 0.3$, $\alpha = 10^\circ - 10^\circ \sin \omega t$, $k = 0.1$.

V-component (vertical) velocities forward of the airfoil surface vary more than the U-component during the airfoil oscillations (5% to 40% of free-stream values) before dynamic stall occurs, as shown in Figure 5.16. Again, the velocities follow the motion of the airfoil to the dynamic stall angle of attack. Peak velocities during the oscillation cycle occur slightly after those seen for the U-component. Velocity reductions after dynamic stall are not as extensive as for the U-component because the streamlines are deflected upward as the flow undergoes deep stall. The V velocity slowly decreases until flow reattachment is complete [Ref. 42]. Disregarding the velocity offset, V velocities overlay each other at the bottom two heights with average values between 0.05 and 0.4 of the free-stream speed. At increasing heights, V velocities decrease slightly.

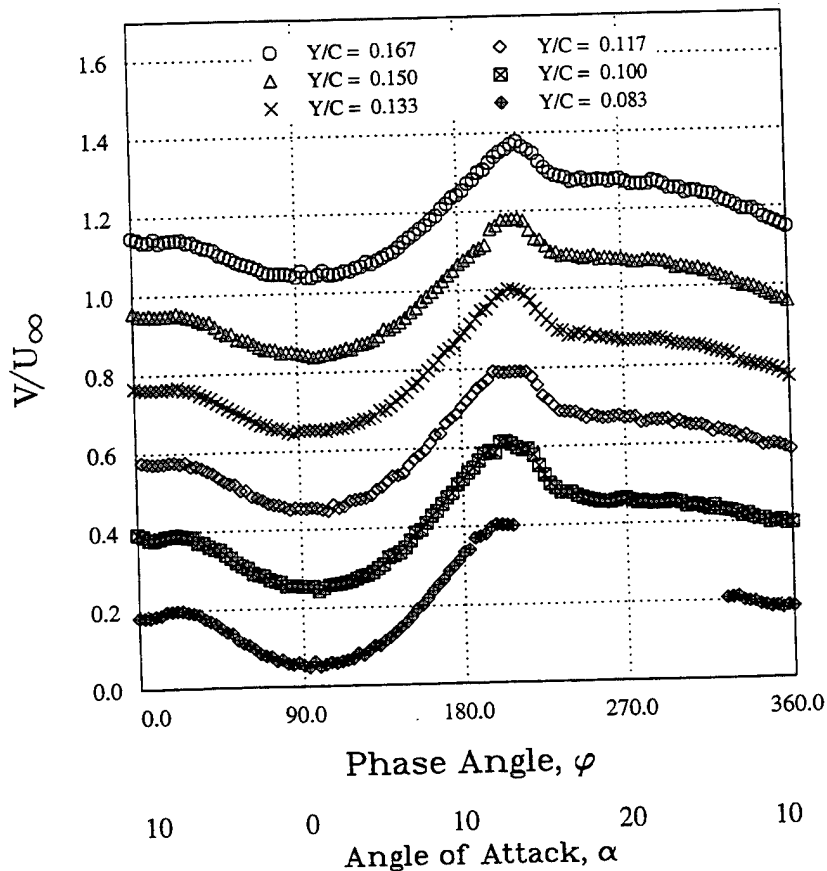


Figure 5.16. Phase Distribution of V-Component Velocities at $x/c = -0.100$. (Velocity offset by $0.2U_\infty$ at each height.) $M_\infty = 0.3$, $\alpha = 10^\circ - 10^\circ \sin \omega t$, $k = 0.1$.

More dramatic changes in the flow are seen above the airfoil surface at $x/c = 0.067$ shown in Figure 5.17. Validated average U-component velocities vary widely from 0.45 to $1.5 U_\infty$ throughout the oscillation cycle. The missing data at the lower heights occur because of laser-beam blockage by the airfoil, and at $y/c = 0.017$ a lack of validated particles is the cause of missing data in some cases. The velocities at this location over the airfoil surface vary more widely than those forward of the airfoil before reaching the dynamic stall angle of attack. At $y/c = 0.167$ and $\alpha = 8^\circ$, velocities are at the free-stream value, but those at $\alpha = 15.9^\circ$ are 50% greater than the free-stream velocity. At the three uppermost (y/c) locations (above or out of the separation bubble) after passing the dynamic stall angle of attack, the velocity drops up to 50% with major velocity fluctuations (0.5 of the free-stream velocity) noted in the measurements. At the lower heights ($y/c = 0.083$ and 0.100), U velocities fall off rapidly already at 7 and 8° angle of attack from 1.35 and $1.4 U_\infty$, getting as low as $0.4 U_\infty$ before the angle of attack reaches 13° . This dramatic drop in velocity is attributable to velocity measurements within the outer region of the separation bubble.

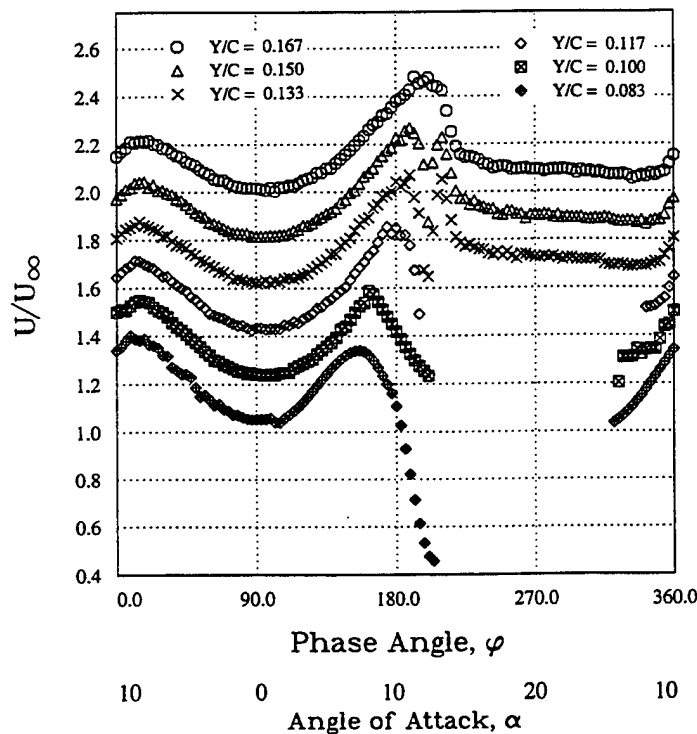


Figure 5.17. Phase Distribution of U-Component Velocities at $x/c = 0.067$. (Velocity offset by $0.2 U_\infty$ at each height.) $M_\infty = 0.3$, $\alpha = 10^\circ - 10^\circ \sin \omega t$, $k = 0.1$.

In Figure 5.18, V-component velocities at $x/c = 0.067$ near the dynamic stall angle of attack show rapid increases, starting just before and then peak at dynamic stall. For example, at $y/c = 0.133$, the V velocities rise abruptly from 0.1 to $0.55U_\infty$ as angle of attack increases from 13 to 16° . During this phase of oscillation, the dynamic stall vortex grows, pushing the outer edge of the enveloping shear layer outwards. At $\alpha = 15.9^\circ$, the dynamic stall vortex is shed [Ref. 26] and the shear layer detaches from the surface everywhere, except at the airfoil leading edge. The large V-component velocities and the simultaneous drop in the U-component velocities are further evidence of separation bubble bursting, which initiates the dynamic stall process.

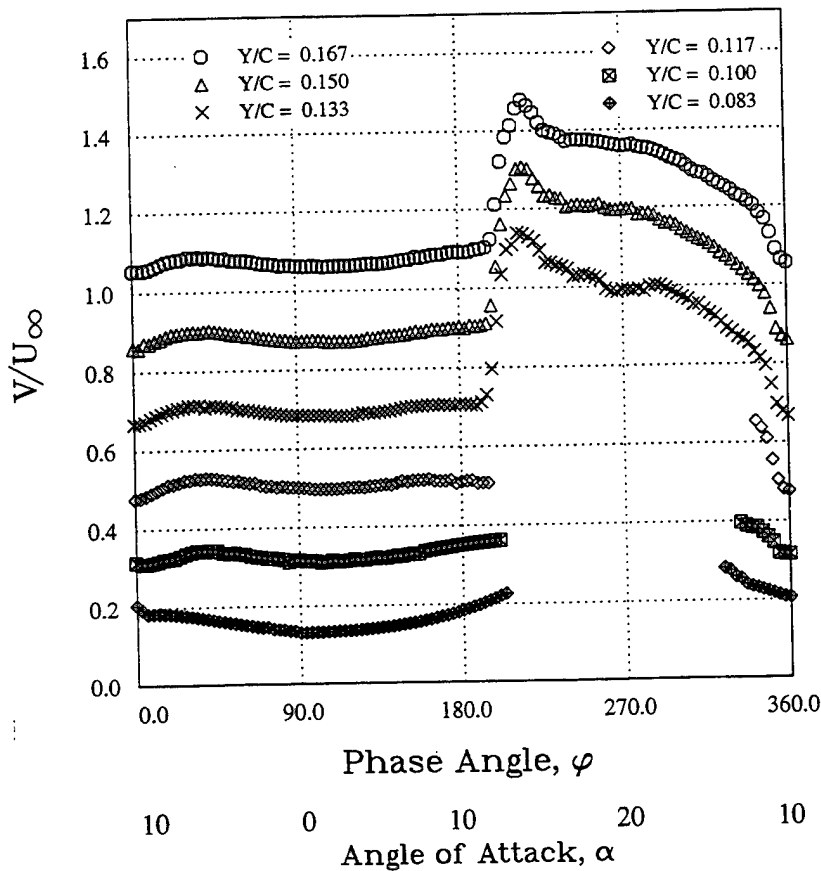


Figure 5.18. Phase Distribution of V-Component Velocities at $x/c = 0.067$. (Velocity offset by $0.2U_\infty$ at each height.) $M_\infty = 0.3$, $\alpha = 10^\circ - 10^\circ \sin \omega t$, $k = 0.1$.

Velocity magnitude profiles are shown at $x/c = 0.067$ and angles of attack from 7 to 16° in Figure 5.19. Velocities at $y/c = 0.083$ continue to decrease from 0.83 to $0.65 U_\infty$ as the angle of attack increases from 7 to 13° . The velocity profiles in the laminar shear layer initially have full laminar shapes, and then exhibit slight inflections at the higher angles of attack. From 14 to 16° angle of attack, inverted “S” profiles appear, indicating unusual shear patterns in the flow. At $y/c = 0.10$ and for $\alpha \geq 14^\circ$, velocities are as low as $0.5 U_\infty$.

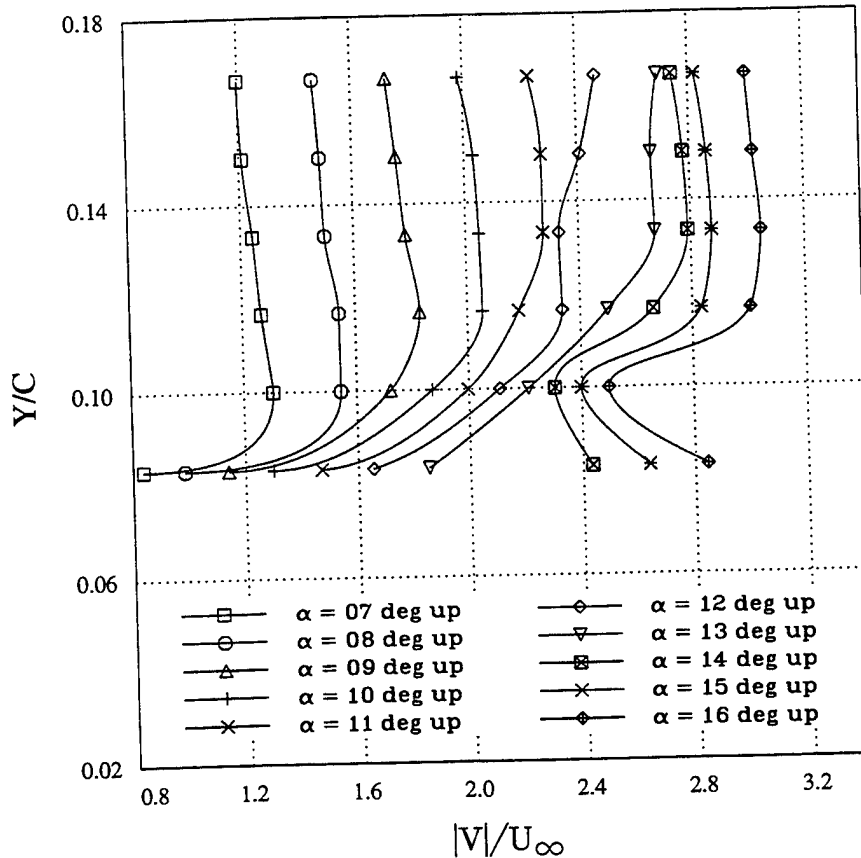


Figure 5.19. Velocity Magnitude $|V|$ Profiles at $x/c = 0.067$. (Profiles offset by $0.2 U_\infty$ at each AOA.) $M_\infty = 0.3$, $\alpha = 10^\circ - 10^\circ \sin \omega t$, $k = 0.1$.

The previous figures describe the dramatic flow physics that are part of the high-amplitude deep dynamic stall flow. Computationally, the problem becomes intractable for such flows, and thus, the low amplitude case was measured, which is shown to present the case of light dynamic stall.

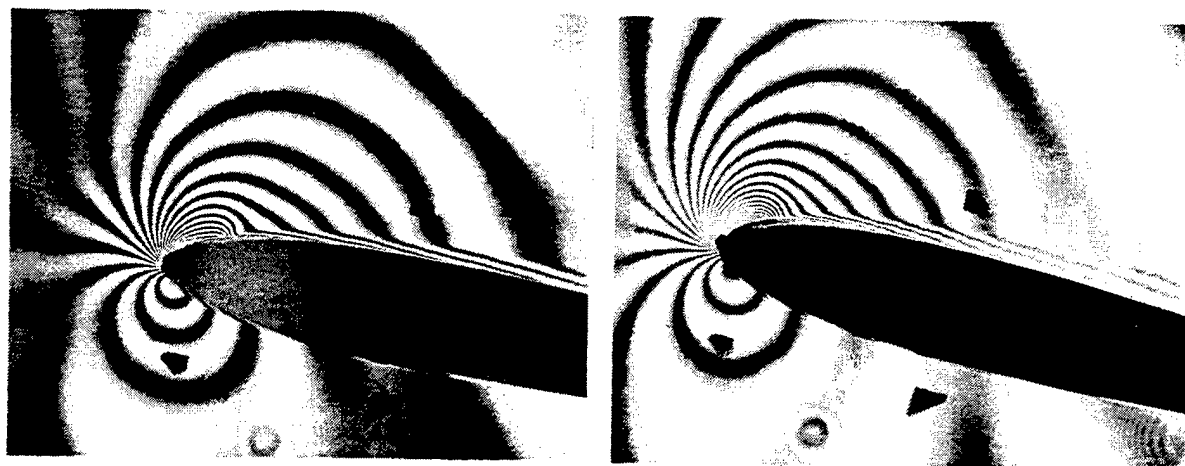
2. Light Dynamic Stall Flow ($\alpha = 10^\circ - 2^\circ \sin \omega t$)

Light dynamic stall occurs when the static stall angle is exceeded only slightly. The extent, severity, and duration of the separation is significant, yet much less than for deep stall. A distinguishing feature of light dynamic stall is that the vertical extent of the viscous zone remains thin (on the order of airfoil thickness) and the thin-layer N-S equations can be used for analysis [Ref. 24]. Detailed experimental flow results are presented for the low-amplitude forced-oscillation test case at $M_\infty = 0.3$, where the top of the oscillation cycle is near the airfoil static stall incidence angle. The new finding in the measurements show that light dynamic stall occurs on the airfoil downstroke below the static stall angle of attack, providing an opportunity to evaluate the capability of the thin-layer N-S equations to describe the flow characteristics, as done in Chapter VII.

a. PDI Images

The images in Figure 5.20 show the flow physics throughout the oscillation cycle for this test case. At the bottom ($\alpha = 8^\circ$) of the oscillation cycle, the flow has established to the point that the picture closely resembles that previously shown for the steady case at 8° angle of attack. This is not surprising because, in fact, the pitch rate is zero deg/s for an instant during reversal of airfoil motion both at the bottom and top ($\alpha = 12^\circ$) of the oscillation cycle, and the reduced frequency is low. As described previously, the suction peak occurs on the upper airfoil surface at the innermost fringe. Immediately downstream of the suction peak, the fringes run parallel with the airfoil surface for some length and then turn abruptly towards the airfoil surface. As before, the distance between the suction peak and the abrupt turning end of the fringes indicates the extent of the separation bubble along the airfoil surface, which is present at all angles of attack on the airfoil upstroke. Later, pressure distributions derived from the PDI images clearly show the separation bubble at $\alpha = 8^\circ, 11^\circ$, and 11.9° . The density contours in the outer flow where no separation bubble is present merge gradually with the airfoil upper surface and turn downstream, defining the edge of the boundary layer downstream. As the airfoil angle of attack increases, additional leading-edge fringes develop. However, the flow everywhere indicates the bubble is fully attached to the top of the cycle.

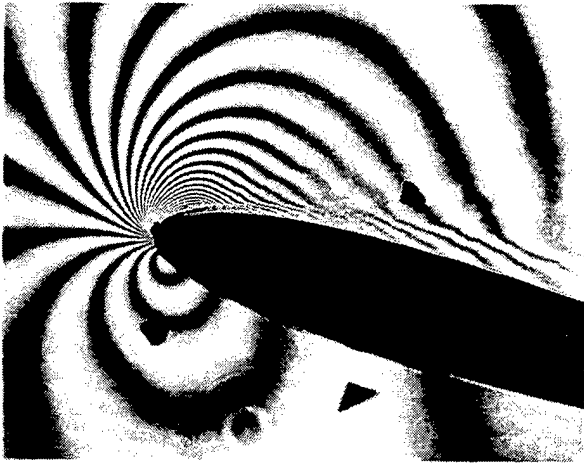
Surprisingly, shortly after the airfoil starts the downward motion from the top of the oscillation cycle, a stalled condition is indicated by the fringes in Figure 5.20d. The flow reattachment process occurs quickly and is well underway at $\alpha = 10.5^\circ$ during airfoil downward motion. The PDI images shown in Figure 5.20f at $\alpha = 9^\circ$ during continued downward airfoil motion show that another separation bubble is fully formed at the airfoil leading edge. The light dynamic stall condition occurs even though the peak angle of attack in the oscillation cycle is at or slightly below the static stall angle of attack. In addition, a mild stall was verified in the flow field vorticity levels by the LDV measurements [Ref. 41].



(a) $\alpha = 8^\circ$ (bottom).

(b) $\alpha = 11^\circ$ (up).

Figure 5.20. Interferograms of the Flow Near the Airfoil Leading Edge. $M_\infty = 0.3$, $\alpha = 10^\circ - 2^\circ \sin \omega t$, $k = 0.1$.



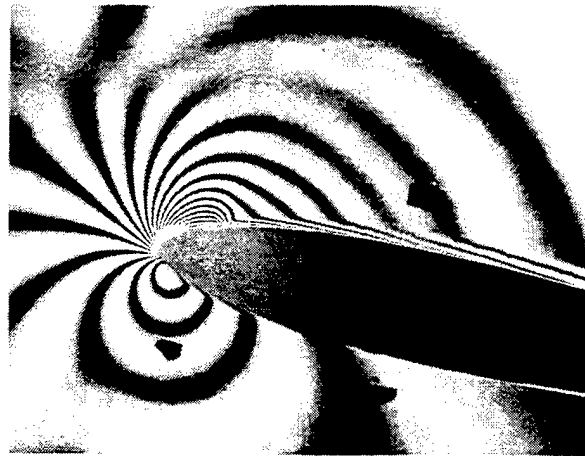
(c) $\alpha = 11.9^\circ$ (up).



(d) $\alpha = 11.5^\circ$ (down).



(e) $\alpha = 10.5^\circ$ (down).



(f) $\alpha = 9^\circ$ (down).

Figure 5.20. (Contd.)

b. Pressure Distribution Derived From PDI Images

Pressure distributions derived from the PDI images near the airfoil leading edge are shown in the next two figures for this low-amplitude oscillatory case. Surface pressure coefficients for airfoil upward motion are shown in Figure 5.21. The suction pressure peak maxima occur in the first 2% chord, moving forward

with increasing angle of attack, as expected. The suction peak is forward of 1% chord at $\alpha = 11^\circ$. The pressure peaks range from $C_p = -3.0$ at 8° angle of attack to $C_p = -4.3$ at 11° angle of attack. However, as the top of the oscillation cycle is approached ($\alpha = 12^\circ$), the pitch rate goes to zero and the minimum C_p decreases to -3.8, as shown in Figure 5.22. The pressure plateaus aft of the pressure peaks, that have been alluded to numerous times, indicate that the separation bubble moves forward with increasing angle of attack from 8 to 11° , but the extent along the airfoil surface remains nearly constant. Aft of the pressure plateau, the adverse pressure gradients are 60 to 70 (compared to 110 to 125 for the steady results) while the C_p decreases from -3.5 to -1.5 over a small chordwise distance, $0.045 < x/c < 0.07$.

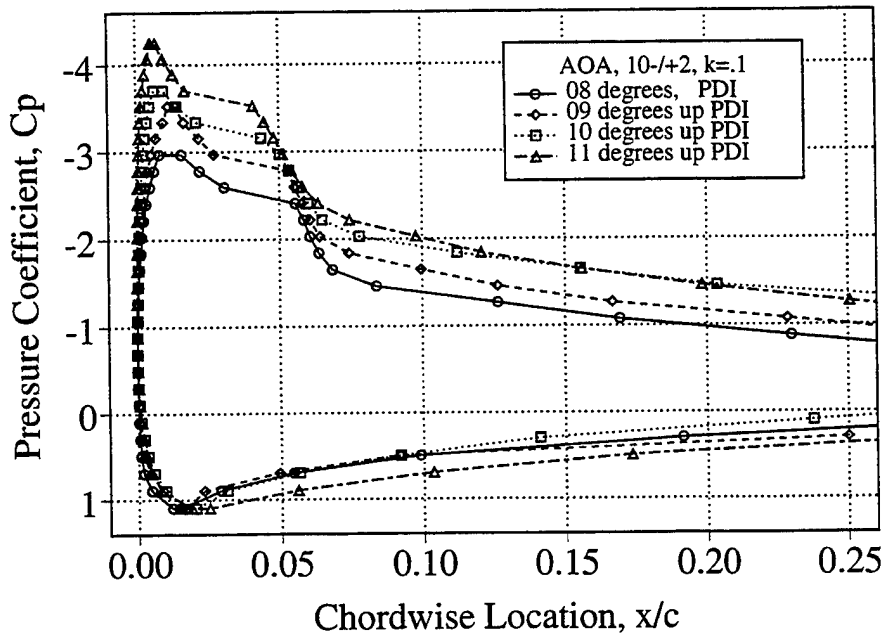


Figure 5.21. Pressure Distributions Near the Airfoil Leading Edge (upstroke). $M_\infty = 0.3$, $\alpha = 10^\circ - 2^\circ \sin \omega t$, $k = 0.1$.

Surface pressure distributions during the airfoil downward motion are given in Figure 5.22. The vortex shedding and light dynamic stall process shown in Figure 5.20d is also indicated by the flat pressure distribution and a minimum C_p of -0.9 at $\alpha = 11.5^\circ$. The PDI images showed that flow reattachment had already begun at $\alpha = 10.5^\circ$ angle of attack. This is also shown by the suction

pressure peak for $\alpha = 10^\circ$ that has increased appreciably ($C_p = -2.0$), but is well below the $C_p = -3.7$ during the airfoil upstroke. At $\alpha = 9^\circ$, the separation bubble plateau is again evident in the pressure distribution. However, the peak suction pressure is lower than at the same angle of attack during airfoil upward motion. If the stall had not occurred during the oscillation cycle, pressure lag effects would give higher suction peaks on airfoil downward motion, much like those calculated with both the potential (UPOT) and N-S codes, as shown in Chapter VI.

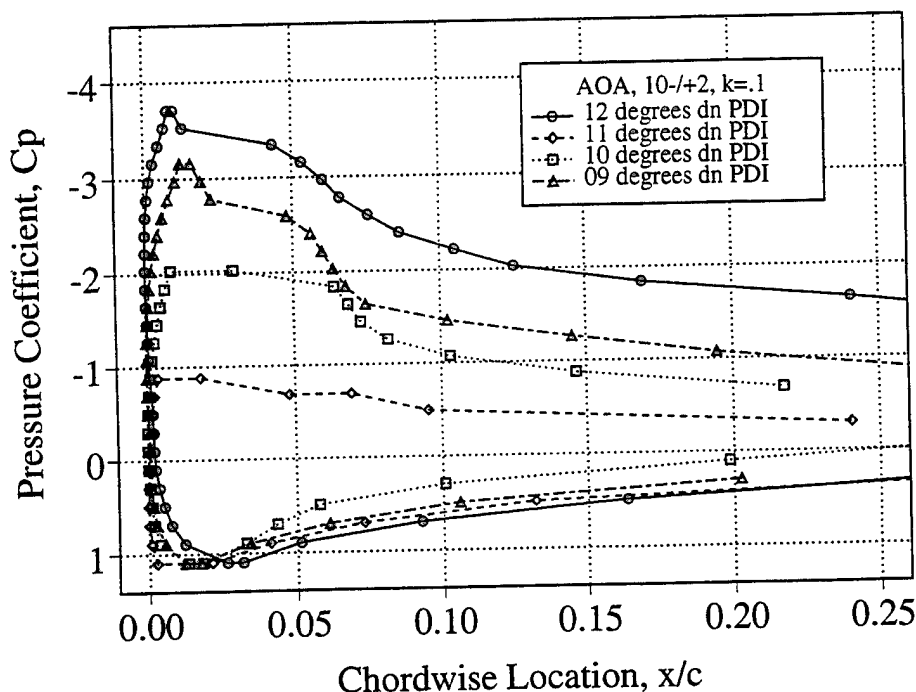


Figure 5.22. Pressure Distributions Near the Airfoil Leading Edge (downstroke).
 $M_\infty = 0.3$, $\alpha = 10^\circ - 2^\circ \sin \omega t$, $k = 0.1$.

c. Phase Distribution of LDV Velocities at (X/C) Locations

The next series of figures present the results from an extensive array of LDV measurements. To review, the LDV probe volume diameter for the tests is 0.191 millimeter (0.25% chord in height), whereas the height of either a laminar or turbulent boundary layer without a separation bubble is 0.121 millimeter and 0.184 millimeter at 5% chord downstream, respectively. Thus, the LDV measurement of reverse flows at the airfoil leading edge is nearly impossible because of the relative size of the probe volume diameter and the thin reverse-flow region in the separation bubble. In addition, the particles tend to deflect

away from the airfoil surface along with the separating shear layer rather than follow the flow into the separation bubble. Particle acceleration rates in the outer region of the separation bubble are on the order of 10^3 m/s^2 [Ref. 34].

As the airfoil rotates upward from 8 to 12° angle of attack, the minimum vertical distance between the measurements and the surface of the airfoil moves forward from 12.3 to 9.3% chord on the airfoil surface, ranging in height from 1.58 to 0.58% chord. The highest velocities in the flow do not coincide with these locations as might be expected, but rather are forward of the locations and reside in the region over the separation bubble.

The U-component velocity at $x/c = -0.100$ shows only minor effects of the downstream oscillating airfoil in Figure 5.23. Again, velocities at each y/c location are offset by $0.2 U_\infty$ for presentation purposes. The velocities vary from $0.9 U_\infty$ to $1.1 U_\infty$ at the lowest and uppermost heights above the airfoil surface. The V-component velocity at this upstream location rises, as expected, as the airfoil angle of attack increases from 8 to 12° . V velocities throughout the oscillation cycle are about one-third of the U component, varying from $0.2 U_\infty$ at the upper heights to as much as $0.35 U_\infty$ at $y/c = 0.083$. The measurements show that the flow remains parallel upstream of the airfoil and that the streamlines are curved through the oscillation cycle as noticed in the V-component.

As the flow passes over the airfoil leading edge in Figure 5.24 at $x/c = 0.017$, U-component velocities are distinctly different at the three lower and three upper heights above the airfoil surface. The velocities do not increase as expected as the airfoil angle of attack increases to the top of the oscillation cycle like at the upper heights, instead the velocities show prominent decreases at the lowest height. At $y/c = 0.083$, average U velocities decrease by more than 20% at the higher angles of attack. Velocities vary from $0.96 U_\infty$ at $\alpha = 11.7^\circ$ during airfoil upward motion to $1.35 U_\infty$ at the bottom of the oscillation cycle, the opposite of what one might expect. The decelerated flow is a result of measurements in the separation bubble. At $y/c = 0.083$, the reduced velocity region continues from $\alpha = 9.3^\circ$ on airfoil upward motion to $\alpha = 11.0^\circ$ on airfoil downward motion with the minimums occurring at $11^\circ < \alpha < 12^\circ$. The maximum U velocities of $1.42 U_\infty$ occur at $y/c = 0.117$ and $\alpha = 10^\circ$, and also at $y/c = 0.133$

and $\alpha = 11.7^\circ$, both on the airfoil upstroke in the flow region above the separation bubble.

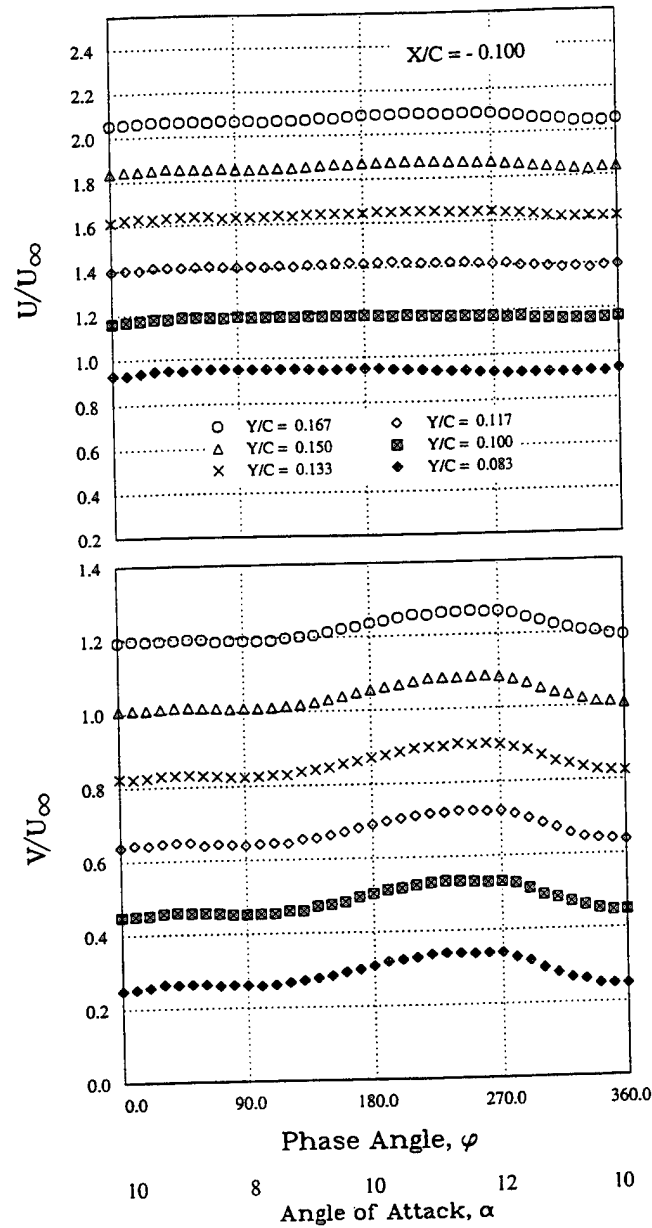


Figure 5.23. Phase Distribution of U- and V-Component Velocities at $x/c = -0.100$. (Velocity offset by $0.2 U_\infty$ at each height.) $M_\infty = 0.3$, $\alpha = 10^\circ - 2^\circ \sin \omega t$, $k = 0.1$.

The V-component velocities at upper heights are much like that forward of the airfoil surface, varying from 0.2 to $0.25 U_\infty$ throughout the oscillation cycle. However, the velocities at the lowest height are nearly constant at all angles of attack and have increased to $0.4 U_\infty$. The higher velocity is reasonable because

the airfoil surface at the $x/c = 0.017$ measurement location presents the steepest angle to the oncoming flow, except at the airfoil leading edge. V velocities in the flow field reach a maximum of $0.5 U_\infty$ at $\alpha = 12^\circ$ and $y/c = 0.10$.

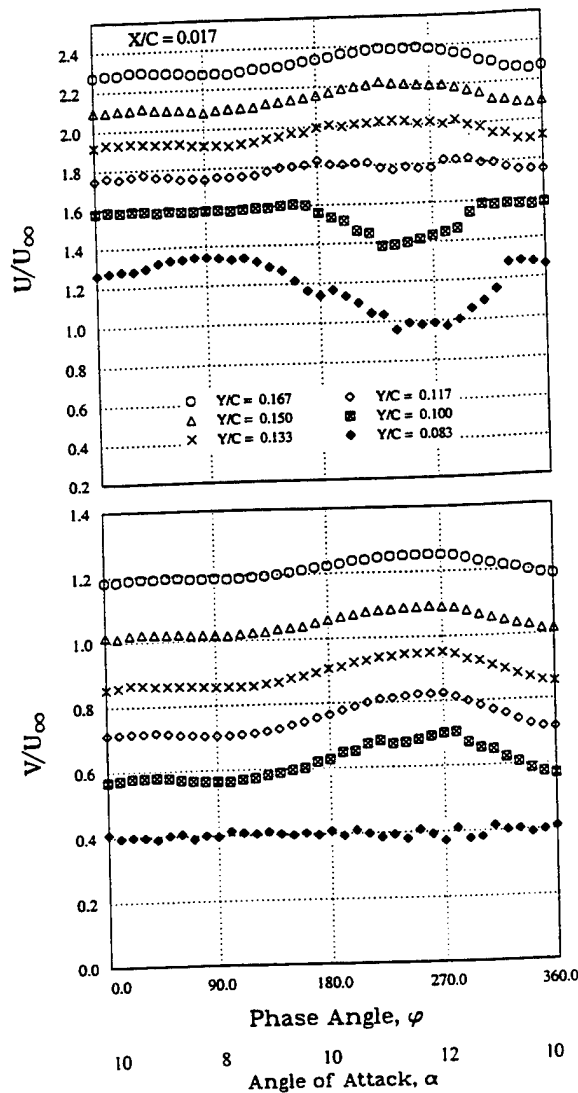


Figure 5.24. Phase Distribution of U- and V-Component Velocities at $x/c = 0.017$. (Velocity offset by $0.2 U_\infty$ at each height.) $M_\infty = 0.3$, $\alpha = 10^\circ - 2^\circ \sin \omega t$, $k = 0.1$.

At $x/c = 0.033$ in Figure 5.25, the U velocity decreases in an expanding angle of attack range at heights closer to the airfoil during airfoil upward motion even though the measurements are 0.533 mm, or 2 to 3 probe volumes closer to

the airfoil surface than at the previous upstream location. U-component velocities for this (x/c) location at the three lowest heights were on the order of 20% less than those shown at $x/c = 0.017$. The velocities at $y/c = 0.083$ drop 30% from the peak velocity of $1.25U_\infty$ at $\alpha = 8^\circ$. The velocity decrease starts with the airfoil upstroke and persists until $\alpha = 10^\circ$ on the downstroke. The V-component velocities at the upper heights followed the motion of the airfoil surface as before, but at the two lowest heights were greatly reduced down to $0.2U_\infty$, giving further evidence of measurements into the separation bubble region.

d. LDV Velocity Profiles (U/U_∞)

Velocity profiles are shown for angles of attack in 1 degree intervals from 8° to the top of the oscillation cycle and then back down to 9° . Velocities are offset by $0.2U_\infty$ at each angle of attack for better presentation and are normalized by the free stream velocity, U_∞ .

Velocity profiles in Figure 5.26 are for locations, $x/c = -0.10$ and $x/c = 0.00$. At $x/c = -0.1$, U velocities ranged from 0.96 to $1.08U_\infty$. At the lowest measured height, velocities were 10% lower than at the uppermost height. All the profiles overlie each other if the offset were removed, except for slight velocity reductions at the top of the airfoil downstroke at 11° angle of attack.

The number of data samples at $x/c = -0.100$ varied from 137 on airfoil downward motion at $\alpha = 11.9^\circ$ to 383 at $\alpha = 8.7^\circ$ during airfoil upward motion. The average number of samples is 274 if evenly distributed. Generally, less validated samples were measured near the top of the oscillation cycle. However, there were always more than 50 to give an acceptable mean value.

In general, over the airfoil leading edge, U velocities have increased appreciably ($1.3U_\infty$), especially at the lower heights in closer proximity to the airfoil surface such that the profiles are now more uniform. Velocities at mid-heights and 12° angle of attack reach as high as $1.4U_\infty$.

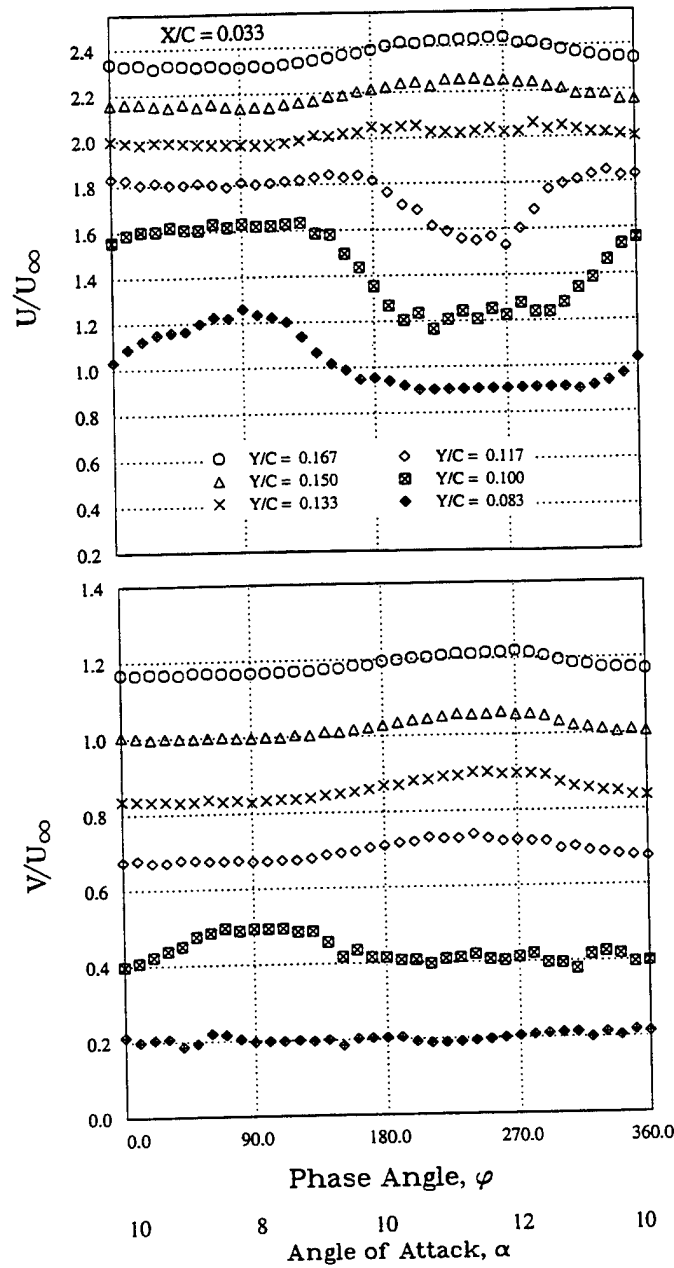


Figure 5.25. Phase Distribution of U- and V-Component Velocities at $x/c = 0.033$. (Velocity offset by $0.2 U_\infty$ at each height.) $M_\infty = 0.3$, $\alpha = 10^\circ - 2^\circ \sin \omega t$, $k = 0.1$.

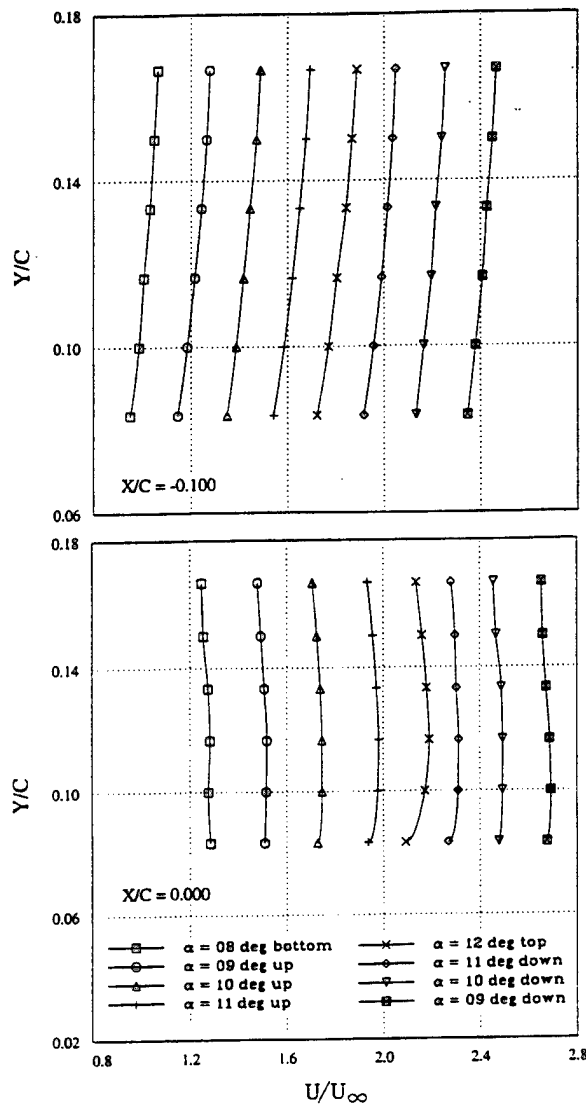


Figure 5.26. U-Component Velocity Profiles at $x/c = -0.10$ and $x/c = 0.00$. (Velocity offset by $0.2 U_\infty$ at each AOA.) $M_\infty = 0.3$, $\alpha = 10^\circ - 2^\circ \sin \omega t$, $k = 0.1$.

U velocity profiles for $x/c = 0.017$ and 0.033 are shown in Figure 5.27. Obvious in both plots are the reduced velocities at lower heights, especially from 10 to 12° angle of attack (up) and continuing to occur during the airfoil downstroke at $x/c = 0.033$. Measured U velocities span a larger range from 0.92 to $1.45 U_\infty$ at these (x/c) locations. Velocity profiles with slight inflections begin at $x/c = 0.017$ and $\alpha = 11^\circ$ (up), and downstream at $x/c = 0.033$ inflections are first seen at $\alpha = 10^\circ$. With the sole use of substantial velocity reductions as a criteria, first indications of the separation bubble appear at $x/c = 0.017$ and 10° angle of attack (up).

The number of validated data samples was widely spread at $x/c = 0.017$, varying from 27 at $\alpha = 12^\circ$ and $y/c = 0.100$ to 474 at $\alpha = 8.3^\circ$ and $y/c = 0.083$. Again, the larger number of validated samples occurs near the bottom of the oscillation cycle on the airfoil upstroke.

At $x/c = 0.033$, U velocity gradients are large from 9 to 11° angle of attack on the upstroke, and the profiles cross each other at the lower heights even with the added offset. At this downstream location, the expanded region of reduced velocities indicates that a larger portion of the flow in the separation bubble is being measured.

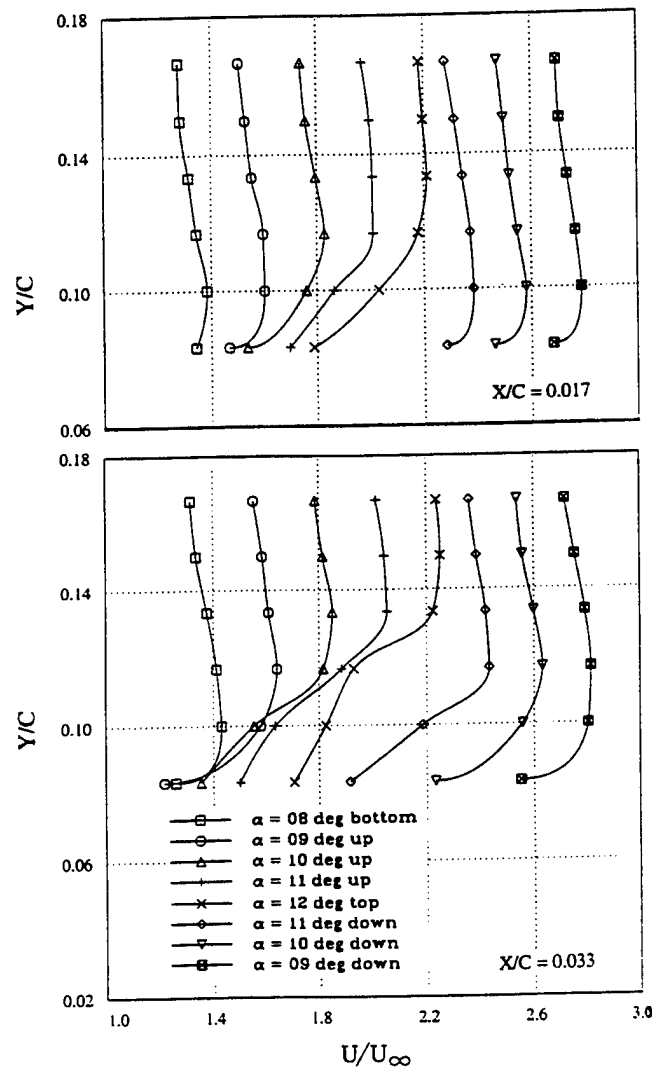


Figure 5.27. U-Component Velocity Profiles at $x/c = 0.017$ and $x/c = 0.033$. (Velocity offset by $0.2 U_\infty$ at each AOA.) $M_\infty = 0.3$, $\alpha = 10^\circ - 2^\circ \sin \omega t$, $k = 0.1$.

In Figure 5.28, velocities are given for $x/c = 0.067$ and 0.083 . Again, steep velocity gradients occurred at the lower heights from 10 to 12° angle of attack (up) at both (x/c) locations. The maximum U velocity ($1.5 U_\infty$) over the airfoil surface occurred at $y/c = 0.133$ and 12° angle of attack. Indications of separation bubble presence are slightly greater at $x/c = 0.067$ than at $x/c = 0.033$. However, velocities at the lowest height ($y/c = 0.083$) and angles of attack of 11 (up) and 12° begin to increase slightly from those at the upstream location.

At $x/c = 0.083$, velocities at upper heights and all angles of attack are slightly lower than at $x/c = 0.067$ and become more uniform in nature. On the other hand, velocities at the lowest height and all angles of attack are greater than at $x/c = 0.067$. The velocity profile at 10° angle of attack (up) is the only one that resembles the profile at the immediate upstream location and same angle of attack. For angles of attack at 11 (up) and 12° , velocities at the lowest height are greater than at the measurement location immediately above, showing an unusual shear pattern in the flow. However, notice that the velocity profile at 11° angle of attack (down) has no inverted characteristic, indicating a rapid flow recovery.

The velocity profiles shown in Figure 5.29 at $x/c = 0.100$ and 0.133 indicate that the measurements are approaching the downstream edge of the separation bubble. At $x/c = 0.100$, the velocity profiles are similar to those shown previously at $x/c = 0.083$ with the absence of the inverted "S" profile characteristic.

Velocity profiles at $x/c = 0.133$ are similar to those previously shown at the airfoil leading edge. No dramatic velocity reductions are shown at any angle of attack. The right edge of the separation bubble appears to be forward of 13.3% chord in the downstream direction if based on the velocity profiles.

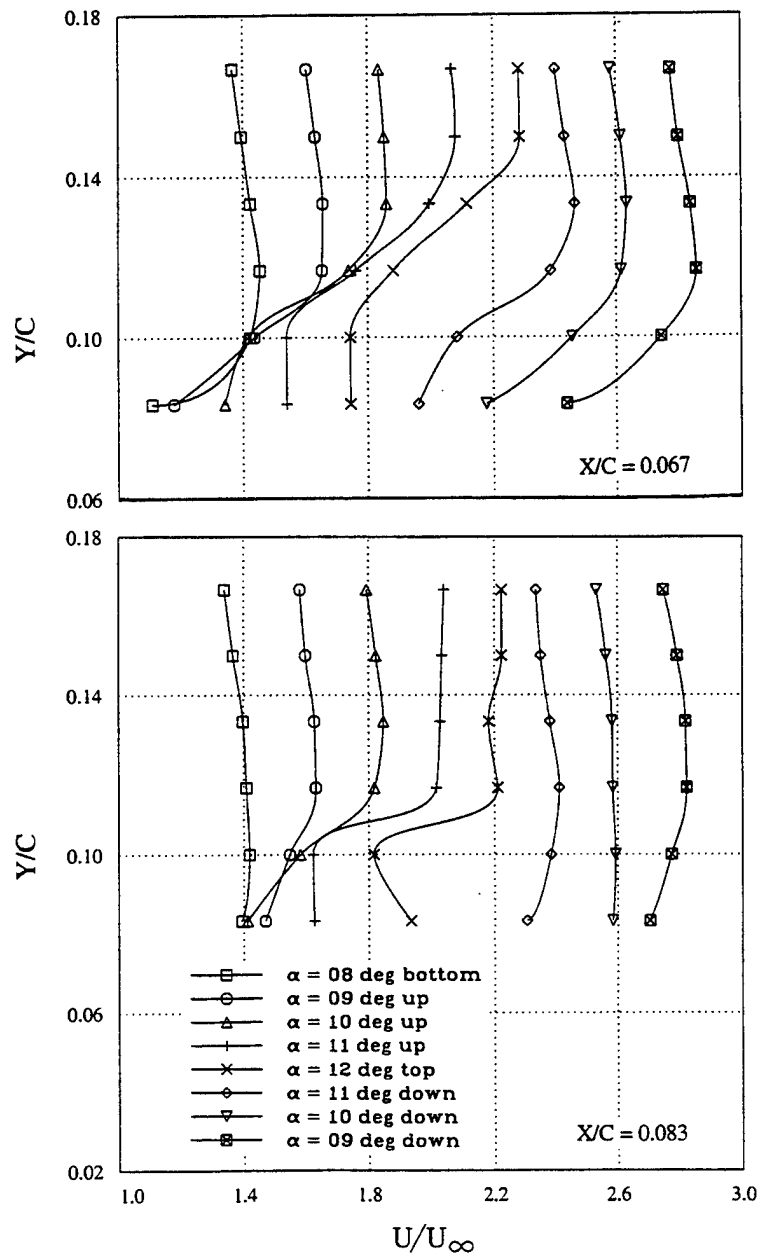


Figure 5.28. U-Component Velocity Profiles at $x/c = 0.067$ and $x/c = 0.083$. (Velocity offset by $0.2 U_\infty$ at each AOA.) $M_\infty = 0.3$, $\alpha = 10^\circ - 2^\circ \sin \omega t$, $k = 0.1$.

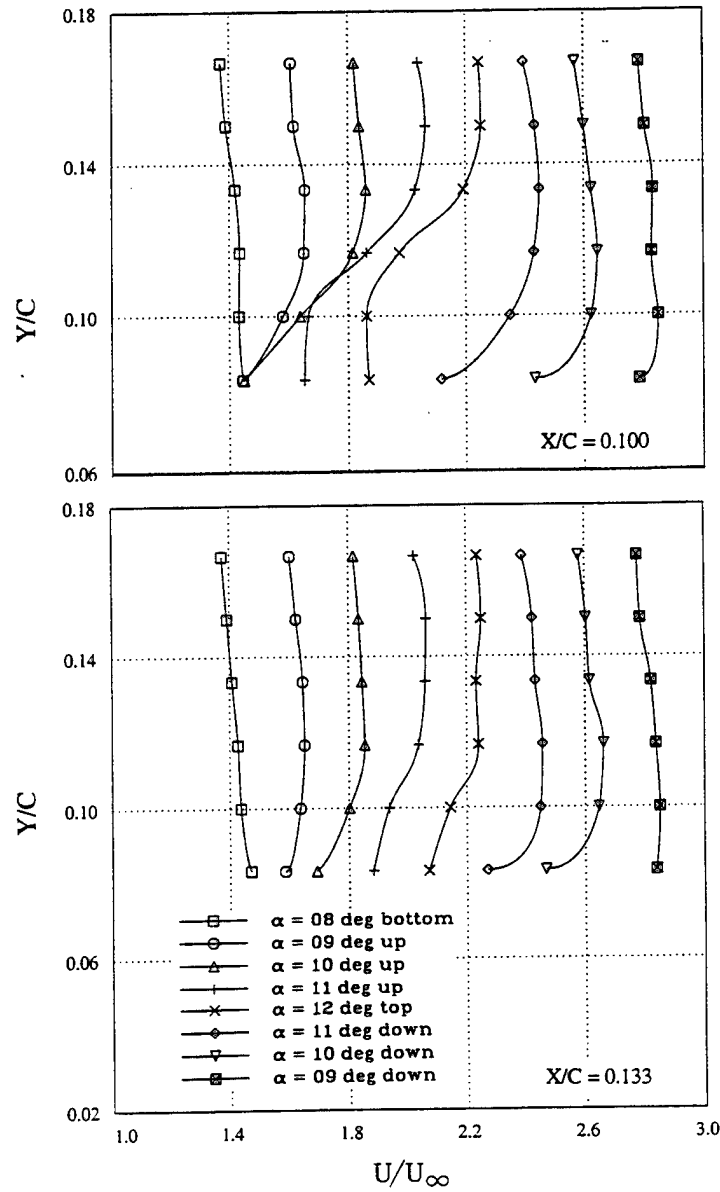


Figure 5.29. U-Component Velocity Profiles at $x/c = 0.100$ and $x/c = 0.133$. (Velocity offset by $0.2U_\infty$ at each AOA.) $M_\infty = 0.3$, $\alpha = 10^\circ - 2^\circ \sin \omega t$, $k = 0.1$.

In summary, over the airfoil leading edge surface, the velocities greatly exceed the free stream, but from 2 to 10% chord downstream, the profiles show that measurements are made in a portion of the separation bubble.

e. LDV Velocity Magnitude Contours

An example of flowfield velocity magnitude contours is given for $\alpha = 9^\circ$ (up/down) in Figure 5.30. The velocity magnitude range in the flowfield is indicated in the legend with velocities normalized by the free stream and shown in $0.06 U_\infty$ intervals.

The oncoming flow velocity is slightly higher during the airfoil upstroke. Also, the maximum flow speed ($1.44 U_\infty$) region is more extensive, starting slightly forward of the airfoil leading edge and continuing around the steep velocity gradient area pointing towards the location of the separation bubble. It is interesting to note that all the measured velocities shown in the flow field are greater than the free stream. For airfoil oscillations in both directions, a decelerated flow region exists over the airfoil leading edge with the minimum velocity contour in each case being $1.02 U_\infty$. The lower velocity region is wider and extends to greater heights above the airfoil surface during the airfoil upstroke. For example, velocity contour number three ($1.02 U_\infty$) during airfoil upward motion exceeds the lateral boundaries of contour number four ($1.08 U_\infty$) on airfoil downward motion.

f. LDV Vorticity Magnitude Contours

The vorticity was obtained by first interpolating the velocity component data and mapping the data with a spline curve fit. Then the z-component of vorticity was calculated from the velocity gradients of the fitted curves. The vorticity was normalized by c/U_∞ and is presented in the next three figures.

Flow field vorticity is given for angles of attack of 8° and 12° in Figure 5.31. The vorticity levels in the flow over the airfoil at 8° angle of attack are low compared with those at the top of the oscillation cycle. Only one region of counterclockwise vorticity occurs in the flowfields at the lowest measurement location and aft of 8% chord near the downstream edge of the separation bubble. Clockwise vorticity (-24 units maximum) exists only near the airfoil leading edge from $0.00 < x/c < 0.08$ and at the lowest heights above the separation bubble for $\alpha = 8^\circ$. At $\alpha = 12^\circ$, the higher levels of clockwise vorticity (-30 units) occur

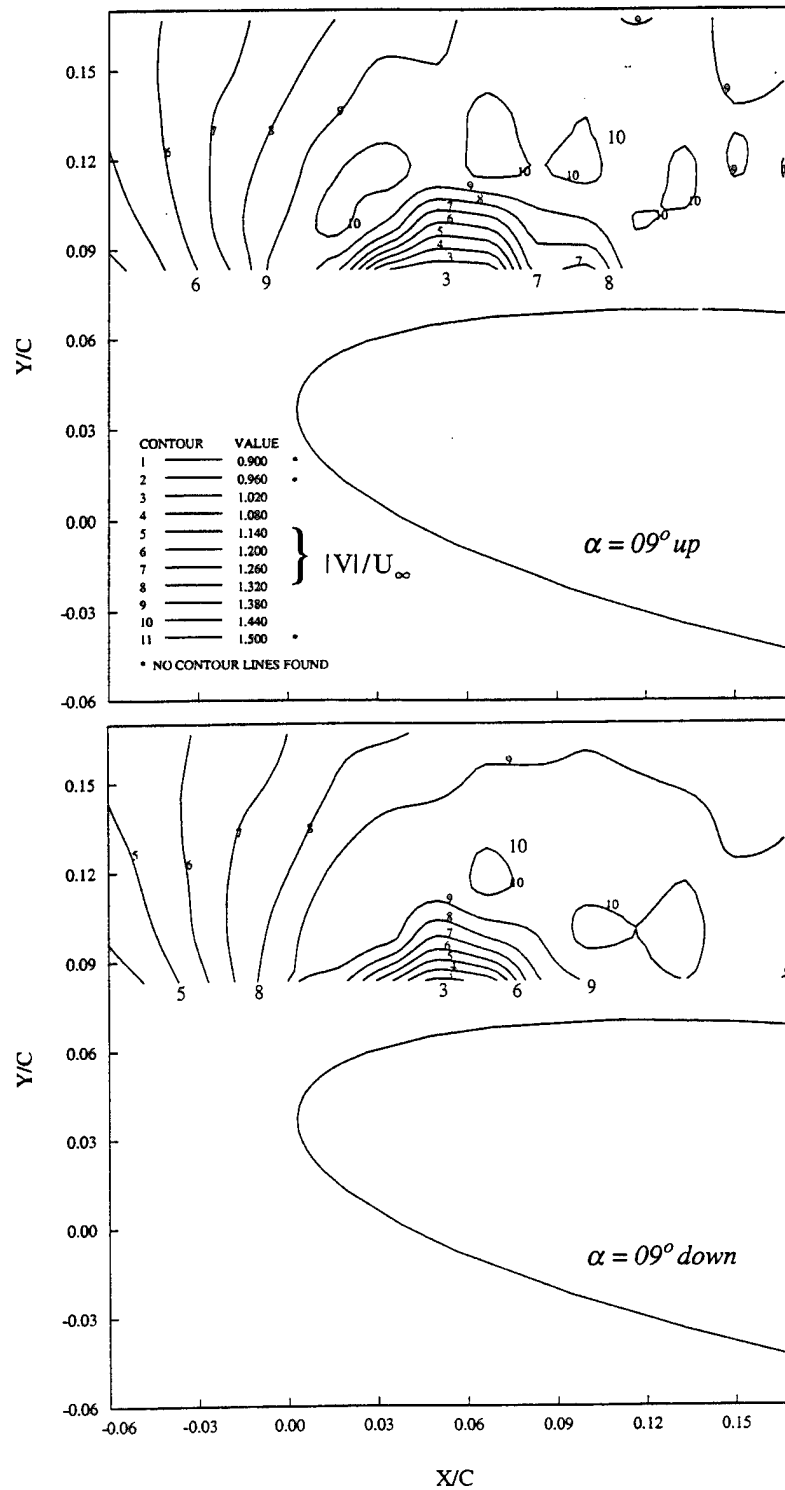


Figure 5.30. Velocity Magnitude $|V|$ Contours Near Airfoil Leading Edge.
 $M_\infty = 0.3$, $\alpha = 10^\circ - 2^\circ \sin \omega t = 9^\circ$ (up / down), $k = 0.1$.

between $0.01 < x/c < 0.03$, extending to 1.7% chord above the airfoil surface. In addition, two pockets of clockwise vorticity (-30 units) occur at 4.5 and 8% chord downstream, both at 5.5% chord above the airfoil surface.

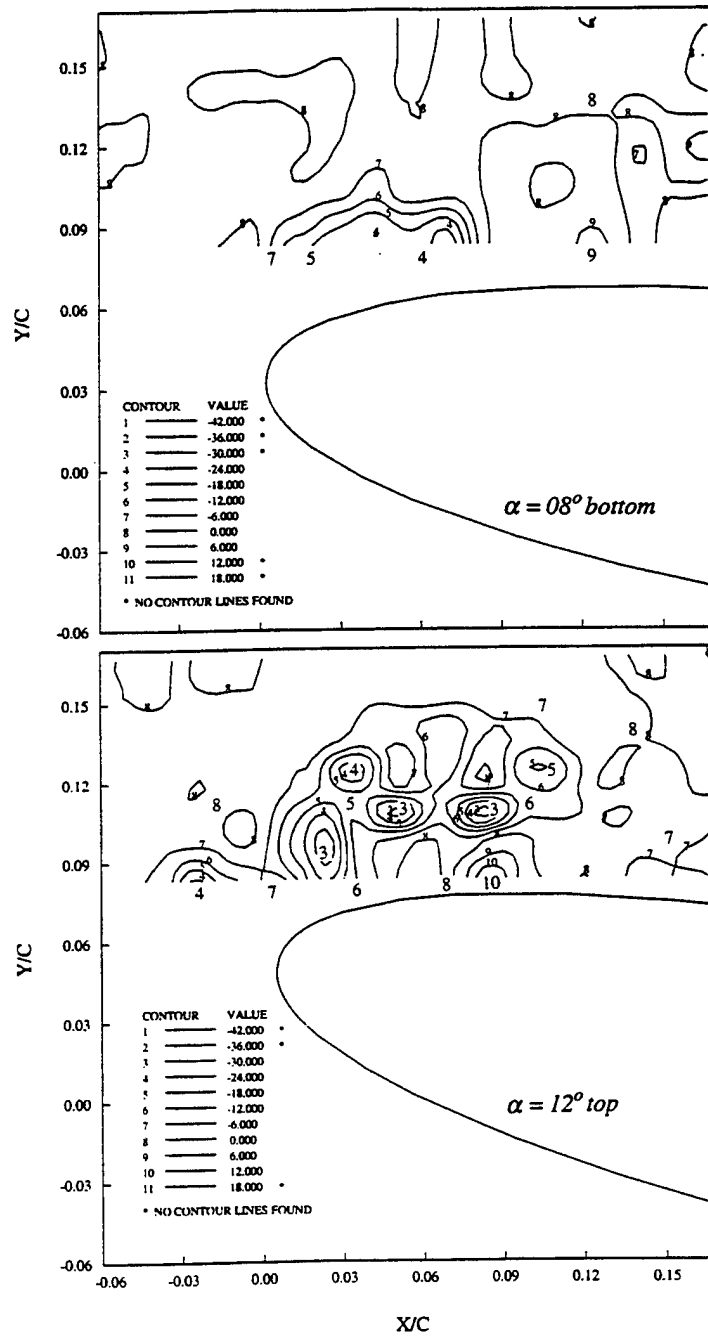


Figure 5.31. Vorticity Contours (z-Component) Near the Airfoil Leading Edge. $M_\infty = 0.3$, $\alpha = 10^\circ - 2^\circ \sin \omega t = 8^\circ$ (bottom) and 12° (top), $k = 0.1$.

In Figure 5.32, vorticity in the flow field is shown for 11° angle of attack during airfoil upward motion and 11.53° angle of attack on the airfoil downstroke. The vortical flow at 11° angle of attack (up) is much like that given for 12° angle of attack in the previous figure with a maximum clockwise vorticity level of -30 units. Although, no counterclockwise vorticity is shown aft of the separation bubble location as at the top of the oscillation cycle. In each case a very small region of clockwise vorticity (+6.0 units) is indicated just forward of the airfoil leading edge between two clockwise vorticity regions. On the airfoil downstroke at 11.53° angle of attack, the clockwise vorticity over the airfoil leading at 2% chord downstream has increased by at least 6 units to -36 units (shown earlier at -40 units, [Ref. 41]), greater than previously measured at 11° (up) and 12° angle of attack. The two pockets of clockwise vorticity discussed for $\alpha = 12^\circ$ have now coalesced into one region of increased vorticity and extends to slightly higher than $y/c = 0.100$ or 4.0% chord above the airfoil surface.

At 10.68° angle of attack (down) in Figure 5.33, the maximum clockwise vorticity has decreased to -24 units. The concentrated areas of high vorticity that existed at $\alpha = 11.53^\circ$ (down) are now seen to move downstream. At $\alpha = 10^\circ$, the vorticity levels increase again in the region over which the separation bubble develops again over the airfoil leading edge. Flow reattachment in the PDI measurements was seen to begin already at $\alpha = 10.5^\circ$ (down), and the increased vorticity indicated by the LDV measurements above what was measured at the higher angle of attack indicates that the vorticity was partially shed between 11.53° and 10° angle of attack. The vorticity distributions corroborate the occurrence of light dynamic stall that was shown earlier in the PDI images. The vorticity apparently can build up only to certain levels before it must be shed by a means other than diffusion through the boundary layer. By having the airfoil oscillate near the stall angle of attack, the vorticity in the flow reached levels that require the vorticity balance to be preserved as the flow attempts to adapt to the decreasing angle of attack and was shed on the airfoil downstroke. The vorticity shedding process occurs over a small range of angle of attack. This surprising result of light dynamic stall is documented by both the PDI and LDV measurements at an angle of attack below the static stall on the airfoil downstroke, enhancing the confidence in the measured data.

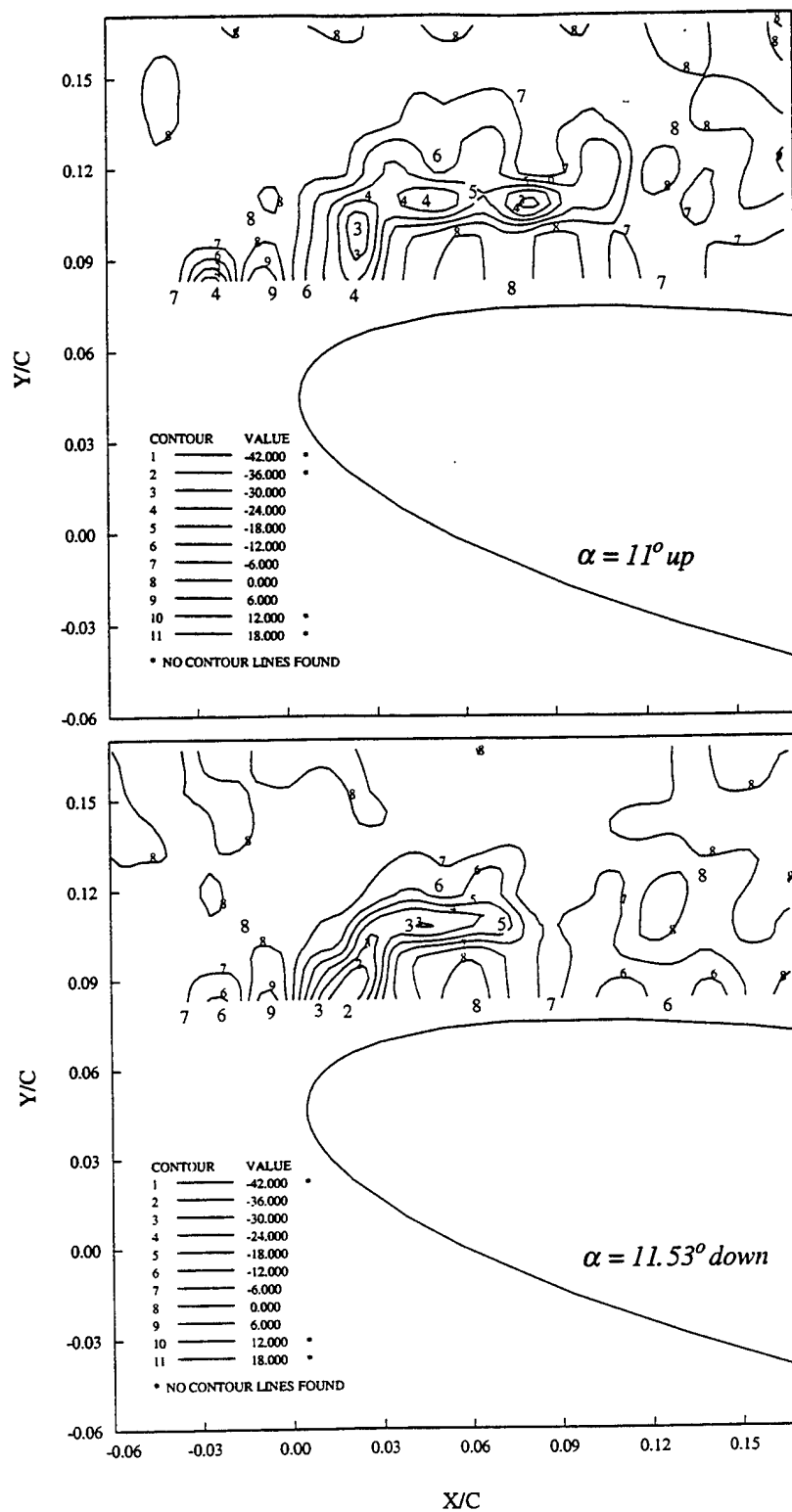


Figure 5.32. Vorticity Contours (z-Component) Near the Airfoil Leading Edge. $M_\infty = 0.3$, $\alpha = 10^\circ - 2^\circ \sin \omega t = 11^\circ$ (up) and 11.53° (down), $k = 0.1$.

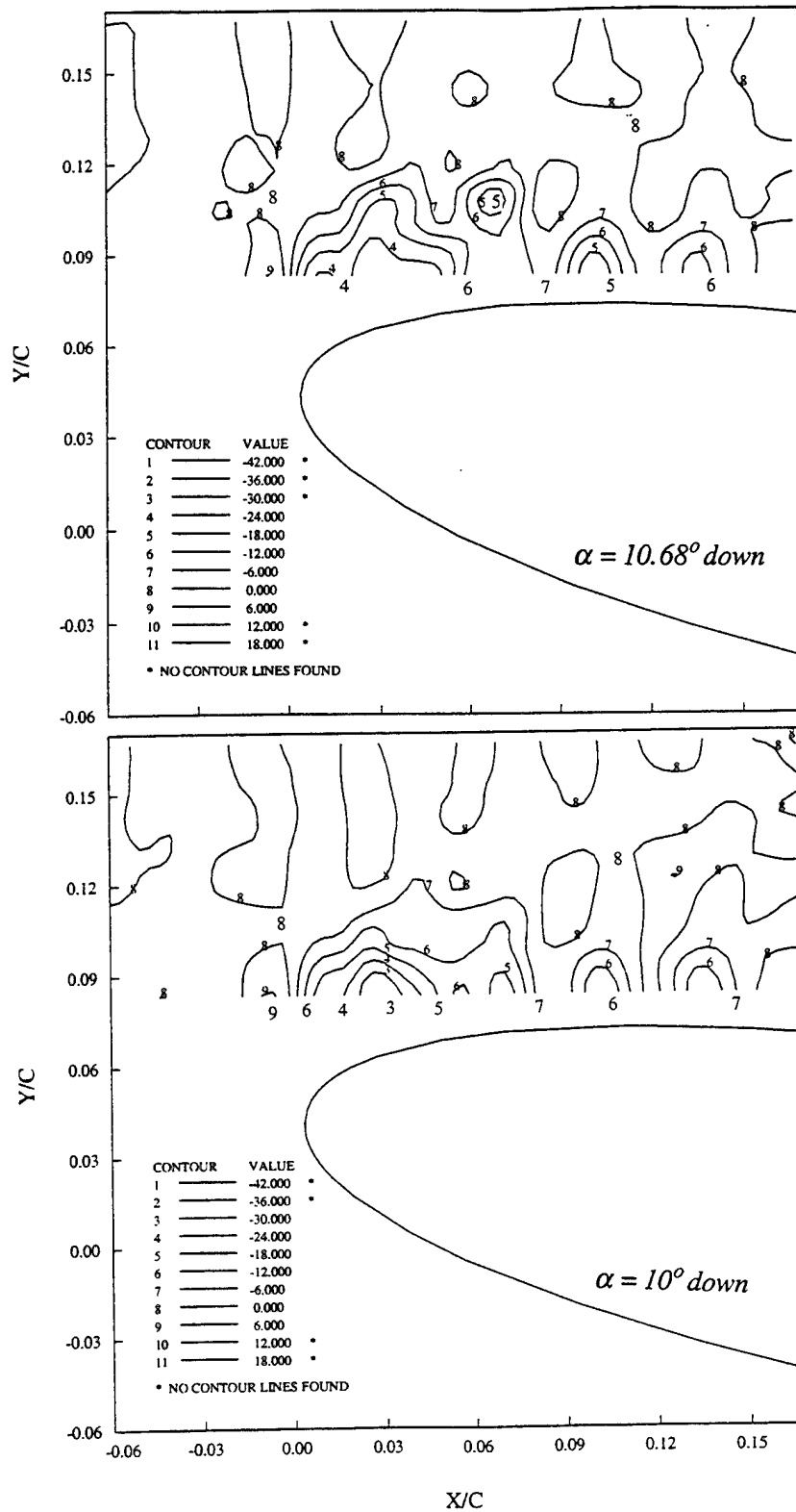


Figure 5.33. Vorticity Contours (z-Component) Near the Airfoil Leading Edge.
 $M_\infty = 0.3$, $\alpha = 10^\circ - 2^\circ \sin \omega t = 10.68^\circ$ (down) and 10° (down), $k = 0.1$.

Previously, it was thought that the separation bubble remained on the airfoil surface, expanding and contracting in size during the oscillation cycle for the low-amplitude test case [Ref. 65]. Both the PDI and LDV test results confirmed the incipient stall, as previously reported in Reference 41. The measurements show that the vertical extent of the viscous zone remains thin and on the order of the airfoil thickness, giving valuable data for making comparisons with computational methods. Thus, the capabilities of the computational methods to reproduce the experimental results are evaluated, using the N-S approach as the main method of analysis supplemented by potential flow and boundary layer methods as discussed in Chapter VI. The computed and measured comparisons are reserved for Chapter VII.

VI COMPUTED RESULTS

In this chapter, computational results are presented using the potential flow, boundary layer, and N-S analysis methods described in Chapter IV. The potential flow method provides a very rapid means of visualizing the effect of angle of attack, amplitude, and frequency of airfoil oscillation on the pressure distribution for both the lower and upper airfoil surfaces. In particular, it permits quantification of the phase lag between the airfoil motion and the pressures induced at various points on the airfoil. The combination of the unsteady potential flow code (panel) with the boundary-layer code provides another efficient and rapid tool to visualize the response of the boundary layer to changes in angle of attack, amplitude, and frequency of oscillation. This combined panel/boundary layer approach is, of course, limited to the analysis of attached flows only because the boundary layer is computed in the direct mode. Furthermore, the calculations are limited to relatively low reduced frequencies of oscillation because the boundary layer code is based on the steady boundary layer equations. This latter limitation is likely to have only a minor effect on the accuracy of the results for reduced frequencies less than one because the boundary layer lag effects are known to be much less than the pressure lag effects. The thin-layer N-S code is used to analyze the development of separations bubbles and the formation and shedding of the dynamic stall vortex.

A. FLOW OVER STEADY NACA 0012 AIRFOIL

1. Pressure Distributions

The experiments have shown that steady-state stall occurs at an angle of attack slightly above 12° at a free-stream Mach number of 0.3 and a Reynolds number of 540,000. Therefore, it is instructive to study the change in pressure distribution as the angle of attack is increased from 0° to 12° . This is shown in Figures 6.1 and 6.2 for the first quarter chord of the airfoil, using UPOT. It is seen that the leading-edge suction pressures increase dramatically with increasing angle of attack while the suction peaks move slightly forward. The stagnation point moves downstream on the lower surface from 1 to 4% chord. The maximum

adverse pressure coefficient gradient reaches a value of 40 at $\alpha = 8^\circ$ and 115 at $\alpha = 12^\circ$.

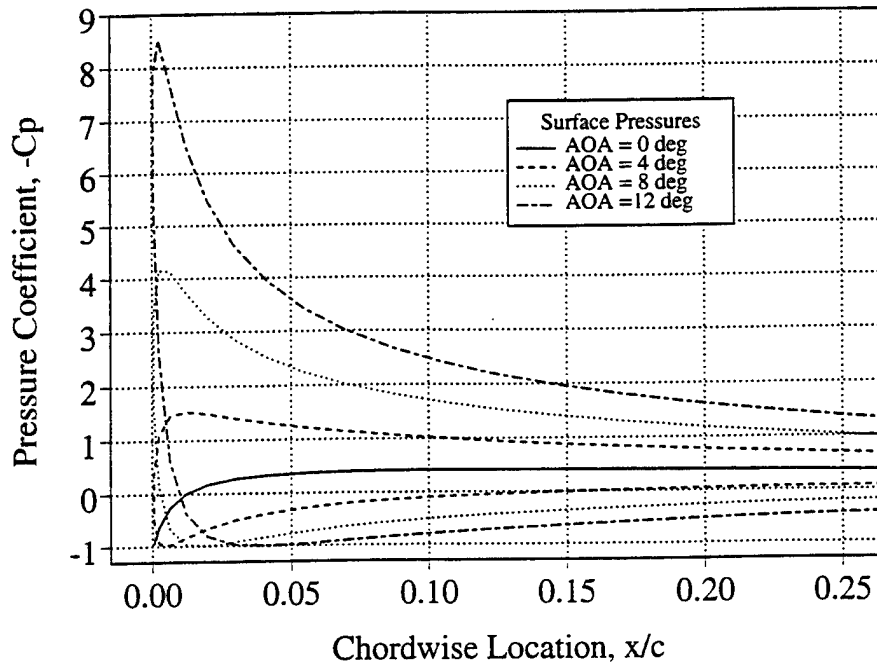


Figure 6.1. Surface Pressure Distribution Near the Airfoil Leading Edge, UPOT. $\alpha = 0^\circ, 4^\circ, 8^\circ$ and 12° .

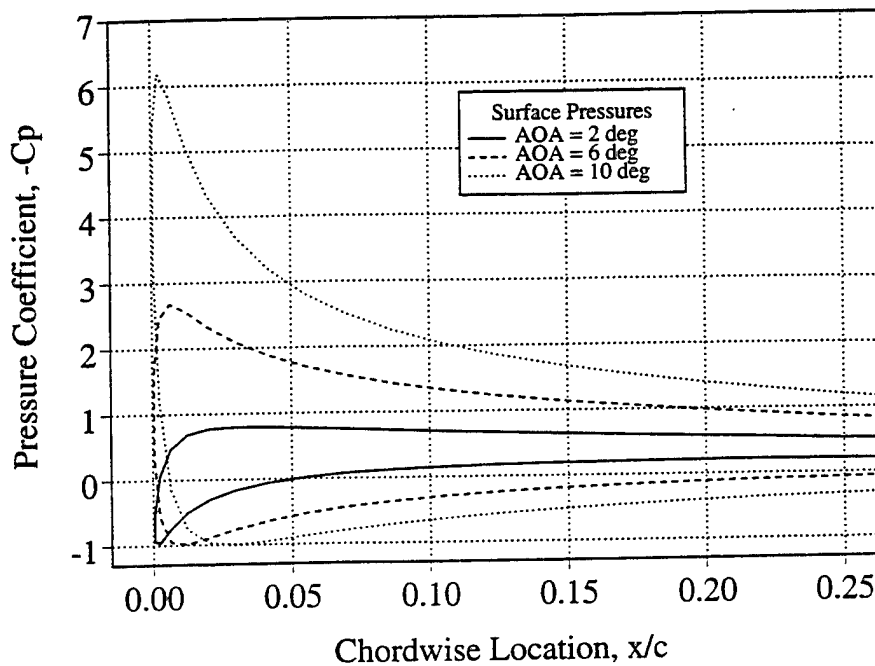


Figure 6.2. Surface Pressure Distribution Near the Airfoil Leading Edge, UPOT. $\alpha = 2^\circ, 6^\circ$ and 10° .

In Figure 6.3, the UPOT-predicted pressure distributions are compared with the N-S code predictions. In the N-S calculations, the effect of boundary layer transition from laminar to turbulent flow is taken into account by specifying the transition onset location and by computing the transition length using the Chen-Thysson transition model. The transition value $G_{\gamma_{tr}}$ in the Chen-Thysson model was chosen to be 200, the basis of which is discussed in detail in Chapter VII. As expected, complete agreement between the two codes is achieved at $\alpha = 0^\circ$, whereas at $\alpha = 6^\circ$, a slight deviation occurs near the suction peak. The N-S predicted suction is slightly lower than the UPOT prediction. However, at $\alpha = 12^\circ$, the suction predictions are distinctly different. The N-S computation shows a much lower suction pressure and a pressure plateau typical for the formation of a small separation bubble; whereas, of course, the UPOT code cannot account for this viscous-dominated phenomenon. It is also important to note that a purely laminar N-S calculation fails to converge, while purely turbulent N-S calculations produce excessive suction peaks much like the UPOT-predicted peaks for flow conditions in the transitional Reynolds number range.

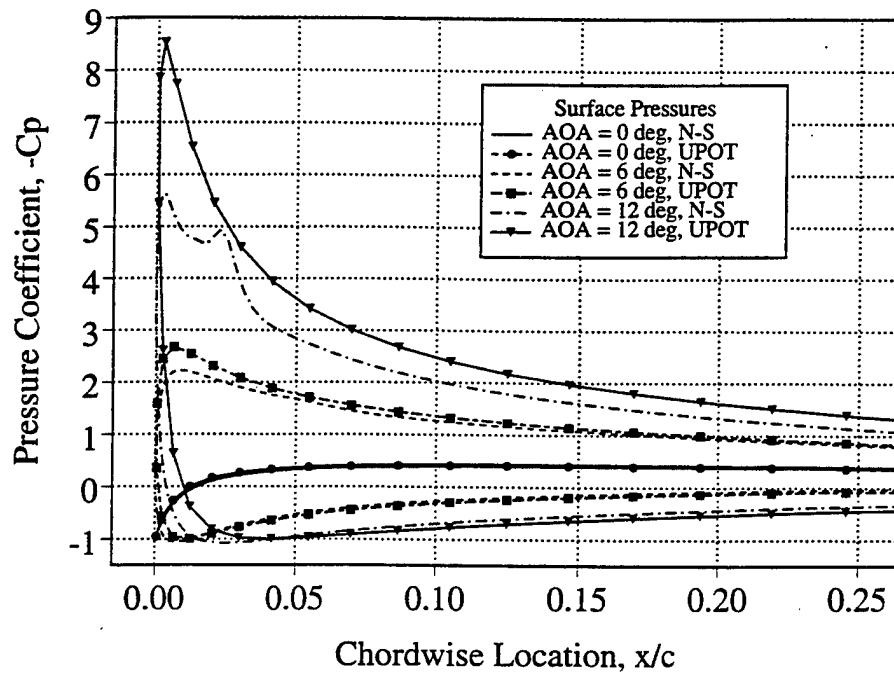


Figure 6.3. Surface Pressure Distribution Near Airfoil Leading Edge, UPOT and N-S Codes. N-S Analysis, $M_\infty = 0.3$, $\alpha = 0^\circ$, 6° and 12° , $Re = 540,000$, $G_{\gamma_{tr}} = 200$.

Figure 6.4 shows that the N-S code first predicts a small separation bubble at $\alpha = 8^\circ$, which is in accordance with the measurements. At $\alpha = 10^\circ$, the predicted separation bubble is significantly bigger and it is located further forward. At $\alpha = 12^\circ$, the N-S calculations showed remarkable sensitivity to the choice of the transition onset location and the transition length. Figure 6.4 shows two calculations for $\alpha = 12^\circ$, one with a separation bubble similar to the bubble obtained at $\alpha = 10^\circ$, the other one showing a fully stalled flow. These two dramatically different solutions were obtained by specifying a slightly earlier-transition onset, moving it from 1.8% chord to 1.2% chord, and by specifying a slightly longer transition length by choosing a $G_{\gamma_{tr}}$ value of 200 rather than 100. The details of transition onset and length effects are covered in Chapter VII. After the transition zone, the Baldwin-Barth turbulence model is used in the N-S code for all the results given in this thesis.

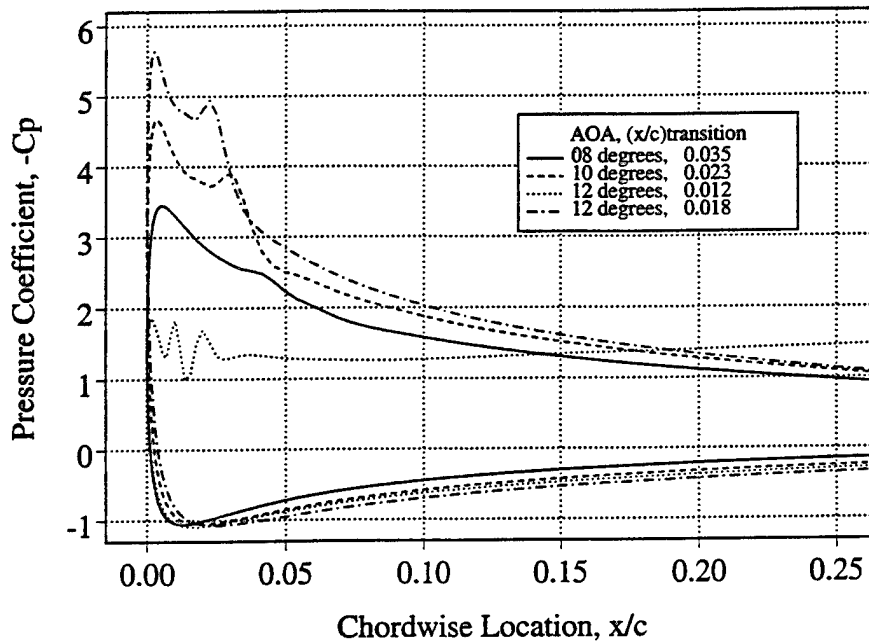


Figure 6.4. Surface Pressure Distribution Near Airfoil Leading Edge, N-S Code, Transition Onset Locations Specified. $M_\infty = 0.3$, $\alpha = 8^\circ$, 10° and 12° , $Re = 540,000$, $G_{\gamma_{tr}} = 200$, or 100 for $(x/c)_{transition} = 0.0177$.

2. Skin-Friction Coefficient Distribution on Suction Surface

The panel/boundary-layer code analysis used 100 and 214 panels to predict the skin-friction coefficient distribution on the suction surface. The

program uses the Chen-Thyson transition model and the Cebeci-Smith eddy-viscosity model. The 100-panel results are shown in Figure 6.5, and the 214 panel results are shown in Figure 6.6. At the lower angles of attack of 0° , 2° , and 4° , differences are noticed in the slightly smoother curves for the denser panel (214) arrangement and in the transition onset locations. Initial transition onset locations were estimated by using Michel's criterion, and in all cases Michel's onset location was aft of the specified transition onset locations used for the final converged solutions in the boundary layer code. The 214-panel solution shows a forward progression of the transition onset location for increasing angles of attack up to 8° , which is in agreement with experimental observations. Transition onset locations for the 100-panel solution are similar, except from $\alpha = 6^\circ$ to $\alpha = 8^\circ$ where the converged solution incorrectly predicted onset to move aft on the airfoil surface.

Flow separation is indicated when C_f passes through 0 to negative values. Negative skin-friction values occur only for 8° angle of attack in a small region near the leading edge of the airfoil, which is in the same general area as the measurements. Specifically, the boundary-layer equations predict negative C_f s at only three airfoil surface locations from $x/c = 0.017$ to 0.021 , which is forward of the measured results. Figures 6.5 and 6.6 show that transition onset was set near locations of minimum C_f and then the flow immediately responds to the transition model. The rapid increase in positive C_f values after the small negative region indicates that the laminar flow has transitioned to turbulent flow and the flow has reattached downstream of the small leading-edge separation bubble.

It can also be seen that the well known breakdown of the boundary-layer equations at the flow separation point does not cause an immediate divergence of the finite-difference solution of these equations. Instead the code is able "to predict" a small region of negative skin friction at $\alpha = 8^\circ$, using either 100 or 214 panels. Hence, the code can be used to identify the angle of attack at which a tiny separation bubble will occur. Obviously, the direct boundary-layer computations are expected to diverge as the region of negative skin friction increases and, indeed, no flow solutions were found for either panel arrangement at angles of attack above 8° . Table 6.1 gives an indication of suggested

transition locations and convergence ranges for the panel/boundary-layer code, using either 100 or 214 panels.

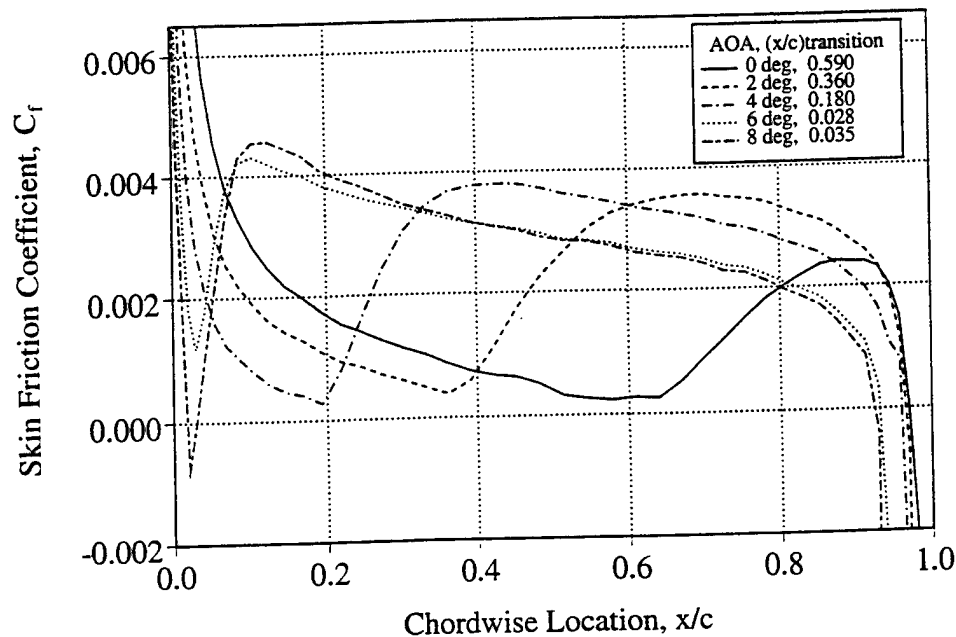


Figure 6.5. Suction Surface Skin-Friction Distributions, Panel/Boundary-Layer Code (100 Panels), Transition Onset Specified. $Re = 540,000$.

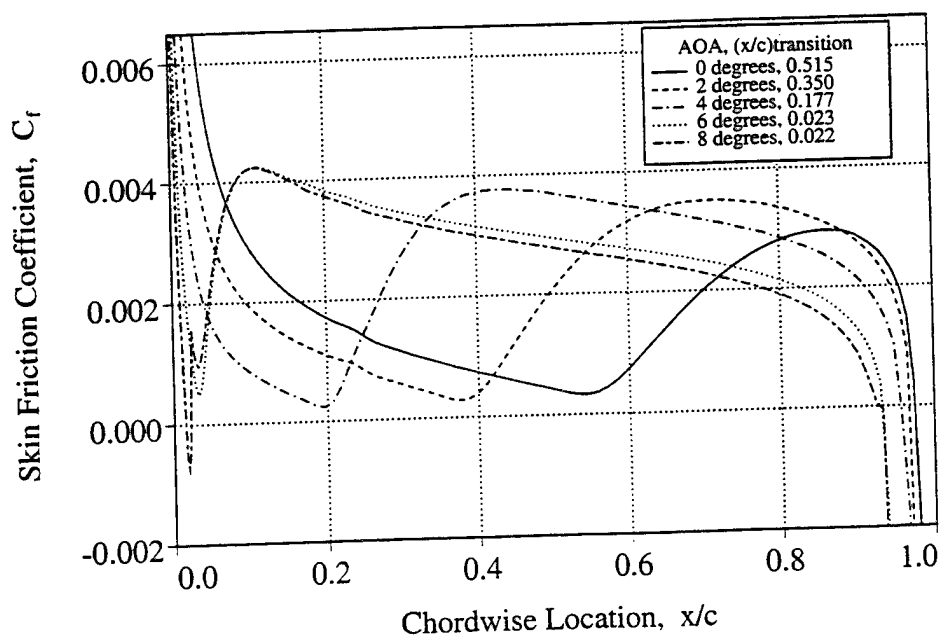


Figure 6.6. Suction Surface Skin-Friction Distributions, Panel/Boundary-Layer Code (214 Panels), Transition Onset Specified, $Re = 540,000$.

Previously, Nowak [Ref. 66] used 100 panels to investigate the effect of Reynolds number. Consistent with the experimental evidence, the predictions showed that as the Reynolds number increased, flow separation was less likely to happen.

Table 6.1. Panel/Boundary-Layer Code Transition Onset Criteria.

Angle of attack, Degrees	0		2		4		6		8	
Number of panels	100	214	100	214	100	214	100	214	100	214
Stagnation panel number	51	101	50	96	49	91	48	87	47	82
Michel's transition onset prediction,										
Upper (x/c)	0.598	0.560	0.380	0.393	0.244	0.258	0.099	0.112	0.164	0.057
Lower (x/c)	0.598	0.560	0.769	0.744	0.839	0.836	0.898	0.877	0.909	0.897
Convergence range										
Upper (x/c)	0.57 - 0.61	0.49 - 0.53	0.33 - 0.37	0.33 - 0.35	0.17 - 0.19	0.17 - 0.20	0.025 - 0.029	0.019 - 0.024	0.029 - 0.041	0.022 - 0.023
Transition onset specified, (best convergence)										
Upper (x/c)	0.59	0.515	0.36	0.35	0.18	0.177	0.028	0.023	0.035	0.022

N-S solutions for the same of attack range are shown in Figure 6.7. The skin-friction curves show the same trends that were obtained with the boundary-layer solutions, including negative values only for the 8° case. Transition onset locations for 0 and 4° were set to values used for the boundary-layer solutions with 214 panels. For other angles of attack, the N-S transition onset values were specified such that the solutions correlated best with the measured results. The initial time steps of the N-S solution were stabilized by using laminar flow calculations. Thereafter, the Chen-Thyson transition and Baldwin-Barth turbulence models are initiated at 100 to 300 time steps, and the predicted onset of flow transition moves dramatically forward on the airfoil surface. However, Michel's criterion for transition onset gave a separation bubble that was much smaller than the measured ones. Therefore, transition onset was specified aft of

Michel's criterion to give predicted results that agreed more closely with the measurements.

As noted before, a $G_{\gamma_{tr}}$ value of 200 was used to set the transition region length. Minimum C_f s move forward, remain positive and increase with increasing angles of incidence for both the boundary layer and N-S solutions until both predict a negative C_f region near the airfoil leading edge for $\alpha = 8^\circ$. Obvious differences between the two solutions include a larger separation bubble predicted by the N-S solution at $\alpha = 8^\circ$. Negative C_f s are predicted at nine surface locations from $x/c = 0.028$ to 0.058 for the N-S solutions, which indicates a laminar separation bubble more in line with the measured results than that predicted by the boundary-layer code. Higher C_f s are predicted along the airfoil upper surface by the N-S code downstream of transition onset and flow reattachment that are in part attributable to differences in turbulent modeling (Baldwin-Barth vs. Cebeci-Smith) and compressible flow considerations that are not considered in the direct boundary-layer analysis.

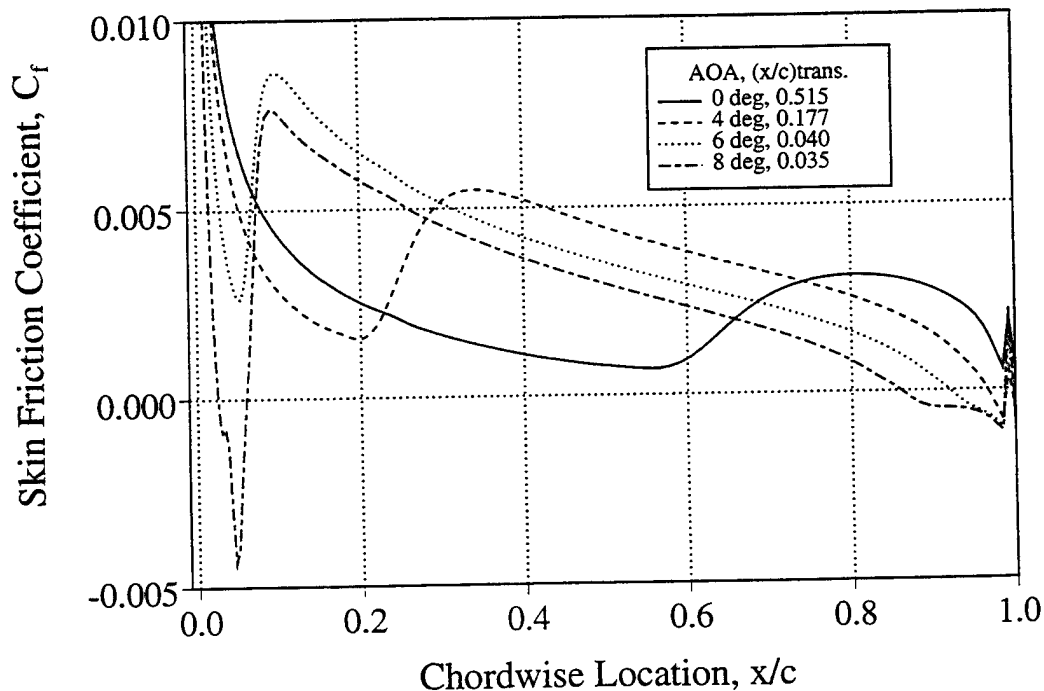


Figure 6.7. Suction Surface Skin-Friction Distributions, N-S Code, 275x81, Transition Onset Locations Specified, $M_\infty = 0.3$, $Re = 540,000$, $G_{\gamma_{tr}} = 200$.

3. Displacement Thickness Distribution on Suction Surface

The boundary-layer displacement thickness distributions on the suction surface as predicted by the boundary layer (214 panels) and N-S codes are shown in Figures 6.8 and 6.9. Both computations yield the well known dip in displacement thickness due to boundary layer transition. The movement of the transition region toward the leading edge is clearly visible as the angle of attack is increased from 0 to 8°. Also, it is seen that the computations agree reasonably well.

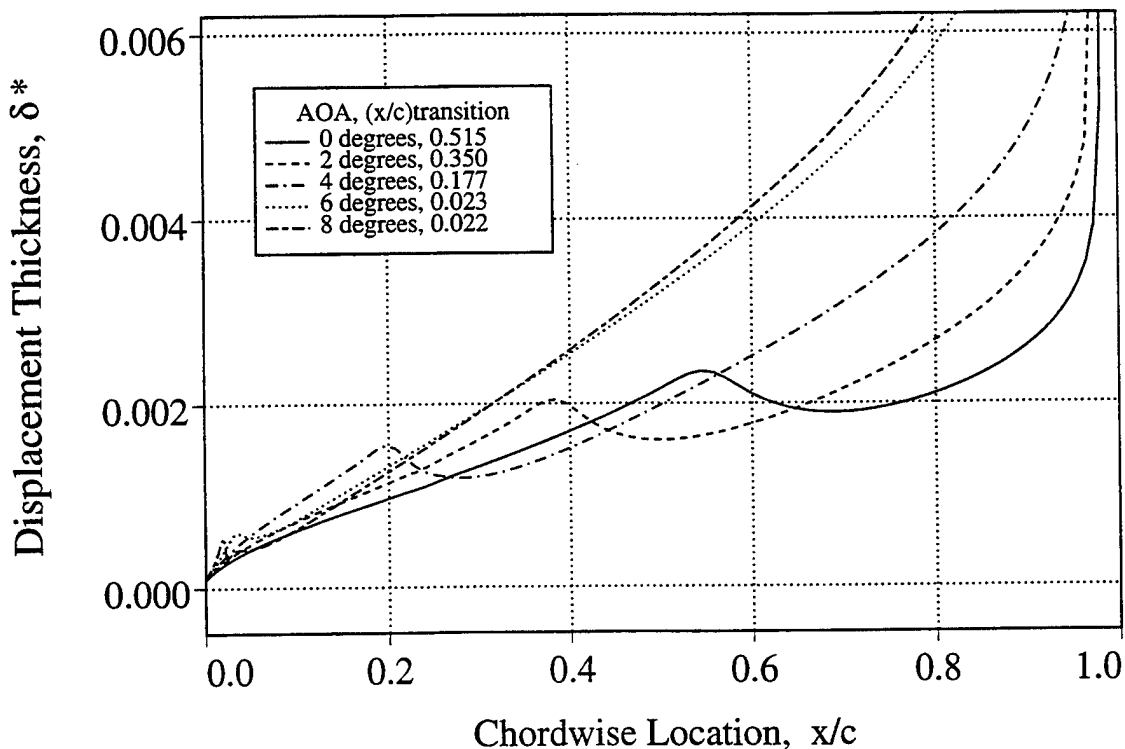


Figure 6.8. Suction Surface Displacement Thickness Distributions, Panel/ Boundary-Layer Code (214 Panels), Transition Onset Locations Specified. $Re = 540,000$.

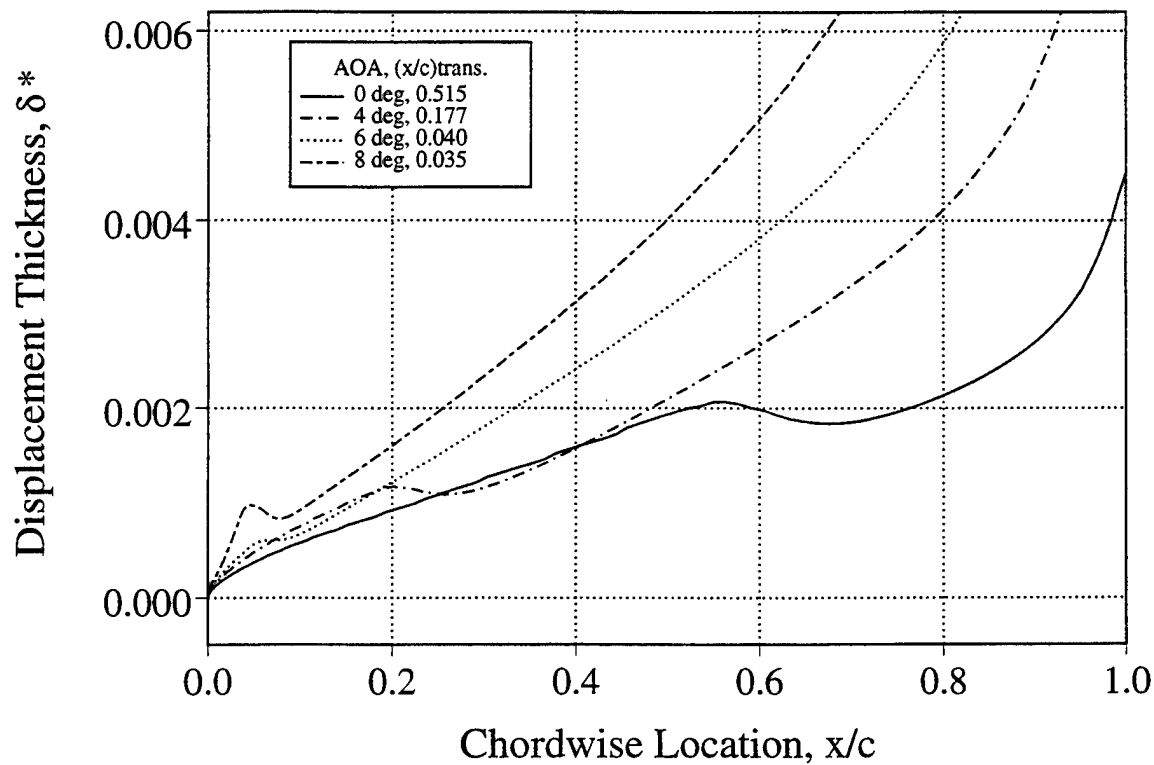


Figure 6.9. Suction Surface Displacement Thickness Distributions, N-S Code, 275x81, Transition Onset Locations Specified. $M_\infty = 0.3$, $Re = 540,000$, $G_{\gamma_{tr}} = 200$.

4. Boundary-Layer Velocity Profiles on Suction Surface

The flow behavior can be understood in more detail by examining the change in boundary-layer profiles as a function of chordwise locations on the suction surface. Therefore, the profiles computed with the 214-panel boundary-layer code are shown for 0, 2, 4, 6, and 8° angle of attack in Figures 6.10 through 6.14. It is readily seen that, in each case, the laminar flow profiles near the leading edge change to profiles with inflection points indicative of flow into an adverse pressure gradient region. This is consistent with the previously shown skin friction and displacement thickness distributions. Laminar flow separation is averted by virtue of the fact that the flow starts to transition to turbulent flow and thereby retains the ability to remain attached. This transition occurs at approximately 50% chord for the zero angle of attack flow and rapidly moves toward the leading edge as the angle of attack is increased. Note that the

velocity profiles are non-dimensionalized by the local external inviscid flow velocity, U_e , giving an indication of the growth of the boundary layer in the streamwise direction. In the Figures, $U_o = 0.995 \times U_e$.

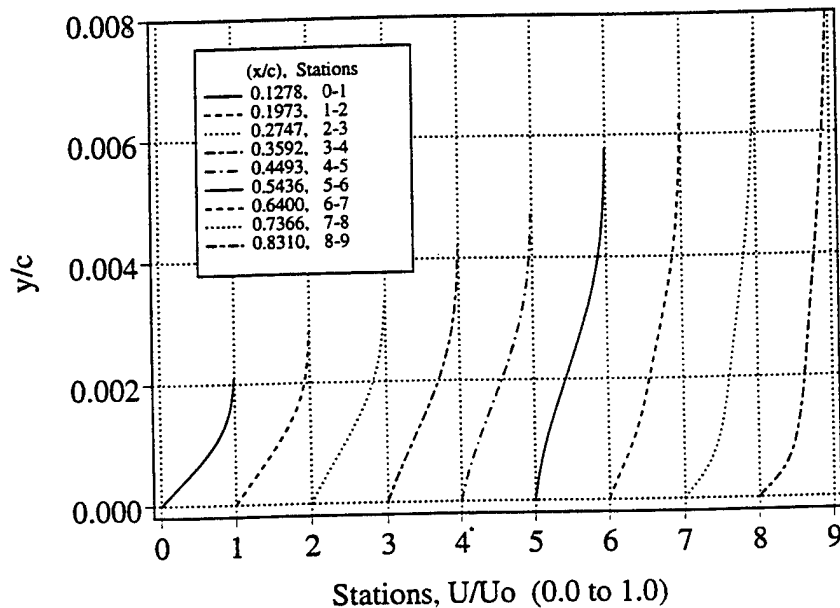


Figure 6.10. Boundary-Layer Velocity Profiles (Panel/Boundary-Layer Code - 214 Panels). $\alpha = 0^\circ$, $(x/c)_{tr} = 0.515$, $Re = 540,000$.

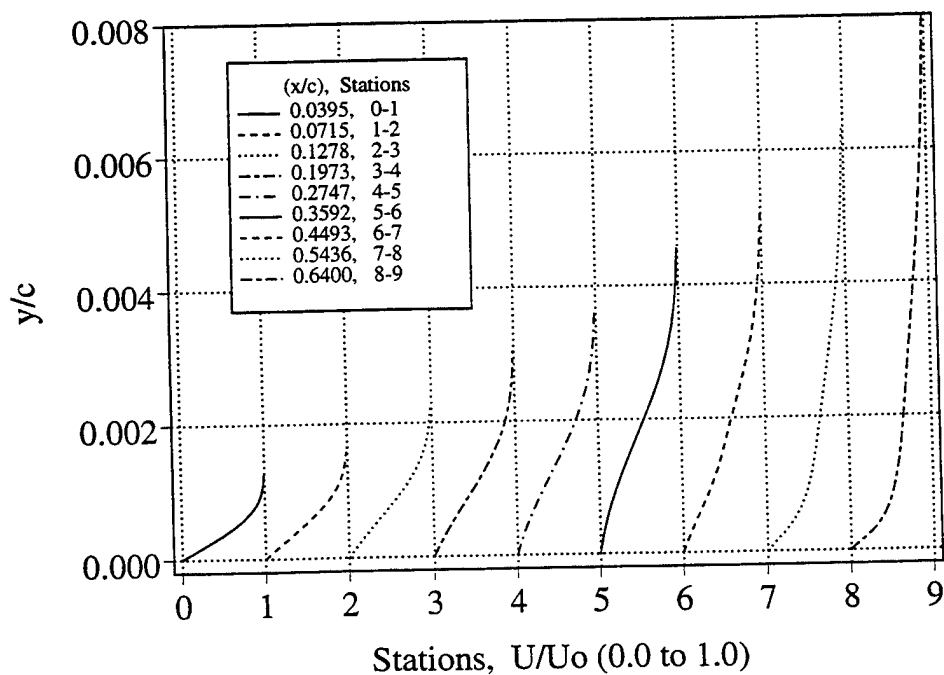


Figure 6.11. Boundary-Layer Velocity Profiles (Panel/Boundary-Layer Code - 214 Panels). $\alpha = 2^\circ$, $(x/c)_{tr} = 0.35$, $Re = 540,000$.

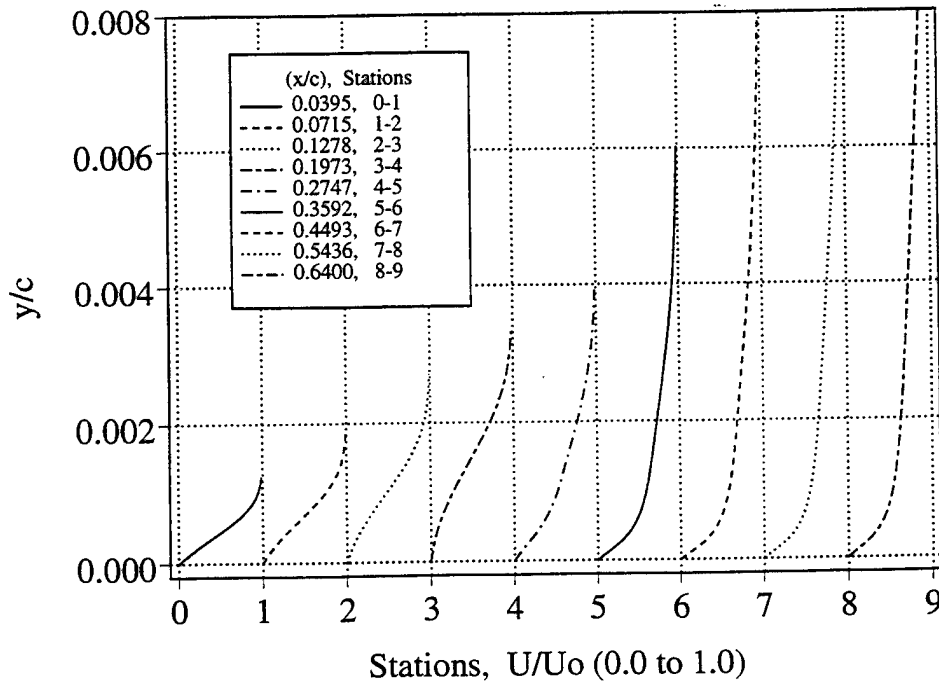


Figure 6.12. Boundary-Layer Velocity Profiles (Panel/Boundary-Layer Code - 214 Panels). $\alpha = 4^\circ$, $(x/c)_{tr} = 0.177$, $Re = 540,000$.

In Figures 6.13 and 6.14, velocity profiles are shown for angles of attack of 6° and 8° , which are much farther forward than those shown in the previous figures. Solution convergence at the higher angles of attack was very sensitive to flow transition onset locations, which was specified at $x/c = 0.023$ for $\alpha = 6^\circ$ and at $x/c = 0.022$ for $\alpha = 8^\circ$. Again, velocity profiles with inflection points are shown forward of the specified transition onset locations, but only slightly. The slight forward movement of the transition onset location, and no indication of full velocity profiles aft of flow transition in the turbulent flow region, points toward prediction of an impending flow separation. Flow separation is predicted by the velocity profiles at $x/c = 0.0298$ and 0.0413 at 8° angle of attack. Thus, the panel/boundary-layer code predicts flow separation at $\alpha = 8^\circ$ with no solutions found above 8° .

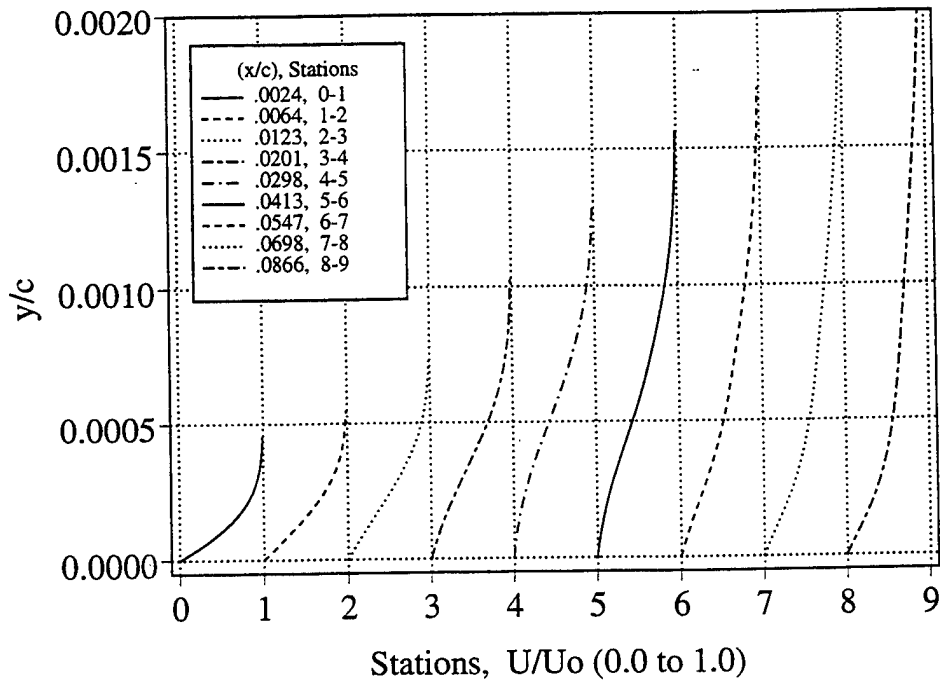


Figure 6.13. Boundary-Layer Velocity Profile Predictions (Panel/Boundary-Layer Code - 214 Panels). $\alpha = 6^\circ$, $(x/c)_{tr} = 0.023$, $Re = 540,000$.

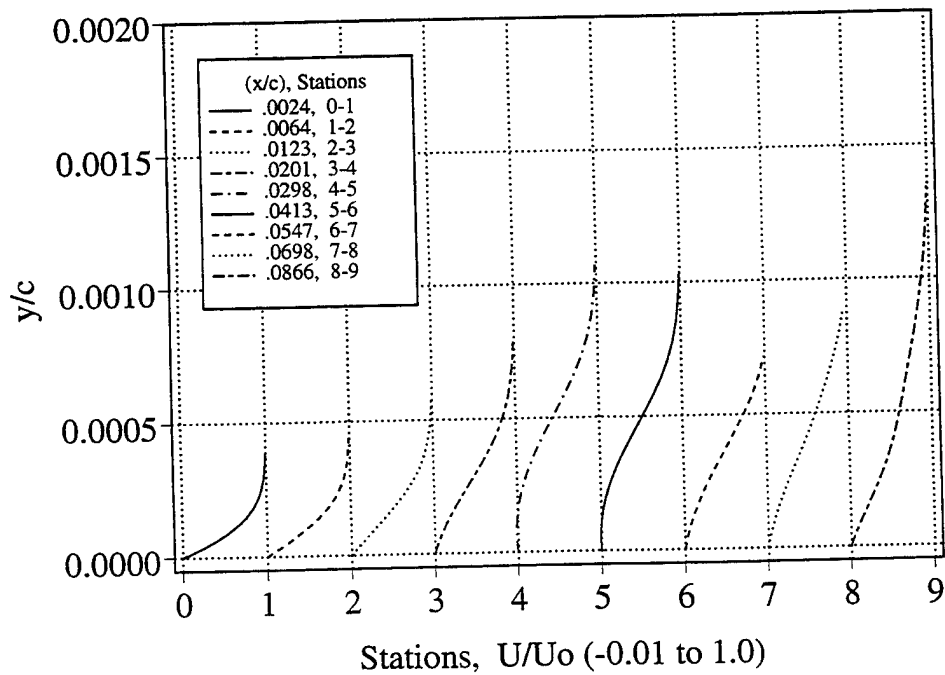


Figure 6.14. Boundary Layer Velocity Profiles (Panel/Boundary-Layer Code - 214 Panels). $\alpha = 8^\circ$, $(x/c)_{tr} = 0.022$, $Re = 540,000$.

Figure 6.15 gives the velocity profiles for both the 100- and 214-panel solutions at 6° angle of attack and the same x/c locations as previously given in Figure 6.13. Only minor differences occur in the computed velocity profiles. Panel densities up to 400 were used to establish grid independence and no differences in velocity profiles were found. However, panel numbers greater than 400 caused a breakdown in the solution with unrealistic multiple dips in the skin-friction coefficient and multiple vortices predicted for $\alpha = 6$ and 8° .

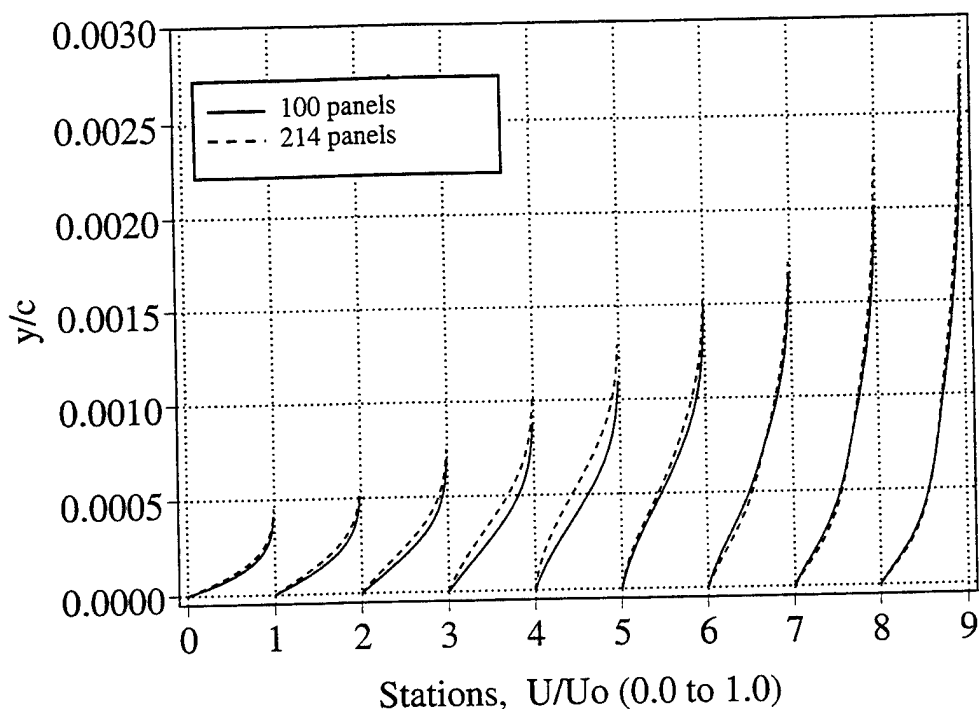


Figure 6.15. Boundary-Layer Velocity Profiles (Panel/Boundary-Layer Code - 100 and 214 Panels). $\alpha = 6^\circ$, $(x/c)_{tr} = 0.023$, $Re = 540,000$.

An advantage of the N-S analysis method over the boundary-layer code is the capability to compute extensive regions of flow separation. The next series of figures give the N-S predictions for angles of attack from 0 to 12° angle of attack. Here the velocity profiles are non-dimensionalized with the free-stream speed, U_∞ .

Figure 6.16 shows the predicted velocity profiles for $\alpha = 0^\circ$ with transition set to $x/c = 0.515$, just as in the boundary layer code. Velocities are seen to exceed the free stream by up to 18% forward of the adverse pressure gradient and the transition onset location.

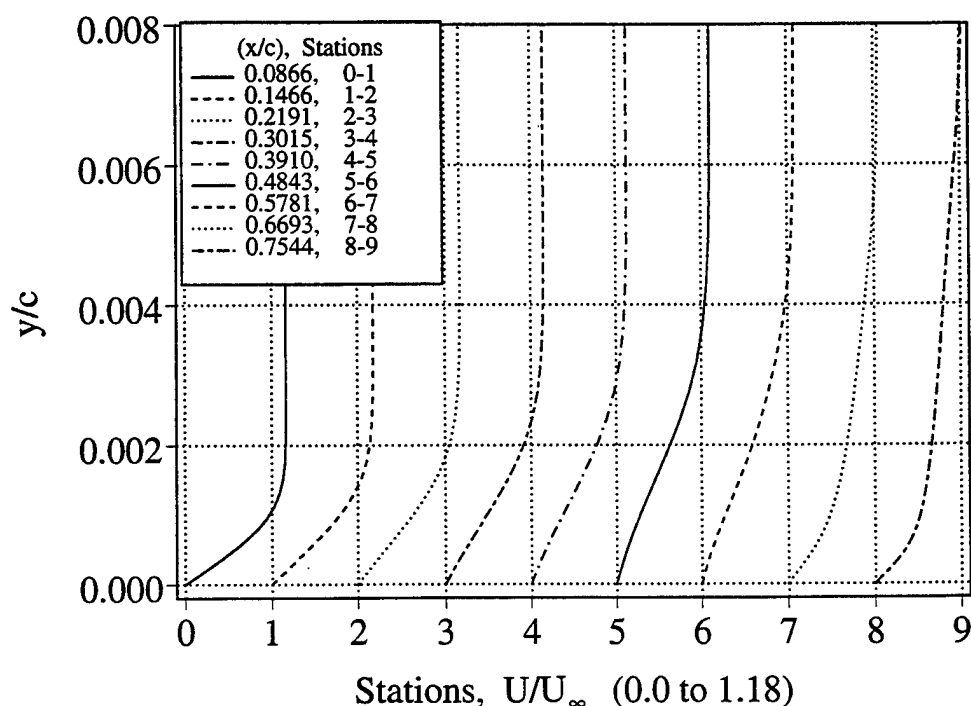


Figure 6.16. Boundary-Layer Velocity Profiles (N-S Code, 275x81). $M_\infty = 0.3$, $\alpha = 0^\circ$, $Re = 540,000$.

Next, velocity profiles are shown at similar x/c locations for $\alpha = 4^\circ$ angle of attack in Figure 6.17. Transition onset moved forward and again was specified at the same location ($x/c = 0.18$) as the boundary-layer code solution. No reverse flow regions are predicted and much higher velocities ($U / U_\infty = 1.33$) are reached forward of the adverse pressure gradient region because of the higher angle of attack. Two velocity profiles show points of inflection. Fully turbulent velocity profiles are evident aft of the flow transition region.

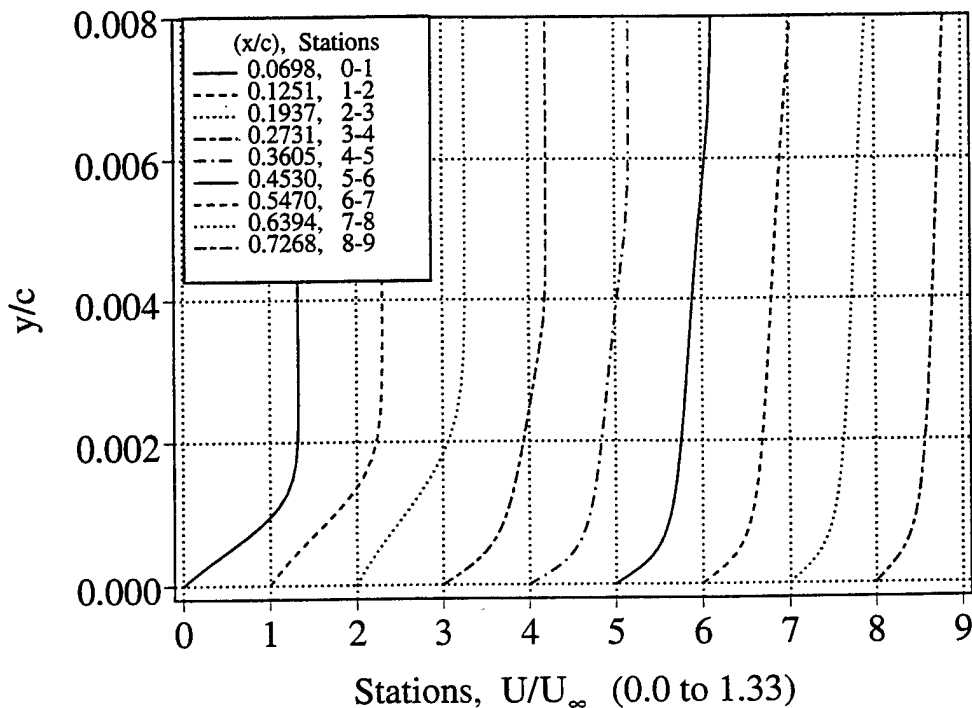


Figure 6.17. Boundary-Layer Velocity Profiles (N-S Code, 275x81). $M_\infty = 0.3$, $\alpha = 4^\circ$, $Re = 540,000$.

The next three Figures give the N-S computed velocity profiles for $\alpha = 8^\circ, 10^\circ$, and 12° near the airfoil leading edge because transition onset has moved to the first 4% chord. As shown in Figure 6.18 for $\alpha = 8^\circ$, the local velocity is predicted to exceed the free-stream velocity by up to 77%. Transition onset was set at $x/c = 0.035$ to give a N-S solution that most closely matched the experimental measurements (C_{ps} from PDI and velocity profiles from LDV). Points of inflection are shown in five profiles around the specified transition onset point. Flow separation is evident at $x/c = 0.0298, 0.0413$, and 0.0547 with an extensive reverse flow region ($U/U_\infty = -0.09$) shown at $x/c = 0.0413$ and $y/c = 0.0002$. Thus, the N-S code predicts a laminar flow separation, which is evident at $x/c = 0.0298$ and forward of the specified transition onset location.

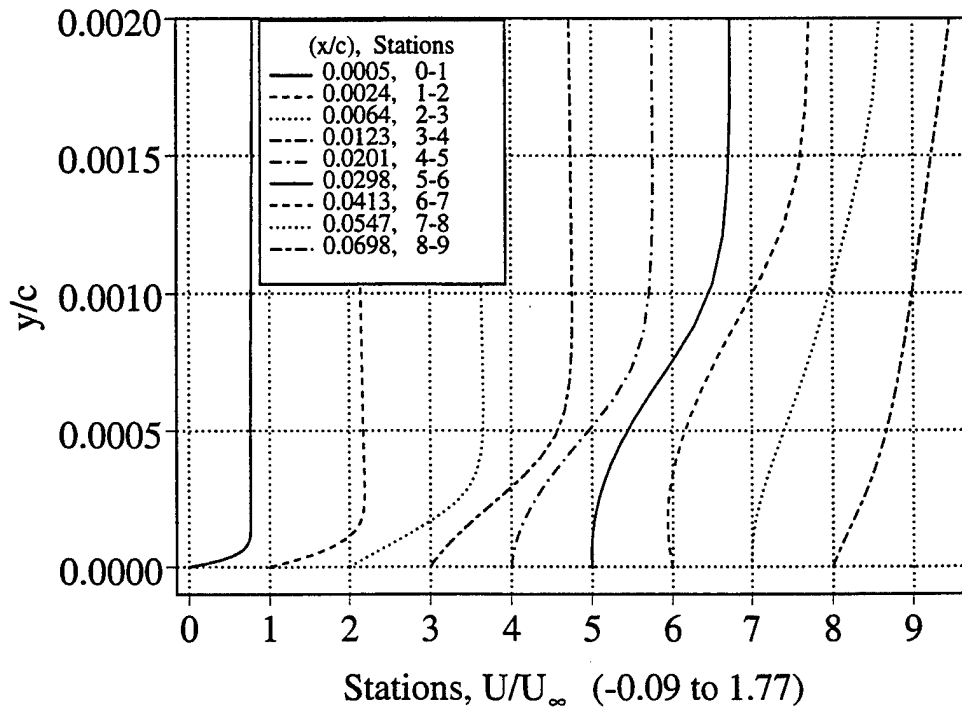


Figure 6.18. Boundary-Layer Velocity Profiles (N-S Code, 275x81). $M_\infty = 0.3$, $\alpha = 8^\circ$, $Re = 540,000$.

Figure 6.19 gives the velocity profiles for $\alpha = 10^\circ$. Transition onset moves closer to the leading edge of the airfoil at $x/c = 0.0225$. All profiles in the first 7% chord have points of inflection, except the first two near the airfoil leading edge. Again, laminar separation occurs just prior to the specified transition onset location. By examining all the velocity profiles in the vicinity of separation, laminar flow separation is first predicted at $x/c = 0.0117$, and separated flow velocity profiles are shown to 7% chord. The predicted separation bubble extends from $0.0117 < x/c < 0.08$ along the airfoil surface and $0.0 < y/c < 0.00085$ for the reverse flow region above the airfoil surface. Local velocities up to $1.95 \times U_\infty$ are shown around the indicated separation bubble.

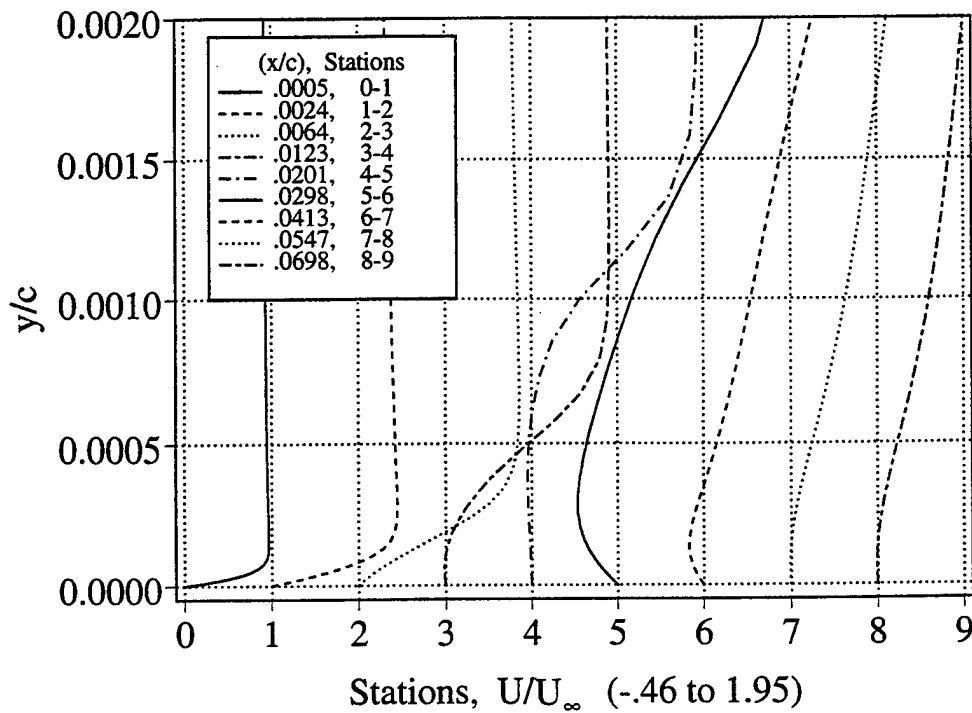


Figure 6.19. Boundary-Layer Velocity Profiles (N-S Code, 275x81). $M_\infty = 0.3$, $\alpha = 10^\circ$, $Re = 540,000$.

Figure 6.20 gives the velocity profiles for $\alpha = 12^\circ$. Transition onset moved forward to $x/c = 0.0177$ and $G_{\gamma_{tr}}$ was set to 100. At this angle of attack near stall conditions, the local flow reaches values of $2.22 \times U_\infty$. Flow separation begins at $x/c = 0.0085$ and appreciable reverse flow extends to 7% chord, indicating a flow on the verge of stall. A maximum negative velocity ($U/U_\infty = -0.48$) is predicted at $x/c = 0.0201$, which again is aft of the specified transition onset location. The extent of the predicted separation bubble ranges from $0.0085 < x/c < 0.10$ in the downstream direction and from $0.0 < y/c < 0.0009$ above the airfoil surface.

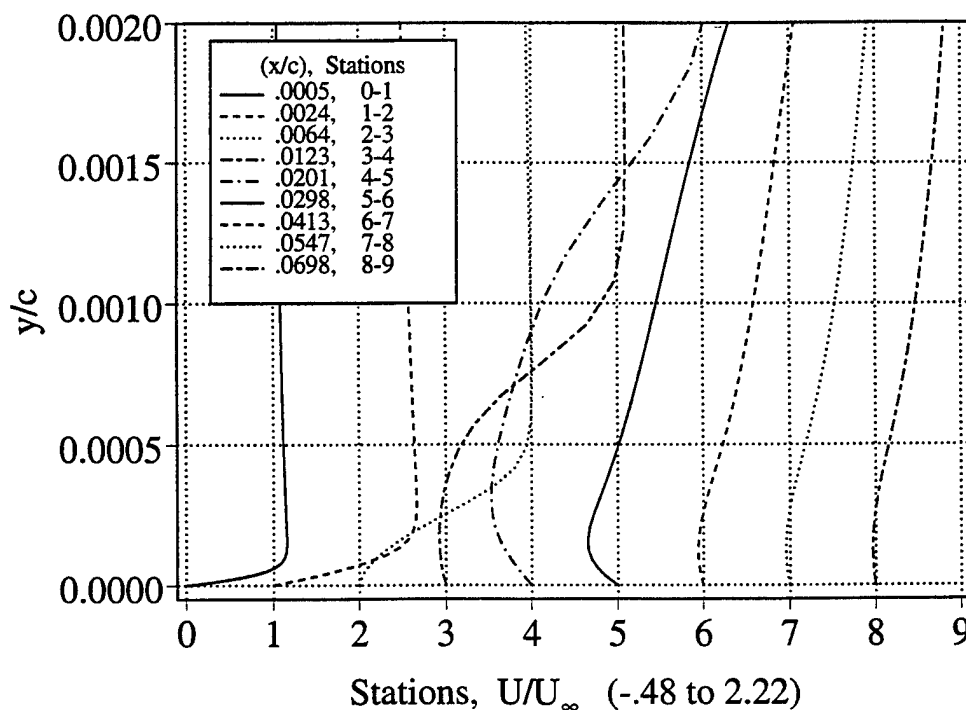


Figure 6.20. Boundary-Layer Velocity Profiles (N-S Code, 275x81). $M_\infty = 0.3$, $\alpha = 12^\circ$, $Re = 540,000$.

It is instructive to compare the boundary-layer and N-S code velocity profiles directly. To this end, velocities are normalized by using the free-stream velocity as the normalization factor in both cases. For these runs, the boundary layer code included a test for laminar separation. If laminar separation is predicted before Michel's transition prediction, then flow transition onset is specified at the panel forward of laminar separation. The aforementioned method precludes the computation of a separation bubble, which is not done well by the boundary-layer code. The comparisons are based on the choices for transition onset specified in Figures 6.10 and 6.12 for the boundary layer calculations and Figures 6.16 and 6.17 for the N-S calculations.

Figures 6.21 and 6.22 show both predicted velocity profiles at $\alpha = 0^\circ$ and $\alpha = 4^\circ$. The boundary layer velocity profiles are output until minimal changes are seen in the outer velocity ratio. Excellent agreement is shown between the

calculations, keeping in mind that the boundary-layer code is based on the incompressible flow equations, whereas the N-S calculations consider a $M_\infty = 0.3$ compressible flow.

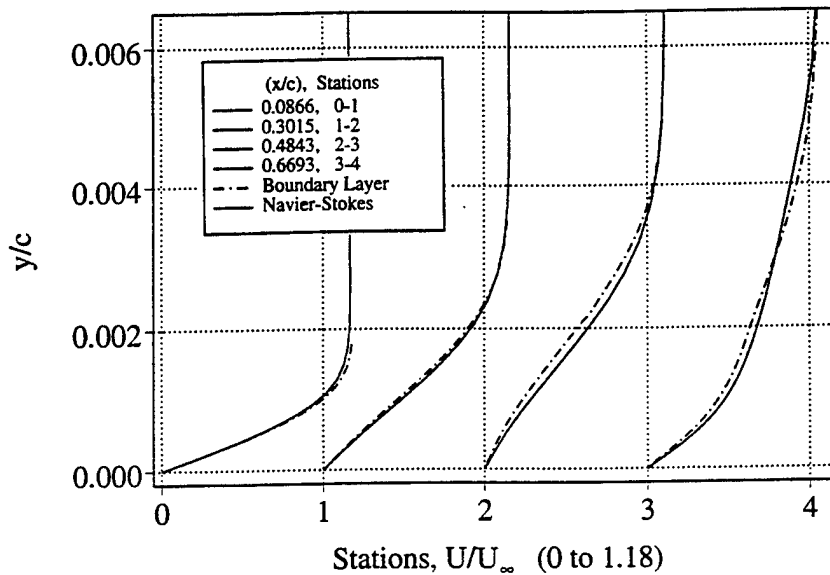


Figure 6.21. Boundary-Layer Velocity Profile Comparisons (N-S and Panel/Boundary-Layer Codes), $\alpha = 0^\circ$, $Re = 540,000$; N - S Analysis, $M_\infty = 0.3$.

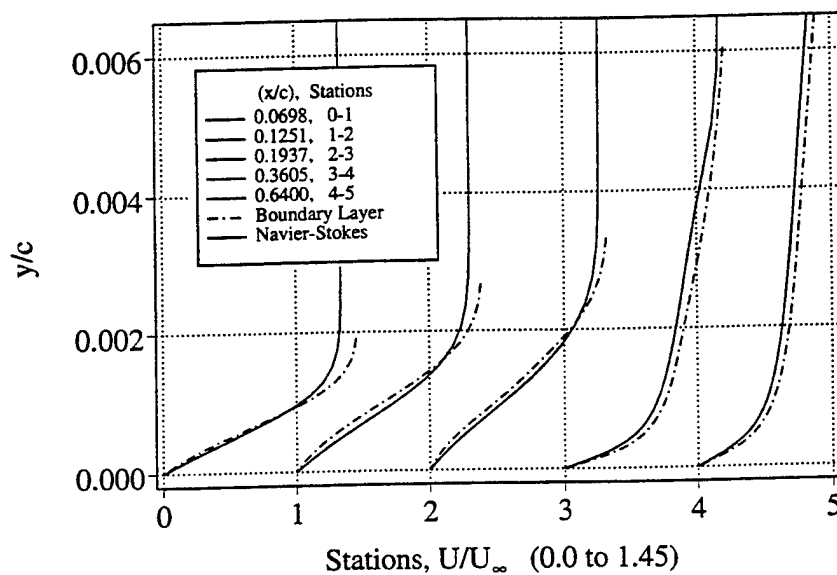


Figure 6.22. Boundary-Layer Velocity Profile Comparisons (N-S and Panel/Boundary-Layer Codes), $\alpha = 4^\circ$, $Re = 540,000$; N - S Analysis, $M_\infty = 0.3$.

For $\alpha = 8^\circ$, the boundary-layer solution predicts a laminar-flow separation forward of Michel's transition prediction, at $x/c = 0.015$, which is markedly forward of the N-S laminar separation prediction at $x/c = 0.0298$. Thus, no comparisons are shown for $\alpha = 8^\circ$ because of the early laminar flow separation predicted by the boundary layer code.

B. OSCILLATORY FLOW OVER NACA 0012 AIRFOIL

For the analysis of the oscillatory pitch tests of the NACA 0012 airfoil described in Chapter V, it is useful to develop an understanding of the inviscid flow effects prior to delving into the unsteady viscous flow phenomena. Therefore, the inviscid, incompressible UPOT code is first used to study the pressure lag effects that are induced by pitch oscillations about the quarter chord point of the airfoil. UPOT results are presented for oscillation amplitudes of 10° and 2° about a mean angle of attack of 10° . The oscillations are $\alpha = 10^\circ - 10^\circ \sin \omega t$ and $\alpha = 10^\circ - 2^\circ \sin \omega t$. In addition, pressure distributions are given for unsteady reduced frequencies ($k = 2\pi fc/U_\infty$) of 0.1, 0.2, 0.5, and 1.0.

Secondly, the unsteady, compressible, and viscous N-S code is used in conjunction with the previously described flow transition and turbulence models to predict the surface and flow field behavior during the forced oscillations. Specifically, the code is used to predict flow behavior in the separation bubble region near the airfoil leading edge, and the subsequent vortex-shedding phenomena for the low-amplitude and low reduced frequency test case.

1. UPOT Pressure Distributions ($\alpha = 10^\circ - 10^\circ \sin \omega t$)

Surface pressure coefficients predicted by the UPOT code are shown for $\alpha = 10^\circ - 2^\circ \sin \omega t$ and $k = 0.1$ in Figure 6.23. Pressure distributions are given for airfoil motion in opposing directions (up/down), but at the same angle of attack. No results are given for angles of attack greater than 12° , since the unsteady stall was known *a priori* to be only slightly higher than 12° . The suction pressure peaks move slightly forward with increasing angle of attack as was the case for the steady angles of attack, but pressure lag effects attributable to the high-amplitude forced oscillation are very much evident even at the low reduced

frequency ($k=0.1$). During the upstroke, the suction pressure peaks are significantly smaller than the steady suction pressures at 8, 10, and 12° angle of attack, as shown in Figures 6.1 and 6.2. During the downstroke, on the other hand, the suction pressure peaks are significantly larger. This lag effect in the build up of the pressure attributable to the pitch oscillation is seen to be largest at angles of attack near 10° where the pitch rate reaches its maximum value.

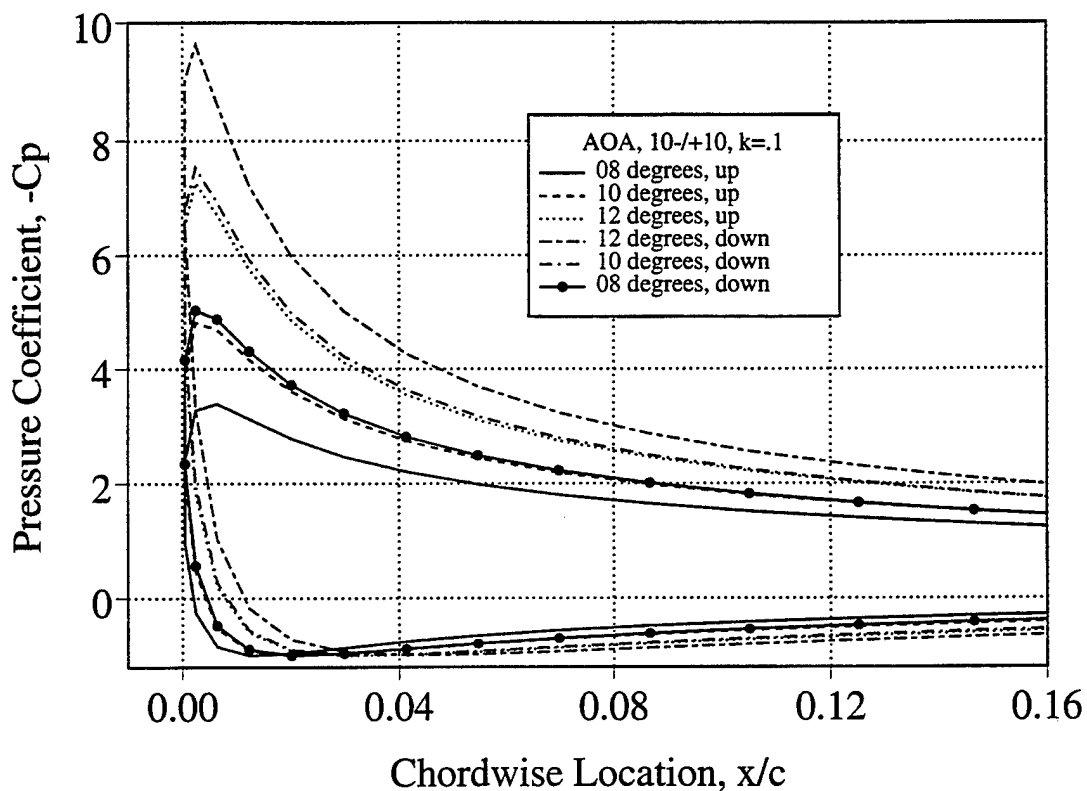


Figure 6.23. Unsteady Surface Pressure Distributions Near the Airfoil Leading Edge (UPOT), $\alpha = 10^\circ - 10^\circ \sin \omega t = 8^\circ, 10^\circ$ and 12° (up / down), $k = 0.1$, pitch axis at quarter chord point.

The effect of increased oscillation rates or reduced frequencies on the pressure distribution during airfoil upward motion are shown in Figure 6.24. The example is for 12° angle of attack (up), indicating smaller suction peaks with

increased oscillation rates. However, the suction peak lag effect is seen to decrease with increasing frequency. At $k = 1.0$, the pressure peak is 3% less than at a reduced frequency of 0.5 and only slight pressure reductions are predicted in the first 2% chord downstream. The most dramatic pressure peak reduction relative to the steady state pressure value occurs for the lowest reduced frequency of $k = 0.1$ near the leading edge with the trend continuing to 10% chord downstream.

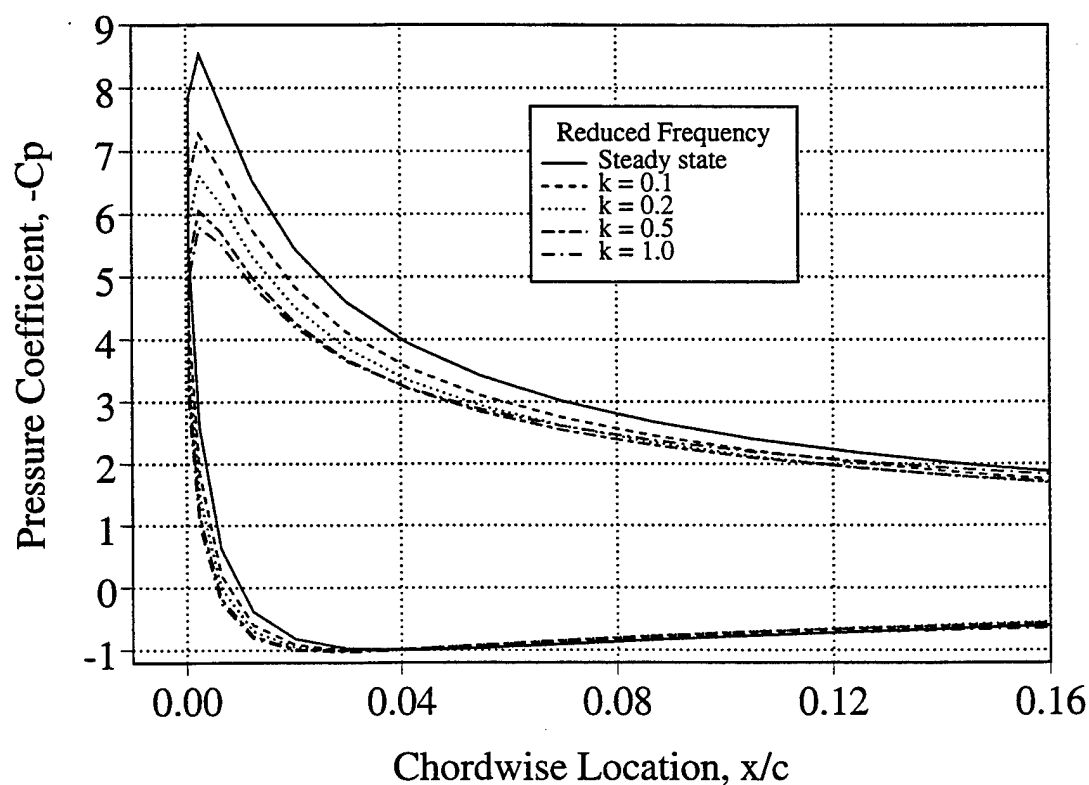
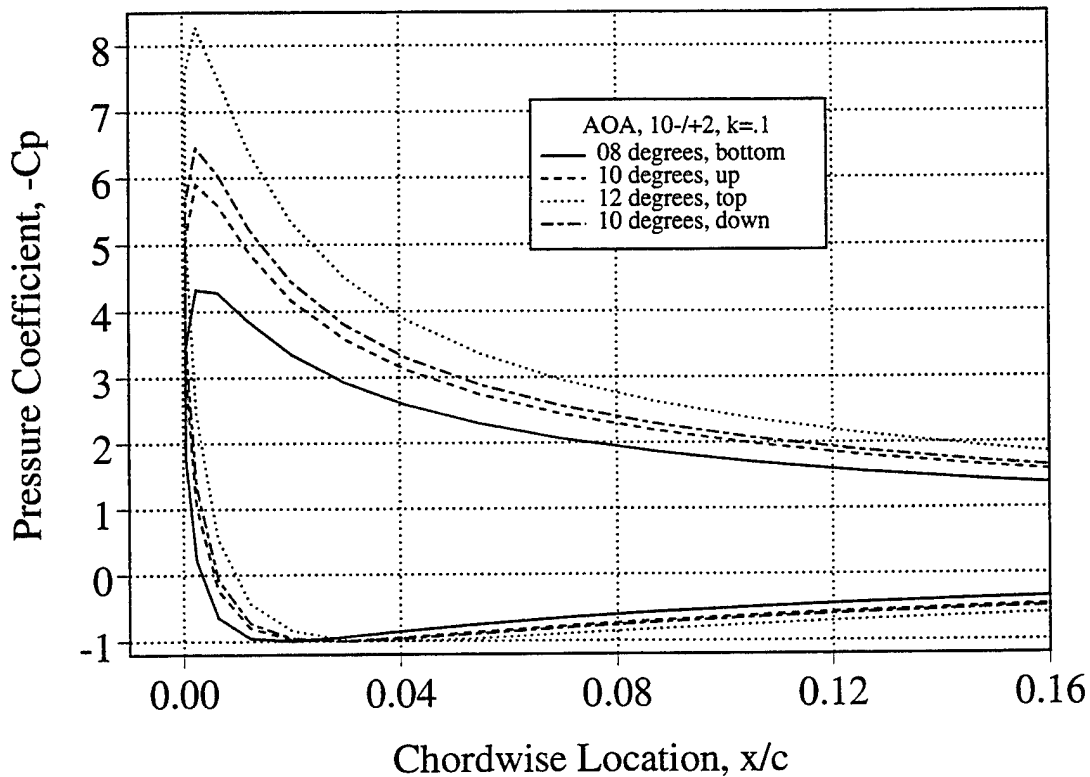


Figure 6.24. Steady and Unsteady Surface Pressure Distributions Near the Airfoil Leading Edge (UPOT), $\alpha = 10^\circ - 10^\circ \sin \omega t = 12^\circ$ (up), $k = 0.1, 0.2, 0.5$ and 1.0 , pitch axis at quarter chord point.

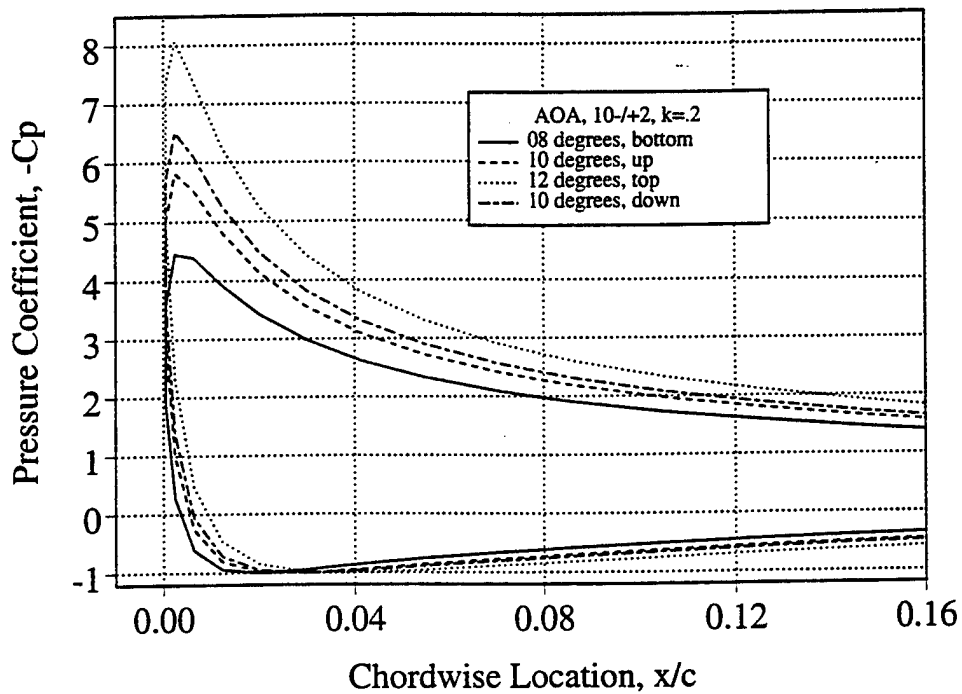
2. UPOT Pressure Distributions ($\alpha = 10^\circ - 2^\circ \sin \omega t$)

Surface pressure coefficients predicted by the UPOT code for the low-amplitude test case ($\alpha = 10^\circ - 2^\circ \sin \omega t$) are shown in Figure 6.25a, b, and c, each with increasing airfoil pitch rates or reduced frequencies of $k=0.1, 0.2$, and 0.5 . Results are presented for airfoil motion in opposing directions (up/down) at 10° angle of attack and at the top ($\alpha=12^\circ$) and bottom ($\alpha=8^\circ$) of the oscillation cycle. As pitch rates increase from $k = 0.1$ to 0.5 , suction pressure peaks decrease slightly at 12° angle of attack and increase slightly at 8° angle of attack. However, the pressure lag effect is still clearly visible at the three reduced frequencies in the pressure differences between the upstroke and downstroke at 10° angle of attack.

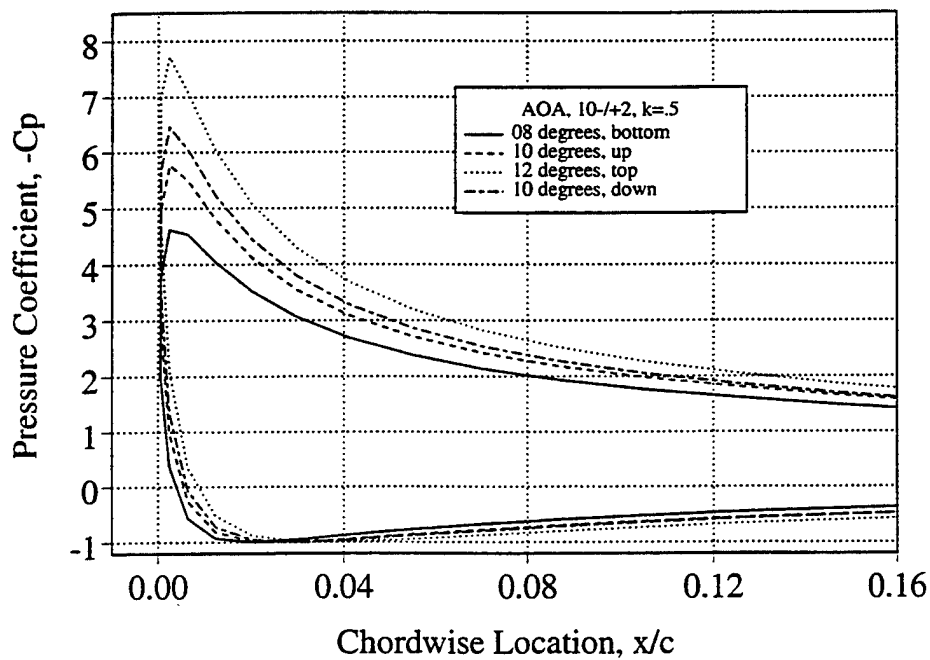


(a) $\alpha = 10^\circ - 2^\circ \sin \omega t = 8^\circ$ and 10° (up / down), and 12° (top), $k = 0.1$.

Figure 6.25. Unsteady Surface Pressure Distributions Near the Airfoil Leading Edge (UPOT), pitch axis at quarter chord point.



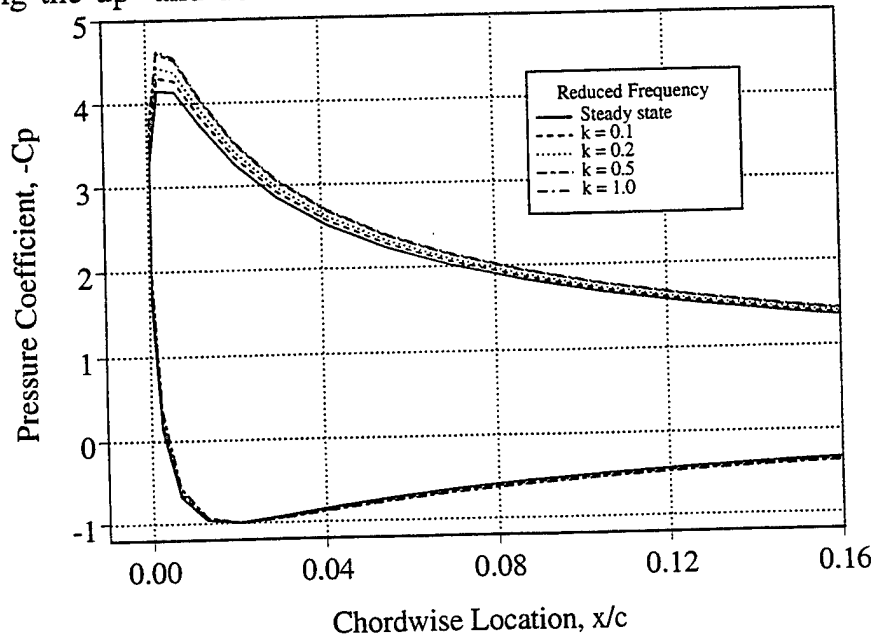
(b) $\alpha = 10^\circ - 2^\circ \sin \omega t = 8^\circ$ and 10° (up / down), and 12° (top), $k = 0.2$.



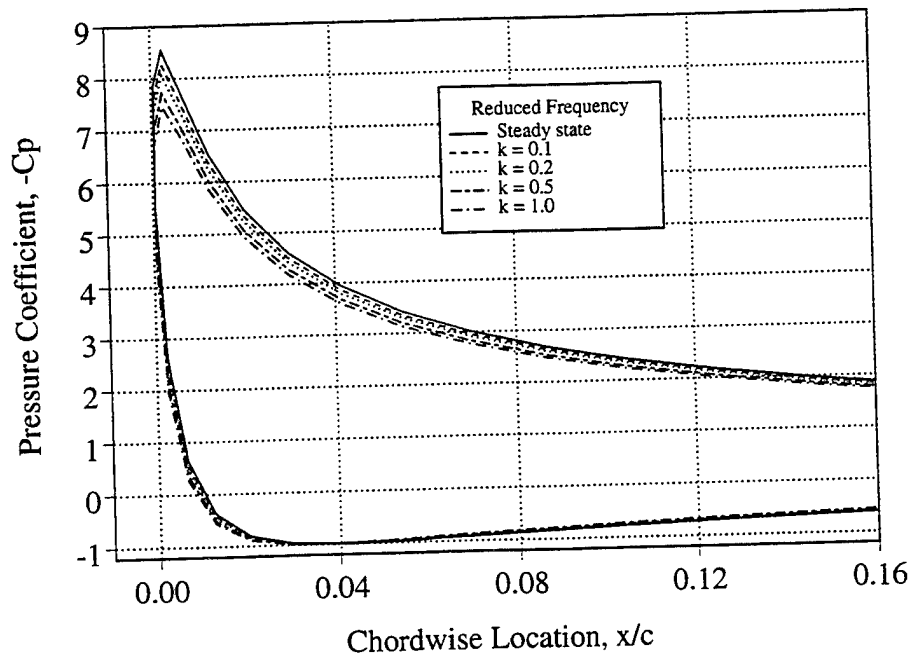
(c) $\alpha = 10^\circ - 2^\circ \sin \omega t = 8^\circ$ and 10° (up / down), and 12° (top), $k = 0.5$.

Figure 6.25. (Contd.)

The magnitude of the lag effect is quantified even better in Figure 6.26a, b, c, and d where the pressures induced by the pitch oscillations at $k = 0.1, 0.2, 0.5$, and 1.0 are compared with the steady pressures at $8^\circ, 12^\circ$, and 10° angle of attack during the up- and downstroke.

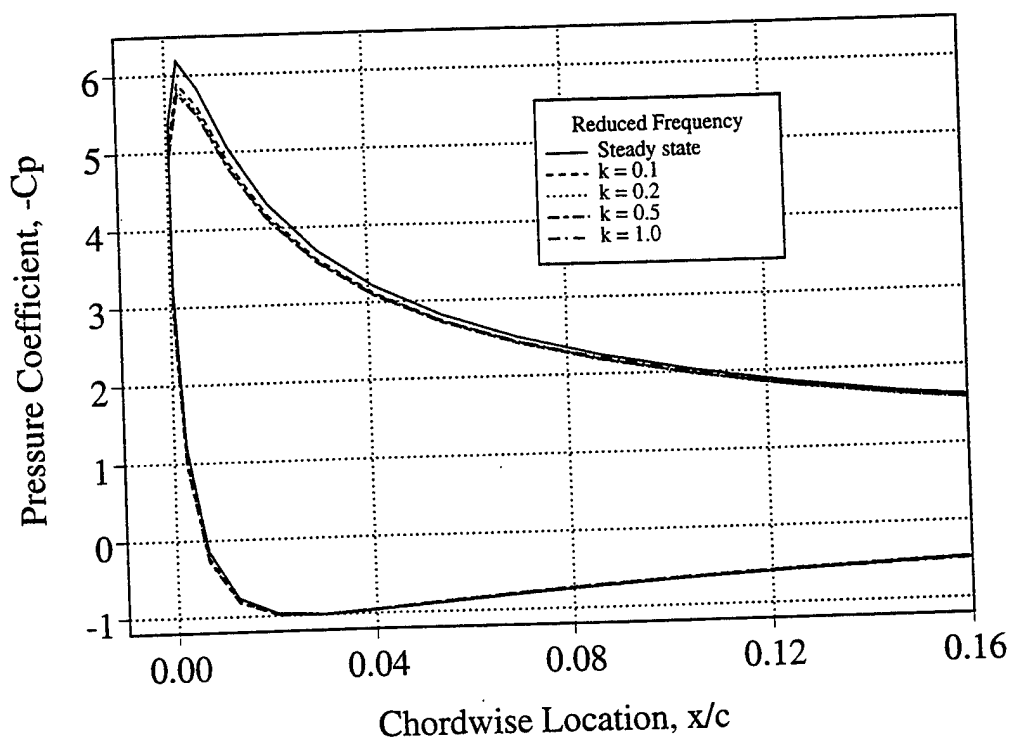


(a) $\alpha = 10^\circ - 2^\circ \sin \omega t = 8^\circ$ (bottom), $k = 0.1, 0.2, 0.5$ and 1.0 .

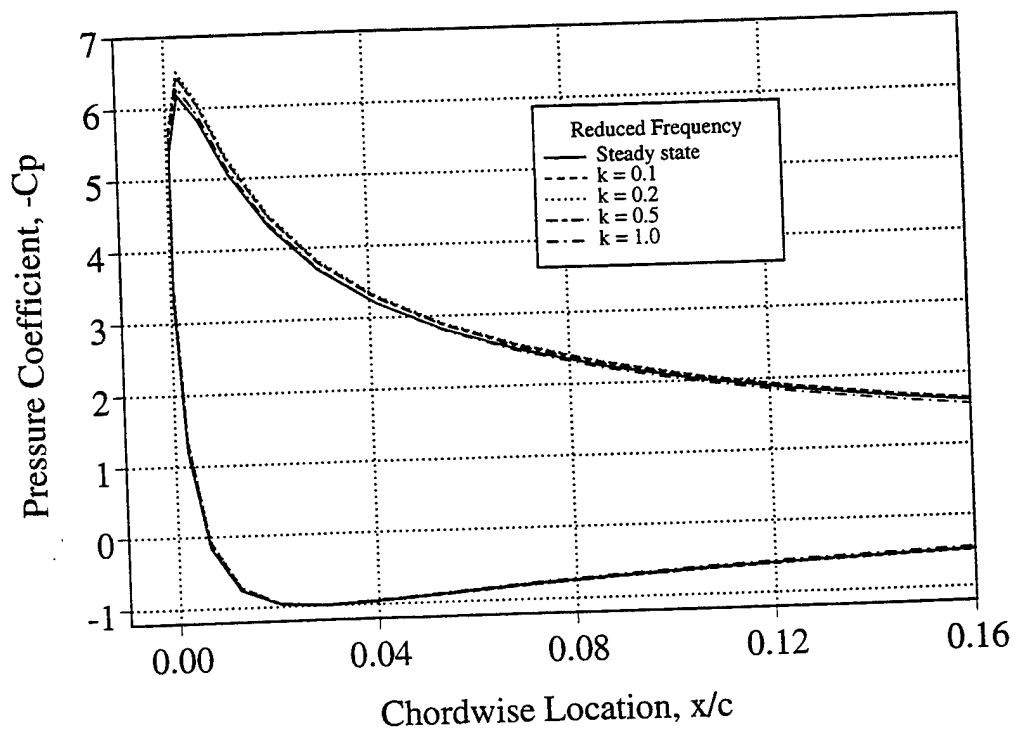


(b) $\alpha = 10^\circ - 2^\circ \sin \omega t = 12^\circ$ (top), $k = 0.1, 0.2, 0.5$ and 1.0 .

Figure 6.26. Steady and Unsteady Surface Pressure Distributions Near the Airfoil Leading Edge (UPOT), pitch axis at quarter chord point.



(c) $\alpha = 10^\circ - 2^\circ \sin \omega t = 10^\circ$ (up), $k = 0.1, 0.2, 0.5$ and 1.0 .



(d) $\alpha = 10^\circ - 2^\circ \sin \omega t = 10^\circ$ (down), $k = 0.1, 0.2, 0.5$ and 1.0 .

Figure 6.26. (Contd.)

3. N-S Pressure Distributions ($\alpha = 10^\circ - 2^\circ \sin \omega t$)

Pressure distributions are computed with the N-S code for the low-amplitude oscillation ($\alpha = 10^\circ - 2^\circ \sin \omega t$) at a reduced frequency ($k = 0.1$). As in the steady flow computations, the Chen-Thyson transition model is used and the transition onset locations were specified during the up- and downstroke, as shown in Figure 6.27.

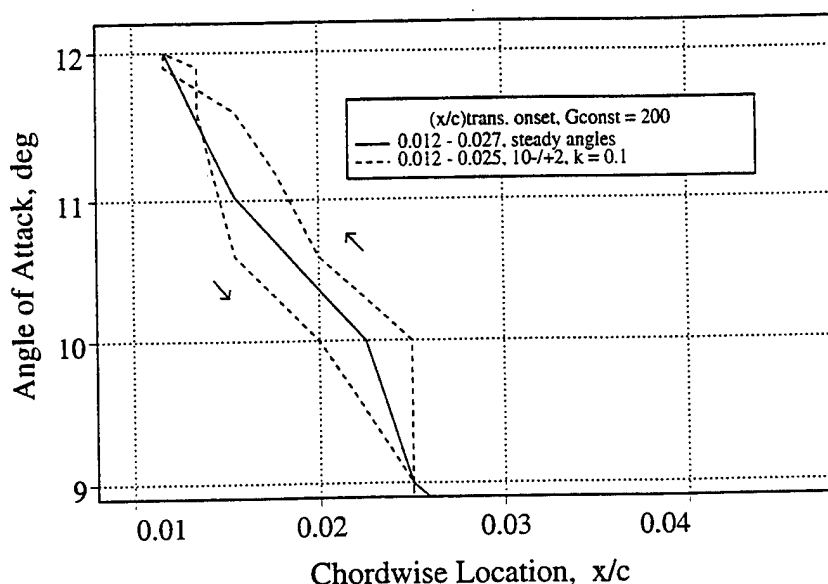
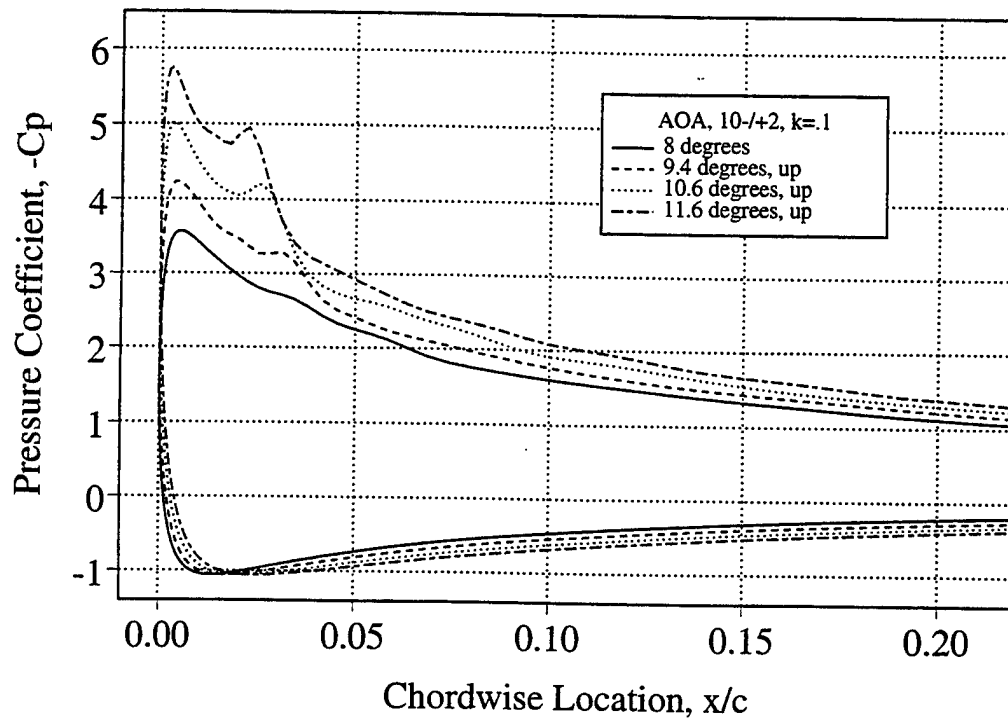
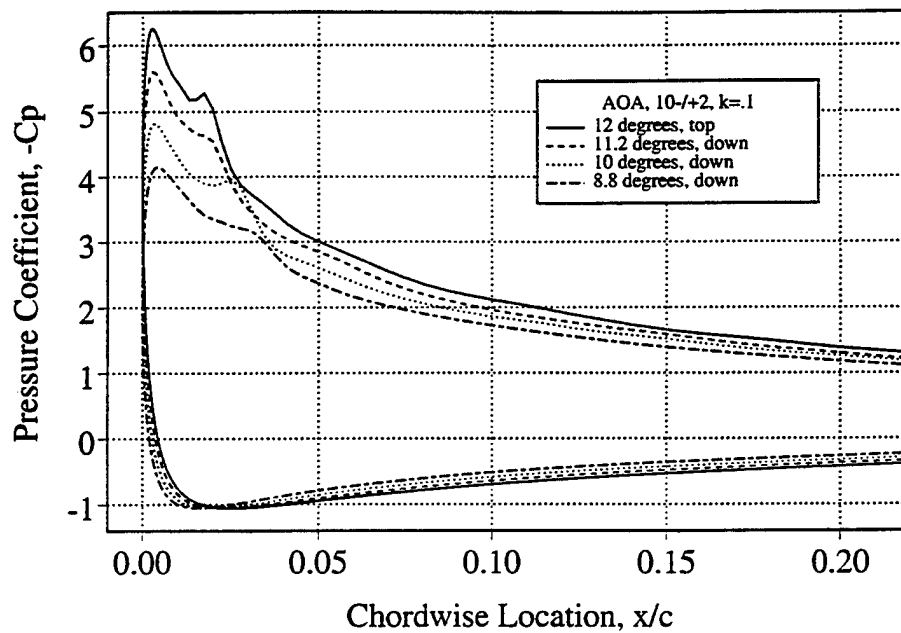


Figure 6.27. Transition Onset Locations for Steady and Oscillatory Airfoil Computations. $M_\infty = 0.3$, $\alpha = 10^\circ - 2^\circ \sin \omega t$, $k = 0.0$ and 0.1 , $Re = 540,000$.

A comparison of the N-S pressure distributions in Figure 6.28a and b with the potential flow computations in Figure 6.25a show that the inclusion of viscous and compressible flow effects produce significantly smaller suction peaks, ranging from -3.5 to -6.3 for the N-S results versus -4.3 to -8.25 for the UPOT results as the angle is changed from 8° to 12° . Similar to the steady flow results, the formation of a leading-edge separation bubble is clearly visible throughout most of the oscillation cycle, changing from a very small bubble at the bottom of the cycle at $\alpha = 8^\circ$ to a bubble that extends from about 1% of chord to 4% of chord at $\alpha = 10^\circ$ and then becomes somewhat smaller at the top of the cycle at $\alpha = 12^\circ$.



(a) $\alpha = 8^\circ$ (bottom), 9.4° , 10.6° , and 11.6° (up).



(b) $\alpha = 12^\circ$ (top), 11.2° , 10° , and 8.8° (down).

Figure 6.28. Unsteady Surface Pressure Coefficients Near the Airfoil Leading Edge (N-S Code, 275x81). $M_\infty = 0.3$, $\alpha = 10^\circ - 2^\circ \sin \omega t$, $k = 0.1$, $Re = 540,000$, $G_{\gamma_{tr}} = 200$.

If one overlays the computed results at $\alpha = 10^\circ$ for both the up- and downstroke as done in Figure 6.29, one sees that both the viscous and inviscid pressure distributions show the pressure lag effect.

In Chapter V, reference is made to the experimental flow visualization results, which clearly show the shedding of a vortex during the airfoil downstroke shortly after passing the top of the oscillation cycle. It is important to draw attention to the fact that the N-S computations similar to the UPOT calculations do not predict the vortex-shedding occurrence evident in the measurements on the airfoil downstroke, but rather indicate a gradual build-down of the separation bubble.

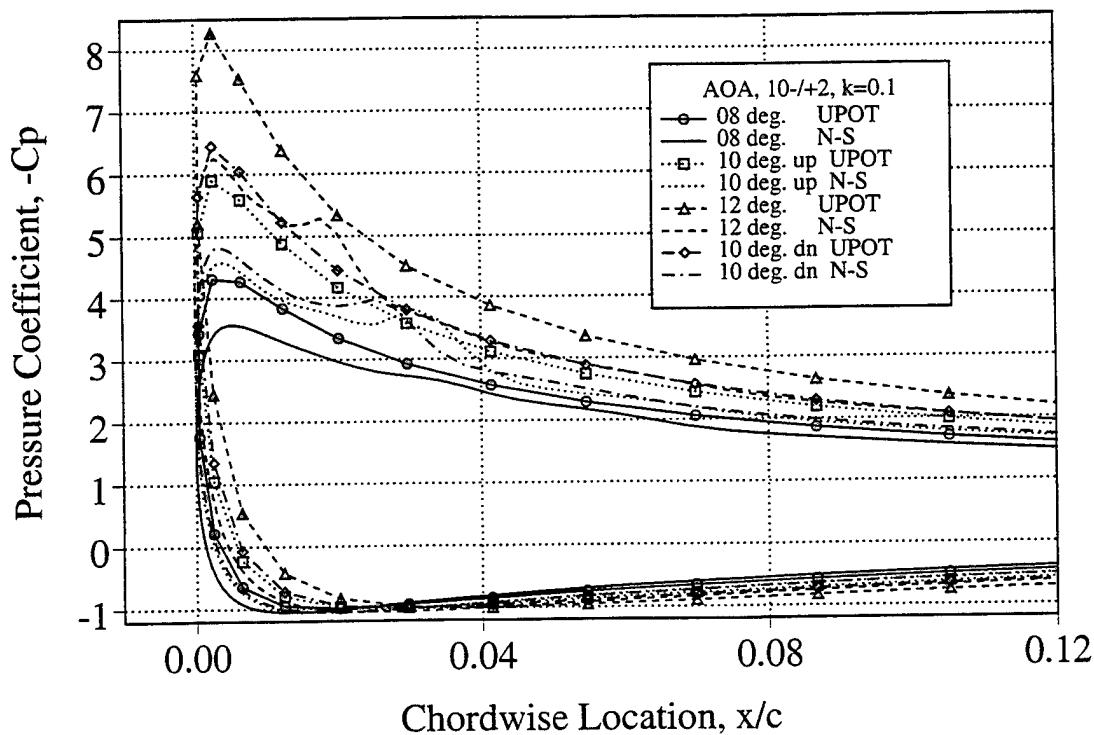


Figure 6.29. Unsteady Surface Pressure Coefficient Near the Airfoil Leading Edge (UPOT and N-S Codes). $\alpha = 10^\circ - 2^\circ \sin \omega t = 8^\circ$ (bottom), 10° (up / down), 12° (top), $k = 0.1$. N-S analysis, $M_\infty = 0.3$, $Re = 540,000$, $G_{\gamma_{tr}} = 200$.

4. N-S Skin-Friction Coefficients

Skin-friction coefficient predictions by the N-S code during the airfoil upstroke are given in Figure 6.30. The beginning of the negative C_f region moves forward on the airfoil surface with increasing angle of attack from $x/c = 0.025$ at $\alpha = 8^\circ$ to $x/c = 0.01$ at $\alpha = 11.2^\circ$. A minimum C_f of -0.0036 occurs at $x/c = 0.038$ and $\alpha = 8^\circ$, whereas at $\alpha = 11.2^\circ$, C_f reaches a minimum of -0.023 at $x/c = 0.028$. Positive C_f s are predicted again at $x/c = 0.054$ and $\alpha = 8^\circ$ and at $x/c = 0.50$ for $\alpha = 10^\circ$, which are downstream of the trailing edge of the predicted pressure plateaus. Thus, the lateral extent of negative C_f s over the airfoil surface is very similar in location to the measured separation bubble area.

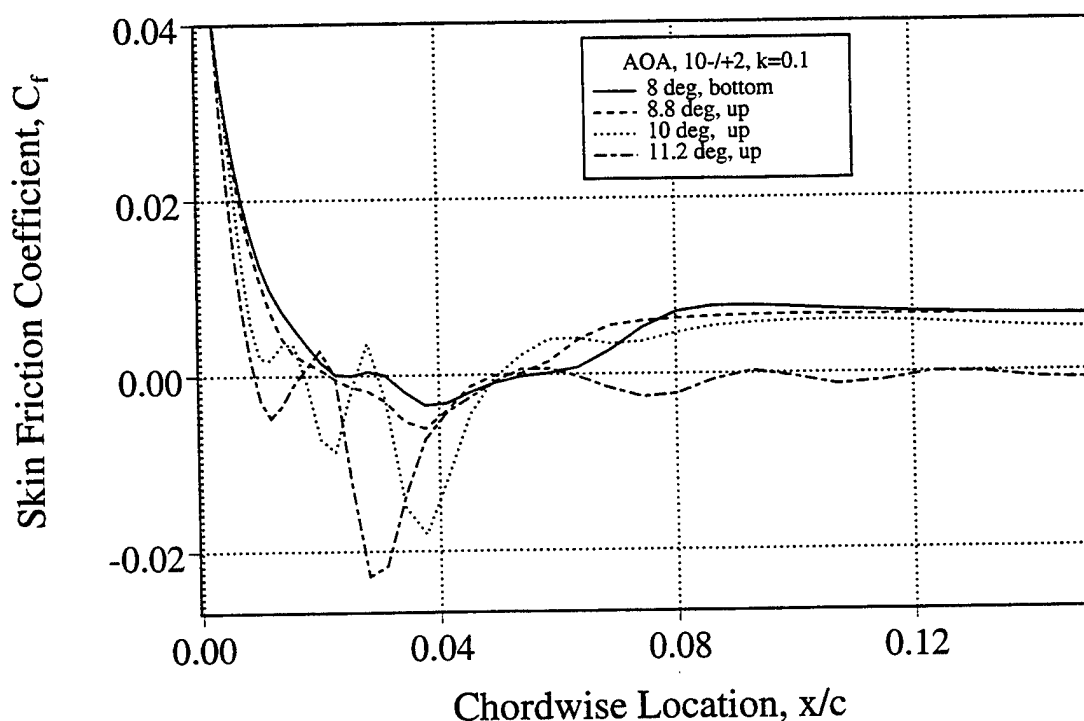


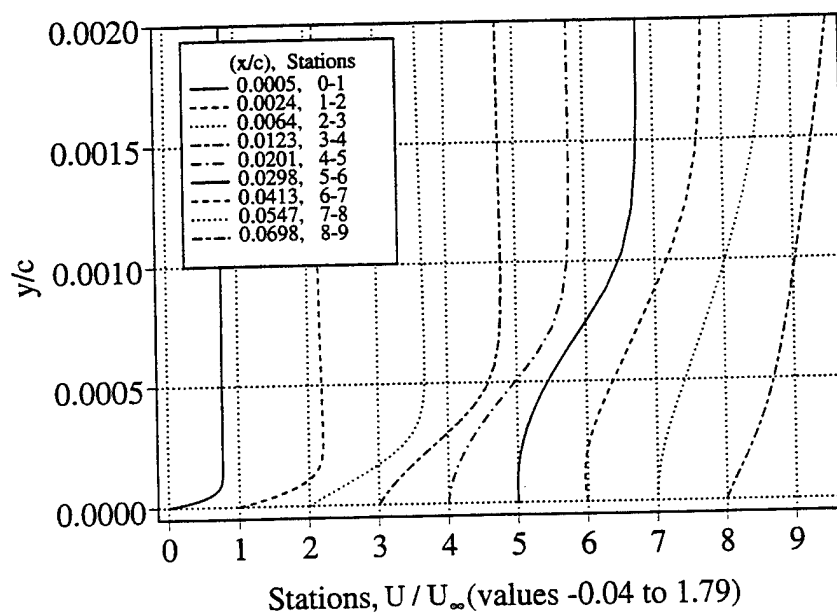
Figure 6.30. Skin-Friction Coefficient Distributions (N-S Code - 275x81). $M_\infty = 0.3$, $\alpha = 10^\circ - 2^\circ \sin \omega t = 8^\circ, 8.8^\circ(\text{up}), 10^\circ$ and $11.2^\circ(\text{up})$, $k = 0.1$, $Re = 540,000$, $G_{\gamma_{tr}} = 200$.

At $\alpha = 11.2^\circ$, C_f s oscillate between positive and negative values. In effect, the N-S code predicts multiple reverse flow regions or multiple leading edge vortices, which were not apparent in the experiments. In addition, the N-S code

does not predict the vortex-shedding process on the airfoil downstroke and, thus, no skin-friction distributions are given.

5. N-S Velocity Profiles

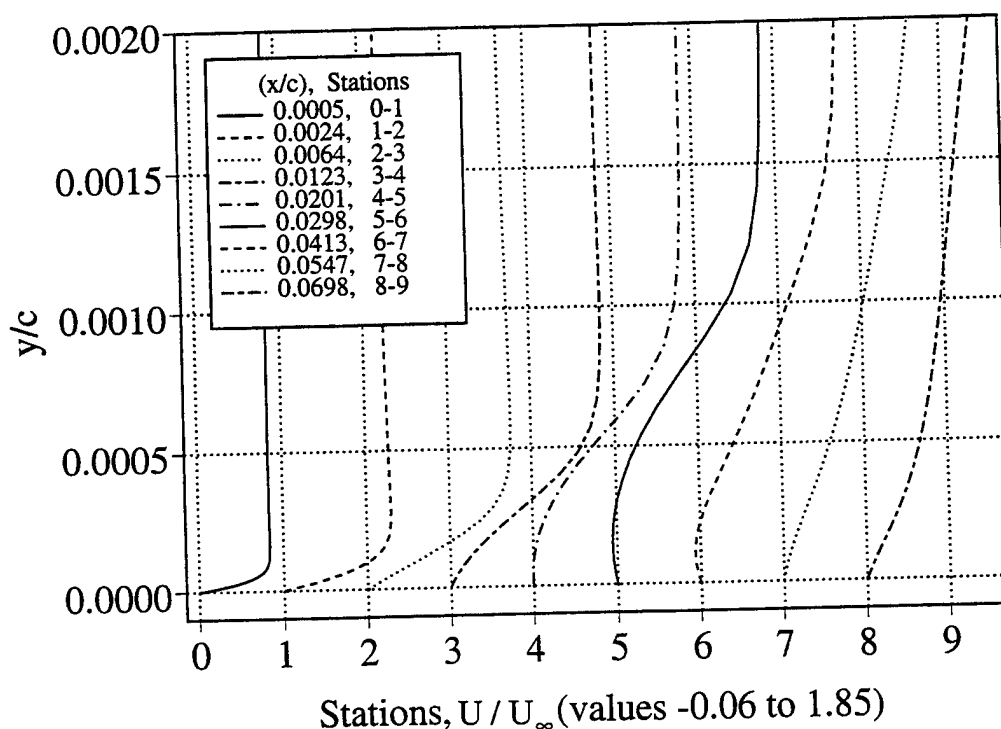
Velocity profiles are shown for only the airfoil upstroke because of the inability of the N-S analysis to predict the vortex-shedding and light dynamic stall process that was evident in the measured data. Unsteady velocity profile predictions from the airfoil leading edge to 7% chord in Figure 6.31a are similar to the steady results given previously at 8° angle of attack in Figure 6.18. This should not be surprising in light of the temporary zero pitch rate at the bottom of the oscillation cycle. The flow is predicted to reach slightly higher velocities ($1.79 U_\infty$ versus $1.77 U_\infty$) during airfoil upward motion at the same forward airfoil location of $x/c = 0.0123$. The unsteady airfoil motion lessens reverse flow predictions slightly ($-0.04 U_\infty$ vs. $-0.09 U_\infty$) at the same downstream (4.1%) chord location. Negative velocities are shown at two downstream locations ($x/c = 0.0298$ and 0.0413) versus three surface locations, including one node downstream for the steady angle of attack at 8° .



(a) $\alpha = 8^\circ$ (bottom).

Figure 6.31. Boundary-Layer Velocity Profiles (N-S Code, 275 x 81). $M_\infty = 0.3$, $\alpha = 10^\circ - 2^\circ \sin \omega t$, $k = 0.1$, $Re = 540,000$, $G_{\gamma_{tr}} = 200$.

Figure 6.31b gives velocity profiles for 8.8° (up) angle of attack. Comparing results with the predicted flow at the bottom of the oscillation cycle, the extent of negative velocities has increased slightly. Negative velocities are now shown one node forward on the airfoil surface at $x/c = 0.0201$, even though the specified transition onset location remained at $x/c = 0.025$. Therefore, the N-S analysis predicts a laminar flow separation at 8.8° angle of attack. The maximum flow velocity ($1.85 U_\infty$) was predicted at $x/c = 0.0123$ and $y/c = 0.001$. The maximum negative flow velocity ($-0.06 U_\infty$) was predicted at $x/c = 0.0298$ and $y/c = 0.00016$.

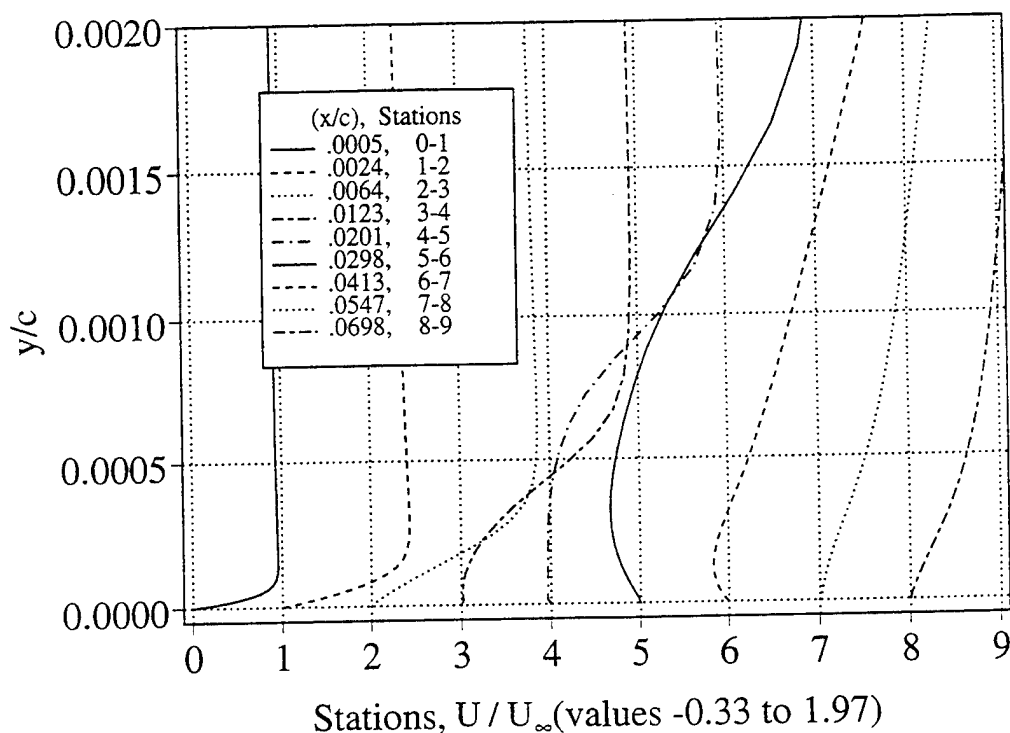


(b) $\alpha = 8.8^\circ$ (up).

Figure 6.31 (Contd.)

The velocity profiles for $\alpha = 10^\circ$ (up) are given in Figure 6.32a. Transition onset was specified at $x/c = 0.025$, which was slightly aft of the location used in steady flow analysis. Velocity profiles with inflection points and the extent of the negative velocity region are less than those predicted for the steady flow at 10° angle of attack, given previously in Figure 6.19. The negative velocity region

extends from $0.0201 < x/c < 0.051$ along the airfoil surface and to a lesser height of $y/c = 0.00079$ above the airfoil surface. Slightly higher velocities ($1.97 U_\infty$ versus $1.95 U_\infty$) than for the steady analysis occur at $x/c = 0.0201$ and $y/c = 0.00158$.

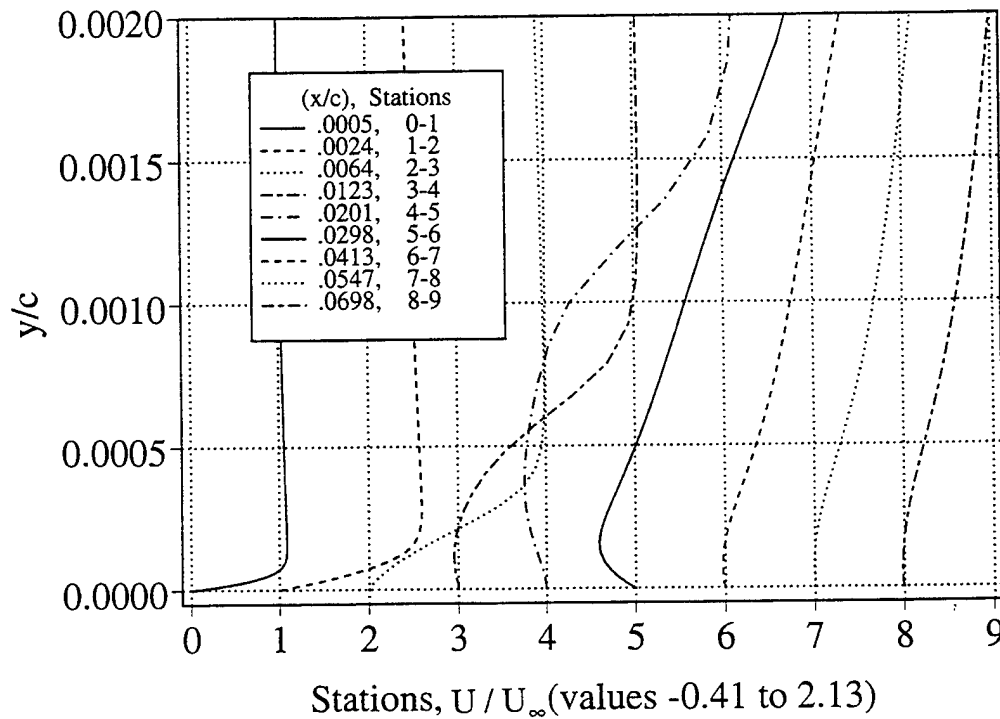


(a) $\alpha = 10^\circ$ (up).

Figure 6.32. Boundary-Layer Velocity Profiles (N-S Code - 275x 81). $M_\infty = 0.3$, $\alpha = 10^\circ - 2^\circ \sin \omega t$, $k = 0.1$, $Re = 540,000$, $G_{\gamma_{tr}} = 200$.

The transition onset location was moved forward to $x/c = 0.0177$ at 11.2° (up) angle of attack. Figure 6.32b shows that the predicted reverse flow region has broadened and moved forward on the airfoil surface compared with the results for $\alpha = 10^\circ$ in Figure 6.32a. At this angle of attack, the flow reached even higher velocities ($2.13 U_\infty$) in the boundary layer at 2% chord downstream and

$y/c = 0.0021$. A maximum negative velocity ($U/U_\infty = -0.41$) is predicted at $x/c = 0.0298$ and $y/c = 0.00016$. The negative velocity region extends from $0.01 < x/c < 0.08$ in the downstream direction and from $0.0 < y/c < 0.00077$ above the airfoil surface. Because of the low-frequency oscillation, a reasonable assumption is that the N-S velocity profiles predict a separation bubble from 1 to 8% chord along the surface and 0.2% chord in height above the airfoil surface.



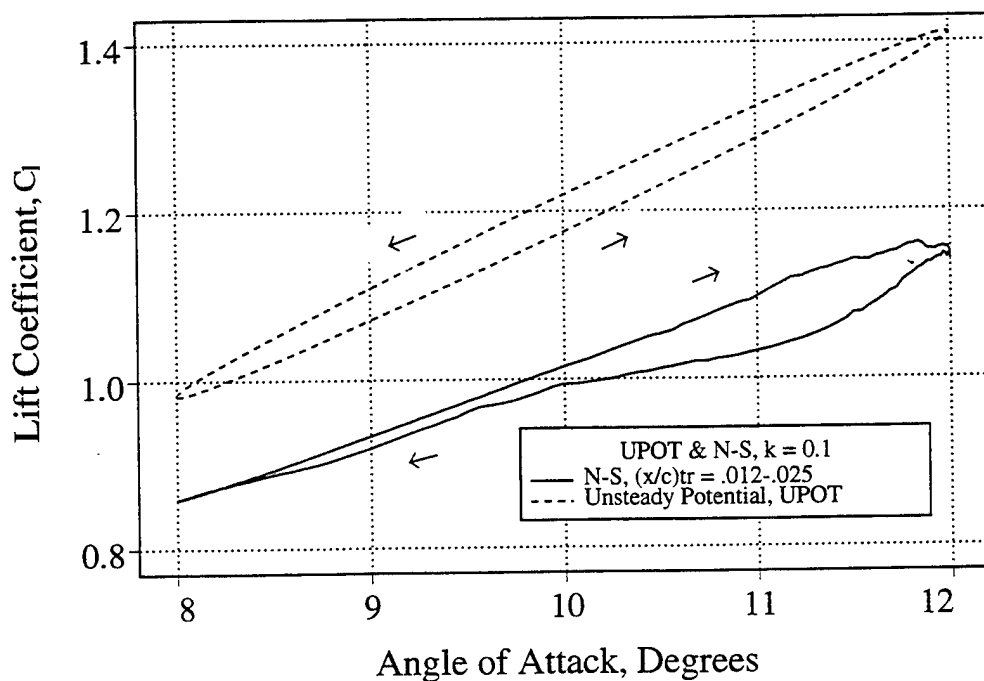
(b) $\alpha = 11.2^\circ$ (up).

Figure 6.32. (Contd.)

6. N-S Lift, Drag, and Moment

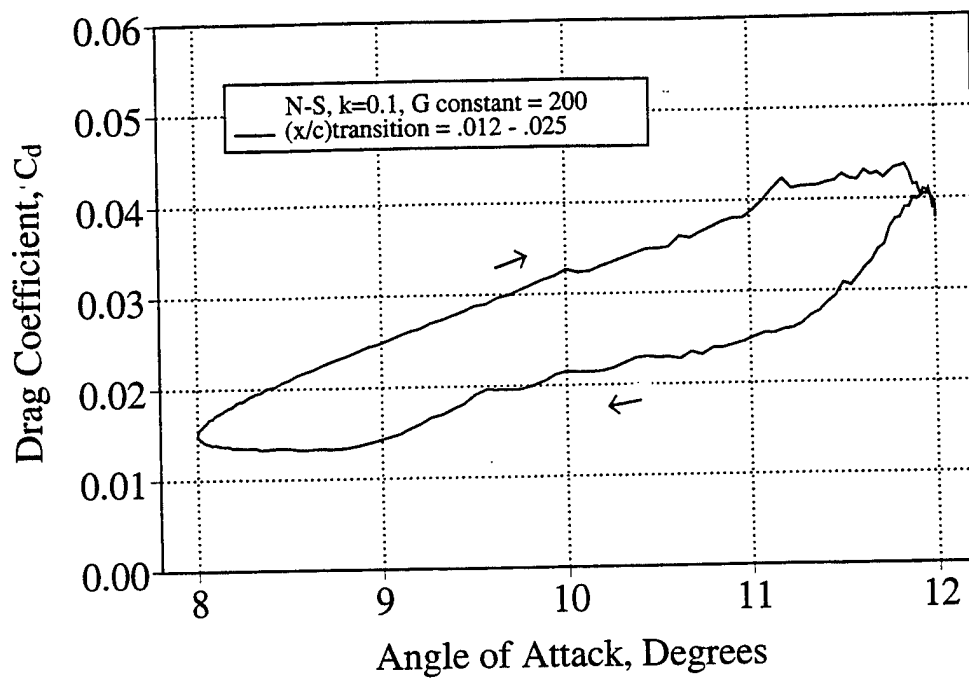
Airfoil section lift, drag, and pitching moment predicted by the N-S analysis during the oscillation cycle are given in Figure 6.33 a, b, and c. Transition onset was specified in the range from $0.012 \leq x/c \leq 0.025$ with forward movement at the higher angles of attack. Lift and pitching moment results from the UPOT code

are included in Figure 6.33a and c. It is seen that the N-S code predicts a clockwise lift curve progression with more lift predicted on the airfoil upstroke. In contrast, the potential flow code (UPOT) predicts a counterclockwise lift hysteresis loop. However, as expected, the N-S predicted lift levels are lower than the inviscid lift predictions, ranging from 11% to 17% less at the top of the oscillation cycle. The pitching moment predictions show counterclockwise loops, using either the N-S or UPOT codes. However, the viscous analysis exhibits positive values throughout the entire cycle. The N-S drag hysteresis loop is clockwise like the lift loop with more drag predicted during the airfoil upstroke and at the higher angles of attack. Since the focus of this work was in the separation bubble region near the airfoil leading edge, no PDI measurements were made for the entire region surrounding the airfoil surface to make comparisons with the predicted loads. However, future work could easily provide such comparisons.

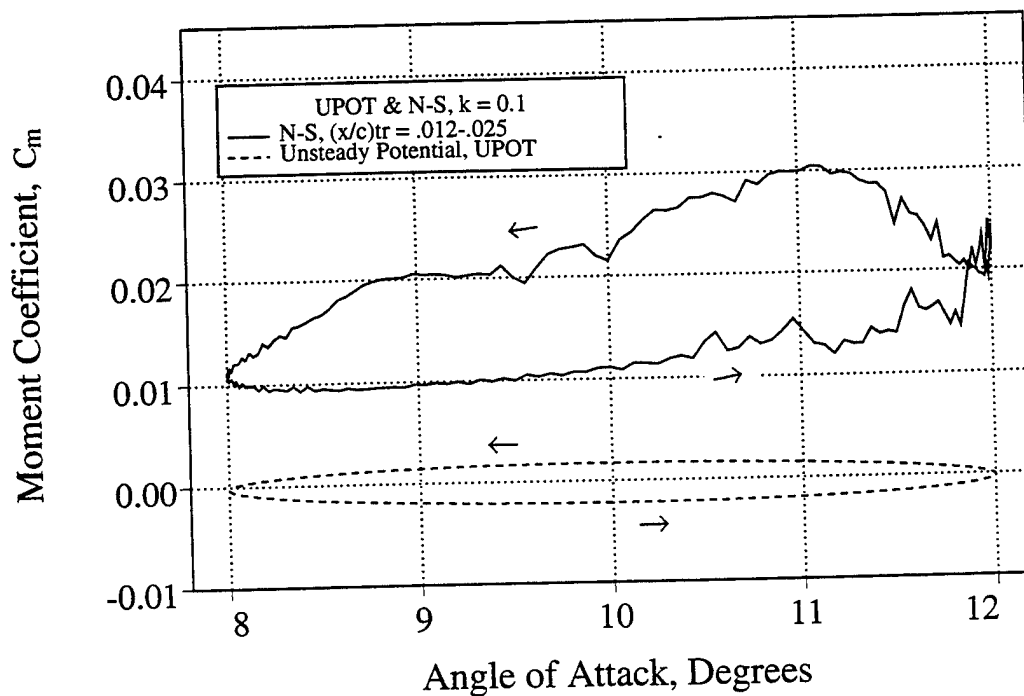


(a) Computed Lift, $\alpha = 10^\circ - 2^\circ \sin \omega t$, $k = 0.1$, $Re = 540,000$.

Figure 6.33. Unsteady Computed Lift, Drag, and Pitching Moment Coefficients (Panel/Boundary Layer and N-S Codes). N-S analysis, $M_\infty = 0.3$, $G_{\gamma_{tr}} = 200$.



(b) Computed Drag, $\alpha = 10^\circ - 2^\circ \sin \omega t$, $k = 0.1$, $Re = 540,000$.



(c) Computed Pitching Moment, $\alpha = 10^\circ - 2^\circ \sin \omega t$, $k = 0.1$, $Re = 540,000$.

Figure 6.33. (Contd.)

VII COMPARISONS OF MEASURED AND COMPUTED RESULTS

Laser-Doppler velocimeter (LDV) velocity data and Point Diffraction Interferometry (PDI) density contours with resultant pressure distributions are used to validate the computational methods. The flow considered for these comparisons is (1) compressible and in a transitional Reynolds number range, (2) predominated by a leading-edge separation bubble at higher angles of attack, and (3) undergoing light dynamic stall on the airfoil downstroke below the static stall angle of attack for the unsteady analysis.

The PDI and LDV measurements both showed the presence of a separation bubble and its subsequent bursting on the downstroke in light dynamic stall, pointing to the need for transitional flow analysis. The laminar separation bubble near the leading edge alters the flow characteristics considerably, as dynamic stall initiates from the bursting bubble as opposed to trailing-edge flow reversal.

In Chapter VI, the potential and boundary-layer analyses were found useful and comparable to the N-S results at the lower angles of attack. However, beginning at $\alpha = 8^\circ$ with a separation bubble present, (1) the boundary-layer code predicted only a limited amount of reverse flow and no solution at higher angles of attack, and (2) the potential code predicted excessive suction-pressure peaks and, of course, no separation bubble. Thus, the summary comparisons are made between the measurements and the N-S analysis, which accounts for the viscous, transition, turbulent, and compressible flow effects.

For the light dynamic stall case being considered, viscous effects in the direction normal to the airfoil surface are on the order of the airfoil thickness. Therefore, the prediction of the flow characteristics was performed by the thin-layer, compressible, Reynolds-averaged, N-S equation formulation.

The unsteady LDV and PDI measurements were among the first attempted and successfully made for the oscillatory cases that are presented in this study. The low-amplitude case with light dynamic stall gives an excellent data set for evaluation of the capability of computational schemes to predict the unsteady flow phenomena. The dynamic stall process is very complex, requiring a more in-

depth study of the underlying flow physics. To this end, the analysis is the first to critically evaluate the effect of transition onset locations and transition length on the flow physics as determined by making comparisons with experimental measurements for identical flow conditions.

A. INTRODUCTION

Two predominant factors were found to be critical in predicting separation bubbles that were similar to the measured ones. The two factors were (1) the transition onset location and (2) the flow transition length over the airfoil surface. As stated before, the Chen-Thyson transition length model [Ref. 20] was used in the present analysis, where flow intermittency is defined to change from 0 to 1.0 during transition from a fully laminar to fully turbulent flow. In the region of intermittency, turbulent spots appear with progression in the streamwise direction. For pressure distributions and skin-friction predictions that are in better agreement with the measurements, the transition length is changed by varying the value ($G_{\gamma_{tr}}$) in the formulation. The transition model is repeated here for completeness.

$$\gamma_{tr}(x) = 1 - \exp\left(-\frac{u_e^3}{G_{\gamma_{tr}} v^2}\right) \text{Re}_{x_{tr}}^{-1.34} (x - x_{tr}) \int_{x_{tr}}^x \frac{dx}{u_e} \quad (7.1)$$

The Chen-Thyson model had already been used successfully in conjunction with a viscous/inviscid interaction analysis method by Walker et al. [Ref. 30] to predict some features of a separation bubble on a low Reynolds number airfoil. The analysis predicted a separation bubble over a NACA 65-213 airfoil from 60 to 84% chord, which was similar to the experiments of Hoheisel et al. [Ref. 67] when the value was reduced to 40. The Chen-Thyson transition model was developed for high Reynolds number flows and specified a $G_{\gamma_{tr}}$ value of 1200. The analysis of the NACA 65-213 airfoil was done for an angle of attack of 0° and a Reynolds number of 240,000.

The second critical factor for obtaining numerical results comparable with the measurements is the proper location for transition onset. Michel's criterion, which was developed for attached flows at higher Reynolds numbers, is used

initially to estimate the transition onset location. Ekaterinaris et al. [Ref. 62] used Michel's criterion and Chen-Thyson's model with some success for a flow at a higher Reynolds number (4×10^6) with deep dynamic stall and a lightly stalled, lower Reynolds number flow [Ref. 58]. Excessive surface pressures were reported for potential and fully turbulent flow analysis, but flow transition consideration led to results more in line with the measurements. For flows at lower Reynolds numbers, transition onset locations were expected to be aft of Michel's prediction. Thus, transition onset locations were varied to give computed results that agreed best with the measurements.

The premise for this work is that if appropriate transition lengths and transition onset locations are found, then the physics of a leading-edge separation bubble could be described sufficiently and adequately. In this work, the sensitivity of the transition onset location and transition length parameters are tested by comparing computed results with the experimental measurements at angles of attack near the stall with substantial pressure gradients. Pressure distributions, skin-friction coefficients, and velocity profiles over the upper leading edge of the airfoil are shown to change substantially when slight changes are specified in location of transition onset and transition length.

B. STEADY FLOW RESULTS

1. Transition Onset and Length Effects

As an example of the effect of the $G_{\gamma_{tr}}$ value (in Equation 7.1) on the transition length, results are presented for $\alpha = 8^\circ$ with transition onset specified at $x/c = 0.04$ in Figure 7.1. The $\alpha = 8^\circ$ case was chosen because it was the starting point for the low-amplitude forced-oscillation calculations and it is also a moderate angle of attack for the steady flow analysis. Values were varied from 460, as computed by Cebeci's correlation formula (Equation 4.27), to 200 and then 50. The intermittency showed extreme sensitivity to changes in the value, reducing the transition length from 12% to less than 4% chord in the value range. The final value used in the analysis was chosen by observing resultant pressure and skin friction predictions that agreed best with the measurements, as shown in Figures 7.2 and 7.3.

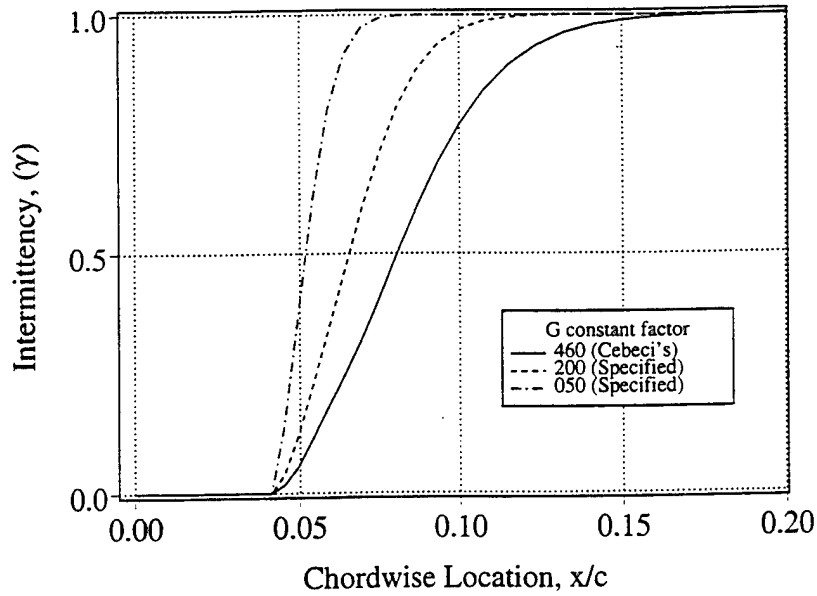


Figure 7.1. Effect of ($G_{\gamma_{tr}}$) Transition Value on Turbulence Intermittency Distribution. $M_{\infty} = 0.3$, $\alpha = 8^{\circ}$, $Re = 540,000$, $(x/c)_{tr} = 0.04$.

Pressure distributions and skin-friction coefficients are shown in Figure 7.2 for the previously stated conditions. As can be seen by the streamwise extent of negative skin-friction values, an order of magnitude change in the value from 460 to 50 greatly reduces the reverse flow ($-C_f$) region along the airfoil surface from 5.4% to 3.5% chord. For the smaller value of 50, the $-C_f$ region extends from $0.023 \leq x/c \leq 0.058$, whereas for 460, the $-C_f$ range is from $0.020 \leq x/c \leq 0.074$. Note that the C_f values are multiplied by 100 in the plots for better presentation. For all values of $G_{\gamma_{tr}}$, a laminar separation bubble is predicted. In each case, negative C_f s are shown forward of the specified transition onset location at $x/c = 0.04$. Additionally, higher values of $G_{\gamma_{tr}}$ give longer streamwise plateaus in the pressure distribution that are typical of flows with separation bubbles. However, values greater than 400 predicted early flow reattachment, secondary suction-pressure peaks, and skin-friction coefficients that become positive in a small range before again turning negative. By contrast, the experimental results do not show what is in effect a secondary separation bubble, or multiple leading-edge vortical structures. Thus, for the predictions, the $G_{\gamma_{tr}}$ value of 200 most closely matched the measurements.

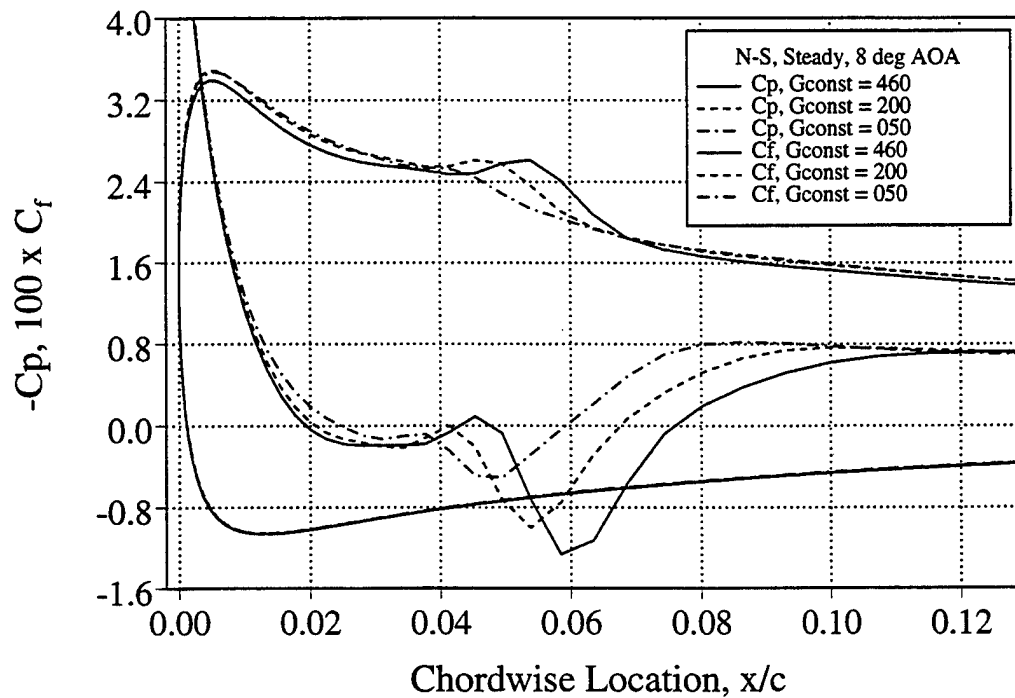


Figure 7.2. Effect of ($G_{\gamma_{tr}}$) Transition Value on Pressure and Skin-Friction Distributions. $M_{\infty} = 0.3$, $\alpha = 8^{\circ}$, $Re = 540,000$, $(x/c)_{tr} = 0.04$.

The effect of different transition onset locations on the flow are shown in Figure 7.3, using a $G_{\gamma_{tr}}$ value of 200 for the same flow at $\alpha = 8^{\circ}$. Choice of the forward transition onset location ($x/c = 0.03$) predicts a reverse flow region of 2.9% chord at the surface and a very slight pressure plateau, whereas a slightly aft transition onset location ($x/c = 0.04$) predicts a reverse flow region of 4.1% chord and a slight secondary pressure peak at the end of the plateau. The calculations at both transition onset locations predict a laminar-flow separation. On the other hand, Michel's criterion predicts transition onset at 2.5% chord (not shown) and a transitional-flow separation with a reverse-flow region from $0.027 \leq x/c \leq 0.051$. The predicted separation bubble in this case is very minute when compared with the experimental results. For transition onset locations that were

specified downstream on the airfoil surface ($x/c \geq 0.05$), the numerical scheme gave the formation of multiple vortical structures over the airfoil leading-edge region. In effect, laminar flow extended too far downstream such that large multiple non-physical reverse-flow regions were predicted. From the combined results shown in Figures 7.2 and 7.3, transition onset was specified at $x/c = 0.035$ and $G_{\gamma_{tr}}$ was set equal to 200 for $\alpha = 8^\circ$.

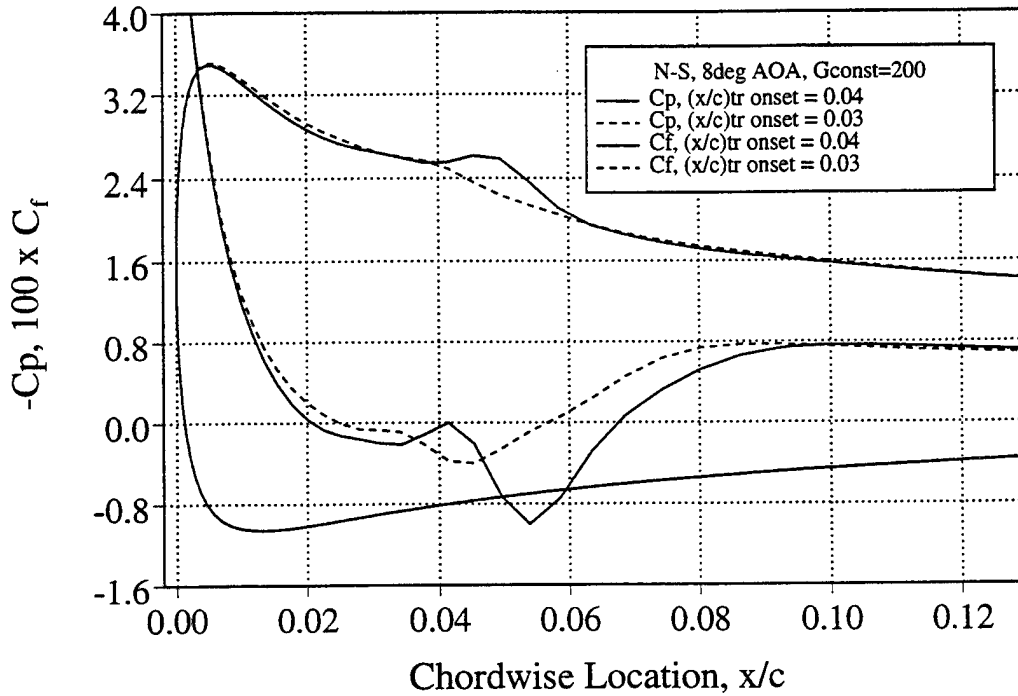


Figure 7.3. Effect of Transition Onset Location on Pressure and Skin-Friction Distributions. $M_\infty = 0.3$, $\alpha = 8^\circ$, $Re = 540,000$, $G_{\gamma_{tr}} = 200$.

2. Density Contour Comparisons

The next series of plots overlies computed and measured PDI density contours. The computed density ratio is ranged to give the same number of contours in the flow field and the same delta ($\rho/\rho_0 = 0.0085$) for each dark fringe to provide direct comparisons with the PDI measurements. Density ratios are noted at the intersections of selected equivalent measured and computed contours. The comparisons are shown in Figure 7.4 at $\alpha = 0^\circ$ with the stagnation point at the leading edge and a symmetry of contours about the airfoil. Eight

contours are shown in the flow field, with the lowest density ratio of 0.944 corresponding to a Mach number of 0.34 both over and under the airfoil leading edge surface. Even though complete agreement is not seen, all contours are within the one fringe uncertainty of the techniques.

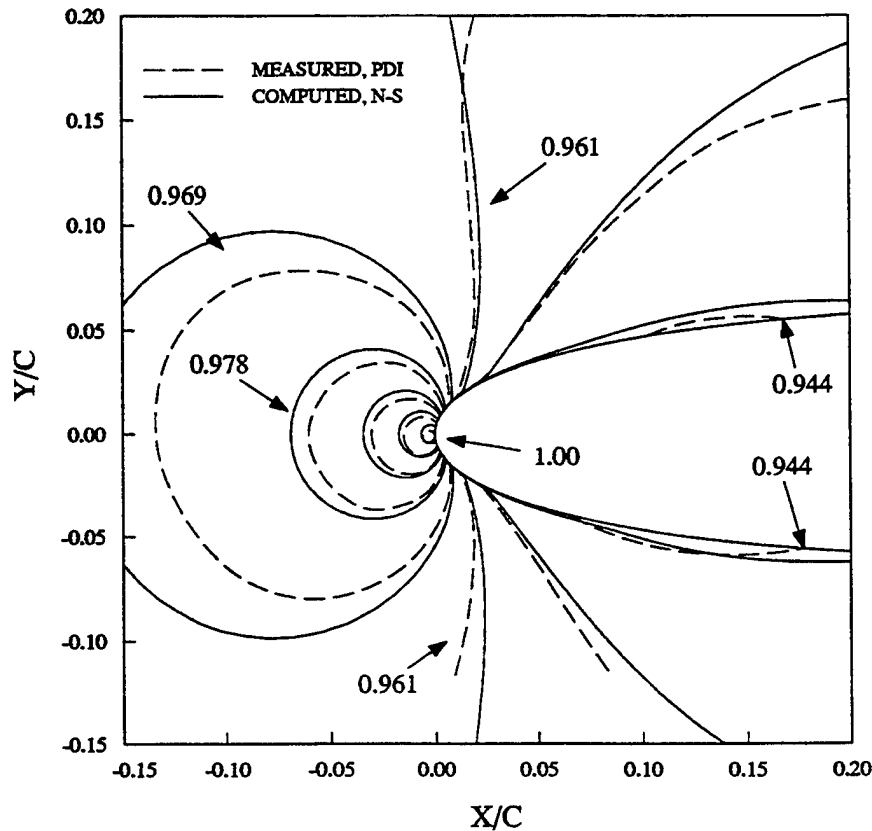


Figure 7.4. Computed and Measured Density Contours (PDI) Near the Airfoil Leading Edge. $M_\infty = 0.3$, $\alpha = 0^\circ$, $Re = 540,000$.

At $\alpha = 6^\circ$, Figure 7.5 shows that the stagnation point has moved under the leading edge of the airfoil and the number of density contours has doubled to 16 from the eight contours at $\alpha = 0^\circ$. The number of contours over the upper airfoil leading-edge surface has increased dramatically. The density contour previously lying on the upper airfoil surface at $\alpha = 0^\circ$ now extends vertically from the leading edge of the airfoil. The minimum flow field density ratio of 0.876 corresponds to a local Mach number of 0.52 over the airfoil leading edge surface. No separation bubble is indicated by either the measurements or computations, as all contours have a continuous and gradual curvature with the upper airfoil

surface. Computed contours converged forward of the measurements on the upper leading edge of the airfoil surface. Part of the reason for the differences was reported by Cho et al. [Ref. 68], resulting from the large density gradients at the airfoil leading-edge and optical distortions causing a slight downstream shift in the measured separation bubble.

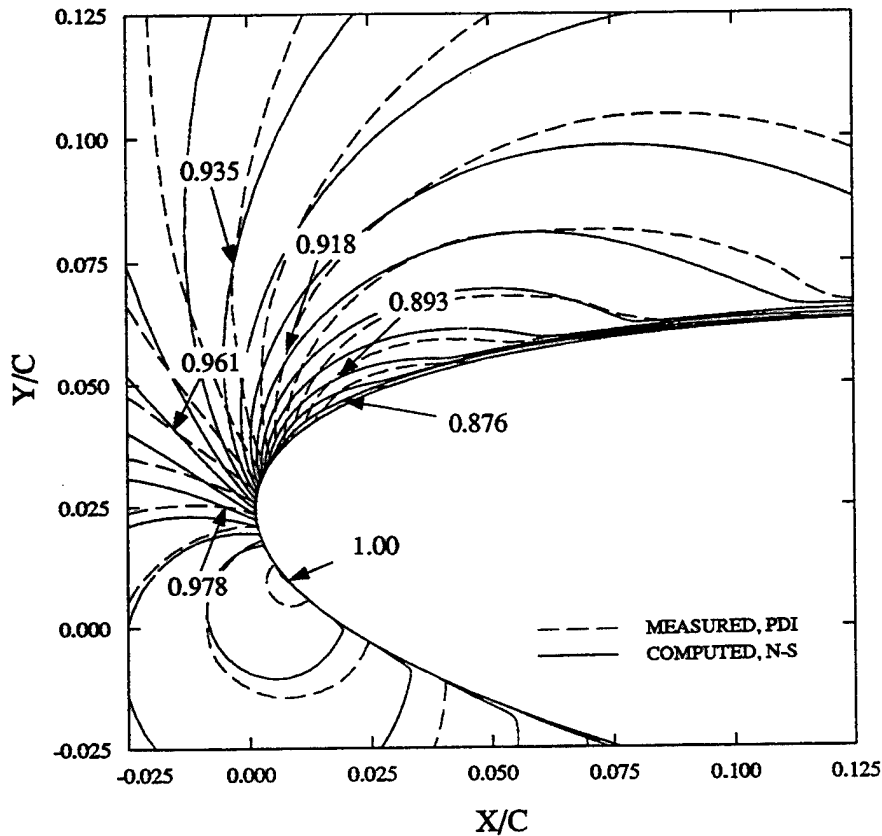


Figure 7.5. Computed and Measured Density Contours (PDI) Near the Airfoil Leading Edge. $M_\infty = 0.3$, $\alpha = 6^\circ$, $Re = 540,000$.

Figure 7.6 shows a comparison of density contours near the leading edge of the airfoil at $\alpha = 10^\circ$. A total of 27 density-flow-field contour levels corresponds to a highly accelerated flow over the leading edge to 2.39 times the free-stream Mach of 0.3 ($M = 0.72$). The formation of a separation bubble is clearly seen in the region where the density contours flatten (plateau) over the airfoil leading edge and then turn perpendicular towards the airfoil surface as was

described when discussing the PDI images. The flat plateaus in the measured contours extend to greater heights above the airfoil and extend further downstream over the airfoil surface than the predicted separation bubble. The measured separation bubble is estimated to extend from $0.01 < x/c < 0.06$ along the surface of the airfoil by including all contours that turn perpendicular to the airfoil surface near 5% chord. By using the same criteria, the height of the separation bubble is estimated to be $y/c = 0.02$. The overall lateral extent of both measured and computed separation bubbles is similar, remaining within the one fringe uncertainty. However, the predicted separation bubble is again slightly forward on the airfoil surface.

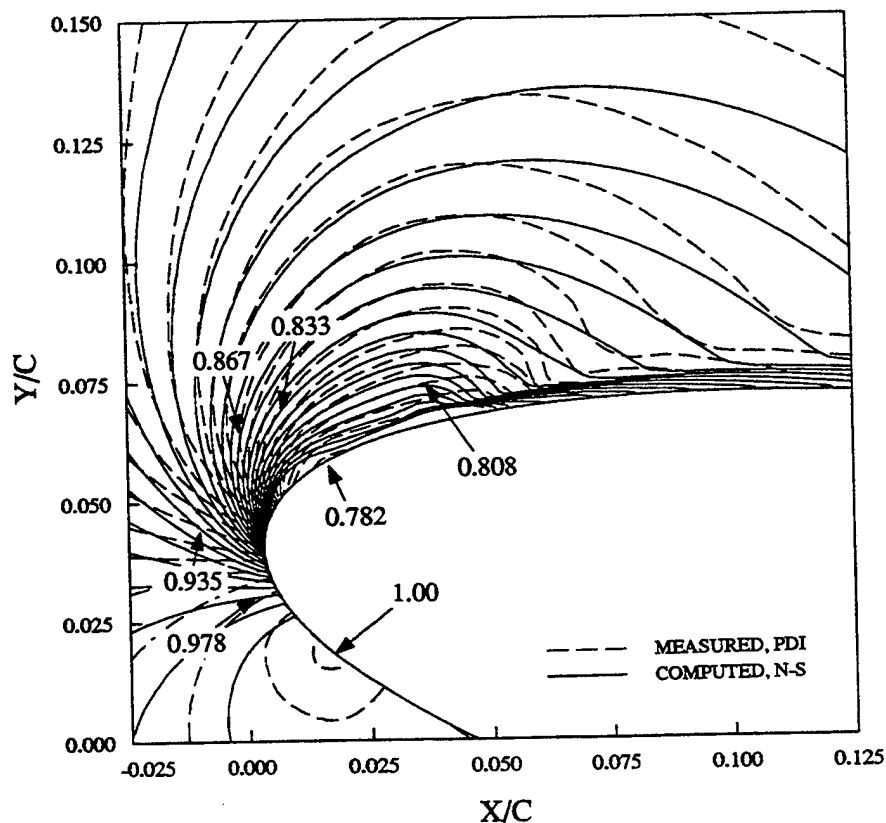


Figure 7.6. Computed and Measured Density Contours (PDI) Near the Airfoil Leading Edge. $M_\infty = 0.3$, $\alpha = 10^\circ$, $Re = 540,000$.

As the angle of attack increases from 10° to 11.9° , the density contour picture does not change significantly, as shown in Figure 7.7. However, the boundary layer thickens slightly aft of the separation bubble and both measured and computed separation bubbles extend to greater heights above the airfoil

surface. The PDI measurements now show six contours as opposed to five turning perpendicular to the airfoil surface at their downstream edges. Now a two-fringe disparity exists between the measurements and computations at some locations in the flow field.

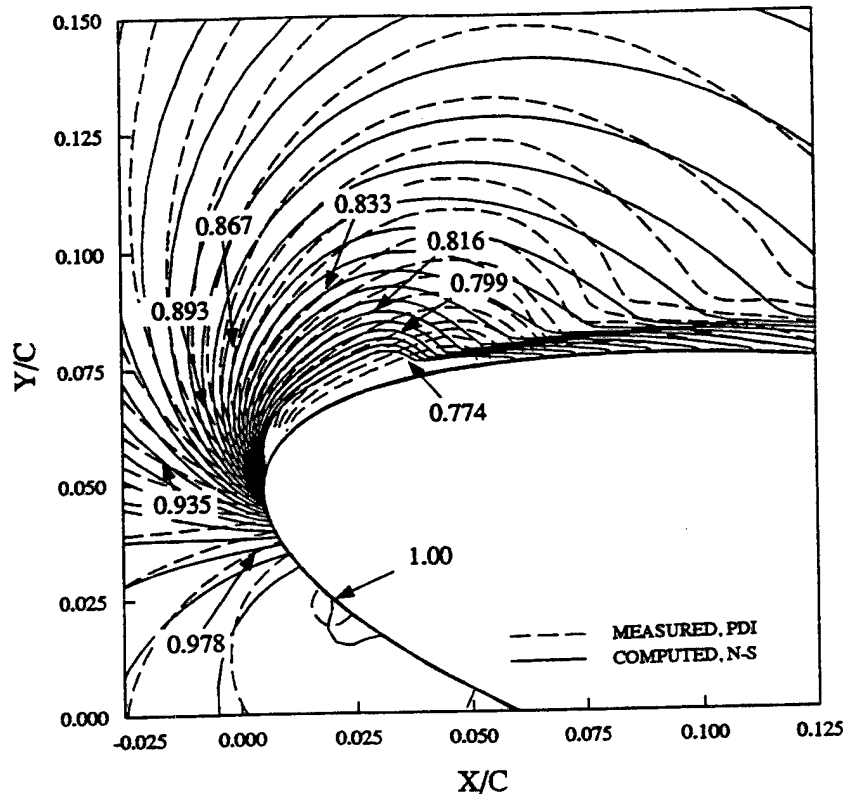


Figure 7.7. Computed and Measured Density Contours (PDI) Near the Airfoil Leading Edge. $M_\infty = 0.3$, $\alpha = 11.9^\circ$, $Re = 540,000$.

3. Pressure Distribution and Skin-Friction Comparisons

Figure 7.8 shows a comparison between PDI derived and computed pressure coefficient distributions at $\alpha = 6^\circ$ in steady flow. For this angle of attack, as previously stated, no separation bubble was found in the measurements. Likewise, the computed skin friction remains positive and thus, predicts no separation bubble. The pressure distributions agree very well with each other.

Differences are well within the experimental and computational uncertainties with transition onset specified at $x/c = 0.04$ and a transition length value of 200.

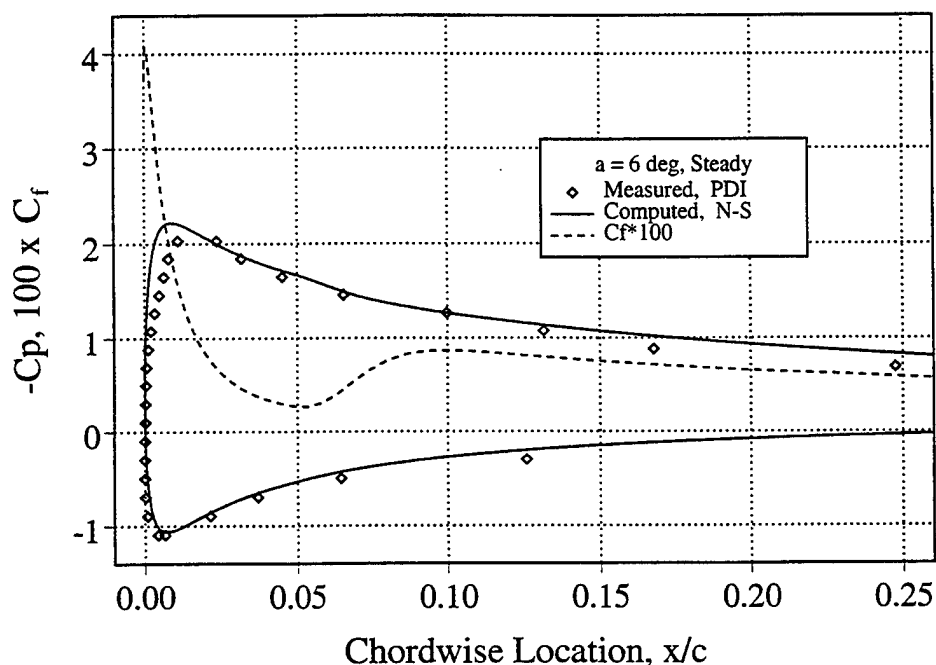


Figure 7.8. Computed and PDI Derived Pressure Distributions Near the Airfoil Leading Edge. $M_\infty = 0.3$, $\alpha = 6^\circ$, $Re = 540,000$, $(x/c)_{tr} = 0.04$, $G_{\gamma_{tr}} = 200$.

In Figure 7.9, a steady-flow solution is given for $\alpha = 8^\circ$ with a specified transition onset location of $x/c = 0.035$. The measured suction-pressure peak is slightly lower than the computed value and the extent of the predicted pressure plateau is less than the measurements. However, the end of the separation bubble cannot be precisely determined from the pressure distributions alone, as previously reported by Gaster [Ref. 15] and Tani [Ref. 5]. The start of predicted flow separation as determined by the region of negative skin-friction coefficient agrees well with the start of the measured pressure plateau. Negative C_f s are indicated at $x/c = 0.028$, which is forward of transition onset, and therefore, a laminar flow separation is predicted. In addition, C_f s become positive at 5.9%

chord, indicating the downstream end of the reverse flow region that nearly coincides with the measured pressure recovery location at 6% chord, confirming agreement between the two data sets.

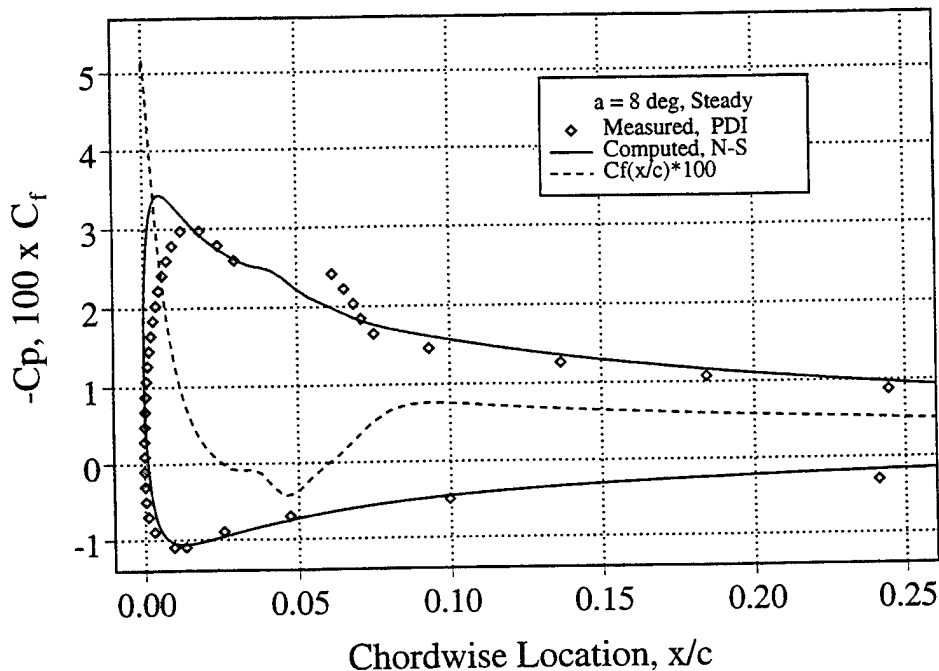


Figure 7.9. Computed and PDI Derived Pressure Distributions Near the Airfoil Leading Edge. $M_\infty = 0.3$, $\alpha = 8^\circ$, $Re = 540,000$, $(x/c)_{tr} = 0.035$, $G_{\gamma_{tr}} = 200$.

Similar results can be seen in Figure 7.10 for $\alpha = 10^\circ$ with transition onset set at $x/c = 0.023$. Here, the computed pressure distributions (C_p) show a second rise and a subsequent fall (secondary-separation bubble), and the extent of the pressure plateau again is smaller than that seen in the measurements. The measured suction-pressure peak is downstream of the predictions, partially because of the optical distortions stated earlier, however, the pressure values are within the one-fringe uncertainty. The extent of the reverse-flow region indicated by negative skin-friction coefficients gives good agreement for the separation-bubble length, and again, a laminar separation is predicted by the computations.

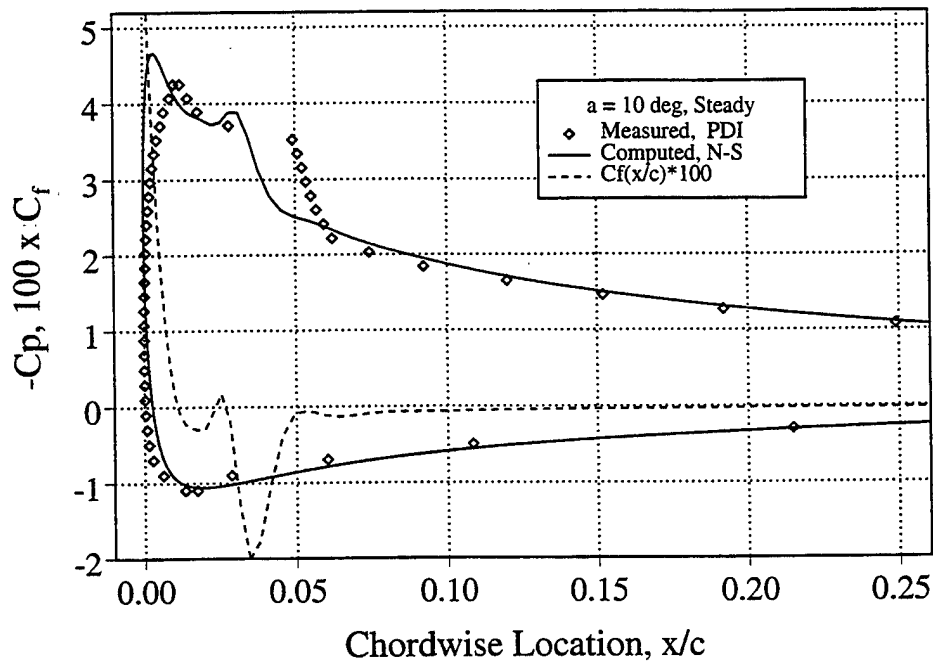


Figure 7.10. Computed and PDI Derived Pressure Distributions Near the Airfoil Leading Edge. $M_\infty = 0.3$, $\alpha = 10^\circ$, $Re = 540,000$, $(x/c)_{tr} = 0.023$, $G_{\gamma_{tr}} = 200$.

Figure 7.11 gives an interesting comparison of computed pressures with the stalled airfoil PDI results at $\alpha = 12^\circ$ by specifying transition onset between $0.012 \leq x/c \leq 0.017$. The experiment showed that $\alpha = 12^\circ$ was the borderline stall angle of attack for a 0.3 Mach number flow. The unsteady nature of flow separation at stall onset gave flows that were intermittently stalled or attached with large levels of suction pressures. For the case of transition onset at $x/c = 0.012$ and a transition length value of 200, the computations reproduced the stalled experimental results. Slight changes in the transition onset location and a lower transition length value of 100 gave a completely attached flow with high levels of suction. Thus, the numerical modeling with a simple transition model

appears to adequately represent the physical flow in the wind tunnel for steady angle of attack analysis. However, the oscillations in the pressure distribution near the leading edge are incorrect predictions of multiple vortical structures.

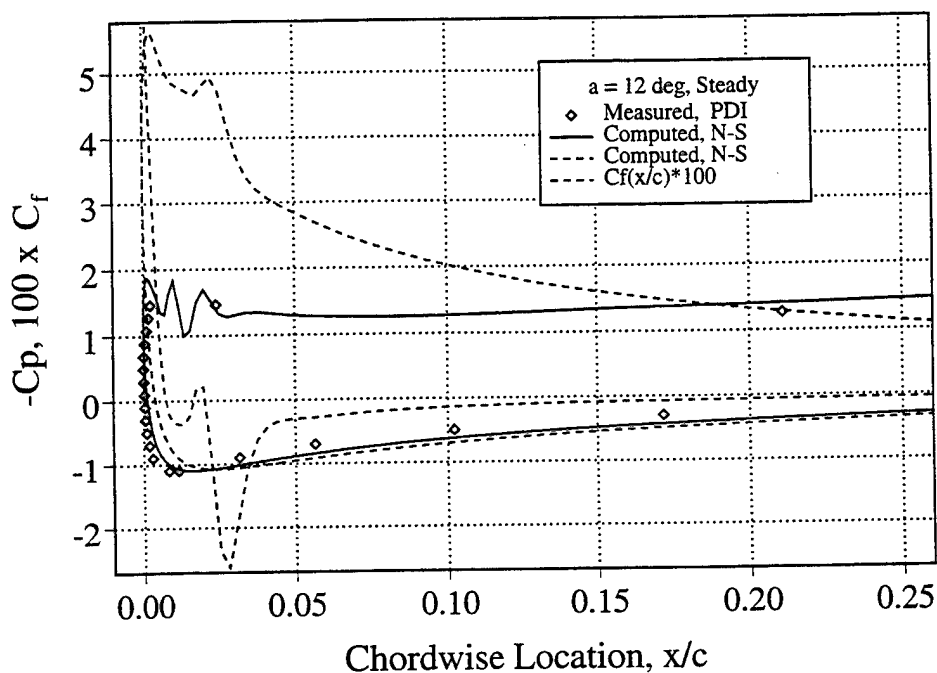


Figure 7.11. Computed and PDI Derived Pressure Distributions Near the Airfoil Leading Edge. $M_\infty = 0.3$, $\alpha = 12^\circ$, $Re = 540,000$, $(x/c)_{tr} = 0.012$, $G_{\gamma_{tr}} = 200$.

As steady angles of attack are increased from 6° to 12° in the previous solutions, the streamwise transition length is greatly reduced. Figure 7.12 shows that at $\alpha = 6^\circ$ the transitional flow intermittency range is predicted to extend from 4% to 12% chord, but at $\alpha = 12^\circ$ the intermittency range extends only from 1.7% to 4% chord. For calculations giving the best agreement with the measurements, Figure 7.12 also shows the upstream progression of the specified transition onset locations with increasing angles of attack. In reviewing Equation 7.1, the predominant term causing a reduced transition length at higher angles of attack is the larger boundary-layer edge velocity. The other factors in the equation are

either constant or shrinking in size with increasing angles of incidence, which would extend the transition length.

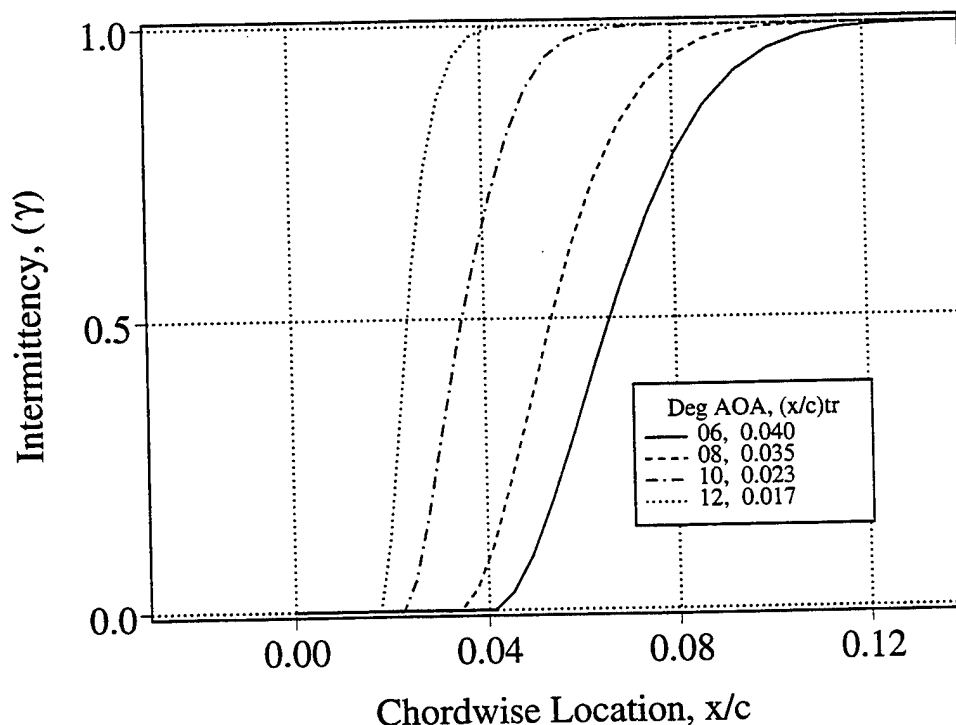


Figure 7.12 Angle-of-Attack Effect on Intermittency, Transition Onset Specified. $M_\infty = 0.3$, $Re = 540,000$, $G_{\gamma_{tr}} = 200$.

4. Velocity Profile Comparisons

Computed and measured U-component velocities are compared for angles of attack of 8, 10, and 12°. In each case, velocity profile comparisons begin at $x/c = -0.167$, which is 0.5 inch forward of the airfoil leading edge, and then proceed over the leading edge of the airfoil from $0.0 \leq x/c \leq 0.167$ in 0.033 chord length intervals. In the plots, both the measured and computed U velocities are normalized by the velocity (U_0) at $y/c = 0.167$. An interpolation scheme was used to predict computed velocities at the nodes of the measurement grid. Only the positive computed velocities are shown close to the airfoil surface, whereas the measured velocities are restricted to some distance above the airfoil because of laser-beam blockage. For all angles of attack, measured and computed

velocities forward of the airfoil at $x/c = -0.167$ are in full agreement and give the same trend with slight velocity reductions at lower heights.

Normalized velocities at 8° angle-of-attack range from 0.0 to 1.42, as shown in Figure 7.13. The maximum computed velocity in the flow field is at $x/c = 0.033$ near the airfoil surface. The maximum measured velocity is aft at $x/c = 0.067$, most likely because of the measurement height restriction. All computed and measured profiles for $x/c \geq 0.067$ are essentially in full agreement. Measured values at $y/c < 0.0117$ above the leading edge of the airfoil are less than the computed values, but are within the accuracy of the LDV system.

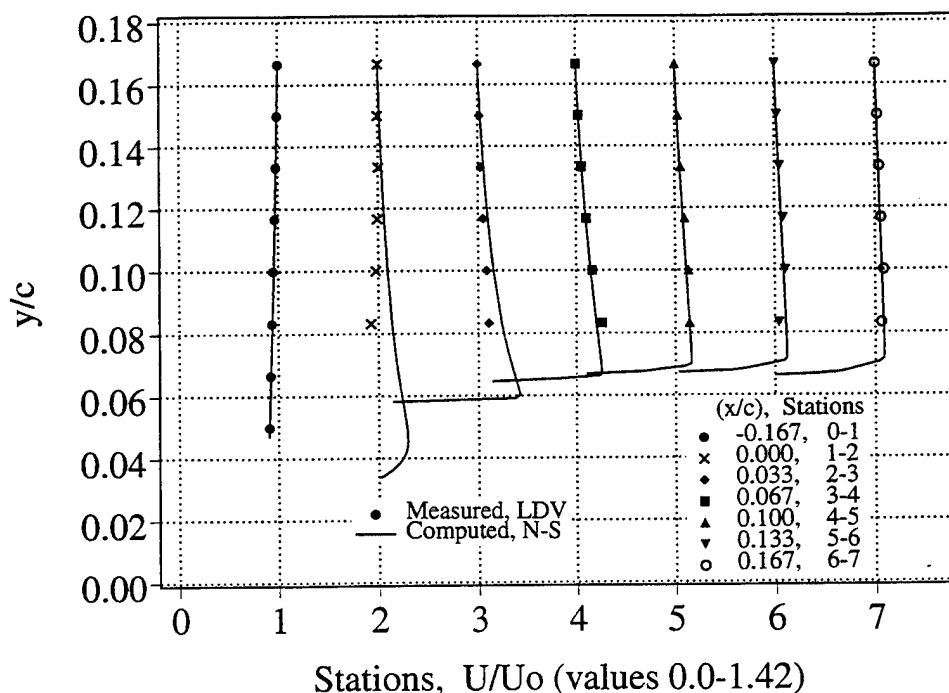


Figure 7.13. Computed and Measured Velocity Profiles Near the Airfoil Leading Edge. $M_\infty = 0.3$, $\alpha = 8^\circ$, $Re = 540,000$.

Comparisons for 10° angle of attack are shown in Figure 7.14. Maximum velocities have increased slightly to $1.54 U_o$, occurring at locations similar to those at 8° angle of attack. Agreement between the data sets is even better than at the lower angle of attack, but the measurements in this case were

restricted to a higher location ($y/c = 0.100$) above the airfoil surface. Maximum computed and measured differences are $<2\%$ over the airfoil surface. Again, slight differences are seen at the airfoil leading edge and the lowest measurement height, where measurements tended to be lower than the computations.

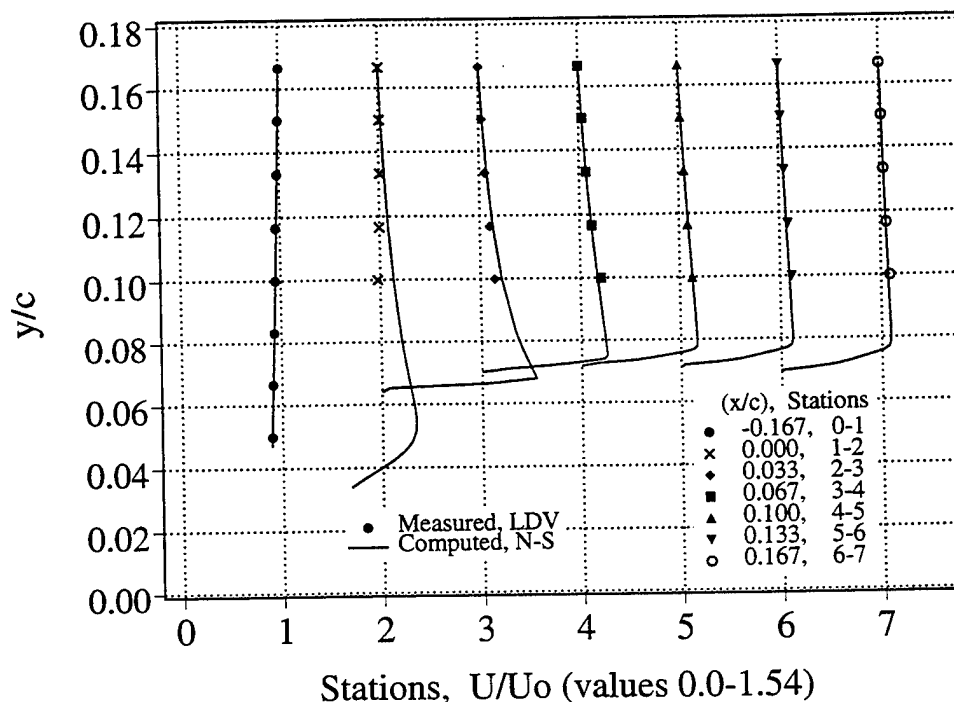


Figure 7.14. Computed and Measured Velocity Profiles Near the Airfoil Leading Edge. $M_\infty = 0.3$, $\alpha = 10^\circ$, $Re = 540,000$.

For 11.95° angle of attack in Figure 7.15, the data comparison region above the airfoil surface is essentially the same as for the previous case at 8° angle of attack. Velocities over the airfoil have increased slightly to $1.62 U_o$, and agreement between the data sets is excellent ($<1\%$). Again, at the lowest measurement height near the airfoil leading edge, slight differences are seen. Because of LDV measurement system limitations, the PDI method was also used to make a better assessment of the extent of the leading-edge separation bubble.

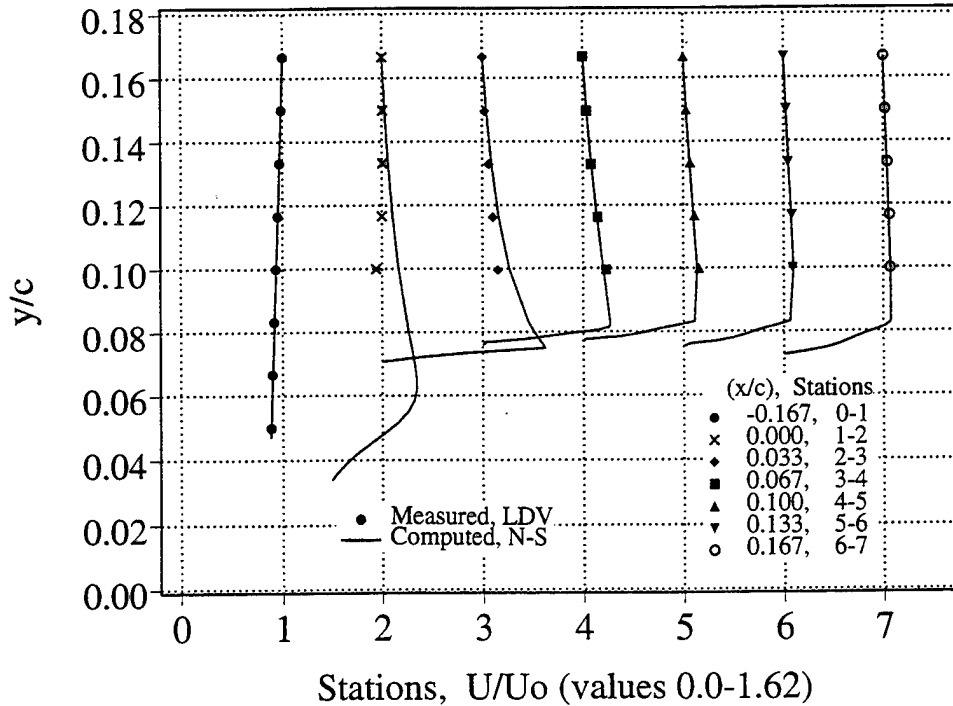


Figure 7.15. Computed and Measured Velocity Profiles Near the Airfoil Leading Edge. $M_\infty = 0.3$, $\alpha = 11.95^\circ$, $Re = 540,000$.

C. OSCILLATING AIRFOIL FLOW ($\alpha = 10^\circ - 2^\circ \sin \omega t$, $k = 0.1$)

The PDI image in Figure 5.20d at 11.5° angle of attack (down) verified a light dynamic stall and the vorticity shedding process over the airfoil surface during the downstroke of the low-amplitude oscillating airfoil flow. Rapid flow reattachment occurs as evidenced by the flow picture in Figure 5.20e at 10.5° angle of attack on airfoil downward motion. Only the N-S analysis method adequately modeled separation bubble formation and development (the focus of this work) at the higher angles of attack over the airfoil leading edge. Thus, only N-S and experimental data comparisons and summary analysis are given for the low-amplitude oscillations ($M_\infty = 0.3$, $\alpha = 10^\circ - 2^\circ \sin \omega t$, $k = 0.1$, $Re = 540,000$). In addition, oscillating airfoil results are given only for airfoil upward motion at angles of attack less than 11.5° because of the limited number of validated LDV samples at higher angles of incidence and an inability of the analysis to predict light dynamic stall during the airfoil downstroke.

1. Density Contour Comparisons

As a result of optical path length differences, the dark and light fringes that were recorded on film represent density contours in the flowfield. Again, the computed density ratio is ranged to give the same number of contours in the flow field and the same delta for each dark fringe (0.0085) as for the PDI measurements to make direct data comparisons. Thus, the figures give a direct comparison of computed and measured fringe locations in the vicinity of the separation bubble. Density ratios are noted in the flow field at intersections of selected equivalent measured and computed contours.

Computed and measured density contours are overlaid for $\alpha = 8^\circ$ angle of attack (bottom of the oscillatory cycle) in Figure 7.16. There are 23 density contour levels shown (one less than for $\alpha = 8^\circ$ steady) with a peak Mach number of 0.65 over the upper surface of the airfoil. The predicted or computed contours in the separation bubble region are shifted forward of the measurements on the airfoil surface. The trailing edge of the measured contours turn abruptly toward the airfoil surface between 6% and 8% chord downstream, converging with the airfoil surface 0.7% to 1.7% chord downstream of equivalent computed contours. The computed contours converge more gradually with the airfoil surface at the trailing ends, predicting a less defined separation bubble. Computed contours begin 0.9% to 1.3% chord forward of the measured contours in an estimated separation bubble region from 1% to 8% chord downstream. Measured density contours extend 0.8% chord higher above the airfoil surface than the predicted contours.

Computed and measured density contours are presented for $\alpha = 8.8^\circ$ (up) in Figure 7.17. Contour levels (25) are shown with a minimum density ratio in the flow field of 0.799, which corresponds to a peak local Mach number of 0.68 over the airfoil surface. The measured contours parallel the airfoil surface for some distance downstream of the suction peak and then turn even more abruptly toward the airfoil surface at the trailing ends between 6% and 8% chord downstream. In the separation bubble region, computed contours begin 0.7% to

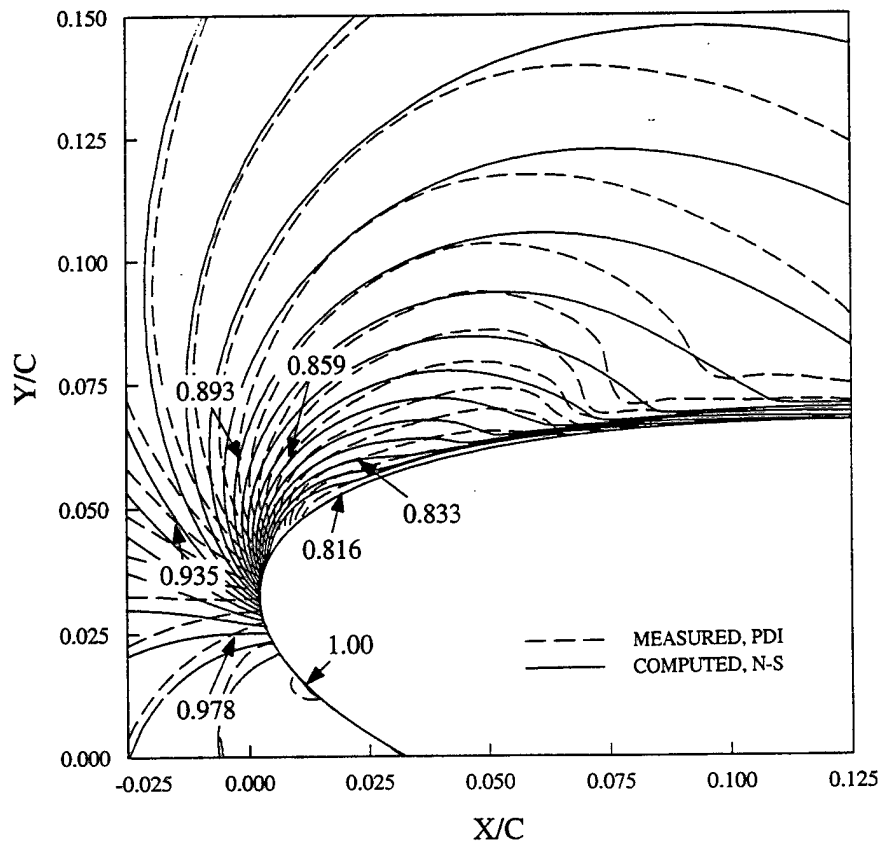


Figure 7.16. Computed and Measured Density Contours (PDI) Near the Airfoil Leading Edge. $M_\infty = 0.3$, $\alpha = 10^\circ - 2^\circ \sin \omega t = 8^\circ$, $k = 0.1$, $Re = 540,000$, $(x/c)_{tr} = 0.025$, $G_{\gamma_{tr}} = 200$.

1.0% chord forward of equivalent measured contours, and the trailing ends converge with the airfoil surface as much as 2% chord forward of the measured contours. Also, measured contours are as much as 2% chord greater in height above the airfoil surface than equivalent predicted contours.

Figure 7.18 compares density contours at $\alpha = 10^\circ$ (up). A total of 24 contours indicates that the flow reaches 2.23 times ($M = 0.67$) the free-stream Mach number. The formation of a separation bubble is shown in the region along the airfoil surface between $0.01 < x/c < 0.07$, where both measured and computed density contours flatten over the airfoil surface and then turn almost perpendicular to the airfoil surface at the downstream ends. At this angle of attack, the flat plateaus in the measured contours extend to only slightly greater

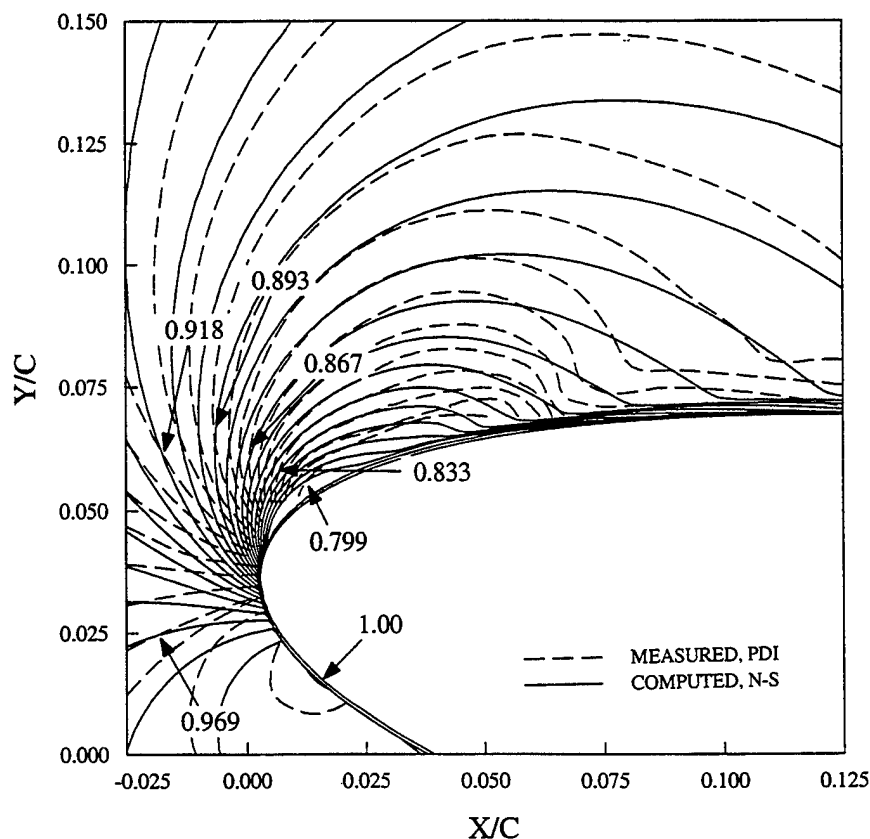


Figure 7.17. Computed and Measured Density Contours (PDI) Near the Airfoil Leading Edge. $M_\infty = 0.3$, $\alpha = 10^\circ - 2^\circ \sin \omega t = 8.8^\circ (\text{up})$, $k = 0.1$, $Re = 540,000$, $(x/c)_{tr} = 0.025$, $G_{\gamma_{tr}} = 200$.

heights (0.5% chord) above the airfoil. But, major differences are evident at the trailing ends of the density contours, where measured contours are up to 2.5% chord downstream of the equivalent predicted contours. Again, computed contours at the forward edge of the separation bubble begin on the order of 1.0% chord forward of equivalent measured contours. The numerical predictions for the oscillating airfoil at $\alpha = 10^\circ$ have fewer density contours in the flow field than in the corresponding flow for steady analysis at the same angle of attack. This is attributable to the lag effects that are inherent to oscillatory/unsteady flows.

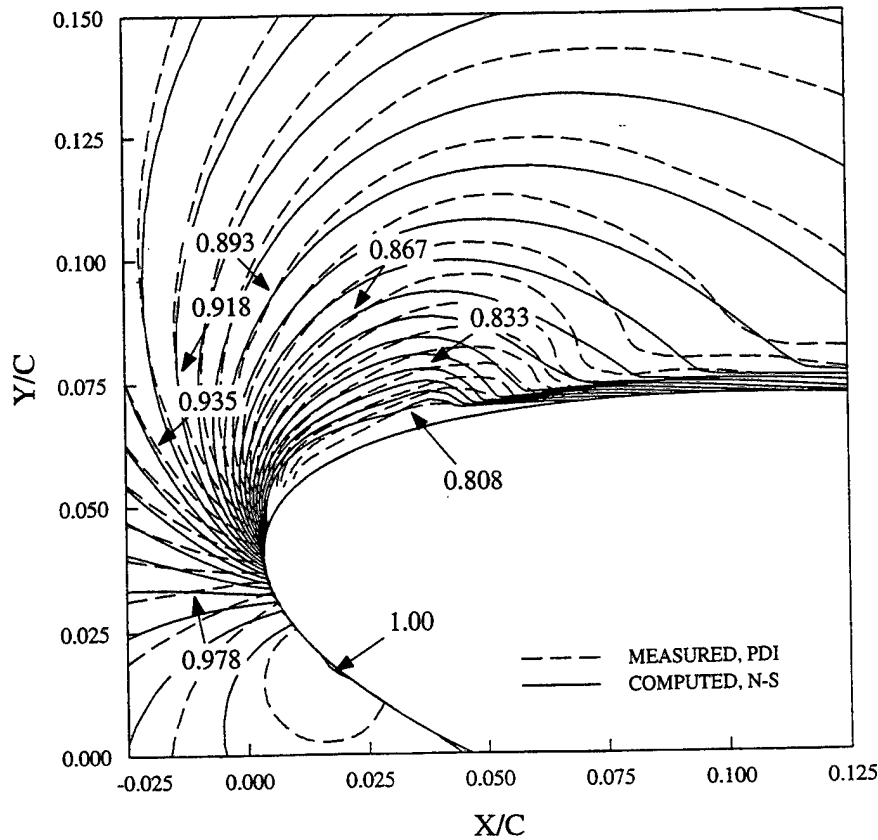


Figure 7.18. Computed and Measured Density Contours (PDI) Near the Airfoil Leading Edge. $M_\infty = 0.3$, $\alpha = 10^\circ - 2^\circ \sin \omega t = 10^\circ$ (up), $k = 0.1$, $Re = 540,000$, $(x/c)_{tr} = 0.025$, $G_{\gamma_{tr}} = 200$.

As the airfoil pitches up from $\alpha = 10^\circ$ to 11.2° , the number of density contours in the flow field has increased to 29 and the local flow attains a maximum Mach number of 0.75. Figure 7.19 shows that measured and predicted contours are more densely packed over the leading-edge airfoil surface. Some inner measured contours are lower in height over the airfoil surface than the predictions and are only slightly higher than the predictions in the flow field at a density ratio of 0.833, for example. Both measured and computed density contours downstream of the suction peak extend along the airfoil surface much the same as those at 10° angle of attack. Again, major differences are seen near the downstream end of the separation bubble, where the measured contours converge abruptly with the airfoil surface and are as much as 3.0% chord downstream of equivalent predicted contours, which merge more gradually with the airfoil surface. The picture at the leading edge of the separation bubble remains, however, the same. Recall, as reported by Cho et al. [Ref. 58], the aft shift in the measured suction pressure peak area is in part attributable to optical

distortions as a result of the large density gradients over the airfoil leading edge. Overall, the density comparisons give a measured separation bubble that is up to 2% chord greater in length and height than the predicted separation bubble.

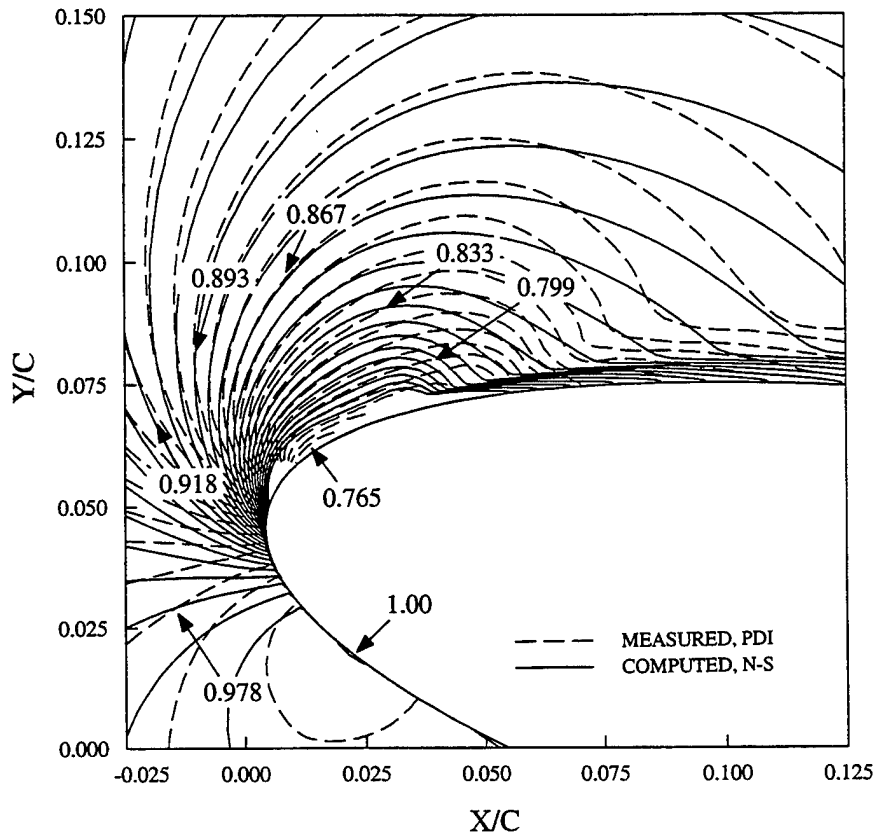


Figure 7.19. Computed and Measured Density Contours (PDI) Near the Airfoil Leading Edge. $M_\infty = 0.3$, $\alpha = 10^\circ - 2^\circ \sin \omega t = 11.2^\circ$ (up), $k = 0.1$, $Re = 540,000$, $(x/c)_{tr} = 0.017$, $G_{\gamma_{tr}} = 200$.

2. Pressure Distributions and Computed Skin-Friction Coefficients

Measured and computed pressure distributions at the extremes of the oscillation cycle, $\alpha = 8^\circ$ and 12° , are compared in Figure 7.20. There is good agreement between a majority of the predicted and measured pressure distributions at $\alpha = 8^\circ$ angle of attack with transition onset specified at $x/c = 0.025$. However, the measured suction-pressure peak is 17% lower than the computed value and the extent of the pressure plateau is greater than in the

computations. Recall, as stated before, that Gaster [Ref. 15] and Tani [Ref. 5] reported that the end of the separation bubble cannot be precisely determined from the pressure distributions alone. The computed suction pressure peak is slightly greater than that previously given for 8° steady angle of attack in Figure 7.10 attributable to airfoil oscillation in the range between 8 and 12° angle of attack. The computed skin friction distribution gives negative values in the separation bubble region from 2.3% to 5.8% chord downstream.

At $\alpha = 12^\circ$ with transition onset specified at $x/c = 0.012$, on the other hand, the computed suction pressures significantly overshoot the measured ones. But, the overall negative computed skin friction area ($0.0116 \leq x/c \leq 0.08$) still indicates a separation bubble of comparable size to the measured one along the airfoil surface. As expected, the onset of stall is delayed during the upstroke yielding a greater suction pressure peak and a stable solution at $\alpha = 12^\circ$ in contrast to the steady case result. For both angles of attack, negative C_{fs} are predicted less than 0.3% chord forward of transition onset, indicating a laminar flow separation.

Computed and measured pressure distributions in Figure 7.21 are for $\alpha = 10^\circ$, during the airfoil upstroke and downstroke. Computed skin-friction distributions are included in the plot. It is apparent from the pressure distribution differences at 10° angle of attack during airfoil downward motion that the computations did not predict the shedding of the dynamic stall vorticity that was described earlier. The transition model was developed for steady flows void of the changing pressure gradients that are part of the oscillating airfoil flow at high angles of attack. The unsteady airfoil motion poses many problems for the numerical modeling as shown by the abrupt changes in the skin-friction coefficient in the separation bubble region. This aspect of the problem requires much further study and therefore is omitted from further discussion in this work. Skin-friction coefficients become negative at $x/c = 0.0135$ for 10° angle of attack (up) and at $x/c = 0.0116$ for 10° angle of attack (down), indicating a laminar separation bubble.

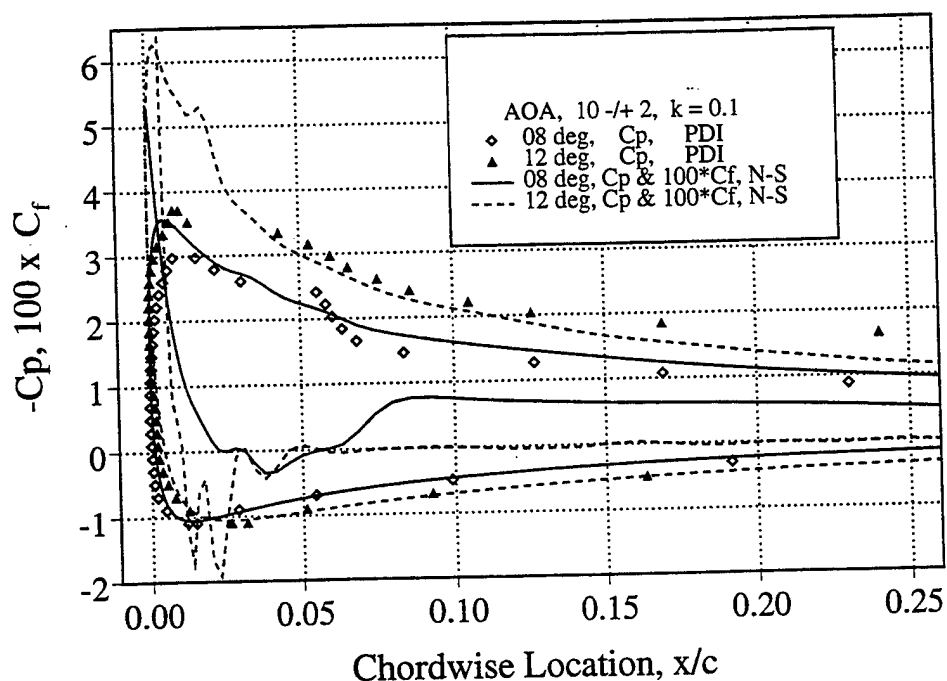


Figure 7.20. Computed and PDI Derived Pressure Distributions Near the Airfoil Leading Edge. $M_\infty = 0.3$, $\alpha = 10^\circ - 2^\circ \sin \omega t = 8$ and 12° , $k = 0.1$, $Re = 540,000$, $(x/c)_{tr} = 0.025$ and 0.012 , $G_{\gamma_{tr}} = 200$.

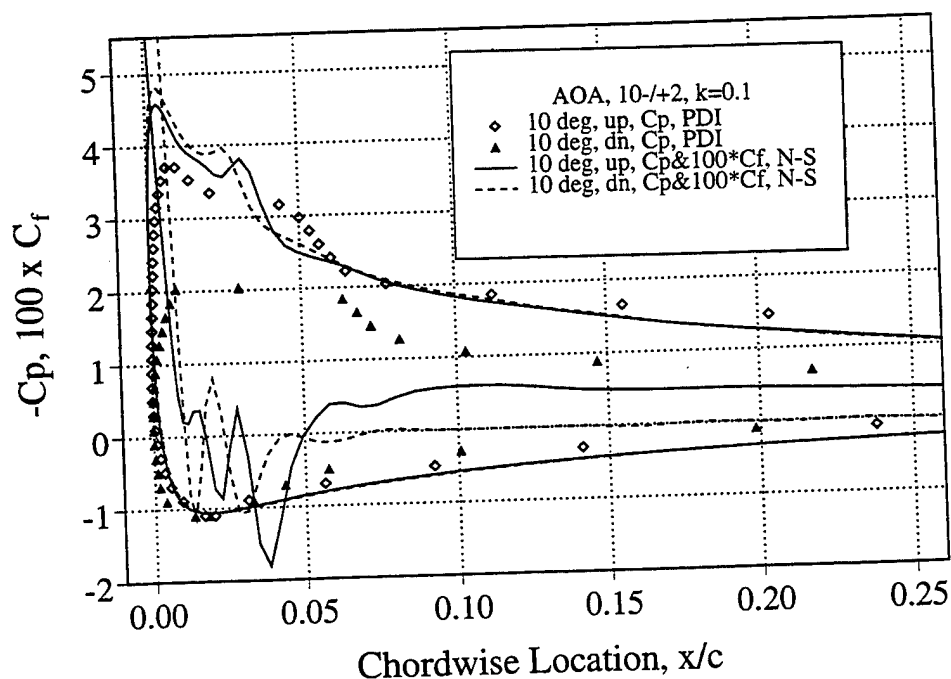


Figure 7.21. Computed and PDI Derived Pressure Distributions Near the Airfoil Leading Edge. $M_\infty = 0.3$, $\alpha = 10^\circ - 2^\circ \sin \omega t = 10^\circ$ (up / down), $k = 0.1$, $Re = 540,000$, $(x/c)_{tr} = 0.025$ and 0.020 , $G_{\gamma_{tr}} = 200$.

3. Transition Onset, Flow Separation and Reattachment

Figure 6.27 showed the specified transition onset locations for both the steady and unsteady N-S analysis, while holding the $G_{\gamma_{tr}}$ value at 200. Transition onset clearly moved forward as the angle of attack increases in both cases. Unsteady transition onset locations were specified aft of steady locations on the airfoil upstroke and forward of the same during the airfoil downstroke. Only a small "window" of solution convergence was possible at $\alpha = 12^\circ$, suggesting a flow on the verge of stall and presenting some of the difficulties in numerically modeling the flow physics.

Flow separation and reattachment locations along the airfoil surface as predicted by the N-S computations are given in Figure 7.22. As expected, flow separation is predicted to move forward as the angle of attack increases. Using negative skin-friction coefficients to indicate flow separation for the low-frequency oscillating airfoil flow as in the steady flow analysis, flow-separation location differences are shown to be relatively minor. Prediction of similar flow-separation locations is consistent with the low frequency airfoil oscillation. Flow reattachment moves downstream as the angle of attack increases and upstream as the angle of attack decreases. Also note that, during the upstroke at angles of attack exceeding 10° , reattachment becomes difficult to define because of multiple separation bubbles that are predicted by the numerical solution. Steady angle of attack computations predict a separation bubble length along the airfoil surface from 2.7 to 5.9% chord at $\alpha = 8^\circ$. At $\alpha = 12^\circ$, the separation bubble length is predicted to increase in size, extending from 1 to 7% chord downstream. The unsteady airfoil flow separation bubbles were similar in size to slightly greater than the steady results for angles of attack less than 10° . Thereafter, multiple areas of reverse flow are incorrectly predicted by the N-S calculations.

A summary of specified transition onset locations and those predicted by Michel's criterion for both the steady flow and the low-amplitude oscillations are given in Table 7.1. Likewise, the transition length values predicted by Cebeci's correlation formula are given in Table 7.1. The N-S solutions for transition onset

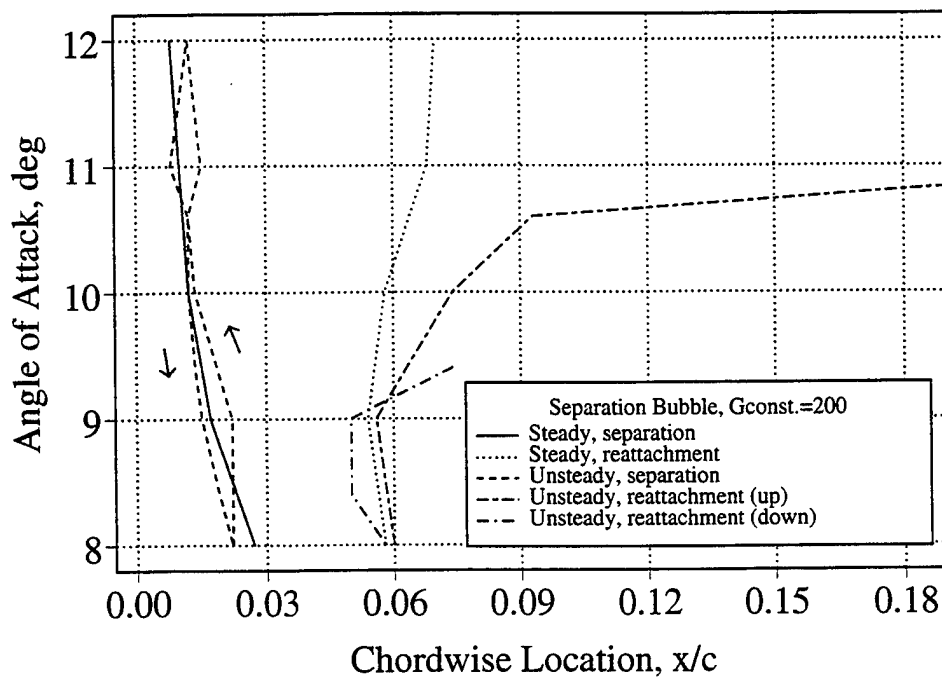


Figure 7.22. Flow Separation and Reattachment Estimates for Steady and Oscillatory Computations. $M_\infty = 0.3$, $\alpha = 10^\circ - 2^\circ \sin \omega t$, $k = 0$ and 0.1 .

that most closely matched the measurements were 1% to 1.5% chord downstream of those predicted by Michel's criterion. This distance downstream along the airfoil surface is appreciable since the predictions for transition onset were generally very close to the airfoil leading edge from 1% to 2% chord. Cebeci's correlation formula for predicting transition length values did not vary widely throughout the angle of attack range. The specified transition length value of 200 was approximately 0.50 of the values predicted by the formulation that gave secondary separation bubbles, unlike the measurements.

Table 7.1 N-S Code Transition Onset and Transition Length Criteria.

	Flow Over Steady Airfoil			Oscillatory Airfoil Flow		
Angle of Attack, deg (Oscill. - up/down)	$(x/c)_{tr}$, (Michel)	$G_{\gamma_{tr}}$, (Cebeci)	$(x/c)_{tr}$ Specified, $G_{\gamma_{tr}} = 200$	$(x/c)_{tr}$, (Michel)	$G_{\gamma_{tr}}$, (Cebeci)	$(x/c)_{tr}$ Specified, $G_{\gamma_{tr}} = 200$
6	0.025	425	0.040	—	—	—
8 (bottom)	0.023	417	0.035	0.015	410	0.025
9 (up)	0.017	400	0.025	0.014	410	0.025
10 (up)	0.0155	390	0.0225	0.013	400	0.025
11 (up)	0.0135	381	0.0155	0.012	380	0.0183
12 (top)	0.009	360	0.0117	0.002	370	0.0117
11 (down)	—	—	—	0.013	380	0.0145
10 (down)	—	—	—	0.014	390	0.020
9 (down)	—	—	—	0.0145	400	0.0245
8 (bottom)	—	—	—	0.015	410	0.025

4. Velocity Profile Comparisons

Computed and measured U-component velocities are compared for angles of attack of 8° , 9° , 10° , and 11.2° during the airfoil upstroke. As in the steady angle of attack presentations, velocity profile comparisons begin at $x/c = -0.167$, which is 0.50 inch forward of the airfoil leading edge, and then proceed over the leading edge of the airfoil from $0.00 \leq x/c \leq 0.167$ in normalized chord intervals of 0.033. Both measured and computed U velocities are again normalized by the outer velocity (U_o) at $y/c = 0.0167$. An interpolation scheme was used to predict computed velocities at the nodes of the measurement grid. Again, as in the steady flow results, measured and computed velocities forward of the airfoil at $x/c = -0.167$ are in full agreement.

Comparisons of velocity profiles for $\alpha = 8^\circ$ (bottom of the oscillatory cycle) are given in Figure 7.23. Solid lines in the figure represent the computed solution and the measurements are depicted by symbols. Normalized velocities range from 0.0 to 1.44 with the maximum computed velocity at $x/c = 0.033$ being slightly greater than the steady maximum velocity at the same location given in Figure 7.13. Maximum measured velocities in the flow field ($1.1 U_o$) are at both the airfoil leading edge and at 3.3% chord downstream. Generally, the data agreement is within 5% throughout the flow field. Exceptions are the measured velocities at the lowest heights and 3.3 and 6.7% chord downstream that are 38% lower than the predictions and up to 40% lower ($0.82 U_o$ vice $1.25 U_o$) than the steady velocities at the same locations in Figure 7.13. The computations predict a slowed flow region only very close to the airfoil surface. As previously discussed, the reduced velocity region points toward the separation bubble region for the measurements, where the surface of the airfoil is from $0.058 < y/c < 0.064$. Thus, an estimated separation bubble height for the measurements is from 2 to 2.5% chord above the airfoil surface.

Figure 7.24 compares velocity profiles at $\alpha = 8.8^\circ$ (up). Normalized velocities range from 0.0 to 1.46 with the maximum velocity predicted at $x/c = 0.033$ and $y/c = 0.063$, which is only 0.3% chord above the airfoil surface. The maximum measured velocity in the flow field ($1.096 U_o$) is above the airfoil leading edge at $y/c = 0.083$ or approximately 4.5% chord above the airfoil surface. Generally, data agreement is within 5% throughout the flow field, except in the region where the reduced measured velocities point toward the separation bubble. Measured velocities for the forced oscillation at the lowest heights and 3.3 and 6.7% chord downstream are as much as 45% less than the predictions. Compared with the previous results at the lower angle of attack, measured velocities are lower by 5 to 10% in the region from 3.3 to 10% chord downstream at the lower heights. Because of the increased angle of attack and the larger region of reduced velocities, the estimated separation bubble height for the measurements at $\alpha = 8.8^\circ$ (up) remains from 2 to 2.5% chord above the airfoil surface.

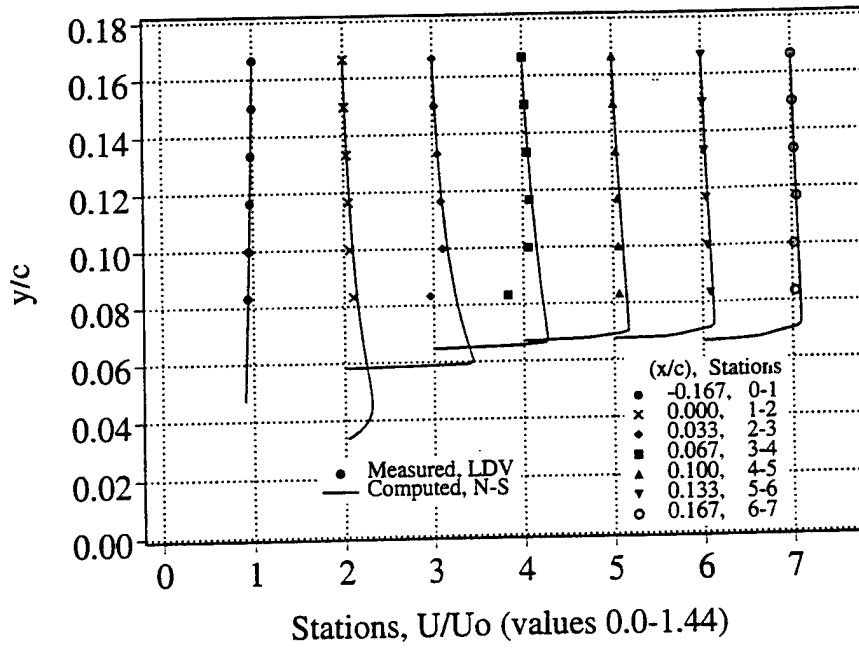


Figure 7.23. Computed and Measured Velocity Profiles Near the Airfoil Leading Edge. $M_\infty = 0.3$, $\alpha = 10^\circ - 2^\circ \sin \omega t = 8^\circ$, $k = 0.1$, $Re = 540,000$.

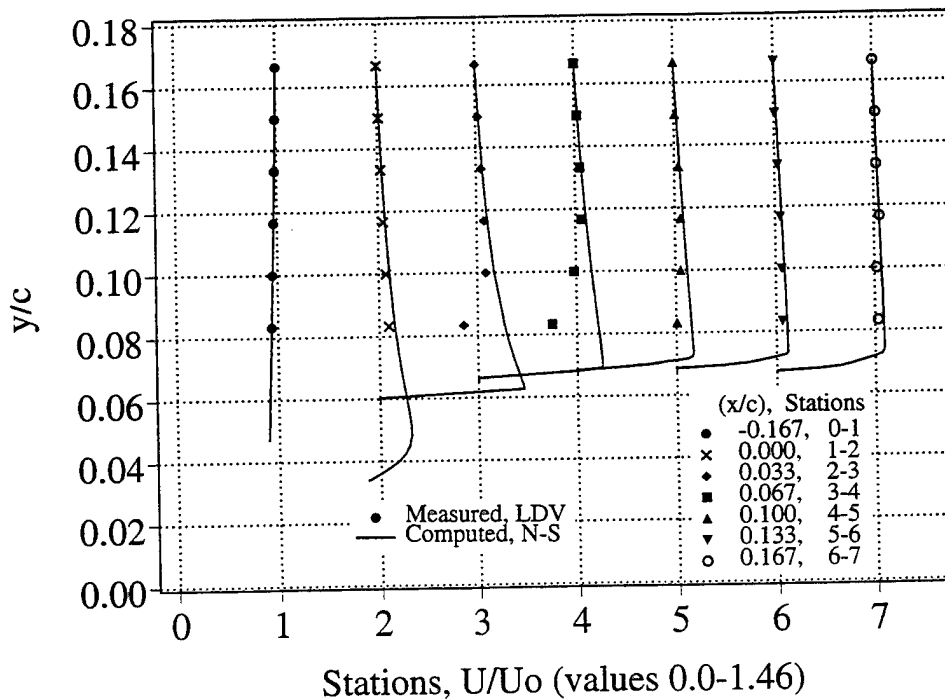


Figure 7.24. Computed and Measured Velocity Profiles Near the Airfoil Leading Edge. $M_\infty = 0.3$, $\alpha = 10^\circ - 2^\circ \sin \omega t = 8.8^\circ(\text{up})$, $k = 0.1$, $Re = 540,000$.

Comparisons for $\alpha = 10^\circ$ (up) are shown in Figure 7.25. Maximum predicted velocities have increased to $1.52U_o$, which is slightly less than the steady results and occurs at 3.3% chord downstream and 0.37% chord above the airfoil surface. Measured velocities are reduced to 0.67 and $0.69U_o$ at the lowest heights and 3.3 and 6.7% chord locations downstream. Increased differences between the data points are seen in the region of the reduced velocities as recorded by the measurements that extend to greater heights in the flow field. Appreciable reductions in the measured velocities are noted at $y/c = 0.100$ or approximately 3% chord above the airfoil surface.

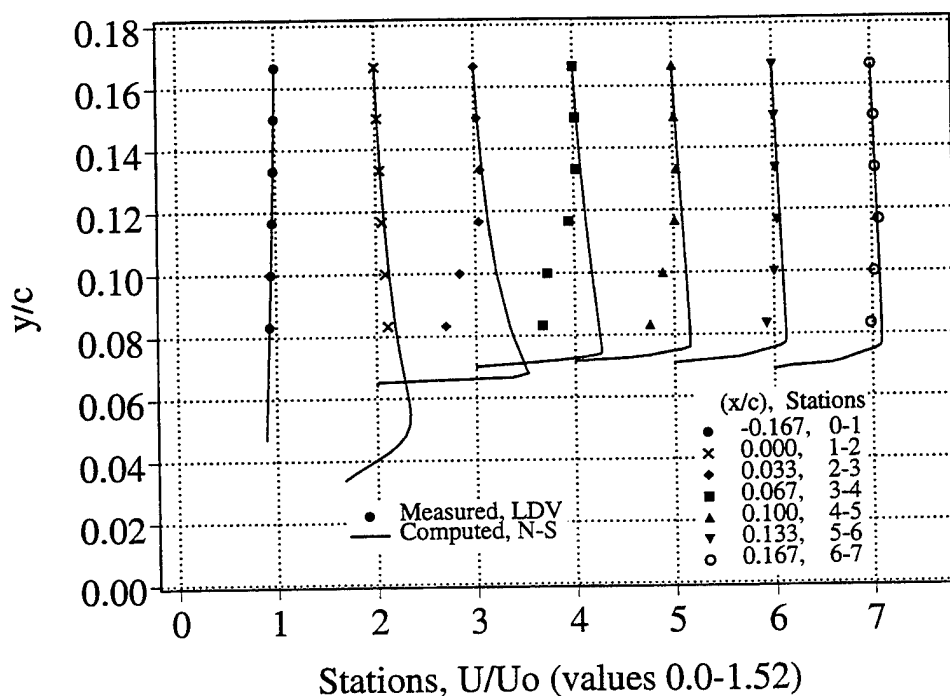


Figure 7.25. Computed and Measured Velocity Profiles Near the Airfoil Leading Edge, $M_\infty = 0.3$, $\alpha = 10^\circ - 2^\circ \sin \omega t = 10$ degrees(up), $k = 0.1$, $Re = 540,000$.

For $\alpha = 11.2^\circ$ (up) in Figure 7.26, the data comparisons show increased differences with even slower velocities measured by the LDV system, extending to greater heights in the flow field. Predicted velocities over the airfoil increased

appreciably to $1.61 U_o$, which occurred at 3.3% chord downstream and 0.35% chord above the airfoil surface. Measured velocities are reduced to $0.64 U_o$ at the lowest heights and 3.3 and 6.7% chord locations downstream. Appreciable reductions in the measured velocities are noted at $y/c = 0.117$, or approximately 4% chord above the airfoil surface.

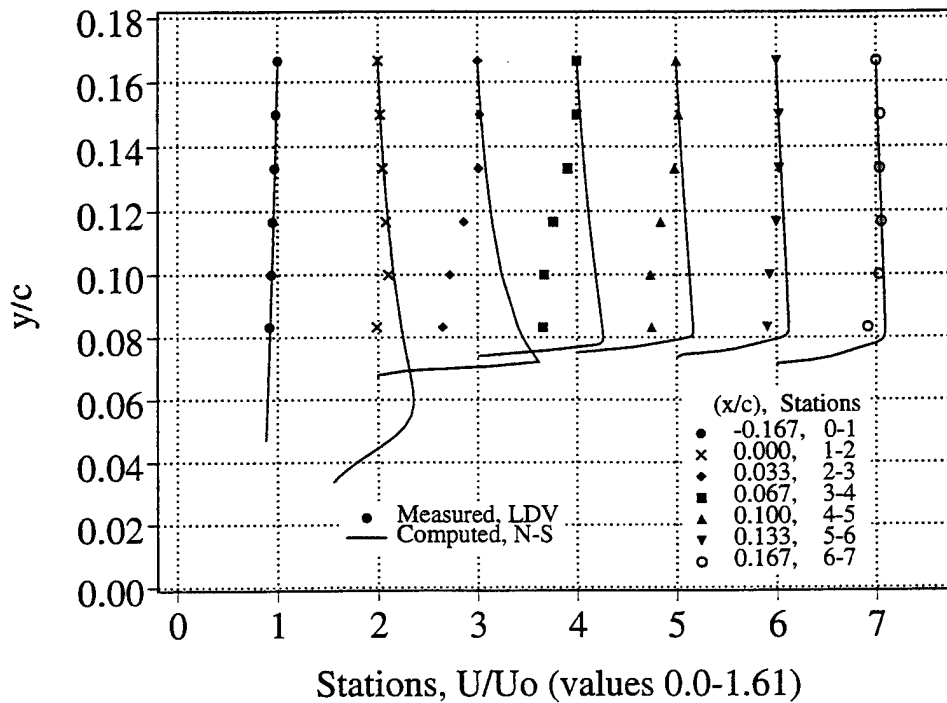


Figure 7.26. Computed and Measured Velocity Profiles Near the Airfoil Leading Edge. $M_\infty = 0.3$, $\alpha = 10^\circ - 2^\circ \sin \omega t = 11.2^\circ$ (up), $k = 0.1$, $Re = 540,000$.

In summary, this study is among the first to critically evaluate the effect of transition onset locations and transition length on computed results by making direct comparisons with experimental measurements under identical conditions. The results of the work were first reported in Reference 69. PDI derived and computed pressure distributions are in excellent agreement for the steady flow analysis, but for the unsteady comparisons the predicted separation bubble starts forward of and is much smaller in height than the measured bubble.

VIII. CONCLUSION AND RECOMMENDATIONS

The formation, development and effect of leading edge separation bubbles on the stalling characteristics of a thin airfoil was the focus of study in this thesis. The LDV velocities and PDI density contours with resultant pressure distributions were used to evaluate computed results from boundary-layer/panel and N-S (thin layer, compressible, Reynolds-averaged) codes. The flow considered for these comparisons was (1) predominated by leading-edge separation bubbles at the higher angles of incidence, and (2) compressible in a transitional Reynolds number range.

Both the PDI and LDV measurements showed that the laminar separation bubble alters the flow characteristics considerably. The experiments indicated that the separation bubble formed at 7 to 8° angle of attack in both the steady and oscillating airfoil tests. The PDI-derived pressure plateau, corresponding to the surface extent of the bubble, ranged from 2 to 6% chord, decreased slightly in size, and moved slightly forward on the airfoil surface with increasing angles of incidence as a result of the increased adverse pressure gradients. LDV velocities were as high as $1.68 U_{\infty}$ at 12° angle of attack in a region from 5 to 9% chord, enveloping the separation bubble.

Light dynamic stall was observed briefly on the downstroke (below the static stall angle of attack) for the low-amplitude oscillating airfoil flow in both the PDI and LDV tests. This surprising and new result was explained by vorticity balance arguments. The vorticity was partially shed on the airfoil downstroke as the flow adapted to the rapidly decreasing angle of attack. Both steady and dynamic stall was initiated from the bursting of the leading-edge bubble as opposed to trailing-edge flow reversal, pointing to the need for inclusion of flow transition modeling in the computations. For the oscillating airfoil, the LDV and PDI measurements were among the first attempted and successfully made for the flow conditions specified.

The highly separated and complex flow physics associated with the high-amplitude, deep dynamic stall made it intractable for detailed analysis by computational methods. However, the viscous effects were much smaller for the

low-amplitude tests, providing an opportunity to apply different computational analysis methods. Thus, the computational studies were limited to steady and low-amplitude, light dynamic stall flow cases.

The computations were the first to incorporate the flow physics of leading edge separation bubbles and to make comparisons with measured results in flows with substantial pressure gradients near the stalling angle of attack. Both the direct boundary layer and thin-layer N-S codes accounted for boundary layer flow transition to analyze the development of separation bubbles for identical experimental conditions. The Chen-Thyson transition model was used to describe the extent of transition flow region and Michel's criterion was used to make initial predictions of transition onset locations. Pressure distributions, skin-friction coefficients, and velocity profiles over the upper leading edge of the airfoil were shown to change substantially with small changes in (1) the transition onset location, and (2) the flow transition length over the airfoil surface.

Computations that incorporate the flow transition process were found to be critical in predicting separation bubbles that were similar to the measured ones. For both the steady and low-amplitude oscillating airfoil ($8^\circ < \alpha < 12^\circ$), the N-S code predicted a negative skin-friction region that agreed well with the beginning of and extent of the pressure plateau derived from the PDI data. Overall, the agreement between the computations and the measurements was good with slight differences observed in the separation bubble sizes during the airfoil upstroke. However, the N-S analysis did not predict the vortex shedding process that was evident in the measurements during the airfoil downstroke.

Transition onset predictions moved forward with increasing angles of incidence, and the range of specified transition onset locations ($0.040 > x/c > 0.012$) was downstream of Michel's criterion ($0.025 > x/c > 0.002$). This was expected because Michel's criterion was developed for higher Reynolds number flows. The range of flow transition length values and transition onset locations are summarized in Figure 8.1 for NACA 0012 airfoil flows in the transitional Reynolds number range ($10^4 < Re_c < 10^6$). The use of Equation 4.22 and Michel's criterion gave separation bubbles that were much smaller than the measured ones

(dashed curve). The characteristics of measured separation bubbles were most closely matched by the predictions when transition onset locations were specified downstream of Michel's criterion and a transition length value ($G_{\gamma_{tr}} = 200$) less than those predicted by Equation 4.22 were specified (solid line).

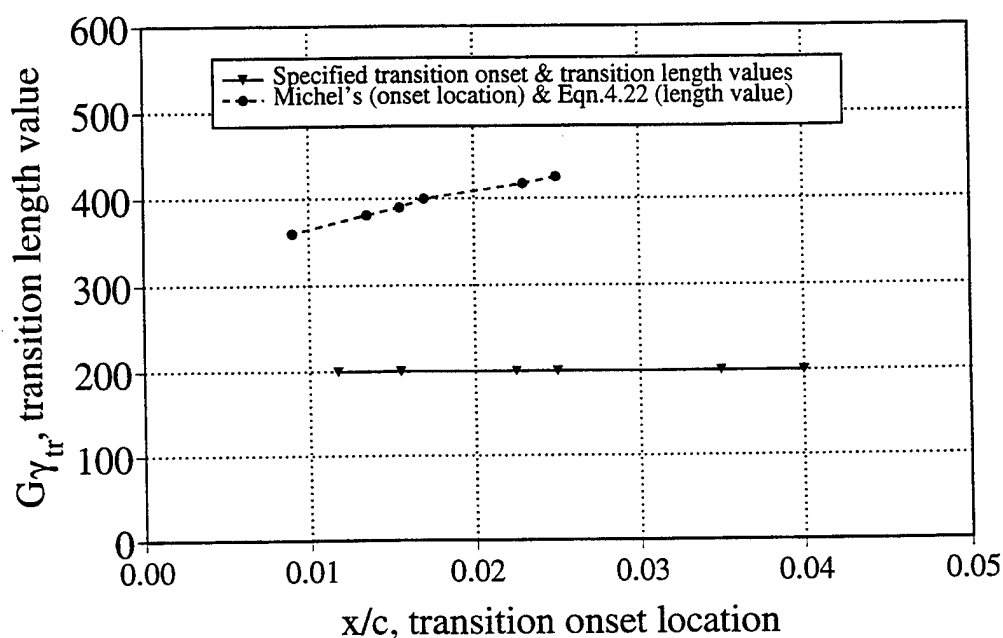


Figure 8.1 Transition Onset and Transition Length Values for NACA 0012 Airfoil Flow, $M_{\infty} = 0.3$, $0^{\circ} < \alpha < 12^{\circ}$, $10^4 < Re < 10^6$.

For future work, more definitive experiments (such as skin-friction measurements) are recommended to determine when and where transition from laminar to turbulent flow takes place, in either the attached or separated boundary layer for flows with airfoil-type pressure gradients. Efforts are needed to understand more fully the vorticity shedding and flow reattachment processes, which require advanced turbulence modeling. Transition length models should account for free-stream turbulence levels, flow curvature effects, and rapidly changing and steep pressure gradients. For higher speed flows, an understanding of shock effects on the behavior of separation bubbles is required. Systematic experimental and analytical studies of the unsteady flow effects on laminar separation and transition should complement each other as in this work.

This research is the first work to critically evaluate the effect of transition onset locations and transition length on computed results by making direct comparisons with measurements for identical conditions. For the oscillating airfoil comparisons, the predicted separation bubble started forward of and was smaller in height than the measured bubble during the airfoil upstroke. The computational schemes need more work to correctly predict the vortex shedding and flow reattachment processes that were evident during the downstroke of the oscillating airfoil. The PDI-derived and computed pressure distributions as well as the LDV and computed velocities were in excellent agreement for the steady angle of attack flow analysis.

REFERENCES

1. Carr, L. W., "Progress in Analysis and Prediction of Dynamic Stall," *Journal of Aircraft*, vol. 25, no. 1 (Jan. 1988), pp. 6-17.
2. Carr, L. W. and Chandrasekhara, M. S., "An Assessment of the Impact of Compressibility on Dynamic Stall," AIAA paper 95-0779, 33rd Aerospace Sciences Meeting, Jan. 1995.
3. Jones, B. M., "An Experimental Study of the Stalling of Wings," *NACA Reports and Memoranda No. 1588*, Dec. 1933.
4. McCullough, B. G. and Gault, D. E., *Examples of Three Representative Types of Airfoil-Section Stall at Low Speed*, NACA TN 2502, Sept. 1951.
5. Tani, I., "Low Speed Flows Involving Bubble Separations," *Progress in Aeronautical Sciences*, vol. 5, 1964, pp. 70-103.
6. McMasters, J. H. and Henderson, M. L., "Low Speed Single Element Airfoil Synthesis," *Tech. Soaring*, vol. 6, 1980, pp. 1-21.
7. Gad-el-Hak, M., "Control of Low-Reynolds-Number Airfoils," Figure 1 in *Low Reynolds Number Aerodynamics*, editor, T. J. Mueller, Springer Verlag, 1989.
8. von Doenhoff, A. E., *A Preliminary Investigation of Boundary Layer Transition Along a Flat Plate with Adverse Pressure Gradient*, NACA TN 639, 1938.
9. Horton, , H. P., *Laminar Separation Bubbles in Two- and Three-Dimensional Incompressible Flow*, Ph. D. Thesis, University of London, 1968.

10. Owen, P. R. and Klanfer, L., "On the Laminar Boundary Layer Separation from the Leading Edge of a Thin Aerofoil," *RAE Rep. Aero. 2508* (Oct. 1953): reissued as A.R.C. Cp 220 (1995).
11. Crabtree, L. F., *The Formation of Regions of Separated Flow on Wing Surfaces*, Reports and Memoranda No. 3122, 1959, London: Her Majesty's Stationery Office.
- 12.. Malkiel, E. and Mayle, R. E., "Transition in a Separation Bubble," *Journal of Turbomachinery*, vol. 118, October 1996.
13. Cebeci, T. and Smith, A. M. O., *Analysis of Turbulent Boundary Layers*, Academic Press, New York, 1974, pg. 332.
14. Gault, D. E., *Boundary-Layer and Stalling Characteristics of the NACA 63-009 Airfoil Section*, NACA TN 1894, June 1949.
15. Gaster, M., "The Structure and Behavior of Separation Bubbles," *ARC R and M no. 3595*, Mar. 1967.
16. O'Meara, M. M. and Mueller, T. J., "Laminar Separation Bubble Characteristics on an Airfoil at Low Reynolds Numbers," *AIAA Journal*, vol. 25 (8), (August 1987), pp. 1033-1041.
17. Cebeci T., and Bradshaw, P., *Momentum Transfer in Boundary Layers*, Hemisphere Publishing Corporation, Washington, 1977, pg. 153.
18. Herbert, Th. and Bertolotti, F. P., "Stability Analysis of Nonparallel Boundary Layers," *Bull. Am. Phys. Soc.*, vol. 32 (1987), p. 2079.
19. Dhawan, S. and Narasimha, R., "Some Properties of Boundary Layer Flow During Transition from Laminar to Turbulent Motion," *Journal of Fluid Mechanics*, vol. 3 (1958), pp. 418-436.

20. Chen, K. K., and Thyson, N. A., "Extension of Emmons Spot Theory to Flows on Blunt Bodies," *AIAA Journal*, vol. 9, May 1971, pp. 821-825.
21. Cebeci, T., "Essential Ingredients of a Method for Low Reynolds Number Airfoil," *AIAA Journal*, vol. 27, no. 12 (Dec. 1989), pp. 1680-1688.
22. Abu-Ghannam, B. J. and Shaw, R., "Natural Transition of Boundary Layers - the Effects of Pressure Gradient and Flow History," *Journal of Mechanical Engineering Science*, vol. 22, no. 5 (1980), pp. 213-228.
23. Gostelow, J. P., Blunden, A. R., and Walker, G. J., "Effects of Free-Stream Turbulence and Adverse Pressure Gradients on Boundary Layer Transition," *ASME Gas Turbine Congress, 92-GT-380*, 1992.
24. McCroskey, W. J., "The Phenomenon of Dynamic Stall," NASA TM 81264, March 1981.
25. Carr, L. W., McCroskey, W. J., McAlister, K. W., Pucci, S. L., and Lambert, O., "An Experimental Study of Dynamic Stall on Advanced Airfoil Sections," Volume 3: Hot-Wire and Hot-Film Measurement, NASA TM 84245, Dec. 1982.
26. Chandrasekhara, M. S. and Carr, L. W., "Flow Visualization Studies of the Mach Number Effects on the Dynamic Stall of Oscillating Airfoils", *Journal of Aircraft*, vol. 27, no. 6 (June 1990), pp. 516-522.
27. Cebeci, T., Platzer, M. F., Jang, H. M., and Chen, H. H., "An Inviscid-Viscous Interaction Approach to the Calculation of Dynamic Stall Initiation on Airfoils," *ASME Journal of Turbomachinery*, vol. 115, October 1993, pp. 714-723.
28. Drela, M. and Giles, M. B., "Viscous-Inviscid Analysis of Transonic and Low Reynolds Number Airfoils," *AIAA Journal*, vol. 25, no. 10 (1985), pp. 1347-1355.

29. Evangelista, R., McGhee, R. J., and Walker, B. S., "Correlation of Theory to Wind Tunnel Data at Reynolds Numbers Below 500,000", in *Low Reynolds Number Aerodynamics*, editor, T. J. Mueller, Springer Verlag, 1989, pp. 146-160.
30. Walker, G. J., Subroto, P. H., and Platzer, M. F., "Transition Modeling Effects on Viscous/Inviscid Interaction Analysis of Low Reynolds Number Airfoil Flows Involving Laminar Separation Bubbles," *ASME Paper 88-GT-32*, American Society of Mechanical Engineers, New York, 1988.
31. McCroskey, W. J., and Fisher, R. K., "Detailed Aerodynamic Measurements on a Model Rotor in the Blade Stall Regime," *Journal of the American Helicopter Soc.*, vol. 17, no. 1. (January 1972), pp. 20-30.
32. Carr, L. W., and Chandrasekhara, M. S., "Design and Development of a Compressible Dynamic Stall Facility," *J. of Aircraft*, vol. 29, no. 3 (June 1992), pp. 314-318.
33. Sticht, C. D., "Development of Drive Mechanism for an Oscillating Airfoil," *Symposium on Aerospace Mechanisms*, NASA Langley Research Center, Hampton, Va., 4-6 May 1988.
34. Chandrasekhara, M. S., and Ahmed, S., "Laser Velocimetry Measurements of Oscillating Airfoil Dynamic Stall Field," AIAA Paper 91-1799, June 1991.
35. Smartt, R. N., "Point-Diffraction Interferometry as a Diagnostic for Alignment," *Optical Alignment II*, SPIE, vol. 483 (1984).
36. Smartt, R. N., and Steel, W. H., "Theory and Application of Point-Diffraction Interferometers," *J. Appl. Phys.*, vol. 14, Suppl. 14-1 (1975), pp. 351-356.

37. Carr, L. W., Chandrasekhara, M. S., Ahmed, S., and Brock, N., "A Study of Dynamic Stall Using Real Time Interferometry," AIAA Paper No. 91-0007, Jan. 1991.
38. Brock, N. J., Chandrasekhara, M. S., and Carr, L. W., "A Real Time Interferometry System for Unsteady Flow Measurements," *ICIASF'91 Record*, International Congress on Instrumentation in Aerospace Simulation Facilities, Rockville, Md., 25-28 October 1991.
39. Chandrasekhara, M. S., Wilder, M. D., Carr, L. W., "Boundary Layer Tripping Studies of Compressible Dynamic Stall Flow," 25th AIAA Fluid Dynamics Conference, AIAA-94-2340, 20-23 June 1994.
40. Goldstein, R. J., *Fluid Mechanics Measurements*, Chapter 8, Hemisphere Publishing Corp., 1983.
41. Chandrasekhara, M. S., and Van Dyken, R. D., "LDV Measurements in Dynamically Separated Flows," *Proc. 5th Laser Anemometry Conference, Advances and Applications*, SPIE vol. 2052, 1993, pp. 305-312.
42. Ahmed, S., and Chandrasekhara, M. S., "Reattachment Studies of an Oscillating Airfoil Dynamic Stall Flowfield," *AIAA Journal*, vol. 31, no. 4 (1994), pp. 1006-1012.
43. Davis, S. S., "Measurement of Discrete Vortex Noise in a Closed-Throat Wind Tunnel," AIAA Paper 75-488, March 1975.
44. Kadlec, R. A., and Davis, S. S., "Visualization of Quasiperiodic Flows," AIAA Paper 78-502R; see also *AIAA Journal*, vol. 17, no. 11 (1979), pp. 1164-1169.
45. Hess, J. L., and Smith, A. M. O., "Calculation of Potential Flow About Arbitrary Bodies," *Progress in Aeronautical Sciences*, vol. 8, Pergamon Press, Oxford, 1966, pp. 1-138.

46. Teng, N-H., *The Development of a Computer Code (U2DIIF) for the Numerical Solution of Unsteady, Inviscid, and Incompressible Flow Over an Airfoil*. Master's Thesis, Naval Post-Graduate School, Monterey, Calif., June 1987.
47. Basu, B. C., and Hancock, G. J., "The Unsteady Motion of a Two-Dimensional Aerofoil in Incompressible Inviscid Flow," *Journal of Fluid Mechanics*, vol. 87 (July 1978), pp. 159-168.
48. Giesing, J. P., "Nonlinear Two-Dimensional Unsteady Potential Flow With Lift," *Journal of Aircraft*, vol. 5, no. 2 (Mar-Apr 1968), pp. 135-143.
49. Rumsey, C. L., and Anderson, W. K., "Some Numerical and Physical Aspects of Unsteady Navier-Stokes Computations Over Airfoils Using Dynamic Meshes," AIAA Paper 88-0329, 1988.
50. Visbal, M. R., "Effect of Compressibility on Dynamic Stall of a Pitching Airfoil," AIAA Paper 88-0132, 1988.
51. Ekaterinaris, J. A., "Compressible Studies on Dynamic Stall," AIAA Paper 89-0024, 1989.
52. Rai, M. M., "Navier-Stokes Simulations of Rotor-Stator Interaction Using Patched and Overlaid Grids," *AIAA Journal of Propulsion and Power*, vol. 3 (1987), pp. 387-396.
53. Osher, S. and Chakravarthy, S. R., "Upwind Schemes and Boundary Conditions With Applications to Euler Equations in General Geometries," *Journal of Computational Physics*, vol. 50 (1983), pp. 447-481.
54. Steger, J. L., and Warming, F. R., "Flux Vector Splitting of the Inviscid Gas Dynamic Equations With Applications to Finite-Difference Methods," *Journal of Computational Physics*, vol. 40 (1981), pp. 263-293.

55. Jang, H. M., Ekaterinaris, J. A., Platzer, M. F., and Cebeci, T., "Essential Ingredients for the Computation of Steady and Unsteady Boundary Layers," *Journal of Turbomachinery*, vol. 13 (1991), pp. 608-616.
56. Mack, L. M., "Transition Prediction and Linear Stability Theory," *Laminar-Turbulent Transition*, AGARD CP-224, paper no. 1, 1977.
57. Stuckert, G. K., Herbert, T., and Esfahanian, V., "Stability and Transition on Swept Wings," AIAA-93-0078, 1993.
58. Ekaterinaris, J. A., Chandrasekhara, M. S., and Platzer, M. F., "Analysis of Low Reynolds Number Airfoil Flows," *Journal of Aircraft*, vol. 32, no. 3 (1995).
59. Baldwin, B. S., and Lomax, H., "Thin Layer Approximation and Algebraic Model for Separated Turbulent Flows," AIAA Paper 78-257, 1978.
60. Baldwin, B. S., and Barth, T. J., *A One-Equation Turbulence Transport Model for High Reynolds Number Wall-Bounded Flows*, NASA TM 102847, 1990.
61. Clarkson, J. D., Ekaterinaris, J. A., and Platzer, M. F., "Computational Investigation of Airfoil Stall Flutter," *Unsteady Aerodynamics, Aeroacoustics and Aeroelasticity of Turbomachines and Propellers*, ed. H. M. Atassi, Springer-Verlag, 1991, pp. 415-432.
62. Ekaterinaris, J. A., and Menter, F. R., "Computation of Oscillating Airfoil Flows With One- and Two-Equation Turbulence Models," *AIAA Journal*, vol. 32, no. 12 (December 1995), pp. 2359-2365.
63. Carr, L. W., Chandrasekhara, M. S., and Brock, N., "A Quantitative Study of Unsteady Compressible Flow on a Oscillating Airfoil," *Journal of Aircraft*, vol. 31, no. 4 (Jul.-Aug. 1994), pp. 892-898.

64. Carr, L. W. and Chandrasekhara, M. S., "A Study of Compressibility Effects on Dynamic Stall of Rapidly Pitching Airfoils," *Computer Physics Communications* 65, pp. 62-68, 1991.
65. Van Dyken, R. D. and Chandrasekhara, M. S., "Leading Edge Velocity Field of an Oscillating Airfoil in Compressible Dynamic Stall," *AIAA Paper* 92-0193, Jan. 1992.
66. Nowak, L. M. *Computational Investigations of a NACA 0012 Airfoil in Low Reynolds Number Flows*, Monterey, Calif., Naval Postgraduate School, Masters Thesis, 1992.
67. Hoheisel, H. et al., "A Comparison of Laser-Doppler Anemometry and Probe Measurements with the Boundary Layer of an Airfoil at Subsonic Flow," in *Laser Anemometry in Fluid Mechanics-II*, Lisbon, Portugal, July 1984, LADOAN, pp. 143-157.
68. Cho, Y. C., Carr, L. W., and Chandrasekhara, M. S., "Corrections to Fringe Distortion due to Flow Density Gradients in Optical Interferometry," *AIAA Paper* 93-0631, Jan. 1993.
69. Van Dyken, R. D., Ekaterinaris, J. A., Chandrasekhara, M. S., and Platzer, M. F., "Analysis of Compressible Light Dynamic Stall Flow at Transitional Reynolds Numbers," *AIAA Journal*, vol. 34, no. 7 (July 1996).

INITIAL DISTRIBUTION LIST

1. Defense Technical Information Center 2
8725 John J. Kingman Rd., Ste 0944
Ft. Belvoir, VA 22060-6218

2. Dudley Knox Library 2
Naval Postgraduate School
411 Dyer Rd.
Monterey, CA 93943-5101

3. Prof. Max F. Platzer 10
Code AA/Pl
Dept. of Aeronautics and Astronautics
Naval Postgraduate School
699 Dyer Road
Monterey, CA 93943-5106

4. Prof. M. S. Chandrasekhara 10
Navy-NASA Joint Institute of Aeronautics
NASA Ames Research Center, M.S. 260-1
Moffett Field, CA. 94035-1000

5. Prof. Raymond P. Shreeve 1
Code AA/Sf
Dept. of Aeronautics and Astronautics
Naval Postgraduate School
699 Dyer Road - Room 137
Monterey, CA 93943-5106

6. Prof. Beny Neta 1
Code MA/Nd
Dept. of Mathematics
Naval Postgraduate School
699 Dyer Road
Monterey, CA 93943-5106

7. Prof. Yogandra Joshi 1
Dept. of Mechanical Engineering
University of Maryland
College Park, MD 20742

8.	Naval Air Warfare Center Weapons Division	1
	Technical Library, Code 4BL0000D	
	China Lake, CA 93555-6001	
9.	Robert Van Dyken	7
	NAWCWPNS, Code 473110D	
	China Lake, CA 93555-6001	
10.	Dr. Richard J. Margason	1
	12763 Lake Wildwood Drive	
	Penn Valley, CA 95946	
11.	Dr. Jerry Higman	1
	c/o Katsumasa Iso	
	5-3 Hanazono-Cho	
	Utsunomiya-Shi, Tochigi-Ken 302	
	Japan	
12.	Edward L. Jeter	1
	NAWCWPNS, Code 4722EOD	
	China Lake, CA 93555-6001	
13.	Dr. Craig Porter	1
	NAWCWPNS, Code 473C00D	
	China Lake, CA 93555-6001	